

***Extracting Reliable Mechanical Properties  
using the Nanoindentation Technique***

*by*

**Noushin Moharrami**

---

*Thesis submitted for the degree of Doctor of Philosophy in the Faculty of  
Science, Agriculture and Engineering of Newcastle University*

---

*School of Chemical Engineering and Advanced Materials  
Newcastle University  
Newcastle upon Tyne, U.K.*

December 2013

## *Declaration*

---

This dissertation is submitted for the degree of Doctor of Philosophy at Newcastle University. I hereby declare that the work described in this thesis is my own work and effort except where acknowledged in the text. This work has not been submitted for any other degree and it was carried out entirely by myself under the supervision of Prof. S. J. Bull in the Department of Chemical Engineering and Advanced Materials at Newcastle University.

Parts of this work have been published:

S. J. Bull, L. Sanderson, N. Moharrami and A. Oila, ‘Effect of microstructure on hardness of submicrometre thin films and nanostructured devices’, *Materials Science and Technology*, Vol. 28, pp.1177-1185, 2012.

N. Moharrami, D. J. Langton, O. Sayginer and S.J. Bull, ‘Why does titanium alloy wear cobalt chrome alloy despite lower bulk hardness: a nanoindentation study?’, *Thin Solid Films*, Vol.549, pp. 79-86, 2013.

N. Moharrami, A. Oila, S. J. Bull, Extracting mechanical properties of copper coatings on oxidised silicon substrates by nanoindentation, *Journal of Physics D: Applied Physics*, Vol.47, Accepted, 2014.

N. Moharrami, S. J. Bull, A Comparison of Nanoindentation Pile-up in Bulk Materials and Thin Films, *Thin Solid Films*, Accepted, 2014.

## *Abstract*

---

Extracting the mechanical properties of thin films and small volumes of bulk materials through the use of nanoindentation is a well established technique but getting good data from all types of test sample is not always easy. Factors such as surface roughness and oxidation, density/porosity of the material, adhesion/detachment of a thin film, pile-up/sink-in, the presence of the substrate, as well as grain size and its distribution have a significant effect on the observed mechanical properties (e.g. Young's modulus and hardness). Considerable differences between predicted and observed performance can be seen depending on the material tested and how it has been prepared. This thesis concerns developing test protocols to get good nanoindentation data and reliable measurements of the properties for a range of material types (chiefly metals and ceramics).

Firstly, this work highlights the effect of crystallographic anisotropy, grain size, shape and orientation on the mechanical response of metallic thin films such as copper used for semiconductor metallisation. Results obtained on highly polished semiconductor materials were compared with those from engineering surfaces with much higher roughness which show increased scatter in results across the complete range of contact scales. Further studies were carried out on hard coatings and bulk materials such as titanium carbide, zirconium nitride and tungsten. The scatter in data obtained at low tests loads is dominated by anisotropy and grain size effects but disappears at higher loads. For soft materials such as copper, the appearance of pile-up was shown to be significant when compared with harder materials which tend to sink-in.

Secondly, to assess the effect of creep (time-dependent behaviour) and also grain boundary effects on the measured mechanical properties, soft materials with a range of grain sizes have been examined. Different indentation control cycles (load and displacement control, single indent and multicycling tests) have been investigated to determine what is most suitable with displacement control being essential in most cases. To study the effect of the density/porosity of the sample and its surface roughness on mechanical properties, the work was carried out on porous coatings of tin, copper and copper-tin alloy coatings with a low density. To further understand the behaviour of porous materials and their mechanical properties, finite element analysis was also used to compare the experimental results with a numerical

model. The size, shape and location of porosity with respect to the indenter is critical in determining the mechanical properties of a porous material obtained from nanoindentation analysis.

Finally, fully processed engineering surfaces were investigated at the component scale to compare with idealised flat plate samples. Titanium-based and cobalt-chrome alloys in the form of femoral heads and stems for replacement hips have been used to assess the effect of in service oxidation on mechanical properties. These have been studied to look at the effects of sample fixturing and support and surface contact in worn and virgin regions of the sample surface. The extent of oxidation and the mechanical properties of the oxide produced are critical in dictating performance.

## *Acknowledgments*

---

First and foremost I wish to deeply thank my supervisor Prof. Steve Bull. His supervision and guidance have been of significant benefit throughout my PhD and I wish to acknowledge his capacity for assistance, regardless of when it was required. I am also grateful to Dr Adrian Oila for his useful advice and discussions.

I am very appreciative to many members of the department for their help. I am specifically thankful to Maggie White and Pauline Carrick for assistance with the XRD, SEM, EBSD and EDX measurements at ACMA, Naoko Sano for assistance with XPS analysis at NEXUS and also thankful for the wide ranging assistance of Neville Dickman throughout my research.

I give my sincere thanks to Peyman Zoroufchian Moghadam for his support and advice during my PhD. I also thank Richard Abernethy for being supportive throughout my time here in Newcastle. I am grateful to all my colleagues from CEAM for their insights, friendship and support. I am also grateful to Dena Ghiasy and Marjan Bojarnejad for their continued friendship.

I would like to acknowledge Swatilekha Ghosh, David Langton, ISO, IMEC, INEX and Teer coatings Ltd for providing me with many of the samples that have been used in this work. However, any opinions, findings, conclusions or recommendations expressed in this publication are those of the author and do not necessarily reflect the views of the companies or organisations which provided the samples.

Last but not least, I would like to extend my deepest gratitude to my parents for their unwavering support, encouragement and faith. Without their devotion and sacrifice, my accomplishments would not have been possible and I would not be the person I am today. As such, I am eternally indebted to them. I also wish to thank my brothers Tohid and Masoud for their continued belief in me.

# *Table of Contents*

<b>Declaration</b> .....	<b>i</b>
<b>Abstract</b> .....	<b>ii</b>
<b>Acknowledgments</b> .....	<b>iv</b>
<b>Lists of Figures</b> .....	<b>viii</b>
<b>List of Tables</b> .....	<b>xiv</b>
<b>Chapter 1. Introduction</b> .....	<b>1</b>
1.1 Hardness .....	1
1.2 Young's Modulus .....	2
1.3 Introduction to Nanoindentation.....	3
1.4 Structure of Thesis.....	4
<b>Chapter 2. Nanoindentation</b> .....	<b>8</b>
2.1 Nanoindentation Procedure .....	8
2.1.1 Load-displacement Curves .....	9
2.1.2 Oliver & Pharr Analysis .....	10
2.2 The Indenter Shape and Geometry .....	14
2.2.1 Berkovich Indenter .....	16
2.2.2 Spherical Indenter.....	17
2.3 Secondary Concepts .....	21
2.3.1 Thermal Drift and Creep .....	21
2.3.2 Machine Compliance and Shape Function .....	23
2.3.3 Initial Penetration Depth.....	25
2.3.4 Piling-Up and Sinking-In .....	25
2.4 Summary.....	26
<b>Chapter 3. Experimental Methods</b> .....	<b>27</b>
3.1 Nanoindentation Instrumentation .....	27
3.1.1 Hysitron Triboindenter .....	29
3.1.2 Tip Selections .....	34
3.1.3 Indentation Types .....	35
3.2 Characterisation.....	40
3.2.1 Atomic Force Microscopy .....	40
3.2.2 Light Microscopy .....	41
3.2.3 Scanning Electron Microscopy.....	41
3.2.4 X-ray Diffraction (XRD).....	44
3.2.5 X-ray Photoelectron Spectroscopy (XPS) .....	44
3.2.6 Raman Spectroscopy .....	45
3.2.7 Object Oriented Finite Element Analysis (OOF2) .....	46
3.3 Summary.....	47
<b>Chapter 4. Studied Materials and Nanoindentation Calibration</b> .....	<b>48</b>
4.1 Copper in Context.....	48
4.1.1 Copper Properties in Microelectronic Devices.....	48
4.1.2 Fabrication of Copper Thin Film.....	49

4.1.3	Copper Texture.....	52
4.1.4	Copper Electromigration .....	54
4.1.5	Challenges for Copper Metallisation: Adhesion and Diffusion.....	55
4.2	Materials .....	55
4.2.1	Fully Dense Thin Films Used in This Study .....	56
4.2.2	Low Density Coatings Used in This Study .....	57
4.2.3	Titanium and Cobalt Chromium Alloys .....	61
4.2.4	Titanium Carbide and Zirconium Nitride.....	61
4.3	Calibration .....	61
4.3.1	Frame Compliance Calibration.....	66
4.3.2	Tip Area Function Calibration.....	68
4.3.3	Targeting Alignment Calibration .....	72
4.3.4	Triboscanner Calibration.....	73
4.4	Summary.....	74

**Chapter 5. Extracting the Mechanical Properties of Thin Films Using Nanoindentation Technique ..... 75**

5.1	Nanoindentation Testing.....	75
5.2	Mechanical Properties of Copper Thin Films.....	76
5.2.1	Single and Multi-cycling Tests Comparison .....	77
5.2.2	Potential Problems with Multi-cycling Tests .....	80
5.2.3	Annealing Effect.....	87
5.2.4	Texture Analysis in Copper Thin Films .....	91
5.2.5	Surface Roughness Effect.....	99
5.2.6	Pile-up Effect.....	100
5.2.7	Transition from Single Grain to Continuum Behaviour .....	101
5.3	Extracting Mechanical Properties of Gold Thin Films.....	102
5.3.1	Adhesion.....	103
5.3.2	Thin Film and Bulk Gold Comparison .....	107
5.4	Why does $E_r$ Decrease with Penetration for Coatings on Silicon?.....	109
5.5	Summary.....	111

**Chapter 6. The Effect of Density and Surface Roughness on the Mechanical Properties Obtained from Nanoindentation ..... 113**

6.1	Nanoindentation Testing.....	113
6.2	Copper .....	113
6.2.1	Potential Issues of Indentation Location .....	117
6.2.2	AFM Image Analysis .....	118
6.3	Tin.....	123
6.4	Copper-Tin Coating.....	129
6.4.1	AFM Images and Load-displacement Curves Analysis .....	131
6.4.2	Annealing Study .....	137
6.5	Modelling of the Indentation Response of Porous Coatings .....	138
6.6	Summary.....	145

**Chapter 7. The Potential Measurement Errors of Mechanical Properties using Nanoindentation Techniques ..... 146**

7.1	Potential Sources of Data Distortion .....	146
7.2	Changes in Contact Area .....	147
7.2.1	The Importance of Pile-up.....	147
7.2.2	Comparison of Pile-up Appearance between Bulk and Thin Film Copper .....	148
7.2.3	Annealing Effect on Pile-up Height and Width.....	154
7.2.4	Further Investigation of Pile-up for Different Multi-cycling Tests .....	158

7.2.5	Effect of Pile-up on the Mechanical Properties of Aluminium .....	160
7.3	The Importance of Power-law Fitting.....	169
7.4	Creep.....	171
7.4.1	High Melting Point Materials.....	173
7.4.2	Low Melting Point Materials.....	178
7.5	Summary.....	186
<b>Chapter 8. Influence of Oxidation on the Materials Mechanical Properties</b>		<b>188</b>
8.1	Oxidation .....	188
8.2	Why Titanium and Cobalt-Chromium Alloys? .....	189
8.3	Mechanical Properties of Co-Cr Alloys .....	191
8.3.1	EDX and XRD Characterisation Analyses.....	197
8.4	Mechanical Properties of Ti-6Al-4V Alloy.....	199
8.4.1	EDX and XRD Characterisation Analyses.....	202
8.5	XPS Characterisation Analysis.....	206
8.6	Summary.....	210
<b>Chapter 9. Loading Curve Analysis .....</b>		<b>212</b>
9.1	Load-displacement Curves .....	212
9.2	General Background Information of the Method .....	212
9.3	Summary.....	220
<b>Chapter 10. Conclusions and Future Work.....</b>		<b>222</b>
10.1	Mechanical Properties of Thin films .....	222
10.1.1	Copper Thin Film.....	222
10.1.2	Pile-up Effect .....	223
10.1.3	Surface Roughness and Density Effects .....	224
10.1.4	Creep Effect.....	225
10.1.5	Oxidation Effect.....	226
10.2	Loading Curve Analysis .....	227
10.3	Possible Future Work .....	227
<b>References .....</b>		<b>228</b>
<b>Nomenclature.....</b>		<b>249</b>

## *Lists of Figures*

---

Figure 2-1. Schematic representation of load-displacement curve in Oliver-Pharr method (Oliver and Pharr, 1992). .....	11
Figure 2-2. A schematic of the cross-section through an indentation with various dimensions (Oliver and Pharr, 1992). .....	12
Figure 2-3. Schematic of (a) a Berkovich tip and (b) an indent from top view; the terms $R_p$ and $r$ are the plastic zone radius and the indenter radius respectively. ....	16
Figure 2-4. Schematic representations of (a) loading a performed impression of radius $R_r$ with rigid indenter radius $R_i$ and (b) the load-displacement curve obtained for an elastic-plastic material using a spherical indenter. Modified from (Fischer-Cripps, 2011).....	19
Figure 2-5. Schematic of load versus time (load function) with two holding segments to minimise the effect of creep and thermal drift on the nanoindentation data. ....	22
Figure 3-1. The schematic of commercial instruments (a) Agilent, Nano-Indenter XP (b) MicroMaterials, NanoTests pendulum based system, (c) CSIRO, Ultra-Micro-Indentation system (UMIS) (d) Hysitron, Tribo-Scope from (Micromaterials Ltd; Bell <i>et al.</i> , 1992a; Mann, 2007; Fischer-Cripps, 2011). ....	28
Figure 3-2. Hysitron Triboindenter (a) Acoustic Enclosure (b) Vibration Isolation Platform (c) closer view of the Triboscanner base, Transducer, Stage, Piezo and Optics, adapted from (Hysitron, 2001; Wang <i>et al.</i> , 2009) .....	30
Figure 3-3. (a) ideal piezo ceramic behaviour (b) realistic piezo ceramic behaviour under the applied voltage illustrating overshoot and ringing during the test (Hysitron, 2001). ....	31
Figure 3-4. Explanation of the three-plate capacitive transducer (a) at rest and (b) under the applied voltage. ....	33
Figure 3-5. SEM images of the Berkovich indenter (a) side view and (b) top view. ....	35
Figure 3-6. Typical load functions (a) with and (b) without holding segment at maximum load. ....	36
Figure 3-7. Schematic of the load function for multi-cycling tests: (a) constant load repetition mode with hold at the maximum load, 7 cycles, (b) ramping mode with increase load, 7 cycles, (c) constant load repetition mode, 10 cycles and (d) load increase mode, 14 cycles (Nowicki <i>et al.</i> , 2003; Chen and Bull, 2008; Bull <i>et al.</i> , 2012). ....	38
Figure 3-8. Schematic of the EBSD technique (Schwartz, 2009). ....	42
Figure 4-1. Flow diagram of a typical trench first damascene process, modified from (Wilson, 2009). .....	52
Figure 4-2. Schematic representation of the Cu or Au thin films deposited on Si substrate. ....	57
Figure 4-3. Hardness versus indentation depth obtained from various materials showing the indentation size effect and material's behaviour at different penetration depths. ....	63
Figure 4-4. Schematic representation showing geometrically necessary dislocations beneath the sharp indenter tip, where $S$ is the spacing between individual slip steps on the indentation surface, $a$ is the contact radius and $\theta$ is the angle between the surface of the plane and the indenter (Nix and Gao, 1998). ....	64
Figure 4-5. Calibration loading functions used for indentations in (a) W and fused silica, and (b) Al. ....	67
Figure 4-6. Typical examples of the measured machine compliance obtained from W (left) and Al (right) which in both cases the total compliance is $0.0035 \mu\text{m}/\text{mN}$ ( $3.5 \text{ nm}/\text{mN}$ ). ....	68
Figure 4-7. Typical load-displacement curves obtained from fused silica at different maximum load ranges. ....	69
Figure 4-8. Contact areas obtained from fused silica versus corresponding contact depths. ....	70
Figure 4-9. Reduced modulus (left) and hardness (right) values obtained from fused silica after both the machine compliance and indenter area function calibrations. ....	71

Figure 4-10. H-pattern calibration on a standard Al sample as seen by the Triboindenter (left) and the magnified view (right). .....	73
Figure 5-1. Load versus time graphs (a) single cycle for low load, (b), (c) and (d) multi-cycling tests with the partial unloading set at 20, 50 and 90% of the maximum load respectively. ....	77
Figure 5-2. Examples of multi-cycling test load-displacement curves: (a) 20% (b) 50% and (c) 90% unloading of the maximum load obtained from a non-annealed Cu thin film. ....	78
Figure 5-3. Comparison of the single and multi-cycling tests for the non-annealed thin film samples (a) hardness and (b) Young's modulus versus contact depth. ....	79
Figure 5-4. (a) hardness and (b) Young's modulus versus contact depth under multi-cycling tests for the non-annealed sample. ....	81
Figure 5-5. Variation of (a) hardness and (b) Young's modulus of bulk Cu measured by nanoindentation under multi-cycling test. ....	82
Figure 5-6. (a) hardness and (b) Young's modulus versus contact depth under multi-cycling tests for the Cu thin film annealed at 100 °C. ....	83
Figure 5-7. (a) hardness and (b) Young's modulus versus contact depth under multi-cycling tests for the Au thin film. ....	85
Figure 5-8. (a) hardness and (b) Young's modulus of W obtained from nanoindentation test under multi-cycling tests. ....	86
Figure 5-9. (a) hardness and (b) Young's modulus data obtained from three different Cu thin films. ....	88
Figure 5-10. (a) hardness and (b) Young's modulus values versus contact depth in multi-cycling tests for annealed Cu thin film at 350 °C I unloading of the maximum load. ....	89
Figure 5-11. SEM images of Cu thin films obtained using the EBSD detector representing (a) non-annealed sample, (b) annealed at 100°C and (c) annealed at 350°C. ....	92
Figure 5-12. Experimental pole-figure maps of Cu thin films obtained by EBSD test (5 $\mu\text{m}^2$ ): (a) non-annealed (b) annealed at 100 °C for 60 minutes (c) annealed at 350 °C for 1 minute and (d) inverse pole figure maps colour bar. ....	93
Figure 5-13. Variation of the amount of (111) oriented grains and fine grained material (<100 nm diameter) as a function of annealing conditions determined from the EBSD results. ....	94
Figure 5-14. The grain size distribution for Cu thin films obtained from EBSD. ....	95
Figure 5-15. XRD patterns for Cu thin films. ....	96
Figure 5-16. Variation of the amount of (111) oriented grains and fine grained material (<100 nm diameter) as a function of annealing conditions determined from the XRD results. ....	97
Figure 5-17. Raman spectra obtained from Cu thin films (a) non-annealed sample, (b) annealed at 100 °C and (c) annealed at 350 °C. ....	98
Figure 5-18. AFM images (90% unload multicycling test) of indentations in a non-annealed Cu thin film which show reduction in pile-up from (a) high (1.5 mN) to (b) low load (0.5 mN). ....	100
Figure 5-19. AFM images for typical indentations on Au thin film, three dimensional views and top-down views of (a) high load (10 mN), (b) medium load (1.5 mN) and (c) very low load (0.4 mN). ....	102
Figure 5-20. Load-displacement curves and AFM images obtained from Au thin film demonstrating a good adhesion condition between the film and substrate under different applied loads. ....	103
Figure 5-21. (a) three dimensional and top view of the AFM image for a failed coated system and (b) the load-displacement curve obtained from the same indentation test. ....	105
Figure 5-22. Failed load-displacement curve for the load originally set at 5 mN. ....	106
Figure 5-23. Microscopic images of two different pads with adhesion failure during the nanoindentation test (arrows indicate nanoindentation). ....	106
Figure 5-24. Microscopic image of the Au thin film, presenting visible large indentations illustrating reduction in stiffness. ....	107

Figure 5-25. (a) AFM image and (b) the load-displacement curve obtained from the same indentation position. ....	107
Figure 5-26. Obtained Young's modulus (left) and hardness (right) results for Au thin film after pile-up correction with standard deviations. ....	108
Figure 5-27. Predicted variation of contact modulus with contact depth for 800 nm Cu on Si with and without a 1 $\mu$ m silica intermediate layer. ....	111
Figure 6-1. SEM images of Cu deposited sample on Cu substrate using the RTIL technique (a) top view and (b) cross-sectional view. ....	114
Figure 6-2. Comparison of nanoindentation tests performed on smooth surfaces of Cu samples showing the Young's modulus (left) and hardness (right) under displacement control. ....	115
Figure 6-3. Comparison of nanoindentation tests performed on smooth and rough surfaces of Cu samples showing (a) the hardness and (b) Young's modulus under displacement control at 40 nm contact depth. ....	116
Figure 6-4. Diagram of a rough surface with various grain sizes illustrating different numbered locations at which the indenter can be seated during an indentation test. ....	117
Figure 6-5. Distributions of the (a) hardness and (b) Young's modulus values obtained from bulk and coated Cu with rough surfaces for different locations at which the indenter tip can be seated. ....	118
Figure 6-6. Schematic representation of the stress produced at the contact point between the indenter and sample for (a) normally constrained contact surface, (b) reduced constraint on a peak and (c) increased constraint in a valley. ....	121
Figure 6-7. Load-displacement curves obtained under nanoindentation tests on dense bulk Cu and deposited low density Cu on Cu substrate. ....	123
Figure 6-8. Nanoindentation test results performed on bulk Sn, Young's modulus (left) and hardness (right) with smooth surface under displacement control. ....	124
Figure 6-9. Load-displacement curves obtained from bulk Sn sample under (a) open loop mode without appearance of nose due to the creep, (b) open loop mode with appearance of nose due to the creep and (c) displacement control. ....	125
Figure 6-10. Nanoindentation test results showing (a) the hardness and (b) Young's modulus performed on a dense Sn coating with smooth surface under displacement control. ....	126
Figure 6-11. SEM images from the Sn coating on a Cu substrate (a) top view and (b) cross-sectional view. ....	127
Figure 6-12. Nanoindentation test results showing the Young's modulus (left) and hardness (right) performed on low dense Sn coating with rough surface under displacement control. ....	128
Figure 6-13. SEM images obtained from the Cu-Sn alloy showing the density and also the thickness of the coating (a) top view and (b) cross-sectional view. ....	129
Figure 6-14. Nanoindentation test results showing (a) the hardness and (b) contact modulus performed on Cu-Sn coatings on Cu and stainless steel substrates under open loop mode. ....	130
Figure 6-15. AFM images obtained from Cu-Sn coating (a) before and (b) after a nanoindentation test as well as (c) load-displacement curve. ....	132
Figure 6-16. AFM images (a) before and (b) after indentation as well as (c) the load-displacement curve obtained from the Cu-Sn coating. ....	134
Figure 6-17. Nanoindentation test results performed on Cu-Sn coating deposited on Cu substrate with low density showing the contact modulus (left) and hardness (right) under displacement control. ....	135
Figure 6-18. Schematic representation of the deforming volume sampling at (a) low contact depth and consequently high values due reduced porosity effect and (b) high contact depth and consequently lower values due to the higher porosity influence. ....	136
Figure 6-19. Cross-sectional SEM image of the annealed Cu-Sn coating. The yellow arrows identify the pores on the coating. ....	137

Figure 6-20. SEM images of the indenter tip (a) top view and (b) cross-sectional view having the geometries of the tip. ....	139
Figure 6-21. Meshes produced by OOF2 modelling (a) diamond indenter and (b) annealed Cu-Sn coating with low density. ....	140
Figure 6-22. Simulated microstructure of annealed Cu-Sn coating with different indentation positions shown with numbers 1, 2 and 3. ....	140
Figure 6-23. Simulated microstructure of position 4 under different displacement (a) 1, (b) 2, (c) 3 and (d) 4 $\mu m$ . ....	141
Figure 6-24. Stress-strain curves obtained from simulated Cu-Sn coating with obtained elastic modulus values at different positions of the coating using OOF2. ....	142
Figure 6-25. Simulated samples (a) with and (b) without the hole beneath the sample surface. ....	143
Figure 6-26. Simulated microstructure of fully dense sample under (a) 1 and (b) 2 $\mu m$ displacement. ....	144
Figure 7-1. (a) and (b) AFM images as well as respective (c) and (d) cross-sectional curves of the drawn lines in the images obtained from bulk Cu after indentation tests under 10 and 9 $mN$ loads for open loop mode. ....	148
Figure 7-2. Young's modulus (left) and hardness (right) values obtained under high load indentation tests for bulk Cu using open loop mode showing data before and after pile-up correction. ....	150
Figure 7-3. (a) height and (b) width of the pile-ups obtained from a single cycle nanoindentation test under open loop mode from bulk Cu. ....	151
Figure 7-4. (a) height and (b) width of the pile-ups obtained from single cycle nanoindentation test under open loop mode on non-annealed Cu thin film. ....	152
Figure 7-5. Schematic representation of the physical indentation process: (a) and (c) top views of the indentation, (b) and (d) the cross-sectional views of the same indentations respectively. ....	153
Figure 7-6. Average pile-up (a) height and (b) width obtained from the single cycle indentation tests under open loop mode for the Cu thin films. ....	154
Figure 7-7. (a) heights and (b) widths of pile-ups measured using the AFM images from nanoindentation tests for non-annealed Cu thin film under the multi-cycling test (90% unload). ....	156
Figure 7-8. Pile-up (a) heights and (b) widths obtained from non-annealed Cu thin film under single and multi-cycling indentation tests (90% unload). ....	157
Figure 7-9. AFM images of high load (1.5 $mN$ peak load) multi-cycling indentations in the non-annealed Cu coating (a) 20% unload and (b) 90% unload as well as the cross-sectional curves obtained from the drawn lines at AFM images. ....	158
Figure 7-10. Average pile-up heights and widths obtained from all three sides of the indentation edges for non-annealed Cu thin film under different multi-cycling test protocols. ....	159
Figure 7-11. Partial load-displacement curves in multi-cycling test for 20, 50 and 90% unloading of maximum load. ....	160
Figure 7-12. Young's modulus (left) and hardness (right) values of bulk Al obtained under open loop mode and displacement control. ....	162
Figure 7-13. AFM images (left) and cross sectional information (right) of the drawn line in the image obtained from bulk Al after indentation tests under (a) 10 (b) 8 (c) 5 and (d) 2 $mN$ loads for open loop mode. ....	163
Figure 7-14. (a) hardness and (b) Young's modulus values of 1400 $nm$ thick Al film for before pile-up correction (measured using the Oliver and Pharr method) and after pile-up correction (measured using the actual contact area). ....	165
Figure 7-15. (a) hardness and (b) Young's modulus values of 375 $nm$ thick Al film, before pile-up correction (measured using the Oliver and Pharr method) and after pile-up correction (measured using the actual contact area). ....	166

Figure 7-16. Schematic representation of the physical indentation process and relative load-displacement curves for the soft Al thin film deposited on a hard glass substrate showing the following scenarios: (a) $h_{max} < h_f$ , (b) $h_{max} \approx h_f$ , (c) $h_{max} > h_f$ and (d) representing elastic recovery for both Al and glass for the position (c) when the indenter is removed. ....	168
Figure 7-17. Young's modulus data obtained by the Oliver and Pharr method for the single indentations using different percentages of the power-law fitting to the unloading curves for various thin films. ....	170
Figure 7-18. Load-displacement curves obtained from bulk Cu under displacement control showing no creep effect on the curves at three different peak loads. ....	173
Figure 7-19. Examples of load-displacement curves obtained under open loop mode for bulk Cu presenting creep behaviour at the maximum load and failure to attain the preferred load. ....	174
Figure 7-20. Examples of load-displacement curves obtained for bulk Cu under open loop mode that illustrate the changes in the maximum contact depths due to creep occurrence. ....	175
Figure 7-21. Contact modulus values obtained from non-annealed Cu thin film and (111) bulk Cu under displacement control at 40 nm contact depth. ....	176
Figure 7-22. Hardness and Young's modulus values obtained from bulk Cu under open loop mode using a 500 $\mu N$ load at diverse loading rates. ....	177
Figure 7-23. Hardness and Young's modulus values obtained from bulk Cu under displacement control at a 40 nm contact depth at diverse displacement rates. ....	178
Figure 7-24. Load-displacement curves obtained using open loop mode with two different holding periods at the maximum load and displacement control from bulk Zn samples. ....	179
Figure 7-25. Comparison of nanoindentation tests performed on bulk Zn sample showing the Young's modulus (left) and hardness (right) under displacement control. ....	180
Figure 7-26. Young's modulus values of bulk Zn obtained under displacement control from different large grains. ....	181
Figure 7-27. Creep factor obtained from Fang and Ngan method for four different materials versus their homologous temperature ( $T_H$ ); open symbols represent the open loop mode data and filled symbols represent the displacement control. ....	182
Figure 7-28. Creep behaviour comparison of bulk Sn, Zn, Al and Cu under the same loading and unloading conditions. ....	183
Figure 7-29. Comparison between the constant $B$ and homologous temperatures for the creep behaviour of bulk Sn, Zn, Al and Cu obtained from indentation strain versus time curves. ....	184
Figure 7-30. The hold-unload sections of four different load-displacement curves obtained from bulk Sn using the open loop mode at very similar loads with different holding periods at the maximum load before unloading. ....	185
Figure 8-1. AFM images obtained from Co-Cr alloy femoral head (a) with and (b) without misalignment between the tip and sample surface. ....	192
Figure 8-2. Comparing both the (a) hardness and (b) Young's modulus for Co-Cr alloy under displacement control and open loop mode. ....	193
Figure 8-3. Comparison of all three sides of pile-ups (a) widths and (b) heights for Co-Cr alloy under displacement control. ....	194
Figure 8-4. (a) hardness and (b) Young's modulus for Co-Cr alloy under displacement control over a straight line across a polished flat on the sample. ....	195
Figure 8-5. Comparison of the hardness results for Co-Cr-Mo alloy before and after electrochemical oxidation. ....	197
Figure 8-6. X-ray diffraction pattern for the implanted Co-Cr-Mo alloy. ....	198
Figure 8-7. Comparison of both the (a) hardness and (b) Young's modulus for the Ti alloy under displacement control and open loop mode. ....	200

Figure 8-8. Comparison of all three sides of pile-ups (a) widths and (b) heights for Ti alloy using open loop mode. ....	201
Figure 8-9. The Young's modulus (left) and hardness (right) for Ti alloy under displacement control over a straight line across a polished flat on the idealised sample. ....	202
Figure 8-10. X-ray diffraction pattern for the Ti-6Al-4V before oxidation. ....	203
Figure 8-11. Comparison of the Ti alloy results for (a) hardness and (b) Young's modulus before and after oxidation under displacement control. ....	204
Figure 8-12. Comparison of the hardness and Young's modulus values between the oxidised Ti alloy and the sample which was implanted in the body. ....	205
Figure 8-13. The set of O 1s spectra measured during the depth profiling experiment of the (a)Ti alloy and (b) Co-Cr alloy in vivo. ....	208
Figure 8-14. XPS depth profile analysis for Ti alloys (a) in vivo, (b) oxidised electrochemically and Co-Cr alloys (c) in vivo and (d) oxidised electrochemically. ....	209
Figure 9-1. Loading portions of the load-displacement curves for various materials with wide ranges of $E$ and $H$ at approximately the same indentation load. ....	217
Figure 9-2. $K_{exp}$ versus $K_m$ plotted for low $H$ and $E$ (a) Al and (b) Cu as well as high $H$ and $E$ (c) fused silica and (d) TiC. The black solid line in each curve indicates the linear fit to the obtained data and the red dashed line indicates the expected line. ....	218
Figure 9-3. $K_{exp}$ versus $K_m$ plotted for various types of materials including both high and low hardness and modulus values. ....	219

## *List of Tables*

---

Table 2-1. Parameters for commonly used indenter shapes (Fischer-Cripps, 2001; Fischer-Cripps, 2004b; Oliver and Pharr, 2004). .....	15
Table 3-1. Measurement capability and accuracy of the transducer used in Hysitron Triboindenter... 34	
Table 4-1. Different deposited samples with low density and high surface roughness. ....	58
Table 4-2. Properties of materials used in this investigation for both the calibration samples and tested samples from literature for comparison. ....	72
Table 5-1. Hardness and Young's modulus values obtained from Cu thin films under single and multi-cycling (90% unload) tests for various contact depths. ....	91
Table 6-1. Comparison of hardness and Young's modulus values obtained from different locations on the rough Cu surface. ....	120
Table 6-2. Average hardness and modulus values obtained from Cu samples with smooth and rough surfaces. ....	122
Table 6-3. Nanoindentation test results obtained for Sn samples.....	128
Table 6-4. The AFM images and load-displacement curves obtained from Cu-Sn coatings. The large circles in the load-displacement curves correspond to the pop-in phenomena. ....	133
Table 6-5. Average nanoindentation test results obtained from different coatings, thin films and bulk samples. ....	138
Table 7-1. AFM images obtained from bulk Cu sample under open loop mode at high loads. ....	149
Table 8-1. EDX results of Co-Cr-Mo alloy samples as received without implantation in the human body and implanted in vivo. ....	198
Table 8-2. EDX results for the Ti-6Al-4V alloy samples.....	206
Table 8-3. Elemental compositions obtained from XPS for the Ti and Co-Cr alloys after oxidation. 207	
Table 9-1. Summary of the materials with various $H$ and $E$ values used to calculate the $K_m$ values. 217	

## Chapter 1. Introduction

*In this chapter, the basic principles of material mechanical properties, such as hardness and elastic modulus, are reviewed. The determination of mechanical properties of materials on a small length scale using the nanoindentation technique is introduced. Finally, the scope of this thesis and the subsequent outline is provided.*

### 1.1 Hardness

Hardness is a measure of a material's resistance to penetration by scratching or indentation using a hard object (an indenter) when a force is applied and can be described as a measure of the strength of a material. It is usually assumed that hardness is a measure of the plastic deformation of the test material as the indenter, being composed usually of materials such as diamond or hardened steel, is much harder than the sample material. Hardness typically has the units of stress and measures a compressive rather than a tensile response.

In 1822 Mohs developed the 10-step scratch hardness scale for minerals with a qualitative hardness indexing scheme named the Mohs scale (Mohs, 1822). This indexing scheme was composed of a list of 10 minerals ordered in terms of their hardness values, ranging from the softest material, talc, at a value of 1 to the hardest material, diamond, at a value of 10 (Tabor, 1954). Since that time, modern hardness measurement techniques have progressed from the use of reference materials to rank scratch resistance to the use of automated instruments based on contact mechanics with sufficient accuracy that they are capable of obtaining mechanical properties at nanoscopic scales. Since 1822, several measurement techniques have been introduced, such as the Rockwell, Brinell and Vickers techniques between 1900 and 1925 (Herrmann, 2011), as the need for testing the hardness of metals emerged. However, in the last two decades, the measurement of hardness for coatings and thin films with less than a 1  $\mu\text{m}$  thickness has been required at a size scale beyond optical capabilities. A powerful and straightforward technique with high measurement accuracy was essential to obtain the hardness of thin films and coatings without substrate influence on the obtained results.

## 1.2 Young's Modulus

The Young's modulus ( $E$ ) is a measure of the *stiffness* or *elasticity* of a material, which defines its resistance against elastic deformation. This can also be described as the elastic properties of a solid when under tension or a compressive load. The greater the modulus value, the more stiff the material, and the less prone the material is to deformation under a given stress. The modulus values for covalently bonded elements are very high, and diamond, with a Young's modulus of  $1140 \text{ GN/m}^2$  ( $\text{GPa}$ ) is the stiffest known material. The stiffness of a material can be defined as the initial gradient in the stress-strain curve and is related to the interatomic forces in the direction of loading. The modulus values of materials can therefore be subject to anisotropic effects if these interatomic forces vary with crystallographic orientation.

There are several traditional measurement techniques that have been developed for the determination of the Young's modulus of materials. The Young's modulus can be calculated using Hooke's law which is based on the gradient of the initial part of the stress-strain curve ( $E = \sigma/\epsilon$ ) and measures the strain with a known compressive force. However, to achieve an accurate measurement using this method, the creep and deflection of the test machine requires consideration as they can have an influence on the measured strain and consequently the determined modulus value.

There are other methods with dynamic measurements, such as the measurement of the natural frequency of vibration of a beam or wire supported at its ends, which can be determined using a central mass and the frequency of oscillation of the wire (Ashby *et al.*, 2013). Another dynamic measurement technique that is more effective and accurate than both previous methods is the measurement of the velocity of sound waves within the material. This velocity is based on the Young's modulus and the density of the tested materials and therefore, if the density of the material is known, the Young's modulus can then be calculated (Ashby and Jones, 2005). All of these techniques however are suited for bulk or large scale materials and thin films that have been removed from the substrate, and none of the aforementioned methods are appropriate and accurate enough to be used in the determination of the Young's modulus of materials at the nanoscale.

### 1.3 Introduction to Nanoindentation

Due to the recent developments in many aspects of technology and nano-structured materials, as well as thin film and coating technologies, there has been considerable interest in the drive to constantly produce smaller components. In these circumstances the determination of accurate mechanical properties, most importantly elastic modulus and hardness, of such small volumes of material becomes crucial. The mechanical and deformation behaviours of materials are the key factors that require consideration to achieve a good design and both factors have a strong influence on the reliability and the performance of designed components. The diversity of thin films and coatings and their mechanical reliability can be varied from fine and delicate designs such as in micro or nano-electronic devices, ion-implanted surfaces, optical coatings and polymer films to very hard coatings used in the pipeline industry. Since the material response to characterisation techniques in such a small volume differs from the bulk form, considerable interest in an instrument with the capability to characterise mechanical behaviour at very small length scales has emerged.

In the last two decades, the nanoindentation technique, also known as depth sensing indentation (DSI), has become one of the most popular techniques in the determination of the mechanical behaviour of materials at the nanometre scale with high resolution. This technique allows for measurement of both the elastic and plastic response of materials at the nanometre scale during the indentation cycle. Initially, this technique was used for the investigation of thin films (Hainsworth *et al.*, 1998; Korsunsky *et al.*, 1998) and the effect of small length scales (Ma and Clarke, 1995; Nix and Gao, 1998). However, nowadays the nanoindentation technique has gained popularity in a variety of test environments such as liquid environments (Mann and Pethica, 1996), which can be extended to testing living cells (Aryaei and Jayasuriya, 2013), various high and low temperature situations (Lucas and Oliver, 1999; Beake *et al.*, 2003) and the testing of materials which are sensitive to strain rates, such as polymeric materials (Constantinides *et al.*, 2008). Therefore, it is possible to obtain mechanical properties using conditions that are representative of the actual environment that a material is used in, thereby increasing the relevance of the results.

## 1.4 Structure of Thesis

The main objective of this work is to evaluate the factors that affect the accuracy of the data determined by nanoindentation and investigate ways in which this can be improved. To illustrate the importance of each factor, work was carried out on various types of material and the results are discussed in this work. This investigation can be divided in two sections. The first part includes chapters 2 to 4 which initially provide a basic introduction to the development of the nanoindentation technique, then presents an introduction to additional techniques that were used to prove the developed hypotheses and finally establish the factors that can affect the accuracy of the obtained data. The second part of the work, chapters 5 to 9, reports on the experimental investigations in this study. Each chapter initially provides a basic description of the need for accurate data followed by a comparison between some established and developed measurement techniques and the nanoindentation technique. The nanoindentation test results and the results from the additional techniques are reported and the results are discussed. Finally, the overall conclusions of this investigation are provided in chapter 10.

**Chapter 2** provides an overview of the nanoindentation technique and introduces the most commonly employed method for determining hardness and modulus values. The determination and analysis of mechanical properties using nanoindentation for both pyramidal and spherical indenter geometries are described. Secondary concepts that influence the obtained indentation data such as thermal drift, creep, machine compliance and the indentation area function are also presented.

**Chapter 3** details the experimental methods used in this work. The nanoindentation instrument used in this investigation is described followed by the characterisation techniques used to measure the crystallographic and microstructural properties of the samples.

**Chapter 4** provides brief background information about copper thin film metallisation, and then moves on to discuss the challenges related to their adhesion onto and diffusion into silicon substrates. The materials investigated in this work are described next. Various materials are of interest due to the different influences in the nanoindentation data that can be magnified by using a specific type of material such

as pile-up in copper or gold thin films. In turn this can facilitate a greater understanding of the cause of these effects in the obtained data. Finally, the desired calibration processes that are required to be undertaken prior to performing the indentation tests are described in detail whilst also presenting the suitable calibration materials.

**Chapter 5** contains the results obtained for the research carried out on thin metal films, such as copper and gold, fabricated for microelectronic devices. Additionally, similar bulk samples were tested under the same indentation conditions for comparison. The nanoindentation tests were conducted on the Hysitron Triboindenter which is of relevance due to the capacity for accurate measurements at very low loads and consequently shallow depths, which is desirable for thin films with a less than  $1 \mu\text{m}$  thickness. The accurate measurement of the mechanical properties of metal thin films has received increased attention due to the importance of the various types of mechanical stress generation in thin films during their nucleation, processing and storage. The generated stress can have a strong influence on the microelectronic device performance. Therefore a reliable technique is desired to accurately measure the stress and strain relationship in metal thin films without removing the film from the substrate. This is necessary, as in an actual device, stress can be produced by the thermal expansion mismatch between the substrate and thin film. Therefore, a measurement technique with high accuracy and a capability at nanometre scale depths is required to measure the mechanical properties of thin films with minimised substrate effect.

The initial aims of the work are introduced in the first section and then a brief explanation of the various test protocols used in this work is provided, followed by the obtained hardness and Young's modulus values for copper thin films. A variety of techniques used to generate and characterise the surface morphology are subsequently described. The comparison between two different types of thin metal films (copper and gold) deposited on similar substrates (silicon) is explored next. Finally, failure mechanisms such as the delamination of the gold thin films using nanoindentation are presented. This is of interest as the adhesion between the deposited film and the silicon substrate is one of the challenges in the fabrication of microelectronic devices and it has a significant influence on device performance and lifetime.

**Chapter 6** details the surface mechanical response obtained using the nanoindentation technique. The effects of porosity and surface roughness on the mechanical properties measured by nanoindentation are explained. Initially, the analysis of the comparison indentation data obtained from fully dense copper coatings and low density coatings is provided. Afterwards, the effects of surface roughness, grain size distribution, the indentation location and porosity of the sample on the obtained indentation results are described. These analyses are of interest as the accuracy of indentation data is highly dependent on the surface morphology.

The variation in the obtained results between the porous coatings and fully dense materials are examined using the obtained load-displacement curves along with the corresponding atomic force microscopy (AFM) images. Moreover, the scatter within the obtained hardness and modulus values from a time dependent material, tin, for both thin film and bulk samples is analysed. Finally, a comparison between the obtained experimental data for porous coatings and the data obtained from the finite element analysis method using object oriented finite element modelling software (OOOF2) are presented. The aim of this analysis was to understand the response of the material to the indenter without the influence of any factors such as pile-up, cracking, detachment and fragmentation of the surface.

**Chapter 7** covers the potential sources of error in the obtained nanoindentation results. The effect of pile-up and creep on the Oliver and Pharr analysis method are described. Firstly, the aims of the work are introduced followed by a comparison of pile-up formation for bulk and thin film copper. Subsequently, the effect of annealing of copper thin films in the formation of pile-up is presented. After that, pile-up appearance for bulk and thin aluminium films deposited on glass substrates are compared to those of the copper samples. This is of interest due to the similarity of the Young's modulus of glass and aluminium, which removes any elastic mismatch effects from the measured data. The AFM images used to identify the heights and widths of the pile-ups are shown. Afterwards, general information with regards to creep and its effect on the load-displacement curves is provided. The effect of creep in the obtained nanoindentation data is explained by dividing the materials in to two different categories; low and high melting point materials. The identified creep influence in the nanoindentation test results using different test protocols for various

materials are presented. Finally, the scatter seen in the obtained Young's modulus values of zinc due to anisotropy is discussed.

**Chapter 8** describes the work performed on titanium-based and cobalt-chrome alloys used in orthopaedic applications. The longevity of these materials is highly influenced by their mechanical properties. This study attempts to understand why a harder cobalt-chrome alloy should become damaged by softer titanium alloy components. Therefore, the importance of investigating the bulk and surface mechanical properties, such as hardness and Young's modulus, of a number of hip implants and test samples is presented. Using the knowledge obtained during this investigation, AFM images were obtained to determine the contact area and hence, pile-up correction factors. This work was carried out due to the interest in the oxidation appearance in vivo and the changes that may occur in the mechanical properties of materials due to their oxidation. Initially some background information on titanium and cobalt-chromium based alloys is introduced, followed by a brief literature review with regards to the effect that the human body can have on their performance and longevity. The obtained results are compared for samples before being used in the body, to account for surface mechanical response due to implant manufacture, and after, to consider the material's response to long-term cyclic loads. The effects of oxidation on the mechanical properties of the alloys treated electrochemically with a sodium chloride (NaCl) solution at body temperature are presented. Sample characterisation as well as the surface morphology is presented using various characterisation techniques.

**Chapter 9** provides brief background information about the loading curve analysis, in contrast to the ordinarily used unloading curve analysis, followed by an introduction to the common method used to analyse loading curves which was proposed by Hainsworth and colleagues in 1996 (Hainsworth *et al.*, 1996). Afterwards, the experimental results collected during this investigation using unloading curves were compared to the results obtained from the loading curve analysis using Hainsworth's method. The reliability of both the loading and unloading curve analyses is then discussed.

**Chapter 10** summarises the conclusions of this investigation, as well as including recommendations concerning relevant future work.

## Chapter 2. Nanoindentation

*In this chapter, first the nanoindentation technique and its applications in various materials are described. Second, the analysis and derivation of basic mechanical properties, such as hardness and elastic modulus, are discussed. Next, different indenter tip geometries and their analyses are provided. Finally, secondary concepts influencing nanoindentation tests as well as the characteristics of materials suitable to meet calibration standards are investigated.*

### 2.1 Nanoindentation Procedure

Nanoindentation is a widely adopted method to measure the elastic, plastic, and time-dependent mechanical properties including the hardness and Young's modulus of thin films and small volumes of bulk materials. The nanoindentation method gained popularity with the development of machines that were capable of recording very small loads and displacements to a high level of precision and accuracy (Constantinides *et al.*, 2007). Analytical models were also developed to estimate contact modulus and hardness using load-displacement data. Nanoindentation is effectively a very high resolution hardness test. The most commonly employed method to determine the modulus and hardness of the indented material is the Oliver and Pharr method first proposed in 1992 (Oliver and Pharr, 1992; Giannakopoulos *et al.*, 1994; Giannakopoulos and Suresh, 1999; Tabor, 2000; Dao *et al.*, 2001; Cheng and Cheng, 2004; Oliver and Pharr, 2004; Ganneau *et al.*, 2006; Fischer-Cripps, 2011). This has become the standard procedure to extract elastic modulus and hardness of the specimen material from load-displacement measurements (Oliver and Pharr, 2004; Schuh, 2006; Li and Vlassak, 2009; Fischer-Cripps, 2011).

In nanoindentation tests, a specified load ( $\mu\text{N}$ - $\text{mN}$  range) is applied to an indenter of known geometry in contact with the sample. The penetration depth ( $\text{nm}$ - $\mu\text{m}$  range) is then measured as the load is applied through the use of a hard indenter tip, typically diamond. The shape and angle of the indenter tip and the penetration depth provide an indirect measurement of the contact area between the tip and the surface of the sample at a specific load, and thus the hardness can be determined by dividing the maximum applied load by the measured contact area (Chakraborty *et al.*, 2012).

### 2.1.1 Load-displacement Curves

Nanoindentation load-displacement curves (often known as  $P-h$  or  $P-\delta$  curves) are the materials response reflected in the continuous measurement of the depth of penetration while the load is increasing from zero to the maximum load (loading curve) and then decreasing from maximum load to zero (unloading curve). According to Page and Hainsworth (Page and Hainsworth, 1993), the mechanical response of the sample material impressed by a harder indenter during the indentation cycle provides a “*micromechanical fingerprint*” of the material. The obtained fingerprint has two portions; the loading portion of the curve which provides information on the materials response to strain, such as elastic, plastic and in some case phase transformation deformation and the unloading portion of the curve, which represents the elastic recovery of the material while the applied load is being removed. A material’s response to the applied load in this initial stage, of loading is elastic and in this stage if the applied load is removed the deformation will be reversible and non-permanent. Eventually, when the applied load is large enough and passes the initial stage, a finite numbers of atomic bonds are broken by the movement of dislocations and some atoms will form bonds with new neighbours. If bond breaking occurs for a large number of atoms and they move relative to each other, they cannot return to their original position even if the stress is removed, therefore the strain is permanent and it is called *plastic* deformation (Jones, 2001; Callister and Rethwisch, 2011). During the nanoindentation test, depending on a material’s response to strain, the transition between elastic and plastic deformation can be different and can occur at various loads for different materials. When the indentation reaches the maximum applied load and plastic deformation has already taken place then during the load removal, the elastic recovery of the sample forms the unloading portion of the curve. The elastic recovery of materials can be divided in to three categories; materials with a low elastic recovery, medium elastic recovery and finally materials with very high elastic recovery. Materials with low elastic recovery such as aluminium (Al) produce an approximately a linear unloading curve and mechanical properties of such materials can be easily provided by measurement of the unloading curve. The second type of materials, such as copper (Cu), provide a non-linear unloading plot due to the greater elastic recovery compared to the first type. The mechanical properties of these types of materials can be obtained by fitting

a power-law relationship to the unloading curve using the Oliver and Pharr method. This method will be discussed in more detail in next section. However, the third type of materials with extremely high elastic recovery such as amorphous carbon nitride ( $CN_x$ ), provide a significantly curved unloading portion to such an extent that even the use of the power-law fitting relationship cannot produce an accurate measurement and consequently the extraction of mechanical properties from such a curved plot is not as straightforward as for the materials with low elastic recovery (Hainsworth *et al.*, 1996). Therefore, for these materials, using the loading portion of the load-displacement curves with a method proposed by Hainsworth and colleagues (Hainsworth *et al.*, 1996) is appropriate. This method will be discussed in more detail in chapter 9.

### **2.1.2 Oliver & Pharr Analysis**

Although there are many analytical techniques (Doerner and Nix, 1986; Oliver and Pharr, 1992; Hainsworth *et al.*, 1996; Cheng and Cheng, 2000; Bull, 2002; Cheng and Cheng, 2004) to determine the load-displacement data from nanoindentation; the most popular one was first suggested by Oliver and Pharr (Oliver and Pharr, 1992). According to this procedure, the hardness and Young's modulus can be determined from the indentation curve during one cycle of loading and unloading (Oliver and Pharr, 2004). The accuracy of these measurements (hardness and modulus) is extremely dependent on the measurement of four important quantities which can all be determined from the load-displacement curve; the maximum load ( $P_{max}$ ), the displacement at peak load ( $h_{max}$ ), the initial elastic unloading stiffness (also known as contact stiffness,  $S$ ) and most importantly the final displacement after complete unloading ( $h_f$ ) (Oliver and Pharr, 2004). A typical load-displacement curve for an indentation experiment is shown in Figure 2-1.

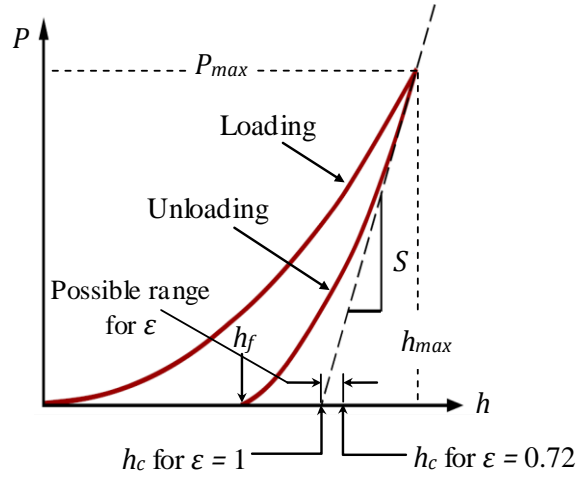


**Figure 2-1. Schematic representation of load-displacement curve in Oliver-Pharr method (Oliver and Pharr, 1992).**

To extract the mechanical properties from symmetrical indenters, Oliver and Pharr expanded on the method of Doerner and Nix (Doerner and Nix, 1986) which is only valid for the flat punch approximation based on the fact that the initial part of the unloading curve is almost linear (Bhushan, 2006). In general, both methods are based on the relationship developed by Sneddon (Sneddon, 1965). In the Sneddon relationship, the indentation contact stiffness was derived as follows (Oliver and Pharr, 1992):

$$S = \frac{2}{\sqrt{\pi}} E_r \sqrt{A_c} \quad (2-1)$$

In this equation,  $A_c$  is the contact area and  $E_r$  is the reduced modulus. Later Pharr, Oliver and Brotzen (Pharr *et al.*, 1992) proved that the equation can be applied to wide range of tips with different shapes. Ultimately, Oliver and Pharr determined that the unloading curves are better described by a power-law relation (Oliver and Pharr, 1992; Oliver and Pharr, 2004) :

$$P = \alpha(h - h_f)^{m_i} \quad (2-2)$$

In Equation (2-2)  $\alpha$  and  $m_i$  are power-law fitting parameters and the values are determined from experimental data. The power law exponent  $m$  varies in the range of 1.2 to 1.6 and it is related to the geometry of the indenter (Bolshakov *et al.*, 1995; VanLandingham, 2003; Oliver and Pharr, 2004). The initial slope of the tangent line

to the unloading curve (the stiffness of the elastic contact) is expressed by evaluating the derivative at the peak load and peak depth of Equation (2-2):

$$S = \left( \frac{dP}{dh} \right)_{h=h_{max}} = \alpha m (h_{max} - h_f)^{m-1} \quad (2-3)$$

By assuming the displacement around the indentation tends to sink-in as shown in Figure 2-2 or that pile-up is negligible (which will be discussed later in section 2.3.4) and that it does not affect the contact area ( $A_c$ ), Equation (2-3) can be used to calculate the contact depth ( $h_c$ ) under the maximum load. For this assumption  $h_c = h_{max} - h_s$  and  $h_s$  is given by:

$$h_s = \varepsilon \frac{P_{max}}{S} \quad (2-4)$$

then  $h_c$  can be considered by:

$$h_c = h_{max} - \varepsilon \frac{P_{max}}{S} \quad (2-5)$$

In Equation (2-5)  $\varepsilon = 0.72, 0.75$  and  $1$  for conical, paraboloid of revolution and flat-ended cylindrical punch geometry respectively (VanLandingham, 2003).

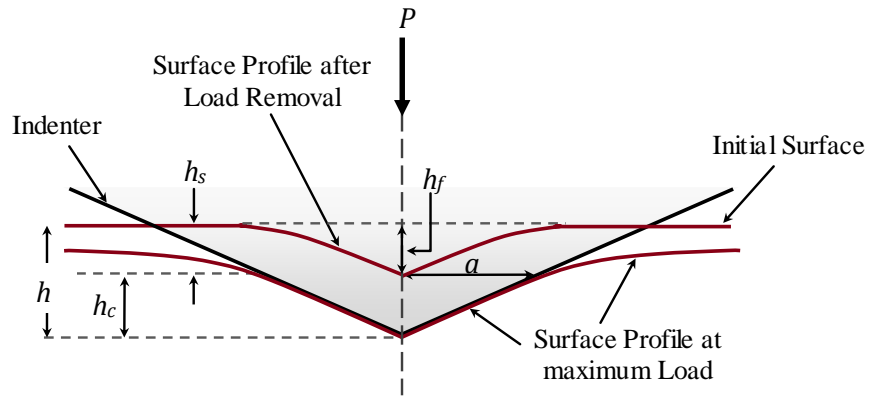


**Figure 2-2. A schematic of the cross-section through an indentation with various dimensions (Oliver and Pharr, 1992).**

For an ideal indenter that does not itself deform significantly, a function,  $f(d)$ , relating the projected contact area,  $A_c$ , to the penetration depth,  $h_c$ , is given by:

$$A_c = f(h_c) = \pi h_c^2 \tan^2 \alpha \quad (2-6)$$

The term  $\alpha$  is the half angle of the indenter and for a Vickers or Berkovich indenter the equivalent cone angle is  $70.296^\circ \approx 70.3^\circ$ , therefore the corresponding projected

area is simplified to  $A_c = 24.5 (h_c)^2$ . Consequently, based on the standard hardness definition and using the load-displacement curve's data, once the supported load and contact area are determined, hardness can be found as below:

$$H = \frac{P_{max}}{A_c} \quad (2-7)$$

$P_{max}$  is the maximum indentation force and  $A_c$  is the contact area at that force. This is essentially an empirical formula and the hardness value will depend on properties such as the yield strength and work hardening parameters.

Effects of non-rigid indenters on the load-displacement behaviour can be considered by defining a reduced modulus,  $E_r$  also known as the contact modulus, which is given by:

$$\frac{1}{E_r} = \frac{1 - \nu_s^2}{E_s} + \frac{1 - \nu_i^2}{E_i} \quad (2-8)$$

The terms  $E_s$  and  $\nu_s$  are the Young's modulus and Poisson's ratio of the sample, and  $E_i$  and  $\nu_i$  are the Young's modulus and the Poisson's ratio for the indenter (1140 GPa and 0.07 for diamond) respectively. The reduced modulus,  $E_r$ , accounts for the fact that the measured displacement includes contributions from both the sample and the indenter (Oliver and Pharr, 1992; Tsui *et al.*, 1996).

By rearranging the Equation (2-1), the elastic modulus of the specimen can be obtained as below:

$$E_r = \frac{1}{\beta\gamma} \frac{\sqrt{\pi}}{2} \frac{S}{\sqrt{A_c}} \quad (2-9)$$

The geometrical factor  $\beta$  is a non-dimensional correction factor which has been introduced to the original stiffness equation (King, 1987). The value of  $\beta$  depends on the tip geometry and can be found in Table 2-1. Moreover, in 1999, the correction factor,  $\gamma$ , was introduced by Hay and colleagues by applying a simple modification to the ideal Sneddon solution based on finite element analysis as well as analytical analysis as below (Hay *et al.*, 1999). The  $\gamma$  factor accounts for the radial deformation which was not included in the Sneddon flat punch approximation.

$$\gamma = \pi \frac{\frac{\pi}{4} + 0.155 \cot \phi \frac{(1-2\nu)}{4(1-\nu)}}{\left(\frac{\pi}{2} - 0.831 \cot \phi \frac{(1-2\nu)}{4(1-\nu)}\right)^2} \quad (2-10)$$

In this equation for the Berkovich indenter,  $\phi$  is equal to  $70.32^\circ$  which is the equivalent cone angle of the indenter tip and  $\nu$  is the Poisson ratio of the indented material. When using a Berkovich indenter, if the  $\gamma$  correction factor is assumed to be 1, the elastic modulus of a material with a Poisson ratio of 0.25 is overestimated by about 8%.

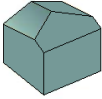
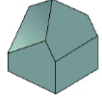
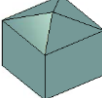
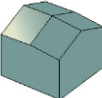
For the cube-corner indenter tip with an equivalent cone angle of  $42.278^\circ$  this equation can be modified to:

$$\gamma = 1 + \frac{(1-2\nu)}{4(1-\nu) \tan \phi} \quad (2-11)$$

The overestimation on the elastic modulus for the cube-corner indenter is even larger and it is approximately 18% compare with when  $\gamma$  is taken to be unity. Therefore, this constant factor can be used to obtain more reliable data for hardness and modulus from nanoindentation load-displacement data. Without this correction factor Sneddon's equation underestimates the contact stiffness which can affect the measured hardness and modulus values.

## 2.2 The Indenter Shape and Geometry

The tip end of the indenter can be made sharp, flat, or rounded to a cylindrical or spherical shape for a specific task. The Brinell sphere, Rockwell conospheroids, and the Vickers and Knoop pyramids are the most used tips for macro-micro scale indentation. Table 2-1 summarises the geometric factors for some of the most common hardness measurement techniques and various indenters along with their impression types.

<i>Test Type</i>	<i>Indentation Shape</i>	<i>Projected Area</i>	<i>Centreline-to-face Angle, <math>\alpha</math></i>	<i>Equivalent Cone Angle, <math>\phi</math></i>	<i>Intercept Factor, <math>\varepsilon</math></i>	<i>Correction Factor, <math>\beta</math></i>
<i>Berkovich</i>		$24.494 h_c^2$	$65.27^\circ$	$70.32^\circ$	0.75	1.05
<i>Cube Corner</i>		$2.60 h_c^2$	$35.26^\circ$	$42.278^\circ$	0.75	1.034
<i>Vickers</i>		$24.504 h_c^2$	$68^\circ$	$70.296^\circ$	0.75	1.012
<i>Knoop</i>		$108.21 h_c^2$	$86.25^\circ$ & $65^\circ$	$77.64^\circ$	0.75	1.012
<i>Sphere</i>		$\pi(2Rh_c - h_c^2)$	-	-	0.75	1
<i>Cone</i>		$\pi(h_c \tan \alpha)^2$	$\alpha$	$\alpha$	$2(\pi-2)/\pi$	1

**Table 2-1. Parameters for commonly used indenter shapes (Fischer-Cripps, 2001; Fischer-Cripps, 2004b; Oliver and Pharr, 2004).**

Generally speaking, we can classify the indenters into two categories, sharp or blunt. At large effective strains, measuring the mechanical properties like hardness requires sharp diamond indenters such as Vickers, Knoop or Berkovich. The Vickers indenter is made of a square-based pyramidal diamond with a half-included tip angle of 70.3 degrees, an angle of 136 degrees between faces and has two distinct force ranges: micro and macro (Smith and Hashemi, 2009; Callister and Rethwisch, 2011). The Vickers and Knoop indenters are mainly known for micro-hardness testing methods on the basis of load (between 1 and 1000 gf) and indenter size. The applied loads are much smaller than for the Brinell and Rockwell tests (Harry, 1999). The Vickers indenter is geometrically similar to the Berkovich indenter with the same area-to-depth relationship (Tsui *et al.*, 1997a). However, the Berkovich design has been developed as the most frequently used sharp indenter in micro and nano-scale tests. Furthermore, compared with the four-sided Vickers pyramid, the edges of the three-sided Berkovich pyramid are more easily manufactured to meet at a single point (Bhushan and Li, 2003).

### 2.2.1 Berkovich Indenter

The Berkovich indenter is a standard tip for nanoindentation with an aspect ratio similar to the four-sided Vickers pyramid to measure the mechanical properties in nano-scale (Hainsworth *et al.*, 1996). These properties, such as the hardness and fracture toughness of materials, can be calculated by sharp indenters like Berkovich (Pharr, 1998; Fischer-Cripps, 2004a). Berkovich indenter has a three-sided pyramid shape, as shown in Figure 2-3 which is geometrically self-similar. This indenter produces well-defined plastic deformation in the surface of the sample at very low loads to minimise indenter tip chisel effects and additionally, it minimises the influence of friction. The Berkovich indenter tip is normally used for bulk materials, thin films, scratch and wear testing. The total included angle on the tip is 142.3 degrees with a face angle of 65.27 degree, as shown in Figure 2-3 (Fischer-Cripps, 2011). The average radius of curvature for the Berkovich tip is normally between 50 and 150 *nm* and it can be used down to indentation depths of approximately one third of the radius of curvature value. This radius is prone to mechanical wear due to tip-surface interactions with hard samples.

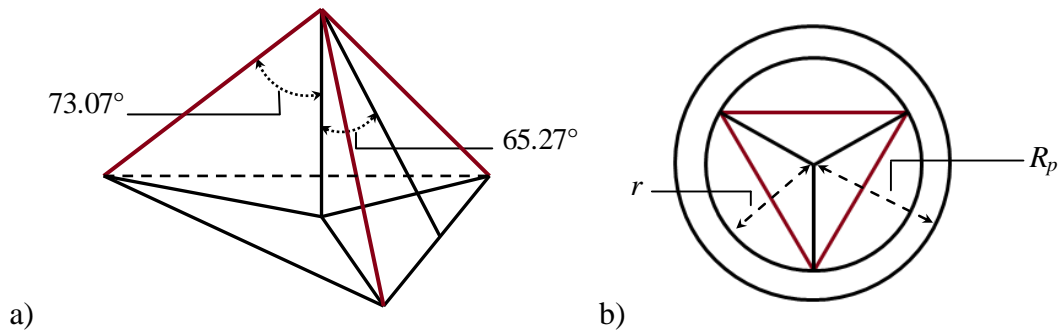


**Figure 2-3. Schematic of (a) a Berkovich tip and (b) an indent from top view; the terms  $R_p$  and  $r$  are the plastic zone radius and the indenter radius respectively.**

In an elastic-plastic indentation, an approximately hemispherical zone of plastic deformation forms beneath the indenter once plasticity is well-established. The radius of this plastic zone may be bigger than that of the impression. The relationship between the radius of plastic zone,  $R_p$ , and the residual depth of the indent is given by (Chen and Bull, 2006a):

$$\frac{R_p}{h_r} = \sqrt{0.3\pi} \sqrt{\frac{E_r}{Y}} \left[ \left( \cot \theta \sqrt{\frac{E_r}{H}} + \frac{\varepsilon\pi}{2} \sqrt{\frac{H}{E_r}} \right) - 0.62\varepsilon\pi \sqrt{\frac{H}{E_r}} \right]^{-1} \quad (2-12)$$

In this equation the term  $Y$  is the yield stress. With regards to the maximum indenter displacement,  $h_{max}$ , Equation (2-12) may be approximated by (Bull, 2002; Chen and Bull, 2006b):

$$\frac{R_p}{h_{max}} = -12.907 \frac{H}{E_r} + 4.5451, \quad \frac{H}{E_r} < 0.35 \quad (2-13)$$

However, for the determination of elastic-plastic properties of materials in appropriate low loads, the spherical indenter attracted the most attention in the past. It has been reported (Lawn and Fuller, 1975; Hagan and Swain, 1978) that at high loads the spherical indenter provides the same patterns as the sharp indenter, and therefore they can be classified as sharp or blunt indenters depending on the applied load (Fischer-Cripps, 2000).

### 2.2.2 Spherical Indenter

Historically, since Brinell proposed the spherical indentation technique, this technique has been used for the determination of material's mechanical properties, mostly for bulk materials (Harry, 1999; Chinn, 2009).

Depending on the indentation tip and size, the stress developed on the sample surface becomes different and is dependent on the ratio between the yield and the actual strain of the material. Usually materials show elastic behaviour when the ratio is low and if the ratio gets higher, the material shows plastic behaviour.

Spherical indenters evaluate hardness by following the transition from elastic to elastic-plastic behaviour providing a smooth contact is maintained. As the indenter goes into the sample, the characteristic strain changes continuously. As the initial contact stress is small it only produces elastic deformation and follows the well-known Hertz law (Field and Swain, 1995). For the spherical nanoindentation, most of the data analysis is based on the Hertz equation (Doerner and Nix, 1986; Field and Swain, 1993; Field and Swain, 1995; Tabor, 2000). The spherical indenter has some advantages such as the extended elastic-plastic deformation when compared to the sharp indenters like Berkovich, which does not have a clear elastic-plastic transition.

In addition, it is useful in the determination of the yield point, and below the yield point it can provide more information on the elastic-plastic transition (Bell *et al.*, 1992b). Furthermore, this information allows for calculation of the yield stress and work hardening (Bell *et al.*, 1992c; Bhushan and Li, 2003).

When the indentation strain exceeds the yield point, the hardness and modulus results can be similar to those obtained using a pyramidal indenter. However, the axisymmetric indenter geometries are not very sharp, and the spherical surface is not always perfect. Therefore, spherical indenters are reasonably useful for measuring the mechanical properties of soft materials (Doerner and Nix, 1986; Zhang and Xu, 2002a).

After the method first introduced in 1992 (Oliver and Pharr, 1992) by Oliver and Pharr to measure the Young's modulus and hardness of materials from the power-law relationship, they found that the method could be readily extended to other indenters, such as spherical indenters, according to Hertz's equation, assuming a linear elastic, isotropic, materials response. In this equation, by considering the penetration of a rigid spherical indenter into a flat sample, the relation between load and indentation depth can be described as below (Oliver and Pharr, 2004):

$$P = \frac{4}{3} E_r R^{1/2} h_e^{3/2} \quad (2-14)$$

where in this equation  $h_e$  is the elastic distance into the surface ( $h_e = h - h_f$ ),  $E_r$  is the contact modulus that can be determined by using Equation (2-8) and  $R$  is the relative radius of curvature based on the radius of the residual impression,  $R_r$ , and the indenter,  $R_i$ . Although it can be defined as  $1/R = 1/R_i + 1/R_r$ , because  $R_r$  approaches infinity for a flat sample, this can be modified to become  $R = R_i$  (see Figure 2-4 ) (Fischer-Cripps, 2011).

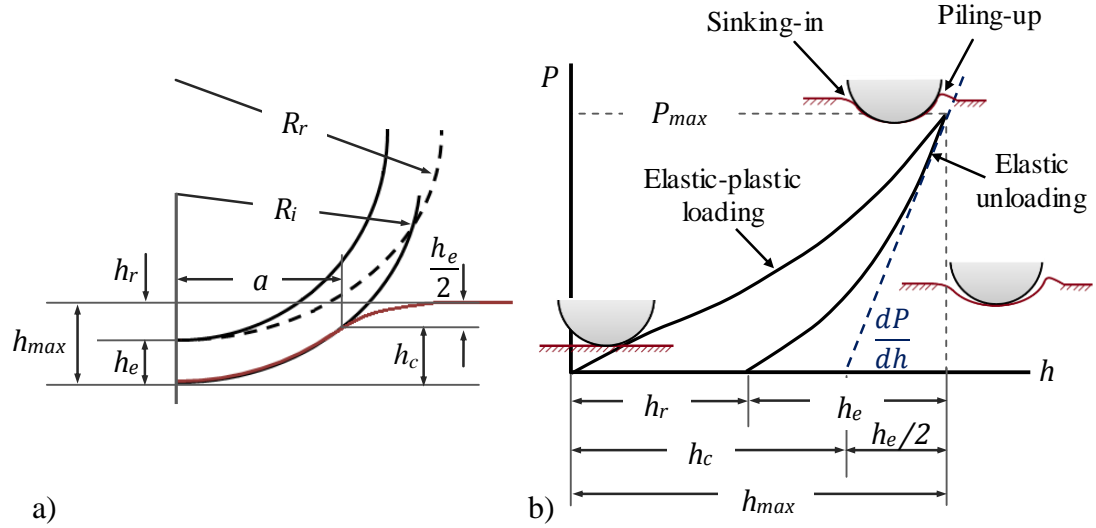


**Figure 2-4. Schematic representations of (a) loading a performed impression of radius  $R_r$  with rigid indenter radius  $R_i$  and (b) the load-displacement curve obtained for an elastic-plastic material using a spherical indenter. Modified from (Fischer-Cripps, 2011).**

The derivative of Equation (2-14) with respect to  $h$  gives the stiffness:

$$S = \frac{dP}{dh} = 2\sqrt{RE_r}h_e^{1/2} \quad (2-15)$$

At the maximum contact depth ( $h = h_{max}$  and  $h_f = 0$ ) for a perfectly rigid spherical tip in the elastic regime, where the elastic displacements of a plane surface are equal above and below of the circle of contact, Sneddon (Sneddon, 1965) established that:

$$h_e = h_t = \frac{a^2}{R} \quad (2-16)$$

where  $a$  is the contact radius during indentation (see Figure 2-4). Combining Equations (2-14) and (2-15) gives:

$$P = \frac{2}{3} \frac{dP}{dh} h_e \quad (2-17)$$

Therefore:

$$h_e = \frac{3P}{2S} \quad (2-18)$$

Finally, contact radius ( $a$ ) can be calculated from Equation (2-16) by the knowledge of  $P$  and  $S$ , once  $h_e$  is known.

In spherical indentation there is an elastic-plastic transition when  $h_f$  is greater than zero. In the elastic-plastic regime, many aspects can be determined from the analytical methods of Oliver and Pharr (Oliver and Pharr, 2004) and Field and Swain (Field and Swain, 1995) similarly to the Berkovich indenter. As an example, stiffness and contact depth can be established from the unloading curve using Equations (2-4) and (2-5) by assuming that the contact depth can be described by using the maximum penetration depth and contact circle as shown below:

$$h_c \approx h_t - \frac{h_e}{2} \quad (2-19)$$

Therefore, combining Equation (2-18) and Equation (2-19), and using the Oliver and Pharr method by noting that  $\varepsilon$  for a sphere is 0.75, the following expression for the computation of  $h_c$  proposed:

$$h_c = h_t - \frac{3P}{4S} \quad (2-20)$$

To extract the hardness and reduced modulus using the Equations (2-7) and (2-9), the contact area function ( $A = \pi a^2$ ) can be determined by use of a reference sample with known modulus for spheres smaller than  $2 \mu m$  in diameter. However, once  $h_c$  is known, for the greater spheres with a perfect geometry and known indenter radius, the contact radius ( $a$ ) and contact area function can be estimated as below:

$$a = \sqrt{2Rh_c - h_c^2}, \quad A = \pi(2Rh_c - h_c^2) \quad (2-21)$$

If the indenter tip is perfectly spherical and  $h_c \ll a$ , then the contact radius can be simplified as:  $a \approx \sqrt{2Rh_c}$ .

As mentioned before, by plotting the stress-strain curve using the spherical indenter, the yield point of material can be determined. By transforming Equation (2-14) to a linear relationship using Tabor's (Tabor, 2000) determination of stress as a function of the contact pressure and representative strain equation, the indentation stress and strain can be estimated respectively as:

$$\sigma_{ind} = \frac{4E^*}{3\pi} \varepsilon_{ind}, \quad \sigma_{ind} = \frac{P}{\pi a^2}, \quad \varepsilon_{ind} = \frac{a}{R} \quad (2-22)$$

Although measuring the contact area is an important concept to obtain accurate mechanical properties such as the hardness and Young's modulus, it should be noted

that there are certain parameters to which the knowledge of contact area does not necessitate. There are certain secondary factors affecting nanoindentation test results. Some of these factors are thermal drift, creep, initial penetration depth, instrument compliance and indentation size effect.

## **2.3 Secondary Concepts**

### ***2.3.1 Thermal Drift and Creep***

Drift can be due to vibration or a thermal drift. Thermal drift refers to the temperature change in the room during the test, a different thermal expansion in the machine between the sample and the indenter or sometimes this appears by heat generation from the electronic unit of the instrument. As the nanoindentation instruments are highly sensitive at very small scales of measurement depth down to a few nano-meters and are constructed of dissimilar materials, any temperature changes can cause dimensional variation of the sample and influence the results (Fischer-Cripps, 2011). Therefore, to avoid expansion or contraction of the indenter tip and specimen surface, it is important to keep the whole indenter system in thermal equilibrium and place it on an anti-vibration table to prevent any negative effect of vibration. There are different ways to minimise the thermally induced displacement drift. The temperature of the testing machine should be maintained over the period of one cycle and the variation should not exceed  $0.5\text{ }^{\circ}\text{C}/\text{h}$  (Nohava *et al.*, 2009). One of the most common ways is placing the system in a highly insulated chamber and by locating it in a laboratory with a controlled temperature. However, the accuracy of the results heavily depends on the true thermal drift rate measurement during each indentation cycle, as it can add an error to the displacement signal. This can be done by holding the load at a fixed low load (typically less than 10% of the maximum load) at the beginning of the test to allow the specimen to stabilise. Alternatively this can be achieved through holding the constant load for a fixed period of time (i.e. over 5 or 10 seconds) at either the maximum indentation force or at the last data point on the unloading curve (usually 20% of the maximum applied load) and measuring the displacement over time. It is important to note that thermal drift can influence the creep data significantly. Although they are two different phenomena, if the drift source is not totally removed, the results can show a different outcome. Figure 2-5

illustrates a typical load function with two different segments that were added to minimise both the thermal drift and creep effects on the nanoindentation data.

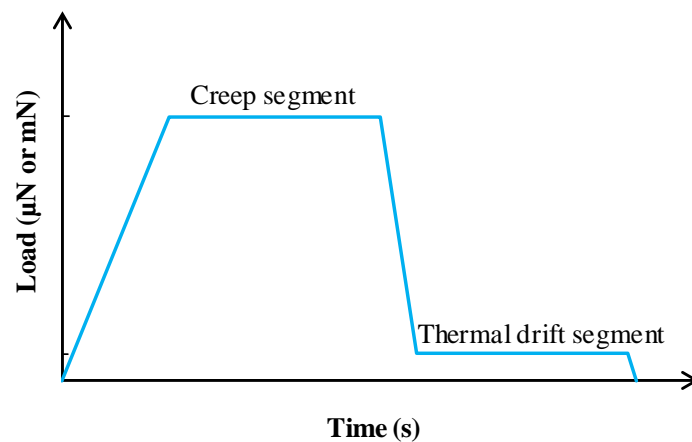


**Figure 2-5. Schematic of load versus time (load function) with two holding segments to minimise the effect of creep and thermal drift on the nanoindentation data.**

Plastic deformation in many materials depends on the stress, temperature and time. Creep appears because of time-dependent plastic flow with extreme effects for soft and low melting point materials. As creep is characterised as deformation under the influence of stress, it can also manifest clearly during indentation. Therefore, a further depth increase arises during the hold period at maximum force, which is due to the fact that materials plastic deformation caused by creep is faster than the elastic recovery due to the load removal during unloading portion of the indentation cycle (Chudoba and Richter, 2001). To minimise the creep effects on the mechanical properties measurements by indentation, the rate and also the amount of applied stress as well as its duration should be considered for different materials. If the hold at maximum load before unload during the indentation cycle is sufficient, the creep displacement remains negligible (Baker *et al.*, 1991; Feng and Ngan, 2002). This is because, at room temperature, the processes involve the rearrangement of existing dislocation arrays by thermally activated processes (dislocation climb) to lower energy configurations (so called exhaustion creep) unless the homologous temperature is sufficiently high. However, if the holding period is very long there are other problems such as stability of the instrument that need to be considered (Goodall and Clyne, 2006).

### 2.3.2 Machine Compliance and Shape Function

During the indentation test when the tip is pushing in towards the sample, according to the Newtonian theory, the machine frame is being loaded as well as the sample. As a result the load frame is elastically deflected by the reaction force. In addition to the indenter tip and the sample, one of the main elastic components in the loading system is frame compliance ( $C_f$ ), i.e., the elastic deformation of the frame due to indentation load (Nohava *et al.*, 2009). Therefore, the indenter depth of penetration into the sample and the relative displacement in the loading system are related to the machine frame stiffness or compliance. When the applied load is relatively large, machine compliance effects can be crucial for the load-displacement data measurement and the accuracy of the results critically depends on the calibration step (Bhushan, 2006). It is possible to calculate the machine compliance by calibrating it with various indents in a reference material with known mechanical properties such as Al for large penetration depths and/or fused silica for smaller depths (VanLandingham, 2003). However at present, fused silica ( $E = 72 \pm 0.2 \text{ GPa}$ ,  $\nu = 0.17$ ) is the most accepted material for calibration because of its depth and time independent properties at room temperature (Nohava *et al.*, 2009).

The total compliance ( $C_{total}$ ) can be calculated from the unloading part of the load-displacement curve as it is related to the total inverse stiffness at the initial unloading point ( $C_{total} = 1/S$ ), and the compliance of the sample ( $C_s$ ) can be defined as the contact stiffness. The difference between the expected value and the calculated value from the unloading curve is due to the machine compliance, including the compliance of the loading frame, the indenter shaft and the specimen mount (Fischer-Cripps, 2011). The impact for sharp indenters, such as Berkovich, using a relatively small load for soft material can be negligible (Wolf, 2000).

The displacement arising from the load frame should be removed from the load-displacement data. The displacement of the sample ( $h_s$ ) along with the displacement of the load frame ( $h_f$ ) gives the total displacement ( $h_{total}$ ) measured by the instrument under the applied load ( $P$ ) (VanLandingham, 2003):

$$h_{total} = h_s + h_f \quad (2-23)$$

The equation that puts the total measured compliance by the instrument in relation with sample compliance and frame compliance, can be defined by dividing both sides of Equation (2-23) by load.

$$C_{total} = C_s + C_f \quad (2-24)$$

Assuming that the system (the instrument and the specimen) act like two springs in series, and the sample and the indenter compliance can be taken as the inverse of the stiffness, this equation can be rewritten as below:

$$C_f = C_{total} - \frac{1}{S} = \frac{dh}{dP} - \frac{\sqrt{\pi}}{2E_r} \frac{1}{\beta\sqrt{A}} \quad (2-25)$$

In Equation (2-25), the load frame compliance is taken to be a constant that is independent of the load (Oliver and Pharr, 2004). Therefore, frame compliance can be obtained by measuring the contact area, contact displacement and total machine compliance by making various indentations on the homogeneous and isotropic reference sample with known properties and finally, correcting the indentation data for the frame compliance (Herrmann *et al.*, 2000). For the Berkovich indenter where,  $A = 24.5 (h_c)^2$ , Equation (2-25) can be rewritten using Equation (2-9) as below:

$$C_f = \frac{dh}{dP} - \sqrt{\frac{\pi}{24.5}} \frac{1}{2\beta E_r} \frac{1}{h_c} \quad (2-26)$$

Alternatively, for the spherical indenter, where  $A = 2\pi R_i h_c$ , this yields (Fischer-Cripps, 2011):

$$C_f = \frac{dh}{dP} - \left[ \frac{1}{2\beta E_r R_i^{1/2}} \right] \frac{1}{h_c^{1/2}} \quad (2-27)$$

It should be noted that, where the Young's modulus and hardness for a given reference material is assumed to be depth-independent (in other words, if  $H$  and  $E_r$  are independent of load), the approach to measure and correct the machine compliance does not require the knowledge of contact area beforehand. As, for the depth-independent materials, the relationship between hardness and Young's modulus is independent from the contact area (Joslin and Oliver, 1990):

$$\frac{P}{S^2} = \frac{\pi}{(2\beta)^2} \frac{H}{E_r^2} = PC_s^2 \quad (2-28)$$

Therefore, combination of this equation and Equation (2-25) gives:

$$\sqrt{P}C_{total} = \frac{\sqrt{\pi} \sqrt{H}}{2\beta E_r} + \sqrt{P}C_f \quad (2-29)$$

This method is one of the most common methods to obtain the frame compliance value. It is possible to derive a simple linear plot of  $P^{1/2}C_{total}$  vs.  $P^{1/2}$  with a slope of machine compliance and a y-axis intercept of  $H^{1/2}/E_r$  (Stone *et al.*, 1991).

### 2.3.3 Initial Penetration Depth

During a nanoindentation test, the preferred measurement of the indenter displacement will use a sample free surface as a reference point. In reality this does not occur, and the benchmarks for displacement measurements are produced by allowing the tip to come into contact with the sample surface. Therefore the contact depth for this benchmarking should be minimised to the greatest possible degree. This can be achieved by using the lowest attainable contact force ( $P_i$ ) of the nanoindentation instrument. Although this contact force is very small, the indenter still slightly penetrates beneath the sample surface. Hence, to account for this error, the initial penetration depth ( $h_i$ ) should be added to all subsequent indentation displacements.  $h_i$  can be calculated from Equation (2-30) that relates load and penetration:

$$h_i = kP_i^m \quad (2-30)$$

where  $m$  and  $k$  constants and are dependent on the indenter shape. This equation is fitted to data from the early stages of loading to back calculate the initial displacement and affect the displacement scale.

### 2.3.4 Piling-Up and Sinking-In

One of the important features in nanoindentation tests is that the material around the contact area is pushed upwards or downwards against the indenter's tip to form pile-ups or sink-ins on the edges, therefore influencing the contact area calculations. The material may either sink-in or pile-up by plastic deformation around the indenter, and generally pile-ups take place in soft metals like Cu. Consequently, the accuracy of the hardness and Young's modulus results, as well as the contact area measurement, depends on the occurrence of pile-ups or sink-ins and this can be different in terms of

strain hardening behaviour of the materials after the tip penetration (Wang *et al.*, 2004). Additionally the indenter tip shape can influence the magnitude of pile-up or sink-in. For example, the hardness for the spherical indenter depends on the load, the tip geometry or both. Furthermore, because of the transition from elastic to elastic-plastic deformation in different penetration depths, pile-up and sink-in occurrence is a function of the indentation depth for spherical indenters (Taljat and Pharr, 2004).

Pile-ups occur when the sample already has residual compressive stresses and is work hardened. Alternatively, when the sample has high strain-hardening potential (i.e., for pre-annealed material) the surface around the indenter tends to sink-in. Pile-ups normally increase the effective contact area. Therefore, if the load is divided by an increased area of contact, the hardness will decrease when compared with that for the area in the absence of pile-up. The influence of pile-ups around various indenters for the evaluation of hardness and Young's modulus has been studied by a number of researchers (Cheng and Cheng, 2004; Elmustafa, 2007; Garrido and Rodriguez, 2007). In general when pile-up occurs, the values of hardness and reduced modulus determined by the Oliver and Pharr method are too high since this method is based on the contact area in the plane of the original surface, rather than the true contact area.

## **2.4 Summary**

An overview of the nanoindentation technique and the most commonly employed method for determining hardness and modulus values were introduced. The determination and analysis of mechanical properties using nanoindentation for both pyramidal and spherical indenter geometries were described. Secondary concepts that influence the obtained indentation data such as thermal drift, creep, machine compliance and the indentation area function were also presented.

After the introduction of the nanoindentation technique and the Oliver and Pharr method along with its advantages and disadvantages in determining the hardness and Young's modulus values in this chapter, the nanoindentation system used in this work is discussed in the next chapter. This is followed by an introduction of the characterisation and analysis methods that have been used in this work to measure the crystallographic and microstructural properties of the samples.

## Chapter 3. Experimental Methods

*This chapter details the testing methods carried out in this work. The nanoindentation method used to measure mechanical properties is described. Sample morphology and structure are characterised using atomic force microscopy, optical microscopy, scanning electron microscopy and electron backscatter diffraction. Furthermore, several X-ray based spectroscopy techniques such as X-ray energy dispersive spectroscopy, X-ray diffraction and X-ray Photoelectron Spectroscopy are described. Finally, Raman spectroscopy is described.*

### 3.1 Nanoindentation Instrumentation

Interest in nanoindentation techniques for the mechanical characterisation of materials spawned several commercial instrument designs of an indentation system. The fundamental clarification of the nanoindentation test is applying a continuously controlled load with a geometrically well-defined indenter to the sample and then removing the applied load as well as monitoring the displacement in loading and unloading using either inductance or capacitance displacement sensors (Hay and Pharr, 2000). The applied loads can be applied using the electrostatic force generation, the expansion of the piezoelectric element or the movement of a coil in magnetic field. Even this basic description provides a range of different designs for the depth sensing nanoindentation tests (Fischer-Cripps, 2011). Figure 3-1 shows a schematic of the most common commercial instruments available.

The implementation of instrument design can be classified by force actuation. There are some advantages and disadvantages with regards to each design. As an example, thermal stability, vibration isolation, force resolution, load and displacement ranges all can vary depending upon the design. In the XP Nano-Indenter shown in Figure 3-1 (a), an electromagnetic actuator is used to provide the applied load. In this design the actuator has a permanent magnet containing a cylindrical slot with a coil of wire inserted into it (Burnham and Colton, 1989), allowing for a wide range of applied loads and displacements. However, in this method the heat generated in the coil as a consequence of the applied current can be considerable and cause a change in the electrical resistance as well as causing thermal expansion in the indenter shaft. The pendulum design shown in Figure 3-1 (b) is one of the well-executed coil actuator

designs that passes a current through the coil at the top of the pendulum and addresses these issues.

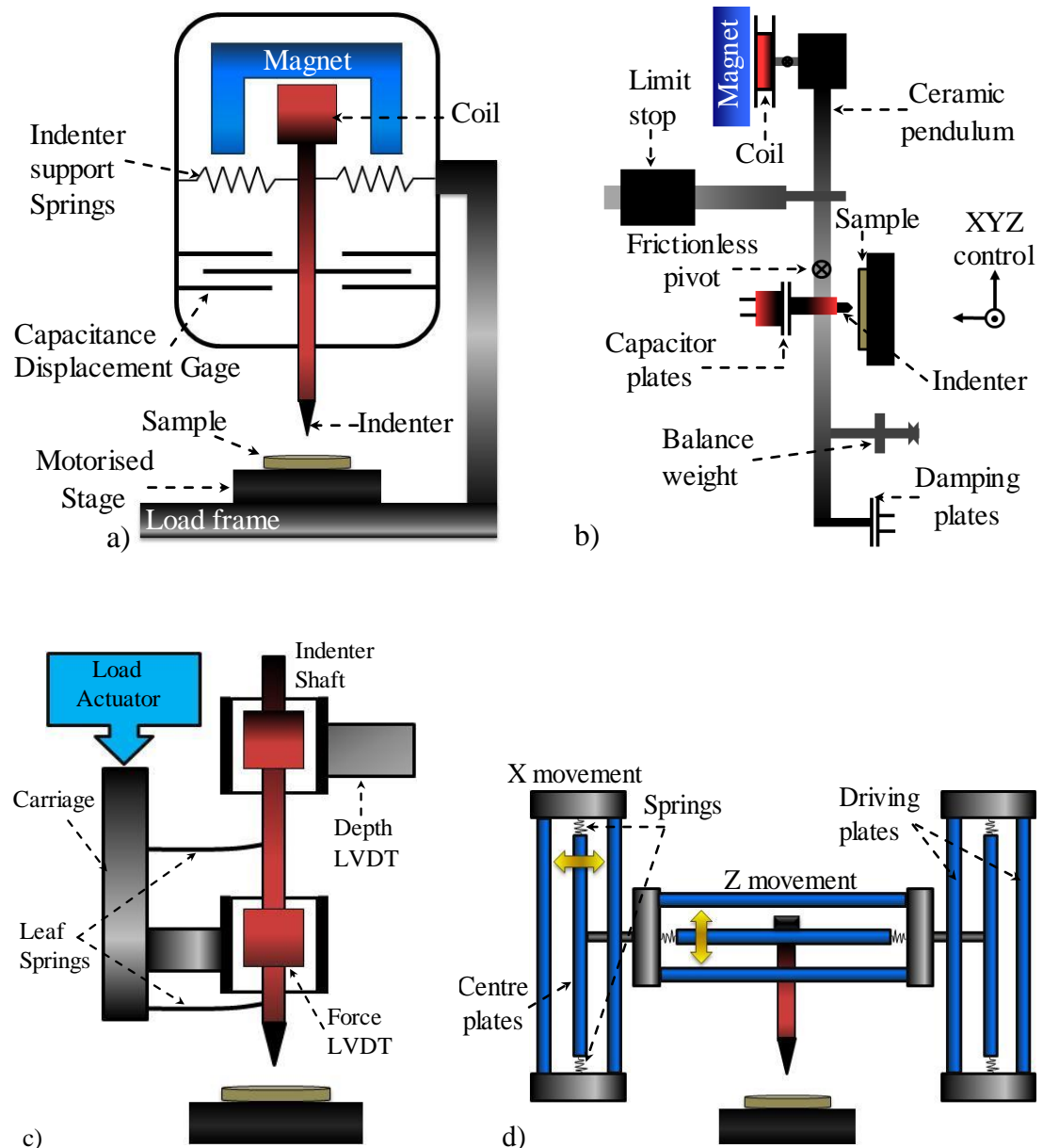


**Figure 3-1. The schematic of commercial instruments (a) Agilent, Nano-Indenter XP (b) MicroMaterials, NanoTests pendulum based system, (c) CSIRO, Ultra-Micro-Indentation system (UMIS) (d) Hysitron, Tribo-Scope from (Micromaterials Ltd; Bell *et al.*, 1992a; Mann, 2007; Fischer-Cripps, 2011).**

The other common method of applying load is via the use of a spring. Figure 3-1 (c) illustrates the Ultra-Micro-Indentation System (UMIS) that transfers force using leaf springs to the indenter shaft. In this case the load application is produced from a piezoelectric actuator. The displacement and depth are recorded via a linear variable differential transformer (LVDT) (Bell *et al.*, 1992a). Another method of applying

load is the use of electrostatic force actuation that was proposed by Lilleodden in 1995 (Lilleodden *et al.*, 1995). In this method a three-plated capacitive transducer system is used to apply the required load by electrostatic actuation (Asif *et al.*, 1999). The schematic of the Hysitron transducer shown in Figure 3-1 (d) illustrates the three parallel plates, the two outer plates having AC signals, and the middle plate with the indenter shaft attached to it.

### **3.1.1 Hysitron Triboindenter**

For the nano-scale surface analysis, the Hysitron Triboindenter with a single platform design and low load indentation system is a high-throughput instrument designed to characterise mechanical properties, especially the hardness and Young's modulus. The special design of the Triboindenter, having a transducer with a three-plate capacitive displacement measurement, electrostatic force application, low noise floor and also its superior temperature stability, make it capable of accurately measuring the mechanical properties in both the nano and micro scales of diverse sample types and sizes ranging from ultra-thin films to bulk materials. It also offers the unique ability to perform microscopy imaging with an in-situ scanning probe microscopy (SPM) (Mondal *et al.*, 2008).

In the current study, all of the depth sensing nanoindentation tests were performed using a Hysitron TI 900 Triboindenter which is shown in Figure 3-2 (a). Furthermore, the essential components of the Triboindenter such as its base, XYZ staging system, top-down optical microscope, Triboscanner, transducer and vibration isolation platform are also shown in Figure 3-2. To achieve the instrument's high stability and also minimise the drift and noise transfer, the XYZ stage which controls the sample and tip positions, optical microscope and Triboscanner are attached to the granite base that is shown in Figure 3-2 (c). This rests in an active piezo base central location stone. The top-down optics, with 100X total magnification of an image between the objective lens and the zooming optics, sends the image to the CCD detector which is connected to the computer system.

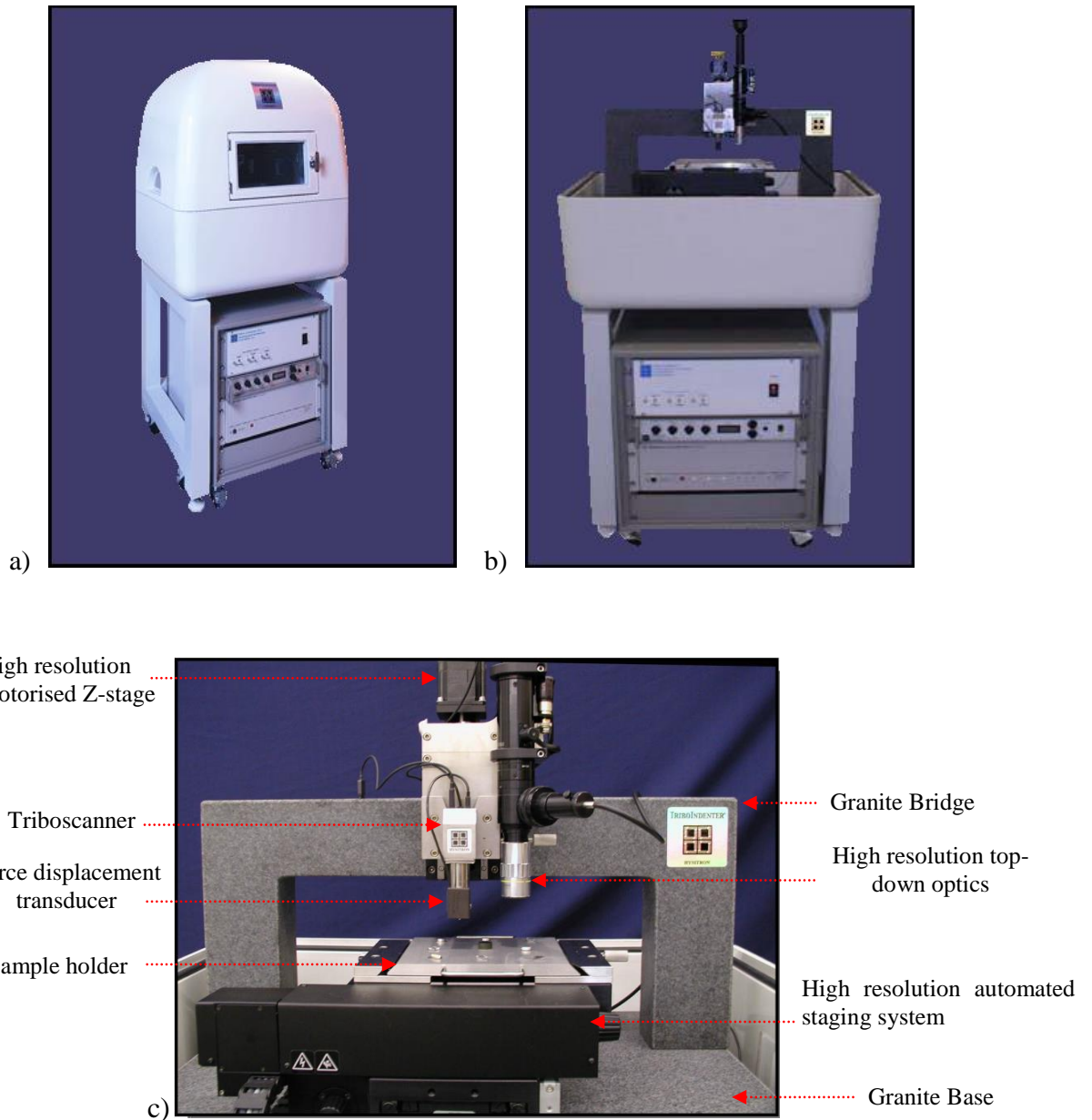


**Figure 3-2. Hysitron Triboindenter (a) Acoustic Enclosure (b) Vibration Isolation Platform (c) closer view of the Triboscanner base, Transducer, Stage, Piezo and Optics, adapted from (Hysitron, 2001; Wang *et al.*, 2009)**

After choosing the preferred area for indentation test via microscope, the Triboscanner with a three axis piezoelectric scanner design offers incredibly accurate positioning of the area of interest as it has much higher precision than the XYZ stage. Moreover, it can be used to capture the surface images before and after indentation tests that would allow for very precise positioning of the indentations and also to find out further information about the sample surface behaviour after the indentation test. It should be noted that this accuracy of tip positioning and surface imaging is due to the use of a rigid tandem piezoelectric ceramic scanning tube which can change

shape by applying high voltage. This change ideally should have a linear relationship with the applied voltage which is shown in Figure 3-3 (a), however in reality creep or hysteresis can affect the deformation and cause non-linearity which is shown in Figure 3-3 (b). Hysteresis occurs when the mechanical response of the ceramic lags behind the applied voltage. This effect can be more significant with increasing and decreasing voltages through cycles. Creep is normally caused as a result of drastic changes in the voltage to the piezo. The piezo continues to deform and often it will overshoot the desired deformation and then ‘ring’ for a short period of time before the final deformation is reached, as shown in Figure 3-3 (b). This can easily be accounted for and eliminated by using short hold times while performing tests and by the Triboindenter software when imaging.

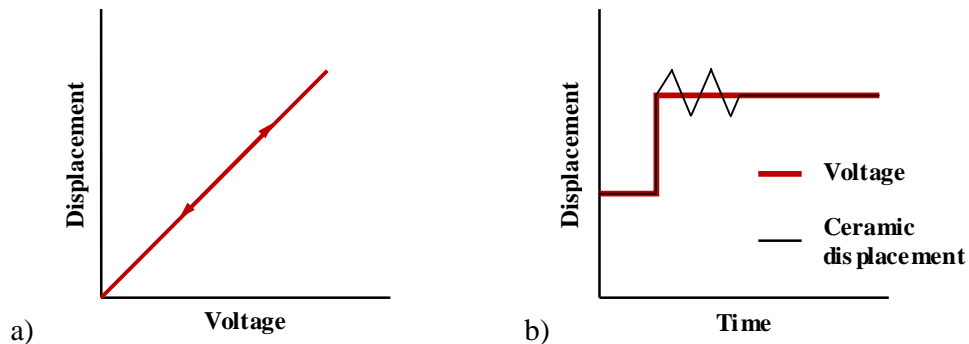


**Figure 3-3. (a) ideal piezo ceramic behaviour (b) realistic piezo ceramic behaviour under the applied voltage illustrating overshoot and ringing during the test (Hysitron, 2001).**

The transducer, with patented three plate capacitive load-displacement (Bonin and Hysitron Inc., 1996; Bonin and Hysitron Inc., 1999) and low head mass, is the key reason that makes the Hysitron more accurate at low loads than other types of nano-indenters since it both functions as the actuator and sensor of the instrument. The unique design of the transducer provides high sensitivity and stability, a large dynamic range, and a linear force/displacement output signal. (Hysitron, 2001). The transducer with a low sprung centre plate mass allows for having minimal external vibration effect with an ultra-low load indentation test which is less than  $25 \mu N$ .

As mentioned previously, the transducer uses electrostatic actuation to apply the load, and during the loading and also the unloading process the changes in the capacitance allows for measurement of the displacement. One of the advantages of

electrostatic actuation is minimisation of the drift, as it needs only an incredibly small amount of current to apply the load. Consequently, the amount of heat produced during actuation is much smaller when compared to the other methods such as those used in the electromagnetic design. This makes performance repeatable with high accuracy (Yu *et al.*, 2005).

### 3.1.1.1 Electrostatic Actuation Force and Displacement Measurement

The electrostatic actuation applies a DC bias (up to 600 V) to the transducer's bottom plate (fixed lower outer plate). The moveable centre plate will be pulled down by the electrostatic attraction between the bottom and centre plates. The mechanical force ( $F_m$ ) of the spring action and electrostatic force ( $F_e$ ) due to the attraction between these plates can be given as follows respectively:

$$F_m = k_s x \quad (3-1)$$

and

$$F_e = \frac{1}{2} \epsilon_0 A E^2 = \frac{1}{2} \frac{\epsilon_0 A}{(d - x)^2} V^2 \quad (3-2)$$

In the Equation (3-1) the term  $k_s$  is the stiffness of the support spring which is constant and  $x$  represents the displacement. The force from Equation (3-2) can be calculated from the applied voltage magnitude ( $V$ ), where  $d$  is plate separation (the nominal gap between the top and middle plates or bottom and middle plates),  $\epsilon_0$  is the dielectric constant of air ( $8.854 \times 10^{-12} \text{ F/m}$ ),  $A$  is the plate area ( $2.03 \times 10^{-5} \text{ m}^2$ ) and  $E$  is the electric field strength in the gap between the electrodes (Yu *et al.*, 2005; Srivastava, 2006). The external applied load can be calculated by combining the Equations (3-1) and (3-2).

The maximum available force from the transducer is around 30 *mN* which is much lower than from electromagnetic actuation. However, it should be considered that the force provided by electrostatic actuation is more than that required for most nanoindentation tests. The amount of current required for the applied force is much lower than for electromagnetic actuation. Consequently the resistivity is lower and the heat generation is less.

Figure 3-4 describes the Hysitron transducer in two different conditions with no applied voltage, which is called transducer at rest, and under applied voltage which is called transducer with applied load.

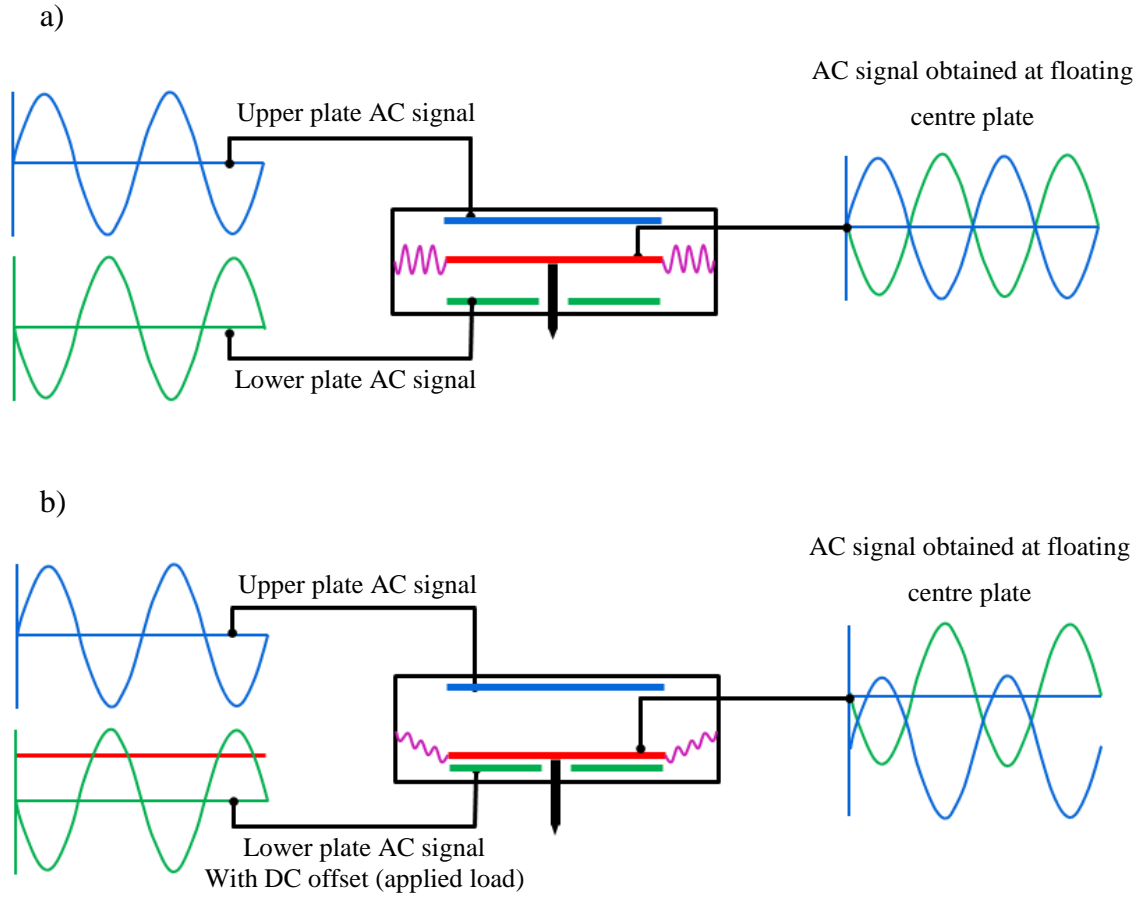


**Figure 3-4. Explanation of the three-plate capacitive transducer (a) at rest and (b) under the applied voltage.**

As it can be seen in Figure 3-4 the force-displacement transducer contains two fixed outer electrodes known as drive plates, with two complementary AC signals that are 180° out of phase with each other and one moveable centre plate (pick-up plate) that applies the load. The sensing output of two applied AC signals with opposite polarity and equal magnitude is an AC voltage signal at the centre (floating) plate which measures the change in capacitance ( $\Delta C$ ):

$$\Delta C = C_2 - C_1 = \frac{\epsilon_0 A}{d - x} - \frac{\epsilon_0 A}{d + x} = \frac{\epsilon_0 A(2x)}{d^2 - x^2} = 2\epsilon_0 A \frac{x}{d^2 - x^2} \quad (3-3)$$

When the centre plate moves, the individual capacitances ( $C_1$  and  $C_2$ ) in both sides of the central plate change. Consequently the vertical displacement of the indenter tip

can be measured (Srivastava, 2006). The main specifications of the transducer such as the maximum load and displacement of the currently used Triboindenter and its available capabilities for measurement are detailed in Table 3-1.

<b>Transducer</b>	<b>Z-axis</b>	<b>X-axis</b>
Maximum Force	10 <i>mN</i>	2 <i>mN</i>
Load Resolution	1 <i>nN</i>	3 $\mu$ <i>N</i>
Load Noise Floor	100 <i>nN</i>	10 $\mu$ <i>N</i>
Maximum Displacement	-	15 $\mu$ <i>m</i>
Maximum Depth	5 $\mu$ <i>m</i>	-
Displacement Resolution	0.04 <i>nm</i>	4 <i>nm</i>
Displacement Noise Floor	0.2 <i>nm</i>	10 <i>nm</i>
Thermal Drift	<0.05 <i>nm/s</i>	<0.05 <i>nm/s</i>

**Table 3-1. Measurement capability and accuracy of the transducer used in Hysitron Triboindenter.**

There are some secondary concepts that should be considered in terms of Triboindenter design such as the acoustic enclosure and the vibration isolation platform. The acoustic enclosure is designed to sound and draft proof the Triboindenter. This also eliminates drift by acting as a thermal buffer.

There are two legs or elements with four piezo-electric accelerometers in each leg running inside the acoustic enclosure under the Triboindenter base. These Piezo-electrics sense displacements in both the horizontal and vertical directions and the electro-dynamic transducers will send amending forces to dampen the vibrations (frequency range between 1 and 200 *Hz*: active dampening). However, under the higher frequencies (frequency range beyond 200 *Hz*: passive dampening) the granite base and the spring system dampen vibration. Consequently, the corrected voltages are sent to the transducer by the control unit.

### **3.1.2 Tip Selections**

As mentioned in section 2.2, there are various tips available in different shapes and sizes for use with Triboindenter. They can be flat, sharp or rounded, with the most often used for indentation being three sided pyramidal tips. In the current study, a Berkovich tip has been used and Figure 3-5 shows the top and side views of the actual tip.

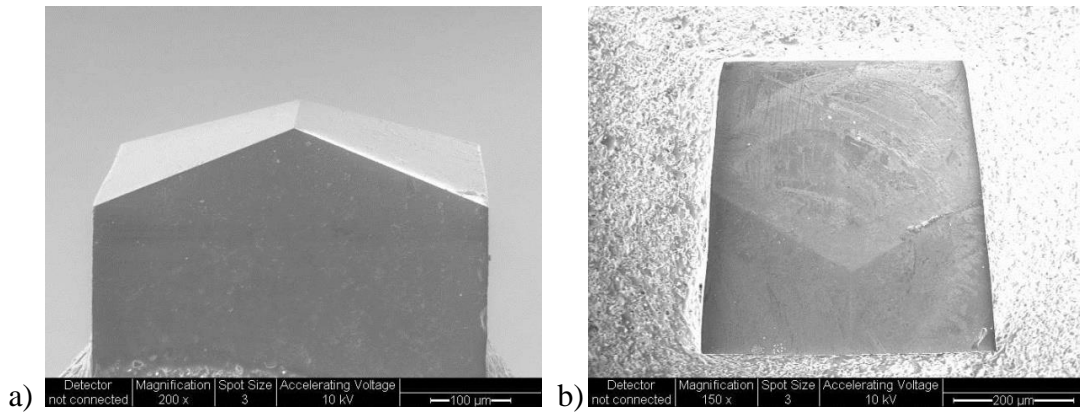


**Figure 3-5. SEM images of the Berkovich indenter (a) side view and (b) top view.**

The qualitative scanning electron microscopy (SEM) observation along with indenting the reference materials using the Oliver and Pharr method assist in monitoring the tip radius and cleanliness to consequently minimise the error in the measured data.

### **3.1.3 Indentation Types**

The variety of mechanical phenomena and their dependence on the loading-unloading conditions causes consideration when selecting the load functions. The effecting phenomena are creep deformation, transition from elastic to plastic deformation, cracking below the surface and even crystallographic phase transition (Bhushan and Li, 2003). These phenomena can be studied using the load-displacement curves.

Therefore, to address these effects there are several different conditions that need to be deliberated when choosing the load function, such as the loading and unloading rate, holding the load at the maximum load before unloading, partial unloading and reloading during each cycle, and superimposing an oscillatory motion on the loading. Each of these conditions can have a significant effect on the resulted load-displacement curve that the Young's modulus and the hardness of the material can be obtained from.

#### **3.1.3.1 Single Cycle Test**

In the current study several different types of load functions were used, as an example Figure 3-6 shows the typical single cycle loading-unloading curves with and without holding period at the maximum load.

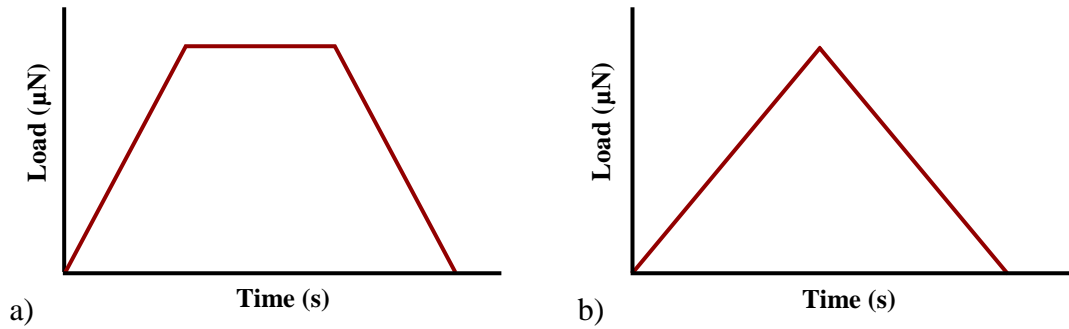


**Figure 3-6. Typical load functions (a) with and (b) without holding segment at maximum load.**

The variation on the loading rate, number and duration of holds and also magnitude of load are dependent on the materials properties. Single loading-unloading cycle test enables characterisation of the mechanical properties of the sample at different areas on the surface and to assess the hardness and Young's modulus of the material at different penetration depths as the load ranges from high load to low can be chosen. Additionally, nanoindentation tests can be used to determine the elastic-plastic deformation behaviour, the single and multiple grain as well as grain boundary effect on the hardness and modulus results, ductile to brittle transition of brittle materials, time dependent creep, fracture toughness and fatigue, etc. To better understand the mechanical properties at different depths and in the same lateral position, continuous stiffness measurement (CSM) or multi-cycling tests have been suggested (Dub *et al.*, 2002; Li and Bhushan, 2002; Lian *et al.*, 2007; Skrzypczak *et al.*, 2009).

### 3.1.3.2 *Continues Stiffness Measurement (CSM)*

The mechanical properties of a material derived from nanoindentation tests can be measured by the CSM technique. In this technique the contact force and penetration depth are measured continuously during the loading of the indenter. The continuous observation of the Young's modulus and hardness as a function of the penetration depth during each indentation is accomplished by imposing a small dynamic oscillation on the force signal where a small, sinusoidally varying signal on top of a DC signal is applied during the loading of the indenter (Li and Bhushan, 2002; Oliver and Pharr, 2004).

The first clear advantage of this method is to offer the direct measurement of the dynamic contact stiffness not only at the end of the loading curve but also at any

point of the loading cycle during the test. There are also several other advantages for using this method, for example both the calibration time and testing procedure time are reduced.

The unloading stiffness is determined at each unloading cycle of the minor oscillations and the Oliver and Pharr method can be used to determine the hardness and reduced modulus at each depth determined by the DC load. However, use of CSM at low penetrations leads to problems of loss of contact and impact loading in highly plastic materials, as there is a large unloading curve and the indenter may come out of contact as the CSM behaviour is altered by a large displacement oscillation. In some cases the indenter is required to be loaded and unloaded several times to ensure that the tip is in contact with the surface of the material (Jian *et al.*, 2012). However, to estimate the mechanical properties at the same lateral position as depth-dependent data with an efficient manner in one experiment, the multi-cycling test method can be used.

#### 3.1.3.3 *Multi-cycling Test*

Multi-cycling, also known as load-partial unload, load functions are used under load control to get depth dependent mechanical properties and to examine the reversibility of the deformation. In order to investigate the changes of the mechanical properties at the same location of the sample surface with penetration depth, a sequence of  $n$  loading-unloading cycles (constant maximum load or increasing load) tests enable the estimation of properties resulting in multi-cycling indentations. Although multi-cycling tests have the benefit of saving time, the collected data does not suffer from lateral inhomogeneities of the material (Wolf and Richter, 2003).

In this work, depending on the test sample for example bulk materials, thin films, coating, etc., the number of loading-unloading segments and the percentage of the partial unloading of the maximum load were chosen to obtain hardness and modulus as depth dependent data. During the multi-cycling tests, after the indenter finds the surface of the sample it reaches the specified load and then is held in the maximum specified load. After the selected holding time the indenter partially unloads to the designated percentage of load, then the indenter is reloaded to higher load in next loading cycle. However, the maximum load can be kept constant. The main purpose

of the rising load is to study the evaluation of the mechanical properties with increasing penetration depths at the same area of the tested sample. Figure 3-7 shows typical multi-cycling load function curves used in various situations.

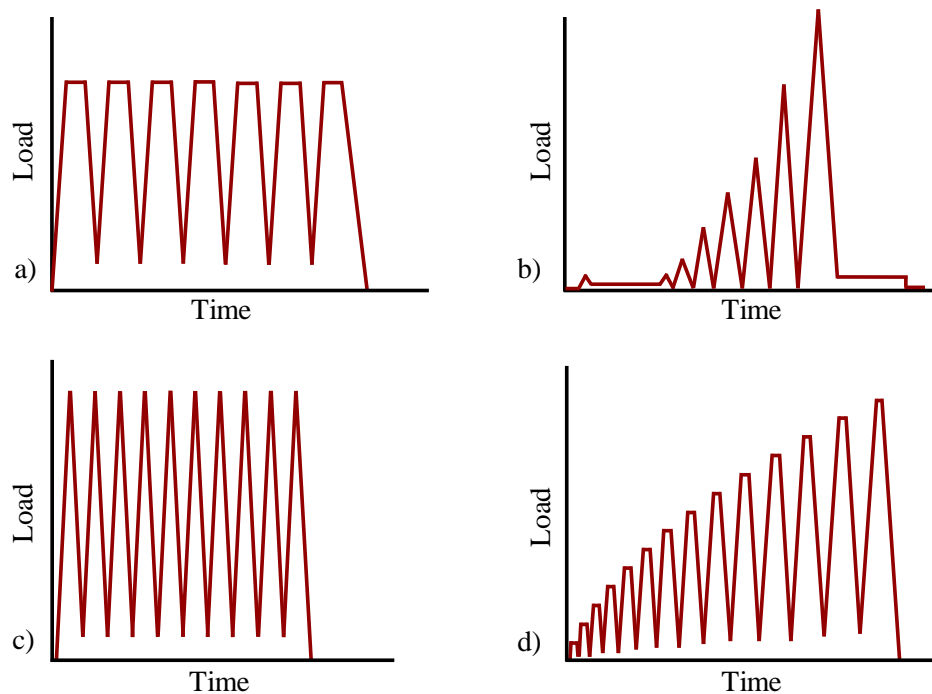


**Figure 3-7. Schematic of the load function for multi-cycling tests: (a) constant load repetition mode with hold at the maximum load, 7 cycles, (b) ramping mode with increase load, 7 cycles, (c) constant load repetition mode, 10 cycles and (d) load increase mode, 14 cycles (Nowicki *et al.*, 2003; Chen and Bull, 2008; Bull *et al.*, 2012).**

However, there are several important factors that need to be considered when using multicycling tests to obtain reliable data. Firstly, due to the time taken for one multicycling indentation to be completed, issues such as thermal drift should be addressed. Change in the thermal drift rate can occur during a single indent cycle, particularly for tests carried out under high percentages of partial unloading, such as 90% partial unloading. Therefore to resolve this problem, the tests need to be carried out using the lowest possible required loads to keep the duration of the tests sufficiently short. For example, if the tests are conducted on thin films with less than  $1 \mu\text{m}$  thickness and the effect of the substrate in the measured hardness and Young's modulus values is of significance, it is preferable that the results are obtained using loads as low as  $2 \text{ mN}$  or even lower.

Moreover, to measure the hardness and modulus values load-displacement curves are analysed. Therefore a sufficient number of data points are required to get an accurate

representation of the load-displacement curves. As the multicycling tests with various loading and unloading segments require the collection of more data points than single indentation tests, it is important to ensure the number of data points chosen for the multicycling test is sufficiently large. For the multicycling tests in this work, it was that 32000 data points gave optimum load-displacement curve resolution.

Another important phenomenon that can occur during nanoindentation tests using the multicycling method takes place when testing materials with a high level of elastic recovery during the unloading part of the indentation cycle. As mentioned in subsection 2.1.1, for single indentation tests carried out on materials with very high elastic recovery, the analysis of the loading portion of the test can be used to verify the reliability of the obtained data. However, when using multicycling tests, the combination of all the segments that the test produces gives the overall appearance of a loading curve but this does not represent the loading curve for a single cycle as relaxation processes occur during each unloading segment and hold. Therefore, the results from multicycling tests for materials with high elastic recovery can show hysteresis during unloading and reloading. This phenomenon is experimentally shown for multicycling tests by Chen and Bull (2008) for a silicon sample under both ramping and constant load modes.

As discussed previously (section 2.3.4), pile-up appearance during the nanoindentation tests is one of the potential measurement errors as it can influence the measured contact area with the nanoindentation tip. Any miscalculation of the contact area can heavily affect the measured hardness and Young's modulus values. In this work, atomic force microscopy (AFM) images, which are described in the next section, were obtained after each single indentation test to correct the measured contact area for pile-up. However, during the multicycling tests, the AFM image is produced only after the entire indentation has taken place, and therefore calculating the true contact area for each single segment of the indentation for pile-up correction is not possible. More details of the importance of pile-up appearance and its effect on the nanoindentation test results as well as a simple method to estimate the quantity of pile-up at different indentation segments is discussed in section 7.2.4.

## 3.2 Characterisation

A wide range of instruments were used to characterise the quantitative and qualitative crystallographic and microstructural properties of the tested samples. These are described in this section.

### 3.2.1 Atomic Force Microscopy

As mentioned previously, the Hysitron Triboindenter is capable of in-situ scanning probe microscopy (SPM) imaging. This allows for precise observation of the test area and also characterisation of the microstructure of the surface by having a pre and post-test observation. By scanning the surface of the sample with a physical probe, the indenter tip in the case of Triboindenter, SPM images can be obtained. The sharp indenter tip moves mechanically across the sample surface in a raster scan pattern. During the scan, the detector of the Triboscanner uses a feedback loop to maintain the scan load constant and records information about the sample such as height. In some cases the data visualisation and analysis were accomplished using Gwyddion software (Necas and Klapetek, 2012).

Similar to all experimental techniques, AFM imaging using the nanoindentation probe can have errors which need to be considered when analysis of the results are on the nano-meter scale. One of these errors can be caused by the tip of the indenter. The geometry of the tip such as the shape and the radius, can be a source of errors. The best results are obtained when using a sharp indenter tip. For example, a sharp Berkovich indenter tip can give a better resolution AFM images than a blunt spherical indenter (Lucas *et al.*, 2008). Moreover, similar to all high precision instruments, a nanoindentation instrument requires calibration to minimise the possible errors to generate the AFM images with high resolution. The necessary calibration required to accurately measure the hardness and modulus values as well as the AFM images using the nanoindentation techniques are detailed in section 4.3.

Finally, it is necessary to consider pixellation errors in the AFM images when determining areas. The images produced in this study are  $1024 \times 1024$  pixels and the scan size was chosen such that the largest indentations occupy about two thirds of the image area. In such cases the pixellation error is less than 1% but increases about 3% for the smallest measurable indents.

### **3.2.2 *Light Microscopy***

All light microscopy and surface optical profilometry of specimens were conducted using a calibrated Olympus BH2-UMA microscope in reflected light mode fitted with a digital Motic Moticam 1000 camera.

### **3.2.3 *Scanning Electron Microscopy***

Scanning electron microscopy (SEM) produces high resolution surface images of a solid sample using a tightly focused beam of high energy electrons which have been emitted from an electron source. The electron source can be a heating type (thermionic guns) or a field emission type and these electron beams can scan across the surface in a raster pattern to form images or they can be static to analyse the specific position. The incoming electrons interact with samples electrons to generate a variety of signals from the examined specimen. The detected signals (out coming electrons or X-rays) can be used to generate information about the surface topography, morphology, chemical composition, crystalline structure and grain orientations of materials used in the sample. The type of signals produced by a SEM can include secondary electrons (SE) which produce SEM images, back-scattered electrons (BSE), diffracted back-scattered electrons (EBSD), auger electrons (AE), characteristic X-rays and other photons of different energies (Danilatos, 1993; Goldstein *et al.*, 2003). In this work, all the SEM images, EDX and EBSD experiments were performed using an Environmental Scanning Electron Microscope FEI XL-30 ESEM FEG (Field Emission Gun).

#### **3.2.3.1 *Electron Backscatter Diffraction***

To characterise the texture in materials, electron backscatter diffraction (EBSD), also known as backscatter Kikuchi diffraction, provided quantitative microstructural and crystallographic information from metal, mineral, ceramics and semiconductor samples as well as being used for phase and strain identification (Randle, 2008). EBSD has the ability to perform measurements at extremely small scales and it also can detect the weak textures. EBSD, when used in a SEM, allows individual grain orientation, local texture and grain sizes and distributions to be determined on the surface of the sample (Schwartz, 2009). In EBSD an electron beam strikes a tilted

crystalline sample and the diffracted electrons shape a pattern on a fluorescent screen as shown in Figure 3-8.

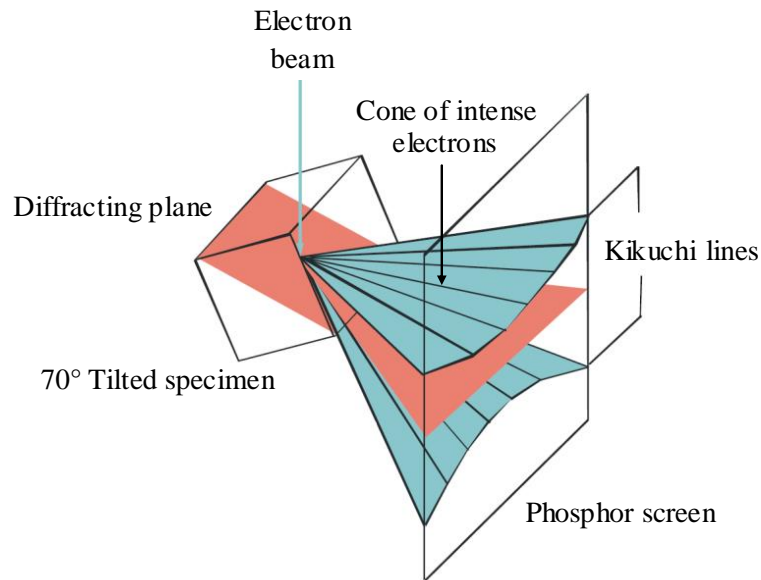


**Figure 3-8. Schematic of the EBSD technique (Schwartz, 2009).**

Because of the steep angle of the beam and the limited penetration distance of electrons, the beam only penetrates at a small depth into the material. The electrons of the beam slightly lose their energy and are scattered in all directions. The electrons are once more scattered by a set of lattice planes, forming cones that are detected on a fluorescent screen (Zhou and Wang, 2007).

The intersection of the cone's edges with the screen result in a geometrical pattern consisting of pairs of parallel lines named Kikuchi bands which are detected by the low light camera. Each band has a distinct width and corresponds to a crystallographic plane and can then be used to statically analyse the grain boundary, size and orientation of material grains. The resulting maps from EBSD can be further processed to generate inverse pole figures along with colour coded surface orientations. Scanning is usually done by either moving the specimen or the electron beam; at each point an electron backscatter pattern shows the preferred texture of the grains in the sample material (Schwarzer, 1997; Wilkinson and Hirsch, 1997). An automatically colour coded unit triangle of the inverse pole figure is used to colour each point. For example, the colour red is assigned to the [001] crystal direction, green to [101] and blue to [111]. A specific point is then shaded according to the arrangement of these three directions in the crystal to a user specified sample

direction. Therefore, if a point in the scan is oriented such that the crystal direction aligned with the specified sample direction is between red (001) and green (101) direction then the point would be shaded in yellow.

In this study, EBSD experiments were performed using the same SEM equipped with EBSD (HKL Technologies) as explained in the previous section. To acquire the EBSD maps, the sample was tilted 70 degrees ( $\theta = 70^\circ$ ) toward the phosphor detector under a condition of  $U = 20 \text{ kV}$  and  $\delta l = 0.1 \text{ }\mu\text{m}$ , where  $U$  is voltage and  $\delta l$  is the size of each movement of the electron beam. After acquisition the data were processed using the open source MTEX tools (Hielscher and Schaeben, 2008).

### 3.2.3.2 Energy Dispersive X-ray Spectroscopy (EDS)

Another non-destructive method to analyse the chemical composition of the sample used in this study is energy dispersive X-ray spectroscopy (EDS also known as EDX) which is attached to the SEM instrument used in this work. As mentioned before, the interaction of the incoming electrons with sample electrons produces different emitted signals including X-ray photons. The energy of detected X-rays by the energy dispersive detector defines the atoms that formed them as each element has a unique atomic structure with a specific energy (between 0.1 and 20 keV depending on the element), therefore each element has a fingerprint X-ray signal (Goldstein *et al.*, 2003). The produced peaks in the spectrum make it possible to collect localised elemental composition data. The identification of the line produced in the spectrum along with the relative intensities of detected signals for each element provides qualitative and quantitative information on the elements present in the sample. Depending on the sample composition, the detecting limit can be in the range of 0.1-0.5 wt % using EDS. However, there are some disadvantages using EDS such as the lack of sensitivity in detecting the light elements, overlapping of the signals as in the case of  $\text{TiK}_\beta$  and  $\text{VK}_\beta$  and furthermore when the samples contain oxygen there is an inherent inaccuracy for quantitative analysis (Egerton, 2005). There are different X-ray techniques that can be used to characterise the materials surface such as X-ray diffraction and X-ray photoelectron spectroscopy. These two methods are described in the next section.

### 3.2.4 X-ray Diffraction (XRD)

X-rays are high-energy electromagnetic radiation with wavelengths similar to the inter-atomic distances between approximately 0.01 nm and 10 nm in a crystal. When focussed on a sample, these can be diffracted due to the interaction between the electrons in the shells of the sample atoms with the incoming X-rays. X-ray diffraction (XRD) is an analytical technique to identify phases and crystalline structure by comparing the obtained data with that of known structures. There are different applications including chemical analysis, texture analysis (i.e. grain or single crystal orientation), measurement of the residual stress and also calculation of the degree of crystallinity in the material.

In XRD a sample is illuminated with a fixed wavelength of X-ray photons and the electrons in the sample atoms scatter the X-ray waves. The produced diffraction patterns give information about the sample structure using Bragg's law. This relates the wavelength of the electromagnetic radiation ( $\lambda$ ) to the spacing of the atomic planes and also to the diffraction angle theta ( $\theta$ ) measured in degrees. This is summarised in Equation (3-4).

$$n\lambda = 2d_{hkl} \sin(\theta) \quad (3-4)$$

where  $n$  is the order of reflection which shows the number of wavelengths in the path difference and  $d$  represent the spacing between planes (hkl) (Waseda *et al.*, 2011).

In this work, XRD was used to determine the crystal structure of the alloys and to look for the existence of surface reaction layers; the strengths and limitations of the technique have been discussed previously (Pecharsky and Zavalij, 2008). A PANalytical X'Pert Pro MPD, powered by a Philips PW3040/60 X-ray generator with Cu K $\alpha$  radiation was used to obtain the diffraction patterns using a step size of 0.0334 degree  $2\theta$  and a scan time of 200 seconds per datum point.

### 3.2.5 X-ray Photoelectron Spectroscopy (XPS)

Another additional surface analysis and characterisation technique to further identify the chemical elements and quantify the elements in terms of atomic percentage used in this work was X-ray photoelectron spectroscopy (XPS). Furthermore, XPS also

known as ESCA (electron spectroscopy for chemical analysis) was used to measure the depth of oxidation in the sample surface.

The principle of XPS is similar to that of XRD however this technique is based on irradiation of the electronic states of atoms at or just below the surface of the sample by soft monochromatic X-rays photons with a specific energy in an ultra-high vacuum (UHV) environment. Since the individual atoms on the surface have a characteristic binding energy (BE) due to their core electrons, the ejected electrons, from the top 10 to 12 nm of the materials surface, can be analysed based on their kinetic energy (KE). The spectra will be a plot of the continuously recorded KE against the intensity of the electrons which are mostly core level (Kalmykov and Denecke, 2010; Riviere and Myhra, 2010).

In this work a thermo scientific theta probe was used with a micro-focussed monochromated Al K $\alpha$  X-ray source having a spot size of 400  $\mu\text{m}$  diameter, a pass energy of 40 eV and a step size of 1.0 eV for a survey spectra to obtain a high resolution spectra of all elements of interest.

### **3.2.6 Raman Spectroscopy**

Raman spectroscopy is a spectroscopic technique that uses the molecular vibrations to provide information about materials and chemicals. This technique is based on inelastic scattering or Raman scattering of monochromatic light usually from a laser source. The interaction of the light with the sample changes the frequency of photons in the light. The detected scattered light is dominantly elastic scattering or Rayleigh scattering that has the same frequency as the emitted light. However, interaction between the incident photons and the molecules in the sample can shift the energy by either giving or removing energy, consequently increasing or decreasing wavelength of the light. The vibrational, rotational and other low frequency transitions in the molecules can be obtained from these shifts.

In this study, the Raman measurements were taken on the LabRAM HR800 system from Horiba Jobin Yvon. This system is an integrated spectrometer and confocal microscope. It briefly comprises of a laser source, a diffraction grating or spectral analyser, confocal microscope and a detection system.

The system was set up as follows:

- Filter: 50%-514.5 nm laser
- Aperture: 300  $\mu\text{m}$
- Slit: 100  $\mu\text{m}$
- Acquisition Time: 5 s
- Accumulation Number: 10
- Grating: 2400

These conditions were chosen as a greater intensity was obtained for the measured peaks of the Cu samples tested in this work.

### ***3.2.7 Object Oriented Finite Element Analysis (OOF2)***

In this work the Object Oriented Finite (OOF2) element analysis (OOF2) code from the National Institute of Standards and Technology (<http://www.ctcms.nist.gov/oof/>, NIST, Maryland, USA) was used to simulate and measure the elastic properties of the imaged sample and to compare it to that of experimental data. The main purpose of using the OOF2 analysis is to accurately model a set of microstructures by assigning the material's properties to the feature. OOF2 can use micrographic images, such as SEM images, as an input to the model and the topology of the image that can be analysed by OOF2 is arbitrary. The quality of the input image and its resolution play a significant role in the outcome of the model and therefore it is important to have high quality SEM images. Once the image is uploaded, the desired single-crystal material properties can be assigned to each component of the microstructure. It should be noted that OOF2 is a colour coded program and each colour can represent one type of material and carries the properties of the represented material. The local material properties in the uploaded image are characterised by individual pixels and each pixel will have the information related that specific local area.

The next step after assigning each material to its pixels is to produce a finite element mesh skeleton. The number of created skeletons should be high enough to follow the materials boundaries very well. Once the best representation of the materials is obtained and all the boundaries are followed by the created skeleton, the next step is to create the actual finite element mesh. After creating the required mesh, the model

is ready for the introduction of the local physical state of the system such as displacement and temperature (Reid *et al.*, 2009). OOF2 can calculate several equations, such as force balances and plane stresses. Once the desired equation is selected, the program can be instructed to solve the equation for the material with the previously assigned properties.

### **3.3 Summary**

The Triboindenter and its capability to accurately measure the mechanical properties at the nanoscopic scale under different test conditions have been introduced. Afterwards, the additional methods, such as characteristic analysis methods, used in this work to provide an excellent knowledge of the surface morphology were illustrated.

Therefore, after introducing the experimental methods used, some background information about the copper thin films and the importance of the accurate measurement of the mechanical properties of thin films has been discussed here. Chapter 4 provides brief background information about copper thin film fabrication, and then moves on to discuss the challenges related to their adhesion onto and diffusion into silicon substrates. The materials used in this investigation are also detailed in the next chapter. Various materials are of interest in order to understand the effect of their microstructure on their mechanical response during nanoindentation. Finally, the necessary calibration processes that are required to be undertaken prior to performing the indentation tests are described in detail whilst also presenting the suitable calibration materials.

## **Chapter 4. Studied Materials and Nanoindentation Calibration**

*The preliminary part of this chapter covers background knowledge of the copper thin films used in microelectronic devices, the importance of understanding the mechanical properties and the influence of these properties on the device lifetime. This is followed by a detailed listing of the materials that have been examined during the course of this thesis. Included in this list are the materials from which samples have been utilised for the calibration of the nanoindentation system. Most of the samples used in this work were provided by manufacturers or external organisations and therefore in each section the corresponding companies or organisations are named. Finally, nanoindentation system calibrations and the data obtained during these calibration processes are described.*

### **4.1 Copper in Context**

#### **4.1.1 Copper Properties in Microelectronic Devices**

Recent developments in microelectronic devices and data storage systems have created the need to understand the nano-mechanical and deformation behaviour in thin films and coatings as they become smaller in size. The mechanical properties of thin metal films are often different from those of the bulk materials due to differences in the grain structure of the thin films and the presence of their attached substrates and surrounding dielectrics. Thin films typically have higher yield strengths than bulk materials and can thus handle high residual stresses but during device operation this residual stress can be relieved through plastic deformation and/or film delamination. Thermal expansion and elastic modulus mismatch with the substrate are also factors affecting stress generation and device performance (Volinsky *et al.*, 2001; Strehle *et al.*, 2010). As a consequence, measuring and understanding the surface mechanical properties is of great importance as the device lifetime and performance depends highly on these properties.

The mechanical properties of materials can have a strong influence on microelectronic device performance. One important failure mechanism can be due to void formation from electromigration. In this situation, current flowing through a conducting line causes a preferential diffusion of atoms in the direction of the electron motion. This is due to the effect of ballistic impacts between electrons and

atoms and causes both void and hillock formation at opposite ends of the wire (Jakkaraju and Greer, 2002). When a residual stress is present in the line, atoms may preferentially diffuse from a high stress to a low stress region. This can also lead to void and hillock formation in a process known as stress migration and can act to increase or reduce the effects of electromigration (Kim *et al.*, 2001).

Mechanical stresses may also initiate dislocations which can have detrimental effects on the functionality of the components. Therefore it is important to reliably measure the mechanical properties of the materials under study. As microelectronic devices get faster, the individual transistors and the wires that connect them are reducing in size and in these circumstances, the size and orientation of individual grains in the metallisation can control the elastic properties and hence the residual stress and device lifetime (Tymiak *et al.*, 2000; Volinsky *et al.*, 2002). Several different thin films and coatings have been investigated in this work including Cu, gold (Au) and Al thin films as soft coatings on hard substrates.

#### ***4.1.2 Fabrication of Copper Thin Film***

Due to the rapid decrease in the dimensions of today's devices, one of the most important technologies that have been used for ultra large-scale integration (ULSI) devices are multilevel interconnections. Al and its alloys have played a significant role in ULSI devices for many years due to their low resistivity ( $2.7 \mu\Omega\text{-cm}$ ) (Hu and Harper, 1998; Kobayashi *et al.*, 2004), but there are other materials with lower resistivities than Al such as Au, silver (Ag) and Cu. Nowadays, Cu may be the most widely used material due to its cost effectiveness and also its good substrate adhesion properties. The mechanical properties of Au thin films used in microelectronic devices and the difficulties that occur as a consequence of adhesion to the substrate will be discussed in detail in section 5.3. However, despite the nobility of Au, it is not a preferred material in silicon (Si) based microelectronic systems for other reasons, such as the porosity of the deposited thin films which allows oxide diffusion in to the substrate and rapid removal by wear which influences the device life time. If the barrier layer is not adequate, Au can easily penetrate through to the substrate by very rapid diffusion and change the microelectronic performance due to the increased electrical resistance (Pinnel, 1979; Lu and Wong, 2008). Because Au diffuses as an ion and not as an atom the smaller size of ion Au, allows it to easily diffuse through

to the open structure of the dielectric (Lloyd *et al.*, 1999). Additionally, since there are other metals such as Al present in device manufacturing, problems such as purple plague ( $\text{AuAl}_2$ ) or white plague ( $\text{Au}_5\text{Al}_2$ ) can be occur due to the inter metallic component of Au and Al (Ji *et al.*, 2007).

In 1997 IBM presented Cu as a Si chip interconnect material for the first time utilising the same methodology that is still in use today (Edelstein *et al.*, 1997). The introduction of Cu thin films as an interconnect material resulted in a number of advantages in the manufacturing of Si chip technologies that included lower resistivity and losses and better electromigration reliability than the Al interconnects that they replaced (Edelstein *et al.*, 1997; Kobayashi *et al.*, 2004). The transition from vacuum-deposited Al based interconnects to Cu based interconnects using an electro-chemical-plating (ECP) methodology in semiconductor manufacture was made possible by the integration of a thin liner material that was conceived at IBM in the early 1990s with the invention and development of the damascene Cu electroplating process for on-chip metallisation (Andricacos, 1999; Vereecken *et al.*, 2005).

As microelectronic devices get faster, the individual transistors and reduction in feature size have been the most important factors in the productivity improvements attained by the semiconductor industries. The investigation of Cu for use as an interconnection metal in the ULSI of Si integrated circuits offers the potential for advantages in performance. The lower bulk resistivity of Cu ( $1.7 \mu\Omega\text{-cm}$ ) results in a decreased  $RC$  (the product of the metal resistance ( $R$ ) and the dielectric capacitance ( $C$ )) delay of approximately 40% and an improved performance reliability. This is based on the greater electromigration resistance due to stronger Cu-Cu bonds as indicated by its high melting temperature, making it robust against electromigration failure (Hu and Harper, 1998; Cook *et al.*, 1999; Cheng *et al.*, 2006).

Several fabrication processes for thin film multilayer structures have been reported (Jensen *et al.*, 1984; Miura *et al.*, 1993). Subtractive reactive ion etching (RIE) is one such method that is used for metals including Al, however, due to the lack of volatile Cu compounds at the temperatures required for this method, it is not easily applied to the patterning of Cu films. With the introduction of Cu metallisation, new fabrication methods have been developed for fabricating devices with Cu, and among those,

electroplating, damascene and dual damascene are the most prominent techniques (Andricacos *et al.*, 1998).

Electroplating is used to deposit a metal or alloy onto a substrate. This technique requires a seeding layer, as electroplating does not occur at a dielectric or barrier surface. The function of this layer is to conduct the current from a contact at the wafer edge to all areas on the wafer where the deposition occurs (Wong *et al.*, 1998). Two approaches can be used in this method; through-mask plating and damascene.

In *through-mask plating*, the seed layer is deposited over the wafer surface prior to patterning. The electroplating only occurs on the areas of the seed layer that are not covered by the mask. This method of plating has been implemented extensively in the fabrication of inductive recording heads and interconnections (Braun and MacDonald, 1982; Andricacos *et al.*, 1998; Andricacos, 1999; Bray, 2002).

In high performance semiconductor devices, the Cu *damascene* technology is used to obtain multilayer metallisation. In damascene plating, which was pioneered in IBM, the deposition of a seed layer occurs over a patterned material that acts as the interconnect insulator. The plated metal then covers the entire surface and the excess metal (Cu) is removed by chemical-mechanical polishing (CMP), as shown in Figure 4-1. The process of Cu interconnect integration with damascene processing can be described in the following steps:

1. Deposition of the damascene or dual damascene inter-metal dielectric. This dielectric may be multilayered and may have etch stops such as silicon nitride ( $\text{Si}_3\text{N}_4$ ).
2. Build the required pattern and etch the damascene or dual damascene structure into the dielectric.
3. Fill the voids with electrodeposited Cu. A barrier stack should be deposited prior to electrodeposition.
4. Anneal the wafers to stabilise the microstructure and avoid recrystallisation effects.
5. Polish the excess Cu using CMP.
6. Repeat previous steps for multilayered interconnects.
7. Passivate the final Cu layer (Merchant *et al.*, 2001; Cheng *et al.*, 2006).

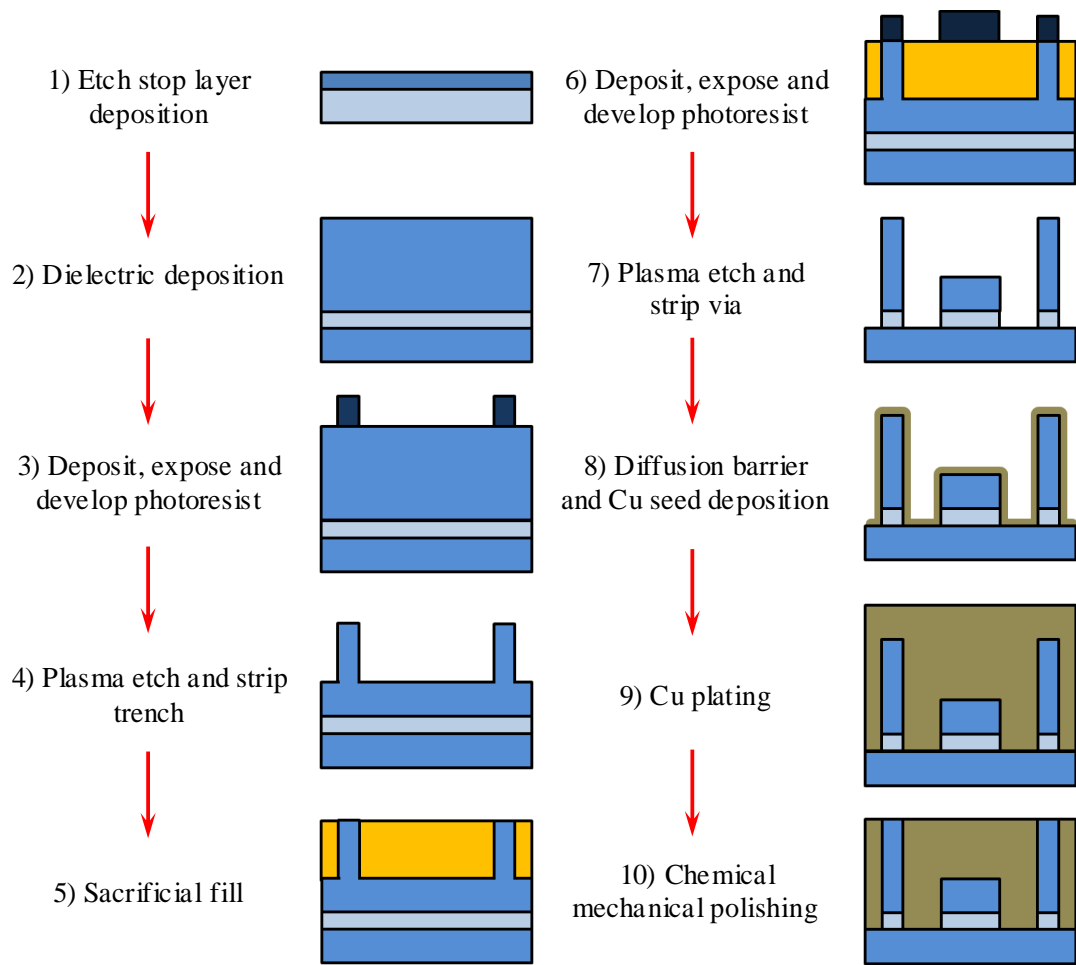


**Figure 4-1. Flow diagram of a typical trench first damascene process, modified from (Wilson, 2009).**

Damascene electroplating is perfectly suited for the fabrication of interconnect structures as it permits the multilayer deposition of metal simultaneously in holes and over trenches. This occurs without any voids or seams through a process called dual damascene. In the dual damascene process, the trenches in the dielectric are defined before metal deposition. Further layers are fabricated by repeating this process. As Cu diffuses rapidly through Si and its oxide, a side wall diffusion barrier is necessary (Andricacos *et al.*, 1998; Hu and Harper, 1998).

#### **4.1.3 Copper Texture**

One of the most important microstructural properties to consider in Cu metallisation is its texture. The elastic and plastic properties of Cu depend on the crystallographic orientation of its grains (Brinksmeier and Schmutz, 1997; Xiang, 2005). Although Cu has a higher melting point than Al, it also has fairly good atomic mobility, even at

room temperature, to allow grain growth during deposition or annealing. The microstructure can significantly influence the thermal, electrical and mechanical properties of thin films, and thus the performance of microelectronic devices, as the interconnect line widths decrease below  $0.5 \mu\text{m}$  (Lee *et al.*, 2005). In an ideal interconnect feature the grain size should be much smaller than the feature size to achieve isotropic properties, but this becomes increasingly more difficult to achieve as the feature size decreases or if grains grow during processing (Jakkuraju and Greer, 2002).

The temperature in the fabrication or operation of Cu interconnects can reach in excess of  $500 \text{ }^\circ\text{C}$  and therefore it is important to consider the effects of temperature on the performance of Cu films during deposition and annealing treatments (Lee *et al.*, 2000). The grain size distribution in Cu films often contains a mixture of large and small grain sizes; an indication of abnormal grain growth during deposition. This is due to variations in the grain boundary mobility which is associated with the different grain boundary types present in Cu (Moriyama *et al.*, 2003). Heating causes the small grains to grow first, followed by the larger grains as the temperature increases. The annealing texture can be driven by different forces such as surface energy, interface energy, grain boundaries and dislocations. For example, anisotropic driving forces can cause grain boundary motion to occur in specific directions (Vlassak and Nix, 1994; Lee *et al.*, 2005). This often leads to a (111) orientation of face centred cubic (FCC) metals like Cu because it has the lowest surface energy and interfacial energy with a substrate. The (100) orientation which has the smallest strain energy density is favoured under conditions where strain is introduced during deposition (either thermal or growth strain).

XRD measurement studies, which have been the primary method for characterisation of textures for many years, show the preferred growth of (100) grains for thicker films and high thermal strains for Ag and Cu (Zhang and Xu, 2002a; Sonnweber-Ribic *et al.*, 2006). A comparison between the (111) and (100) grain textures in similar grain-size distribution samples produced by various deposition methods has shown that the (111) orientation in interconnects has a better lifetime under electromigration. Cu is elastically anisotropic and its Young's Modulus parallel to

the (111) orientation is 2.9 times that measured parallel to the (100) orientation (Zhang *et al.*, 2004).

Thin films fabricated by physical vapour deposition (PVD) have shown a predominant texture of (111). Due to epitaxial growth, the (100) texture is observed on a (100) Si substrate however in blanket Cu films, grain growth favours the (111) texture. The annealing of blanket Cu films can reduce the amount of the (111) texture. Cu only remains in the damascene trenches when using CMP, causing grain growth to occur in isolated lines forming the (111) texture on the sidewalls (Lingk *et al.*, 1999; Jakkaraju and Greer, 2002). Barrier layers like tantalum (Ta), along with the presence of impurities, can also influence the texture in the Cu deposition and annealing processes (Volinsky *et al.*, 2002).

Therefore, the texture transformations are strongly dependent on various parameters including the trench line width, passivation layer, annealing temperatures, stress and impurities. Consequently, it is difficult to accurately predict the effects of these parameters on the texture evolution in Cu interconnects, making experimental measurements essential in optimise device processing.

#### ***4.1.4 Copper Electromigration***

Electromigration in Cu can be described as the motion of Cu atoms driven by momentum transfer from collisions between conducting electrons and diffusing metal atoms (Liu *et al.*, 2004). Due to the small cross-sectional area of thin films in microelectronic devices, the current density is usually high. This may cause electromigration induced mass transport through diffusion. Consequently, this phenomenon creates voids in the interconnection, resulting in high line resistances that can lead to operational circuit failure. Therefore the integrated circuits should be fabricated with a specified maximum allowable current.

In addition to Cu having a lower resistivity compared to Al as discussed earlier in this chapter, it has also stronger interatomic metallic bonds which make it robust against electromigration failure. These characteristics make Cu a suitable material as a reliable conductor in interconnect devices (Cheng *et al.*, 2006).

#### **4.1.5 Challenges for Copper Metallisation: Adhesion and Diffusion**

The *adhesion* between thin Cu layers and the barrier layer as well as the dielectric is of great importance as it affects the mechanical and electrical properties of the microelectronic devices. The adhesion between Cu and dielectric layers like SiO<sub>2</sub> is weak. The Cu roughness has to be carefully monitored to ensure a reliable peel strength (adhesion) and good electrical performance. Moreover, the surface must be even to produce fine lines (Wiedenman *et al.*, 2007). Several methods have been developed to improve adhesion, such as treatment of the substrate surface prior to Cu deposition (Ruoff *et al.*, 1988; Bachman and Vasile, 1989). The use of adhesion promoting films (such as chromium (Cr) and titanium (Ti)), increasing the substrate temperatures during deposition and the use of sputtering instead of evaporation can also enhance adhesion (Schwartz and Srikrishnan, 2006). However, due to the high diffusivity of Cu, it is essential for the adhesion layers to also be good diffusion barriers to prevent both Cu penetration into the substrate device and diffusion into the insulator between the Cu lines during device operation (Hu and Harper, 1998).

A robust diffusion barrier effective in preventing the diffusion of Cu should possess specific requirements. Firstly, Cu is not protected against oxidation and can readily diffuse through SiO<sub>2</sub> which can cause device degradation and is capable of causing corrosion. Therefore, the barrier should have effective Cu diffusion blocking capabilities to prevent the diffusion of impurities such as oxygen through to the Cu and into the Si substrate (Li *et al.*, 2004). Secondly, it should give good adhesion between the Cu films and insulators and finally, it must have a low electrical resistance, a low thermal stress and a diminutive chemical reactivity with Cu (Murarka *et al.*, 1993; Schwartz and Srikrishnan, 2006). Materials such as tantalum (Ta), titanium nitride (TiN) and titanium/tungsten (Ti/W) alloys have been shown to possess good barrier performance (Holloway *et al.*, 1992; Min *et al.*, 1996).

## **4.2 Materials**

Due to the differences in the mechanical properties of bulk materials and thin films or coatings, two different types of materials were investigated in this work. The obtained properties from the coatings were divided in two different categories; fully dense thin films such as Cu, Al, Au and low density coatings such as tin (Sn) and

copper-tin (Cu-Sn) coatings. The thin films with high density are described initially, followed by the low density materials.

#### ***4.2.1 Fully Dense Thin Films Used in This Study***

##### *4.2.1.1 Copper Thin Films*

800 nm thick blanket Cu metallisations were electrodeposited on thermally oxidised 0.5 mm thick <100> Si wafers at IMEC in Belgium. Prior to film deposition, the Si substrates were oxidised to produce a 1  $\mu\text{m}$  thick silicon oxide layer. Afterwards, the oxidised silicon was coated with a 25 nm TiW inter-layer diffusion barrier layer, followed by a thin Cu seed layer of 20 nm thickness by sputtering before electrodepositing. After Cu deposition, the samples were annealed at 100 °C for 1 hour or 350 °C for 1 minute and one control sample was not annealed. These annealing processes are designed to remove defects but will also change the grain sizes and distribution of orientations in the Cu thin films. All of the wafers were passivated by means of an 8 nm sputtered TiW layer to prevent oxidation during annealing.

As mentioned before, the mechanical properties of bulk materials are different from that of thin films. Therefore, a bulk Cu sample was also investigated to identify and understand the effect of chosen nanoindentation techniques on the mechanical properties. The rolled Cu sample was 99.9% pure but contained some oxygen impurities (0.03%). The sample was rolled to 8% reduction and then vacuum annealed at 300 °C for 1 hour to reduce the defect density in addition to promoting recrystallisation and grain growth. After removal of the sample from the vacuum furnace, some surface oxidation occurred before the nanoindentation testing, but the bulk oxygen content was maintained at the as-delivered level.

##### *4.2.1.2 Gold Thin Films*

As mentioned previously, one of the main issues in microelectronic devices during the fabrication of multiple layers is adhesion between the deposited metal and the dielectrics. As Au and Cu are the two most established metals used in microelectronic devices, work was carried out on Au thin films to identify the adhesion issues and their influence on the performance of microelectronic devices.

Pure gold thin films with a 1  $\mu\text{m}$  thickness were vapour deposited onto 0.5 mm thick  $\langle 100 \rangle$  Si substrates. The Si substrates were oxidised before film deposition to produce a 2.3  $\mu\text{m}$  oxide layer. Following this, a 25 nm thick TiW layer was deposited onto the oxidised silicon substrate to improve the adhesion between the substrate and Au films as well as to create a diffusion barrier layer. Gold films were then deposited onto the TiW layer. Finally, similar to the Cu thin films, the Au thin films were passivated by means of an 8 nm sputtered TiW layer. These samples were provided by INEX in Newcastle University. The results were compared to that of pure single crystal bulk Au. Figure 4-2 shows a schematic representation of the deposited layers of thin films for both the Cu and Au on a Si substrate.

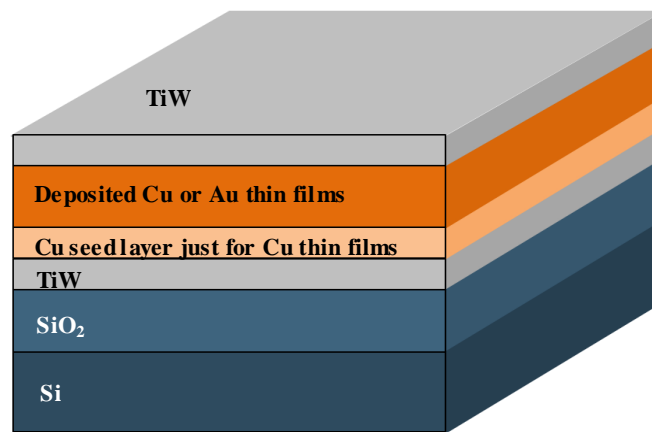


**Figure 4-2. Schematic representation of the Cu or Au thin films deposited on Si substrate.**

#### 4.2.1.3 Aluminium Thin Films

In addition to the Cu and Au thin films, nanoindentation tests were also performed on Al thin films. Two Al thin film samples were sputter coated onto 0.8 mm thick glass substrates with different Al thicknesses of 375 nm and 1400 nm. The obtained results were compared to that of a pure bulk Al (100) single crystal sample with a 12 mm diameter and a 3 mm thickness that was provided by the International Organisation for Standardisation (ISO) for the international comparison on nanoindentation.

#### 4.2.2 Low Density Coatings Used in This Study

To investigate the effect of surface roughness as well as the effect of density on the mechanical properties (such as hardness and Young's modulus data) obtained from

nanoindentation techniques, coatings composed of Cu, Sn and Cu-Sn deposited from a room temperature ionic liquid (RTIL) onto Cu and stainless steel substrates were examined. A Cu substrate was specifically chosen to minimise the effect of the substrate on the obtained results. This type of coating procedure produces a very rough surface finish as well as a low density coating, both of which were required in this work. The obtained data were compared to that of fully dense thin films and also to that of bulk materials with both rough and polished surfaces.

#### 4.2.2.1 Copper, Tin and Copper-Tin Coatings

The experiments were carried out using two different substrates, Cu and stainless steel, to compare the variation in mechanical properties caused by the substrate. All deposition experiments were carried out using Cu and Sn chloride baths and the constant current method as the constant potential method results in extremely rough deposits. The coatings conditions are shown in Table 4-1. The obtained Cu-Sn deposits contain 25 wt% Sn in each scenario. All the samples were tested as deposited although one Cu-Sn coating was annealed at 400°C for 30 minutes. The annealing process was performed in a nitrogen atmosphere to prevent oxidation.

Coated sample	Substrate types	Applied current ( $mA/cm^2$ )	Duration (h)	Estimated minimum coating thickness ( $\mu m$ )
Cu	Cu	7.49	1	9.91
Sn	Cu	1.80	2	10.83
Cu-Sn	Cu	1.77	4	11.93
Cu-Sn	Stainless steel	1.77	4	11.93
Cu-Sn, Annealed at 400°C/30min	Stainless steel	1.77	2	5.97

**Table 4-1. Different deposited samples with low density and high surface roughness.**

These samples were provided by S. Ghosh and Prof. S. Roy's at Newcastle University and further information about the sample preparation can be found in the relevant paper (Ghosh and Roy, 2013).

The estimated thicknesses of the coatings shown in Table 4-1 were predicted using Faraday's law since in electroplating this is one of the fundamental methods of estimating the thicknesses of deposited coatings on metal substrates assuming fully

dense film formation. According to Faraday's law, there is a relationship between the current, the duration of deposition and the quantity of the metal that is electroplated. As given by the law, the amount of material deposited on to the metal substrate is directly proportional to the quantity of the electricity transferred at the electrode, and the amount of material that is deposited from a given amount of electricity is proportional to the atomic weight of the deposition material. To estimate the thickness of the coating in this work and compare the results with the actual thickness to determine the porosity of the coating, Faraday's law was used as a foundation and expanded upon as shown below. The total electric charge ( $Q$ ) is:

$$Q = It \quad (4-1)$$

where  $I$  is current and  $t$  is time. Furthermore, the relationship between the total charge passed through the cell to the amount of the product ( $N$ ) as given by Faraday's law is:

$$Q = nFN \quad (4-2)$$

where  $n$  is the valence of the dissolved metal in solution and  $F$  is Faraday's constant ( $96485.3 \text{ C mol}^{-1}$ ). Substituting Equation (4-1) into Equation (4-2):

$$It = nFN \quad (4-3)$$

Since the amount of product measured in moles is equal to the mass of the product ( $w$ ) divided by the atomic mass of the product ( $A_r$ ) ( $N = w/A_r$ ), Equation (4-3) can be rewritten as below:

$$It = nf \frac{w}{A_r} \quad (4-4)$$

Using the assumption of a fully dense coating, the volume ( $V$ ) of the coating and the density ( $\rho$ ) of the coating can be related as below, since:

$$V = Ax \quad (4-5)$$

and

$$\rho = \frac{w}{V} \quad (4-6)$$

where  $A$  is the plated area and  $x$  is deposited thickness. Combining Equation (4-5) and (4-6) gives Equation (4-7):

$$w = \rho Ax \tag{4-7}$$

Therefore, substituting this into Equation (4-4) gives Equation (4-8) which relates the thickness of the coating to the conditions of the deposition and the material that is deposited.

$$x = \frac{A_r It}{nF\rho A} \tag{4-8}$$

The results from Cu coatings with porosity were compared with those from thin films with a high density. Moreover, to compare the surface roughness effect on the obtained data, the Cu coatings were also compared to bulk Cu with a rough surface. This bulk Cu sample is very similar to the previously described bulk Cu but differs because this sample was etched to produce a fully dense bulk Cu sample with rough surfaces by dissolving the grain boundaries. The etching used in this work after polishing the sample was alcoholic ferric chloride which was made from 96 ml ethanol, 59 g ferric chloride and 2 ml hydrochloric acid (1.19 g/cm<sup>3</sup>). After etching for 30 seconds, the sample was washed with acetone to remove the solution from the surface.

Furthermore, the porous Sn coating results were also compared to a bulk 99.99 % pure Sn sample with a smooth surface and a 1.4 μm thick, fully dense Sn coating that had been electrodeposited onto a Cu substrate. The second of these comparisons was undertaken to allow for a comparison between low density Sn coatings and high density Sn thin films.

As the Sn samples are highly time-dependent materials when subjected to the nanoindentation process, 99.99 % pure bulk Zinc (Zn) sheets were also examined using nanoindentation to substantiate the effects of time-dependency on the obtained mechanical properties under different test protocols. The Zn samples were also used to investigate the effect of anisotropy on the obtained mechanical properties as the presence of large grains allowed for indents to be performed easily on different grains allowing for a determination of the orientation effect on the obtained mechanical properties.

### ***4.2.3 Titanium and Cobalt Chromium Alloys***

In this work, the mechanical properties of a cobalt-chromium femoral head (Co-Cr-Mo) and a titanium-based alloy stem (Ti-6Al-4V) used in metal-on-metal hip implants have been investigated. The tests were carried out on two different categories of sample: new samples that had not been used in the human body and oxidised samples. To oxidise the tested samples, the alloys were treated electrochemically in a 500 ml solution of distilled water containing 175.32 g/l (3 M) of sodium chloride (NaCl) at a fixed temperature of 37 °C, which is equivalent to body temperature. To assess the effect of electrochemical oxidation, the samples were connected with a fine wire to ensure good electrical contact before immersion in the salt solution for a period of two weeks. The fine wire was used to simulate the contact between the two metals that occurs in the human body, allowing for analogous galvanic coupling to take place. The properties of samples with different designs that have been recovered after use in the body were investigated for comparison. These samples were ideal for detecting the effect of oxidation on the mechanical properties of these materials.

### ***4.2.4 Titanium Carbide and Zirconium Nitride***

Samples of titanium carbide (TiC) and zirconium nitride (ZrN) deposited using magnetron sputtering onto M42 steel substrates were provided by Teer Coatings Ltd. Both of these coatings had a thickness greater than 25  $\mu\text{m}$  thick, and consequently the effect from the substrate on the obtained mechanical properties was minimised.

## **4.3 Calibration**

Similar to all high precision instruments, the nanoindentation instrument requires calibration and calibration standards to accurately measure the hardness and modulus values using nanoindentation techniques, particularly at shallow depths. There are three main calibration measurements which are necessary to obtain accurate results. These measurements are frame compliance, indenter area function and cross-hair or targeting alignment. This section describes a standard calibration procedure using the ISO protocol which is based on the Oliver and Pharr method. The frame compliance and indenter area function calibration analyses were described in section 2.3.2. These

two calibrations require specific standard material properties for their calibration standards.

A standard material should ideally have very limited creep, have no significant pile-up or sink-in behaviour, be elastically isotropic, have the potential to be polished to a high standard and also have a high degree of thermal stability allowing for the capability to run the experiment at different temperatures. Firstly, the primary creep can be minimised or even run out entirely by choosing an appropriate load function procedure and a suitable holding time at the maximum load. Secondly, the quantity of pile-up can be reduced by choosing a material with a high hardness to reduced modulus ratio ( $H/E_r$ ). Finally, the elastically isotropic property indicates that at any range of indentation depths the material has the potential to provide highly consistent modulus values and show a depth independent characteristic.

The aforementioned properties are important, but the most important property of the standard sample is its indentation size effect (ISE). The perfect standard sample should show very little or ideally no indentation size effect. The indentation size effect can manifest in the hardness results at small indentation depths. For those small values of contact depth, although the modulus value is constant at the range of contact depths, the hardness value increases at lower contact depths with decreasing the indentation depth/size. This means that materials have a tendency to appear harder when measured using smaller indentation sizes. Figure 4-3 illustrates hardness as a function of contact depth for various materials obtained in this work showing the indentation size effect. It should be noted that all of these hardness values were corrected for the effect of pile-up, which will be discussed in more detail later in this work.

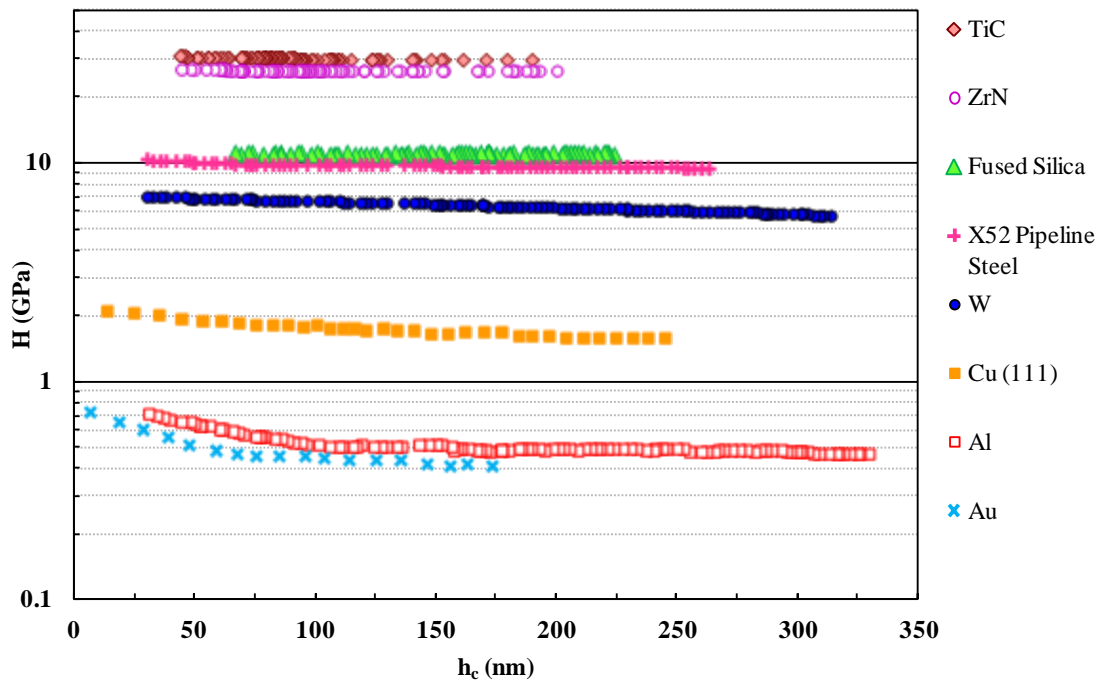


**Figure 4-3. Hardness versus indentation depth obtained from various materials showing the indentation size effect and material's behaviour at different penetration depths.**

In the recent years, the indentation size effect has attracted the most attention in nanoindentation research and there are numerous investigators (Ma and Clarke, 1995; Kulkarni and Bhushan, 1996; Nix and Gao, 1998; Soifer *et al.*, 2002; Schoberl *et al.*, 2003; Fischer-Cripps *et al.*, 2006) with various theories that have tried to explain the main causes of this phenomenon, however the mechanisms underlying it are complex. Some examples of these theories include: the presence of oxides or chemical contamination near the surfaces (Pethica and Tabor, 1979), characteristic size plastic band deformation (Bull *et al.*, 1989), the effect of friction between the indenter and sample (Li *et al.*, 1993), the effect of work hardening at the surface layer (Pelletier *et al.*, 2000), strain gradient plasticity and geometrically necessary dislocations (GND) underneath an indenter tip (Nix and Gao, 1998; Fleck and Hutchinson, 2001), a critical thickness layer (Dunstan and Bushby, 2004) and dislocation starvation and mechanical annealing (Shan *et al.*, 2008).

As mentioned before there are various mechanisms influencing the indentation tests and consequently contributing to the indentation size effect. However, the geometrically necessary dislocation model is one of the most appropriate models that can be used to describe the indentation size effect for the metals tested in this study.

This is because the metal films tested here plastically deform by dislocation processes, contain statistically stored dislocations after deposition and the plastic deformation pattern produced follows the geometry of the indenter used. The indentation size effect can be modelled in terms of geometrically necessary dislocations due to the non-uniform plastic deformation in metals. If there is a non-uniform plastic deformation, an extra storage of dislocations is required to accommodate the lattice curvature. This occurs in the form of geometrically necessary dislocations (Gao and Huang, 2003).

In 1998 Nix and Gao developed an expression for the ISE using the Taylor dislocation model (Taylor, 1938) as a foundation, which is based on the relation between the shear strength and dislocation density in a material (Equation (4-9)), to estimate the density of the geometrically necessary dislocations underneath a sharp indenter tip. Figure 4-4 illustrates the model of geometrically necessary dislocations underneath a conical indenter with idealised circular dislocation loops (Gao *et al.*, 1999).

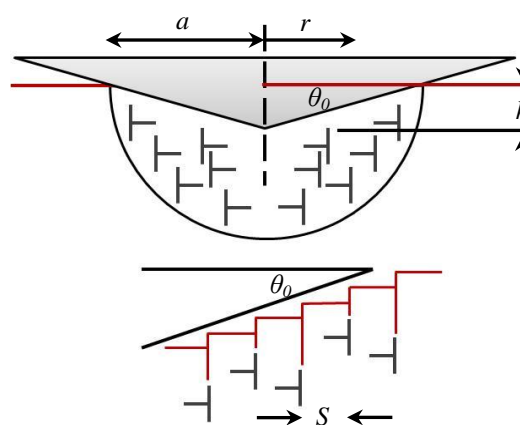


**Figure 4-4. Schematic representation showing geometrically necessary dislocations beneath the sharp indenter tip, where  $S$  is the spacing between individual slip steps on the indentation surface,  $a$  is the contact radius and  $\theta$  is the angle between the surface of the plane and the indenter (Nix and Gao, 1998).**

During the indentation test, when the indenter causes a permanent plastic indent in the surface of the indented material, the plastic deformation beneath the indenter tip is accommodated by geometrically necessary dislocations as shown in Figure 4-4. These produce atomic steps on the indented surface.

Based on the Taylor model the relationship between the shear strength ( $\tau$ ) and total dislocation density ( $\rho_T$ ) can be defined as below:

$$\tau = \alpha\mu b\sqrt{\rho_T} = \alpha\mu b\sqrt{\rho_S + \rho_G} \quad (4-9)$$

In this equation  $\mu$  is the shear modulus,  $b$  is the Burgers vector and  $\alpha$  is a constant factor which can be in the range of 0.2-0.5. Moreover,  $\rho_S$  and  $\rho_G$  are the densities of statistically stored dislocations and geometrically necessary dislocations respectively.

The expression that Nix and Gao developed for the strain gradient plasticity is:

$$\sigma = \sigma_Y \sqrt{f^2(\varepsilon) + l\eta} \quad (4-10)$$

where  $\eta = \rho_G b$  is an effective strain gradient and  $l$  is the material length scale which was developed by Fleck and Hutchinson (1997) (Fleck and Hutchinson, 1997):

$$l = 3\alpha^2 \left(\frac{\mu}{\sigma_Y}\right)^2 b \quad (4-11)$$

Nix and Gao also assumed that the von Mises flow rule applies and to convert the equivalent flow stress to hardness. Tabor's factor of 3 was used (Nix and Gao, 1998):

$$\sigma = \sqrt{3}\tau, H = 3\sigma \quad (4-12)$$

Finally, they established the relation between the hardness ( $H$ ) and the indentation depth ( $h$ ) as below:

$$\left(\frac{H}{H_0}\right)^2 = 1 + \frac{h^*}{h} \quad (4-13)$$

where  $H_0$  is the bulk hardness and  $h^*$  is a characteristic length scale which depends on the properties of the indented material and the geometry of the indenter tip which is related to the spacing of the geometrically necessary dislocations (Huang *et al.*, 2006; Bull *et al.*, 2012). It should be noted that the original method introduced by Nix and Gao (Nix and Gao, 1998) was based on an indentation experiment performed on annealed (111) Cu single crystal and cold worked polycrystalline Cu for indentations deeper than 100 nm depth. The model does not agree with the indentation data on hardness reported in literature (Lim and Chaudhri, 1999; Elmustafa and Stone, 2003; Feng and Nix, 2004; Durst *et al.*, 2005; Kim *et al.*, 2005; Huang *et al.*, 2006; Bull *et al.*, 2012) for indentation depths less than 100 nm. This can be explained by the indenter tip radius effect (Xue *et al.*, 2002; Qu *et al.*, 2004)

and storage volume for the geometrically necessary dislocations (Swadener *et al.*, 2002; Feng and Nix, 2004; Durst *et al.*, 2005).

However, it should be noted that the magnitude of the indentation size effect in the results generated here is small since a small range of depths of indentation was used for metals tested in this work (50-100 *nm* depth).

Therefore, the choice of an appropriate material with a limited indentation size effect for the determination of the indenter area function is essential. Consequently, a harder material with a relatively high stiffness is required to minimise the indentation size effect. For these materials, at very low penetration depths, the applied load may not cause plastic deformation but at higher loads where plastic deformation is observed, the indentation size effects are minimised.

Prior to accurately determining the indenter area function, it is necessary to perform the frame compliance calibration. For this calibration, a standard material with a low  $H/E_r$  ratio, such as Al, with the capability of obtaining large and stiff indentation contacts even at low penetration depths is required.

#### ***4.3.1 Frame Compliance Calibration***

To accurately calibrate the compliance of the Triboindenter instrument in this work, two materials, bulk Al (100) single crystal and high purity (99.99 %) bulk tungsten (W) (100) single crystal, both provided by ISO, were used. The W sample had an elastic modulus of 411 *GPa* and a Poisson's ratio of 0.29. Both of the materials are elastically isotropic under indentation tests and can provide constant modulus values at a variety of penetration depth ranges (Vlassak and Nix, 1994). To measure the instrument compliance using the W and Al samples at various peak loads, two different loading functions were used. These loading functions were suggested by ISO for an international comparison in nanoindentation and are shown in Figure 4-5 (a) and (b).

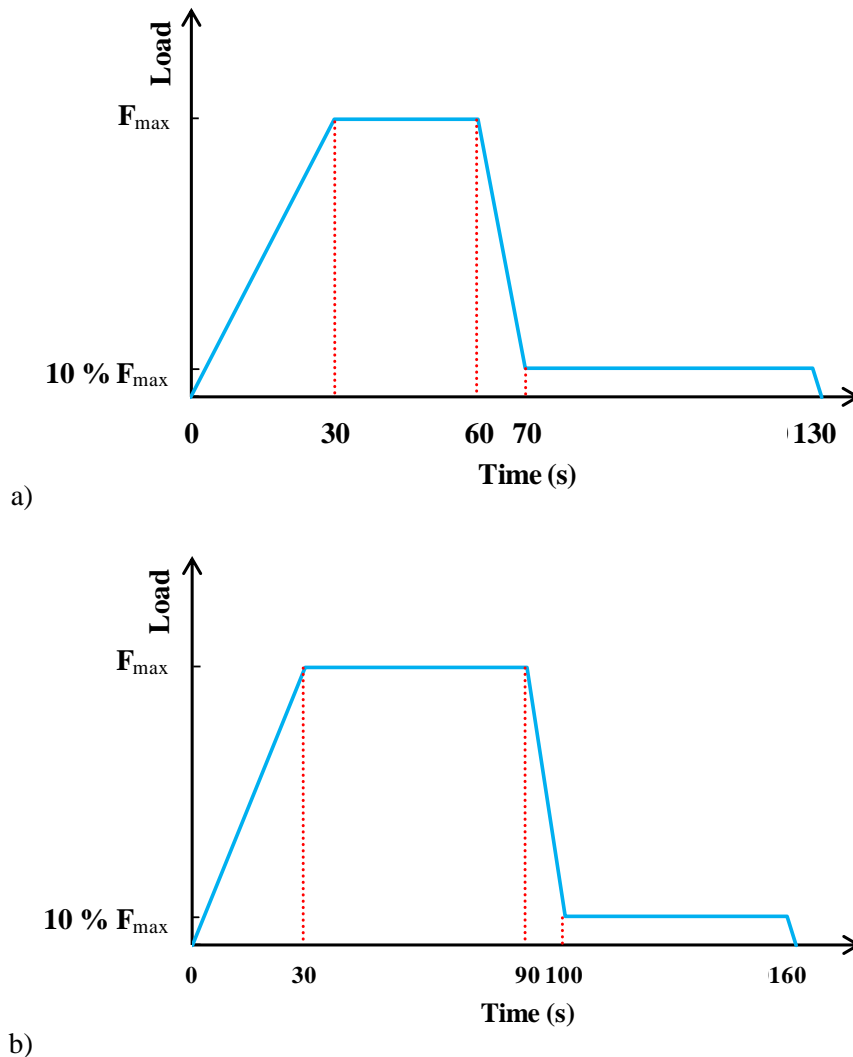


**Figure 4-5. Calibration loading functions used for indentations in (a) W and fused silica, and (b) Al.**

The measured value of the machine compliance ( $C_f$ ) was  $3.5 \text{ nm/mN}$ . This value is similar to the machine compliance measured by Hysitron when the transducer was originally calibrated at the company. It should be noted that whenever it was required that the indentation tip be changed, the machine compliance was recalibrated. The reasoning behind this is that most of the indentation tips are hand made using different amounts of epoxy and also that the length of the tip shaft can be different in each individual tip. Both of these factors can modify the total compliance justifying the process of recalibration.

Figure 4-6 shows two examples of the measured compliances as a function of the reciprocal of the square root of the maximum load obtained from W and Al single crystal samples. A linear trendline, shown as a red line in both graphs in Figure 4-6,

was used to find the y-intercept which is the total machine compliance (combining the transducer, Triboindenter and tip) in  $\mu\text{m}/\text{mN}$ . This value can be multiplied by 1000 to attain the machine compliance in  $\text{nm}/\text{mN}$  which can be input as the transducer calibration constant.

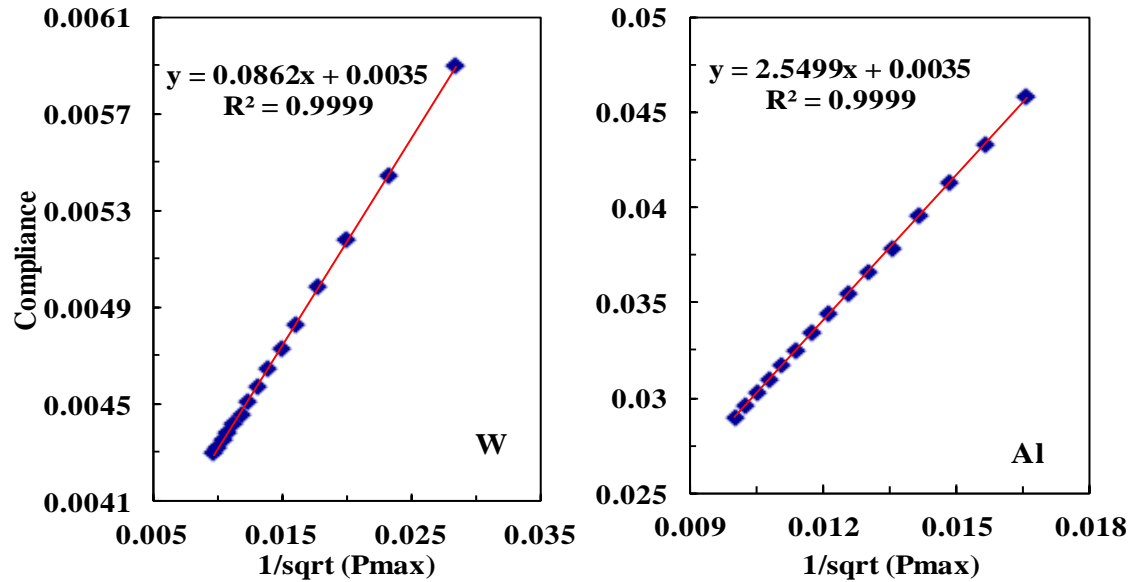


Figure 4-6. Typical examples of the measured machine compliance obtained from W (left) and Al (right) which in both cases the total compliance is  $0.0035 \mu\text{m}/\text{mN}$  ( $3.5 \text{ nm}/\text{mN}$ ).

#### 4.3.2 Tip Area Function Calibration

To accurately measure the hardness and Young's modulus of materials, especially when working at shallow contact depths (less than  $100 \text{ nm}$  depths), an accurate knowledge of the contact area is crucial. The shape of any indenter tip is not perfect and therefore requires the use of tip shape calibration which is based on determining the area function of the indenter tip. As mentioned previously in section 2.1.2, for an ideal Berkovich indenter the projected contact area ( $A_c$ ), which relates the contact area to contact depth ( $h_c$ ), is  $A_c = 24.5 \times (h_c)^2$ . Based on the Oliver and Pharr method, this equation can be rewritten from the relationship between the contact area and the contact stiffness as below:

$$A_c = \frac{\pi}{4} \left( \frac{S}{E^*} \right)^2 \quad (4-9)$$

To therefore determine the projected contact area and tip shape, a standard material with a known modulus value that remains constant at any range of contact depths is

required for tip calibration, such as sapphire or fused silica. In this work, a 4 mm thick, 20 mm diameter fused silica (quartz glass) sample possessing a 72.5 GPa elastic modulus and a Poisson's ratio of 0.17 that had been provided by ISO was used for the determination of the area function of the indenter tip. Fused silica was selected as it has elastic isotropy, very little creep, and is additionally economically preferable. Figure 4-7 illustrates several examples of load displacement curves obtained from fused silica that confirm the consistency of the loading and unloading slopes at different peak loads. This demonstrates that the obtained reduced modulus values from these curves are constant.

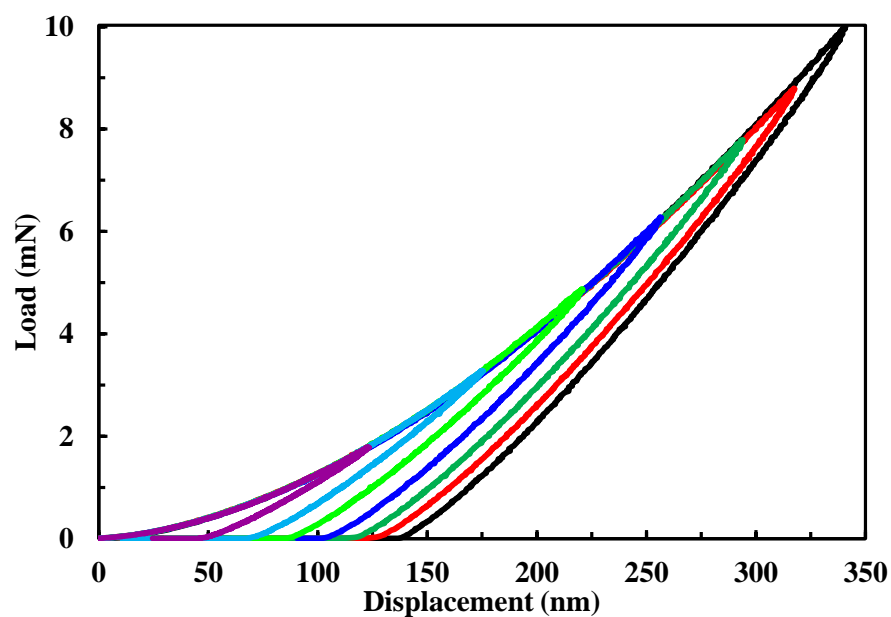


**Figure 4-7. Typical load-displacement curves obtained from fused silica at different maximum load ranges.**

Therefore, to accurately measure the contact area function, fused silica was chosen as the calibration specimen. A set of indentations (in this case 100 indentations) were performed on the specimen using the loading function shown in Figure 4-5 (a) at a diverse range of loads. Afterwards, the corresponding projected contact area was measured using the aforementioned Equation (4-9). By plotting the measured area versus contact depth Figure 4-8 can be obtained.

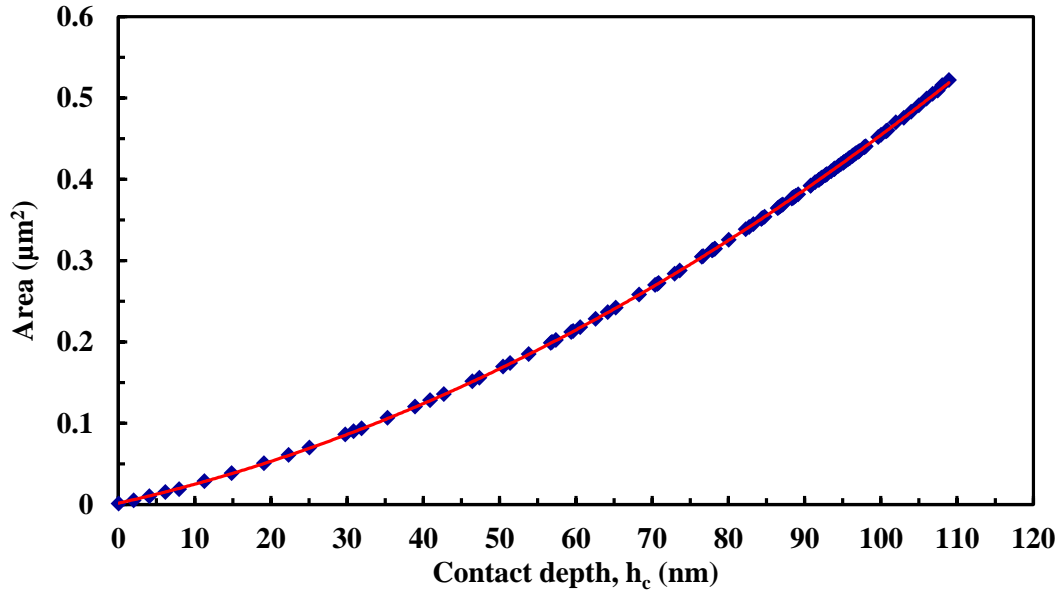


**Figure 4-8. Contact areas obtained from fused silica versus corresponding contact depths.**

The tip area function can be determined by fitting procedure of a fifth order of a polynomial fit to the curve obtained by deriving the contact area as a function of contact depth given by following equation:

$$A(h_c) = C_0 h_c^2 + C_1 h_c^1 + C_2 h_c^{1/2} + C_3 h_c^{1/4} + C_4 h_c^{1/8} + C_5 h_c^{1/16} \quad (4-10)$$

The area function of the Berkovich indenter was found in this part of the work to be:

$$A(h_c) = 24.5 h_c^2 + 2084.6 h_c^1 + 321980 h_c^{1/2} - 804980 h_c^{1/4} - 1313500 h_c^{1/8} + 1976400 h_c^{1/16}$$

The number of coefficients included in the area function can be different for various indentation instruments. For the Hysitron Triboindenter used in this work, between 2 and 6 coefficients can be selected from which the maximum of 6 were used. It should be noted that the area function curve shown in Figure 4-8 and the determined projected contact area function form just one example of an area function calibration. As the contact area plays a significant role in the obtained hardness and Young's modulus values, it is important to perform the tip area function calibration on a regular basis. In this study, area function calibration was implemented after each set of 100 indentation tests to confirm the accuracy of the obtained data. Figure 4-9 shows the hardness and reduced modulus values obtained from fused silica after both machine compliance and indenter tip area function calibrations.

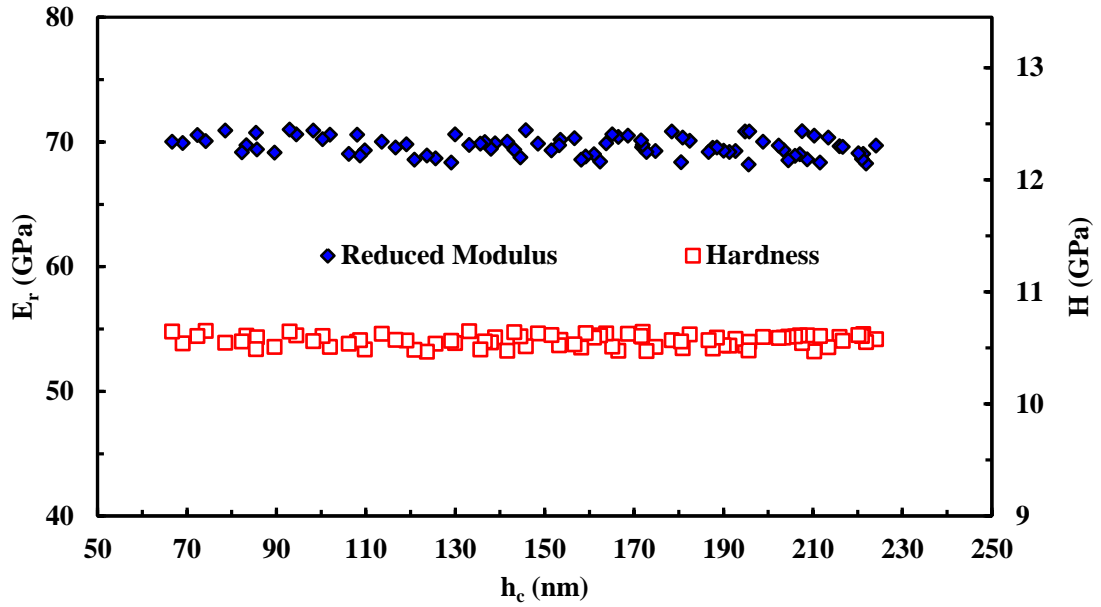


**Figure 4-9. Reduced modulus (left) and hardness (right) values obtained from fused silica after both the machine compliance and indenter area function calibrations.**

The obtained average hardness and reduced modulus values are  $10.56 \pm 0.05 \text{ GPa}$  and  $69.64 \pm 0.76 \text{ GPa}$  respectively. The Young's modulus value can be calculated using Equation (4-11), which was described in more detail in section 2.1.2 and the knowledge of the elastic modulus and Poisson's ratio of the diamond indenter tip which are  $1140 \text{ GPa}$  and  $0.07$  respectively.

$$\frac{1}{E_r} = \left( \frac{1 - \nu^2}{E} \right)_{\text{sample}} + \left( \frac{1 - \nu^2}{E} \right)_{\text{indenter}} \quad (4-11)$$

The calculated Young's modulus for the fused silica after calibration was  $72 \text{ GPa}$  which is almost identical to the modulus value of  $72.5 \text{ GPa}$  specified by ISO when the sample was received.

A summary of the properties of the materials used in this investigation such as hardness, elastic and reduced modulus acquired from literature is provided in Table 4-2. Additionally, the corresponding Poisson's ratio is provided that has been used to measure the Young's modulus of materials by means of Equation (4-11) when used in conjunction with the relevant diamond indenter properties. The table also includes the commonly used standard calibration materials which were used in this work to calibrate the nanoindentation instrument.

<b>Material</b>	<b>Elastic Modulus, <i>E</i> (GPa)</b>	<b>Poisson's Ratio, <math>\nu</math></b>	<b>Hardness, <i>H</i> (GPa)</b>	<b>Reduced Modulus, <i>E<sub>r</sub></i> (GPa)</b>
Diamond (Oliver and Pharr, 1992)	1141	0.07	> 100	n/a
Fused Silica (Zheng <i>et al.</i> , 2007)	72.5	0.17	9-10	69.6
Tungsten (Abadias <i>et al.</i> , 2006)	411	0.29	7-8	322
Aluminium (Tsui <i>et al.</i> , 1997b)	70.8	0.36	0.45-0.9	76
Copper (Suresh <i>et al.</i> , 1999)	120-160	0.33	1-1.5	120-155
Gold (Siller <i>et al.</i> , 2005)	77	0.42-0.44	0.64	88
X52 Steel (Micromaterials Ltd)	220	0.3	9-10	200
Zinc (Tohid and Bull, 2007)	41-110	0.33	0.6-1.3	44-111
Glass (Saha and Nix, 2002)	70	0.23	5-8	69.5
Tin (Chen <i>et al.</i> , 2009)	40-47	0.33	0.2-0.4	43-50

**Table 4-2. Properties of materials used in this investigation for both the calibration samples and tested samples from literature for comparison.**

The other important factor which needs to be considered during the area function calibration is the contact depth at which the tests are taking place. For example, when dealing with a very thin layer of coating, such as the Cu thin films tested in this work, it is important to perform the contact area calibration at very low loads and consequently low penetration depths. However, when the tests are extracting mechanical properties at high contact depths, the bulk materials tested in this work for example, the tip area function calibration should be undertaken at both low and high loads and therefore at a range of indentation depths.

#### **4.3.3 Targeting Alignment Calibration**

Cross hair or targeting alignment calibration, which is also called ‘H-pattern’ calibration, is another desired calibration in nanoindentation tests. The aim of the H-pattern calibration is to detect and subsequently correct the offset between the indenter tip location and the positioning stage using the centre of the focus of the microscope attached to the transducer. The H-pattern calibration requires the use of a soft material allowing for clearly visible indentations in the shape of an ‘H’, which are carried out automatically by the Triboindenter. Figure 4-10 shows the presence of indentations in an ‘H’ shape in the middle of the microscope image.

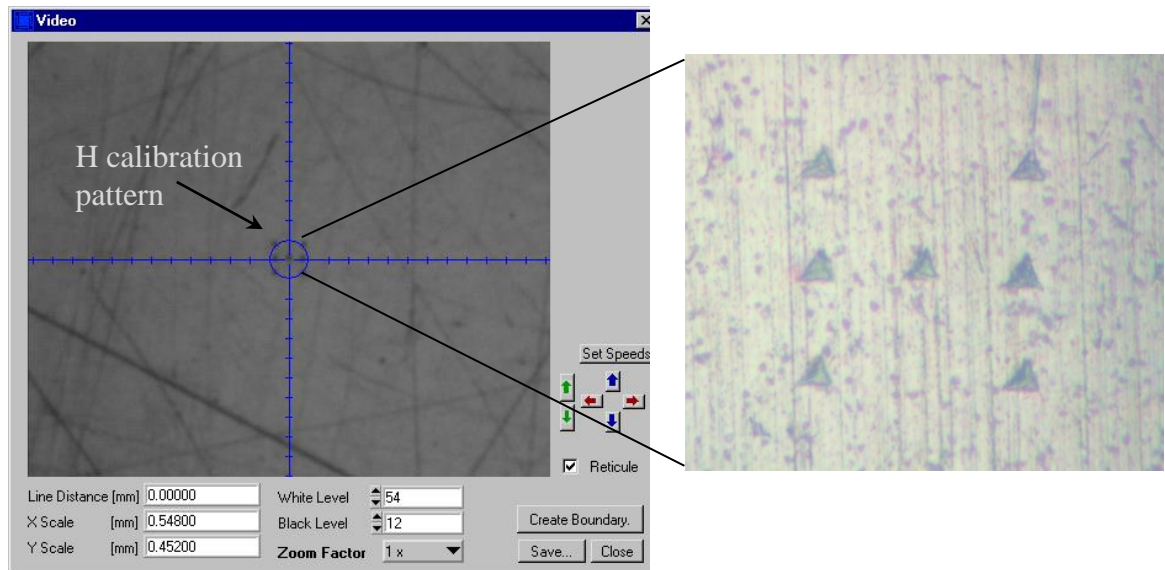


**Figure 4-10. H-pattern calibration on a standard Al sample as seen by the Triboindenter (left) and the magnified view (right).**

The standard sample for this type of calibration requires both a high polish capability and the ability to easily form a very flat surface. Due to the need for H-pattern calibration to be undertaken more frequently than the two previously detailed calibrations, the sample should be chosen so that the process is economically viable. Consequently, a well polished bulk Al sample can be used as the standard sample for this type of calibration. As the tests are in nanometre scales, an accurate knowledge of the indentation location is crucial, especially when the test requires indenting specific regions of a sample. This can occur, for example, when the indentation of a single grain or grain boundaries is desired.

#### **4.3.4 Triboscanner Calibration**

Finally, one of the most essential calibrations for the nanoindentation system to be capable of producing an AFM image with correct dimensions is the Triboscanner calibration. The Triboscanner calibration is necessary as the accuracy of the AFM images in depth (z-axis) and also positioning (x and y-axes) both prior to and proceeding the indentation depend on it. To calibrate the scanner, a standard AFM calibration grid pattern sample is required. This certified sample, which is made of silicon, has precisely defined grids ( $1 \mu\text{m} \times 1 \mu\text{m}$  in x and y,  $1 \mu\text{m}$  and  $0.2 \mu\text{m}$  in z) and can be used to calibrate the scanner in the x, y and z directions. Once the sample is placed on the stage, it is important to make sure that the grids run parallel with the

sides of the stage. After placing the sample in the correct direction, the calibration begins using the indenter probe to image the surface. There are two different scan sizes that need to be used for calibration;  $6 \mu m^2$  and  $20 \mu m^2$ . The scan rate during the scanner calibration is 1 Hz. When the image is sufficiently visible, the x and y directions can be measured using the features of the grid. This allows for a comparison to be made of the actual size of the grid to the measured directions and adjustments can be made by increasing or decreasing the value if the measurement is too large or too small.

Once both the scan sizes are calibrated using the normal scanning, the calibration for vertical scanning is required. The same procedure applies for the vertical scanning calibration as for the normal scan and both of the scan sizes ( $6 \mu m^2$  and  $20 \mu m^2$ ) must be performed for vertical scanning calibration. After all four scans are completed, the z-piezo can be calibrated by adjusting the z-piezo gain. If the measured dimensions are too large in the z-direction, they can be corrected by reducing the piezo gain and conversely if the dimensions appear too small, the piezo gain needs to be increased.

#### **4.4 Summary**

After providing background knowledge of the Cu thin films and the importance of the mechanical properties role in their performance, the samples used in this work were described in detail and the importance of the calibration of the nanoindentation instrument was discussed. As mentioned previously, this work is divided in to two sections and the second part of the work from Chapter 5 to 9 includes the results obtained during the course of this investigation. The accurate measurement of the mechanical properties of metal thin films has received increased attention due to the importance of the various types of mechanical stress generation in thin films during their nucleation, processing and storage. Chapter 5 provides the initial aims of the work in the first section and then a brief explanation of the various test protocols used in this work is provided, followed by the obtained hardness and Young's modulus values for copper thin films. The variety of techniques used to generate and characterise the surface morphology are subsequently described. The comparison between two different types of thin metal films (copper and gold) deposited on similar substrates (silicon) is explored next. Additionally, similar bulk samples are tested under the same indentation conditions for comparison.

## **Chapter 5. Extracting the Mechanical Properties of Thin Films Using Nanoindentation Technique**

*In this chapter, the hardness and Young's modulus results obtained from nanoindentation tests of copper thin films are investigated. Moreover, these results are compared to the nanoindentation results obtained for gold thin films. Additionally, the hardness and Young's modulus values of bulk copper and gold samples are compared. The correlation between the nanoindentation results and the coating microstructure has been investigated by using EBSD to map the distribution of the copper thin film grain orientations. XRD tests were also used to detect different orientations of copper in the thin films. Finally, Raman spectroscopy was used to observe the effect of annealing as well as oxidation appearance in the copper thin films.*

### **5.1 Nanoindentation Testing**

There are several measurement techniques available to accurately measure the mechanical properties of thin film materials. Over the last decade, techniques such as nanoindentation (Oliver and Pharr, 1992; Baker and Nix, 1994; Mencik *et al.*, 1996) and lattice strain measurement have been developed to precisely estimate the relationship between the stress and strain in thin metal films. These techniques are suitable for the thin films that are still attached to the substrate during the measurement (Brotzen and Moore, 1994; Hong *et al.*, 2005). However, there are some other high accuracy measurement techniques to assess the mechanical properties of thin films that are removed from the substrate. Examples of these techniques include bulge tests (Cardinale and Tustison, 1992; Vlassak and Nix, 1992), micro-cantilever beam bending tests (Hsu *et al.*, 2007) and micro-tensile tests (Espinosa *et al.*, 2003). Each of these techniques, however, has their own unique difficulties in application, especially when applied to submicron metal films (Tong *et al.*, 2010). By comparison, the nanoindentation technique is a widely established method for determining mechanical properties of thin films on the nano-metre scale (Volinsky and Gerberich, 2003; Volinsky *et al.*, 2004; Yeap *et al.*, 2013).

## 5.2 Mechanical Properties of Copper Thin Films

To investigate the mechanical properties of Cu thin films, nanoindentation experiments were carried out under load and displacement control using the Berkovich indenter with an effective tip radius of 150 nm. To obtain the hardness and Young's modulus as a function of penetration depth, single indentations and multi-cycling tests were used.

As mentioned in section 3.1.3, one of the widely used techniques to measure the variation of hardness and Young's modulus of coatings with indenter penetration is the continuous stiffness method (CSM) (Li and Bhushan, 2002; Oliver and Pharr, 2004). However, when the measured results are compared to the single indentation data there are some issues. For materials such as Cu, which have a small amount of elastic recovery during the unloading part of the test, there is a possibility of the indenter coming out of contact with the test sample. Consequently, to investigate the variation of the hardness and modulus values of materials at the same position but at different displacements, the multi-cycling test method was used under the load control protocol. To assess the potential problem when using the multicycling test, the partial unloading part of the test was set at 20, 50 and 90% of the maximum load of an individual test segment. In each peak load, a 4 second hold was applied at every cycle before partial unload. After that, the indenter was reloaded to a higher load in each loading cycle. These test conditions reduce the effect of time-dependent deformation on the results. A 40 second hold at a 2  $\mu N$  load prior to each indentation was used to allow stabilisation of the system; the displacement in the last 20 seconds of this hold was being used to determine the thermal drift rate. All load-displacement curves were subsequently corrected for thermal drift prior to the calculation of hardness and Young's modulus by the Oliver and Pharr method. The tip was then removed to a height of 10 nm above the surface before the indentation cycle was started.

The load versus time graphs (load functions) for the single cycle and multi-cycling tests used to study the mechanical properties for the thin films are shown in Figure 5-1. Both linear and parabolic loading behaviour was assessed.

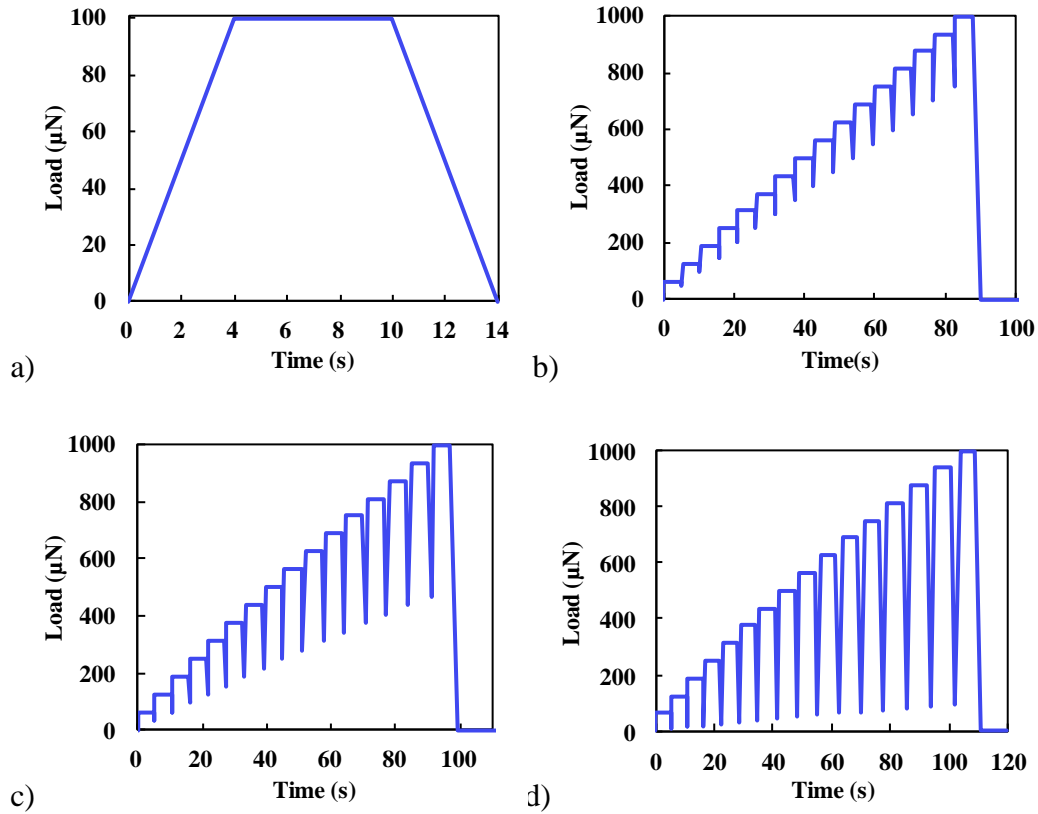


**Figure 5-1. Load versus time graphs (a) single cycle for low load, (b), (c) and (d) multi-cycling tests with the partial unloading set at 20, 50 and 90% of the maximum load respectively.**

To extract the nanoindentation results from the unloading curves for both the single and multi-cycling tests, the power-law fit was set between 20% and 95% respectively to lower and upper fit of a power-law following the Oliver and Pharr method (Oliver and Pharr, 1992) to minimise the effect of creep at or near to the peak load. The ISO standard (ISO/FDIS, 2002) specifies that the upper 80% of the unloading data be used in the fitting procedure for nanoindentation testing.

### **5.2.1 Single and Multi-cycling Tests Comparison**

To investigate the mechanical properties of Cu thin films, the work was carried out under single and multi-cycling test methods. On each sample, 100 single indentations and 50 multi-cycling indentations were performed, each in a single location. Moreover, the multi-cycling test results were averaged to get smooth curves of hardness and Young's modulus on each coated samples at a range of maximum displacements up to 120 nm. Single indentations were performed at larger ranges of maximum displacement; in some cases multiple indentations were produced at the

same displacement. Finally, the mean and standard deviation were determined to assess the scatter in the results. Figure 5-2 shows typical load-displacement curves obtained from a non-annealed thin film under the conditions of 20, 50 and 90% unloading of the maximum load in each cycle.

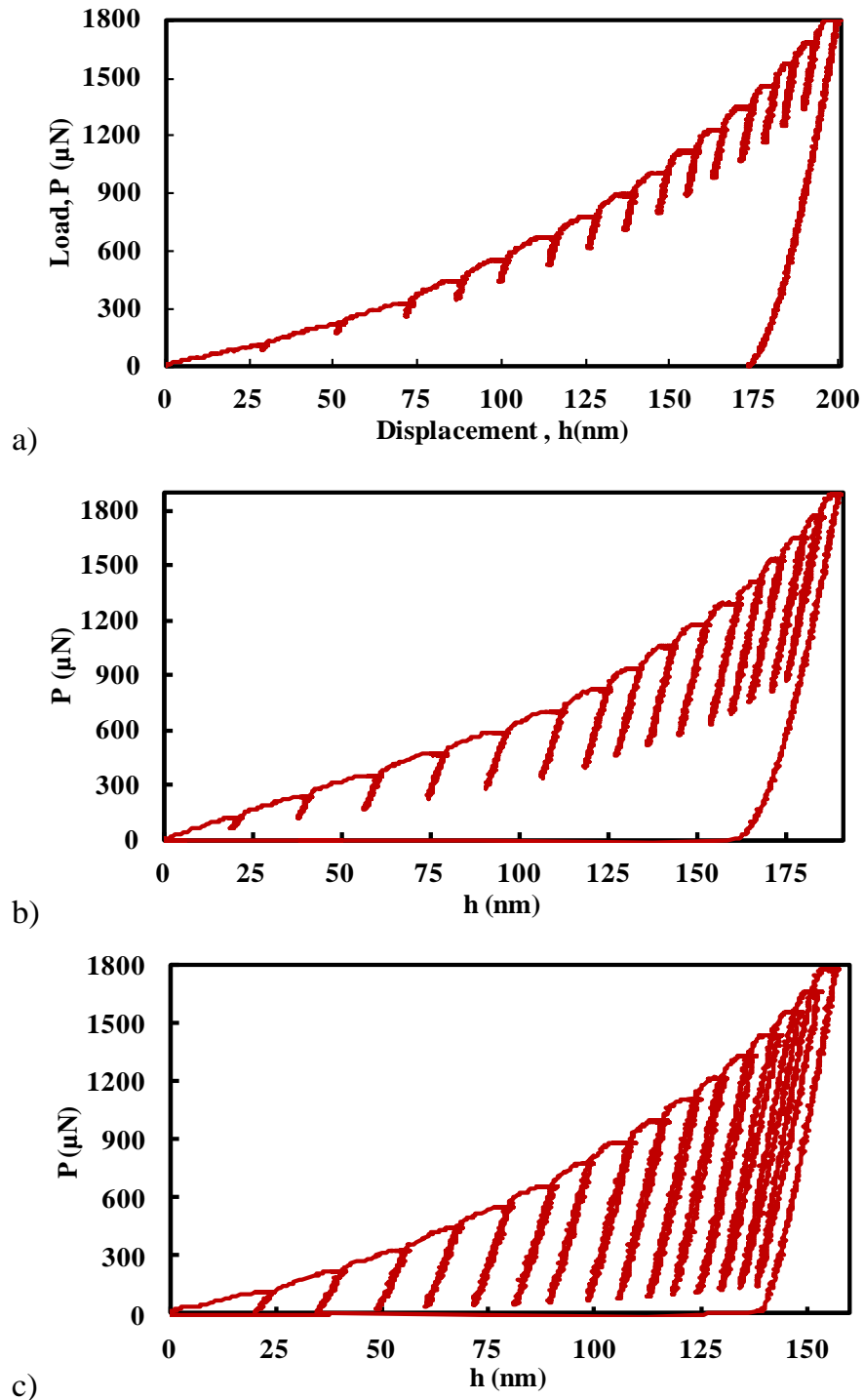


**Figure 5-2. Examples of multi-cycling test load-displacement curves: (a) 20% (b) 50% and (c) 90% unloading of the maximum load obtained from a non-annealed Cu thin film.**

Initially, the hardness and Young's modulus results obtained from the single and an average of 50 multi-cycling indentations under 90% unloading of maximum load for non-annealed Cu thin film were compared; this is shown in Figure 5-3.

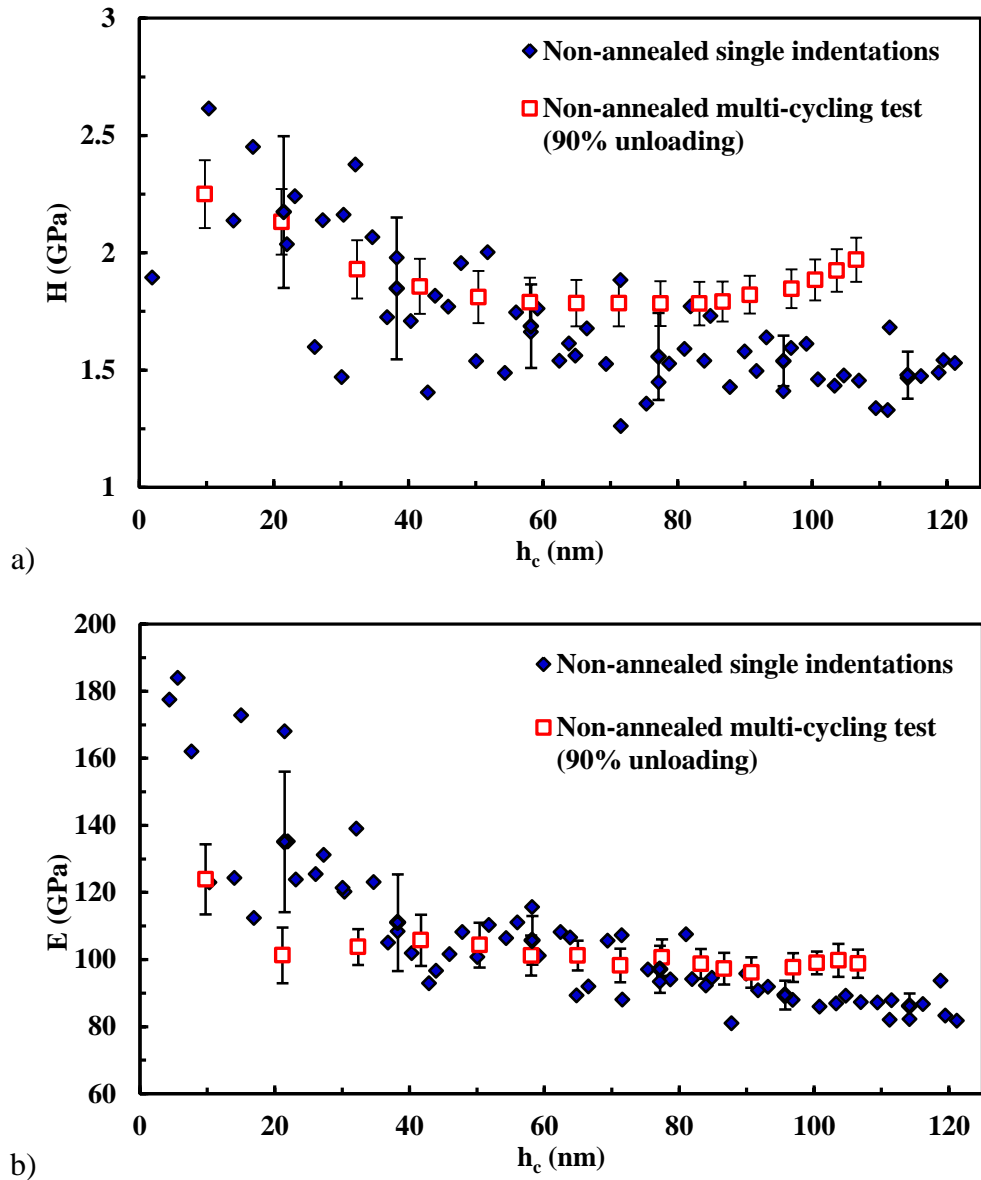


**Figure 5-3. Comparison of the single and multi-cycling tests for the non-annealed thin film samples (a) hardness and (b) Young's modulus versus contact depth.**

As expected the hardness values obtained from the multi-cycling tests increase at lower penetrations depth which is due to the indentation size effect. However, the values also increase at higher contact depths ( $h_c$ ). It is usually assumed that the indentation depth should be limited to less than 10% of the film thickness to avoid any substrate effect. However, this technique is not practical for very thin films (Saha and Nix, 2002). In this case the thickness of the film is 800 nm and consequently, the

results obtained for contact depths of more than 80 *nm* can be affected by the substrate. The Young's modulus results obtained from the multi-cycling test increase slightly as the contact depth decreases but they do not show a significant indentation size effect as might be expected since indentation size effects in carefully-prepared metal samples are plasticity controlled (Bull, 2003).

With regards to the single indentation data, the plots show increased scatter at lower penetration depths followed by a reduction in the variation of hardness and modulus with increasing contact depth when the contact depth is between 40 and 100 *nm*. This effect is more pronounced for the Young's modulus data. Only the first three or four single indentation data points and the first multicycling data point are likely to be affected by errors in indenter tip shape and so this variation is probably caused by the single indentations being carried out in a range of grains with different orientations whilst the multi-cycling tests take place in a single grain. At higher penetration depths many grains contribute to the deformation, giving the bulk polycrystalline material behaviour where anisotropy effects are averaged out. The multi-cycling behaviour appears to deviate from single cycle data at higher penetration depths which could be caused by dislocation rearrangements during indenter unloading that change the extent of pile-up. This is investigated in more detail, as well as grain size, distribution and boundary effects later.

### ***5.2.2 Potential Problems with Multi-cycling Tests***

Initially, to assess the potential problems with the multi-cycling test method, the work was carried out for non-annealed Cu thin film at conditions of 20, 50 and 90 % unloading of the maximum load in each cycle as illustrated in Figure 5-1. The average hardness and Young's modulus data obtained from 50 multi-cycling indentations into the non-annealed Cu thin film under different conditions are compared in Figure 5-4. The error bars shown are the standard deviations obtained from 50 indentations at each individual contact depth. The obtained results are almost identical when tested using 20 and 50% unloading conditions. Compared to the 90% unloading case, both the hardness and Young's modulus results vary for both 20 and 50% unloading, which can be caused by different relaxation processes occurring during unloading in the 90% case.

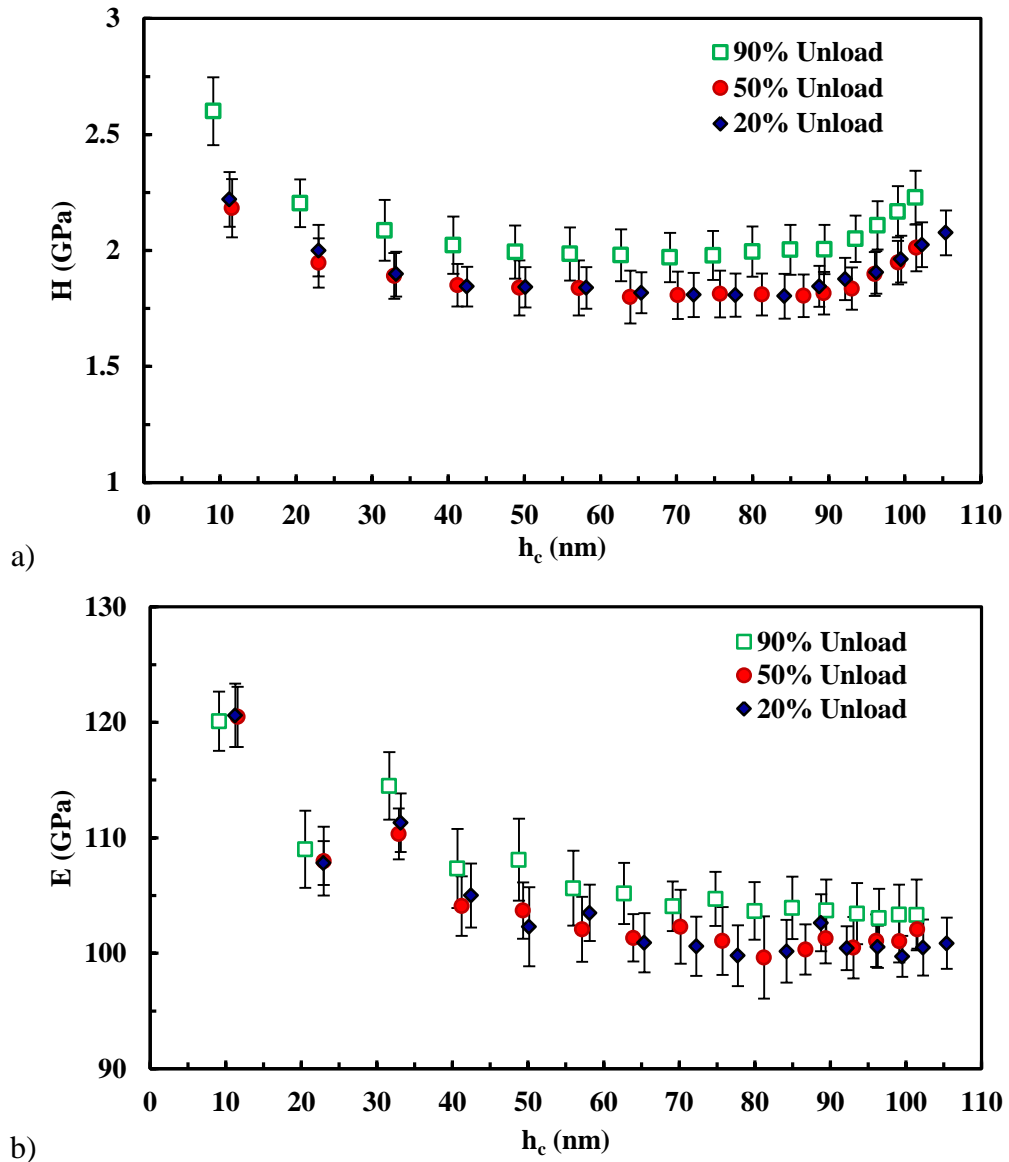


**Figure 5-4. (a) hardness and (b) Young's modulus versus contact depth under multi-cycling tests for the non-annealed sample.**

A similar difference in behaviour for 90% unloading compared to 20 and 50% unloading is shown by bulk Cu tested under similar conditions (see Figure 5-1) as shown in Figure 5-5. The hardness is the same for the bulk material tested with 20% and 50% unloading and increases slightly with contact depth due to the effect of pile-up. All values are lower than those measured with 90% unload. There is no apparent indentation size effect at low loads.

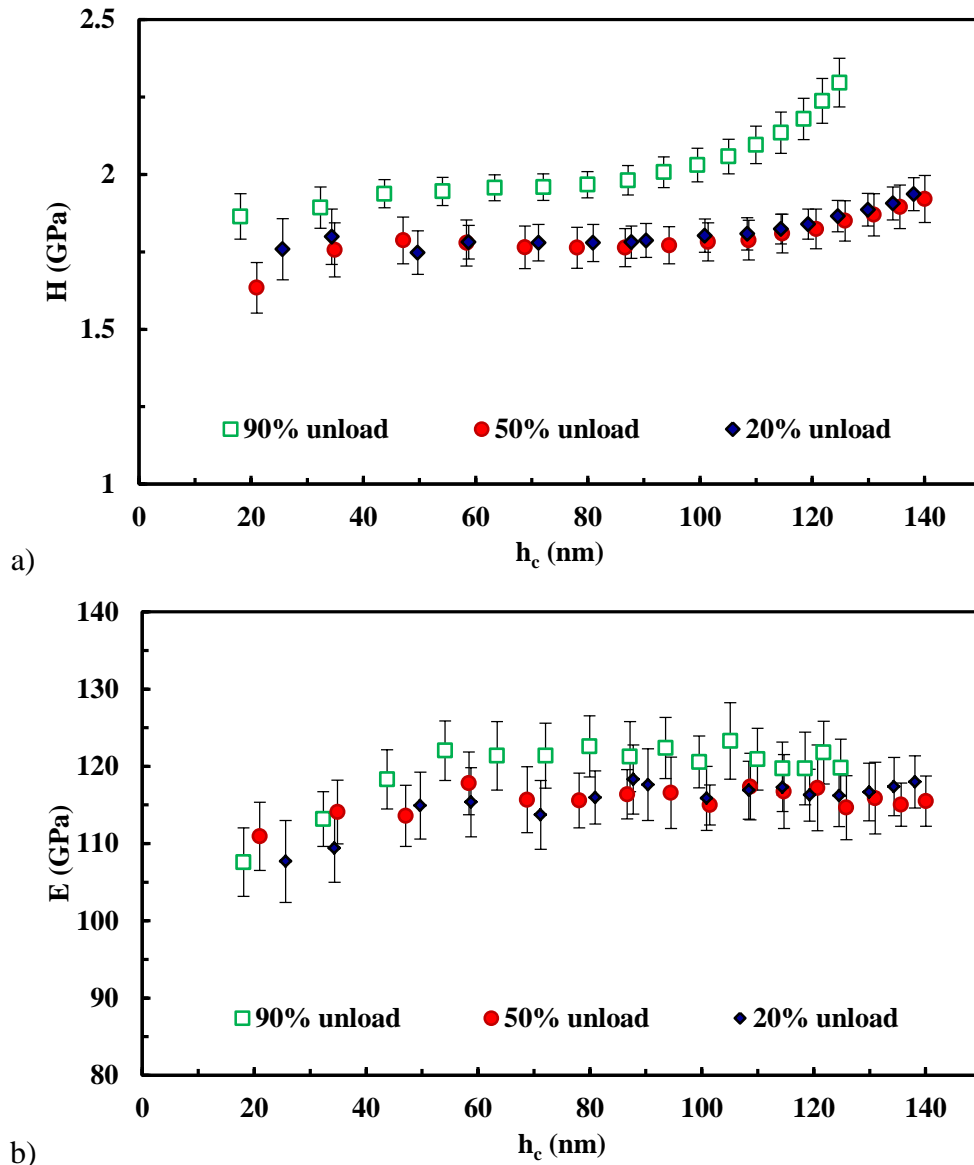


**Figure 5-5. Variation of (a) hardness and (b) Young's modulus of bulk Cu measured by nanoindentation under multi-cycling test.**

The elastic modulus is constant with depth above a 50 nm contact depth and at 120 GPa is close to the expected value for the bulk material. The slight reduction near the surface is due to oxidation as the Young's modulus of CuO is 80 GPa (Tan *et al.*, 2007). Although the effect of oxidation is expected to be very significant for thin films, in this work, all wafers were successfully passivated by 8 nm TiW layer to prevent surface oxidation. To confirm that the oxidation did not accrue, ion beam analysis was undertaken using a 4 MeV helium beam. The results showed that no measurable oxidation occurred within the Cu thin films. However, some oxygen (~30 atom %) was detected at the bulk Cu surface. The significance of the oxidation influence on the mechanical properties of materials and consequently its effect on the

nanindentation test results are discussed in Chapter 8. To further study the effect of different loading conditions on hardness and Young's modulus values using the multi-cycling test method, further the work was carried out on annealed Cu thin films. To detect the effect of annealing in the mechanical properties of Cu thin films, the films were annealed at two different temperatures; 100 and 350 °C. Prior to discussing the aforementioned annealing effect on the mechanical properties of the thin films, the average hardness and Young's modulus data obtained from the Cu thin film annealed at 100 °C under multi-cycling tests at different unloading conditions are shown in Figure 5-6.

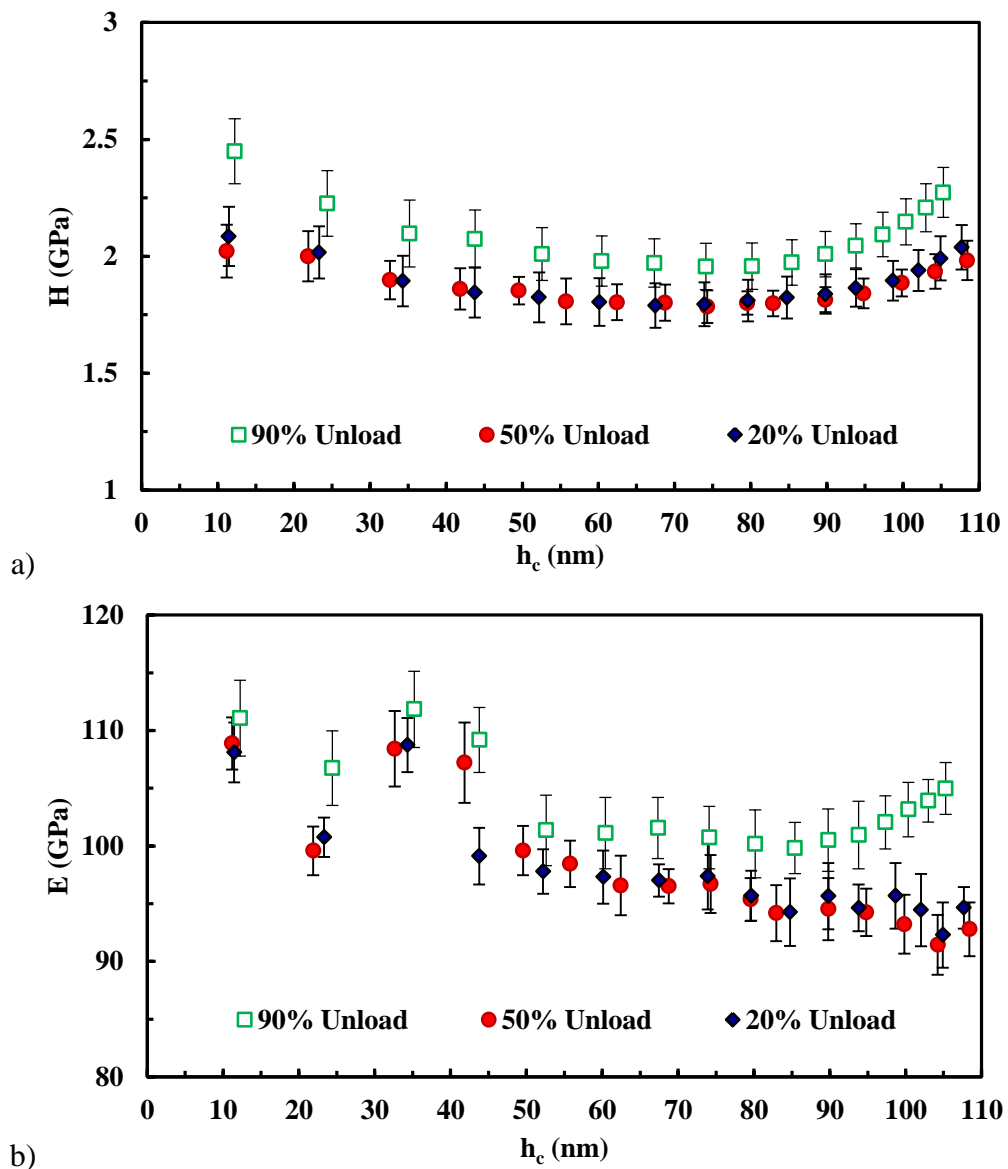


Figure 5-6. (a) hardness and (b) Young's modulus versus contact depth under multi-cycling tests for the Cu thin film annealed at 100 °C.

As can be seen, both the hardness and modulus values obtained from 20% and 50% unloading conditions show similar behaviour, however the 90% unloading differs from the other two conditions. The obtained hardness results for the annealed sample show similar behaviour to the results obtained from the non-annealed sample. For both the annealed and non-annealed samples at contact depths lower than 40 nm, the hardness values are higher than the average values obtained at contact depths between 40 and 80 nm.

As mentioned earlier, Cu is an anisotropic material therefore the variation on the results at very low loads and/or displacements can be explained by the indentation size effect, grain size and individual grain orientations as the indentations can take place within single grains. However, for contact depths higher than 80 nm depth, the hardness increases for both the annealed and non-annealed samples. This behaviour can be due to the pile-up effect or the substrate effect on the obtained results. As mentioned before, at contact depths above 100 nm, the effect of pile-up is dominant and the obtained values are highly dependent on the height of pile-up. The effect of pile-up on the mechanical properties obtained from nanoindentation test for both the single and multi-cycling methods under different conditions for various materials will be discussed in more detail in Chapter 7.

#### *5.2.2.1 Comparison with Gold Thin Films*

Further investigation was carried out on the 1  $\mu\text{m}$  Au thin film deposited on as oxidised silicon for comparison using the same indentation conditions as the Cu thin films, with the multi-cycling test protocol. Au was chosen due to the similarity of the crystal structure to Cu which can facilitate identifying and also confirming the potential issues of multi-cycling indentation tests under diverse unloading conditions. Figure 5-7 illustrates the average hardness and Young's modulus values obtained from 25 multi-cycling indentation tests with the calculated standard deviation for the Au thin film. The obtained values behave in a similar manner to that of thin Cu films under different multi-cycling test conditions. Both the hardness and modulus values obtained using the 90% unloading of the maximum load condition are higher than the results for the 20% and 50% unloading conditions. Since Au is in the same column of the periodic table as Cu with the same crystal structure, similar behaviour was expected to be seen.

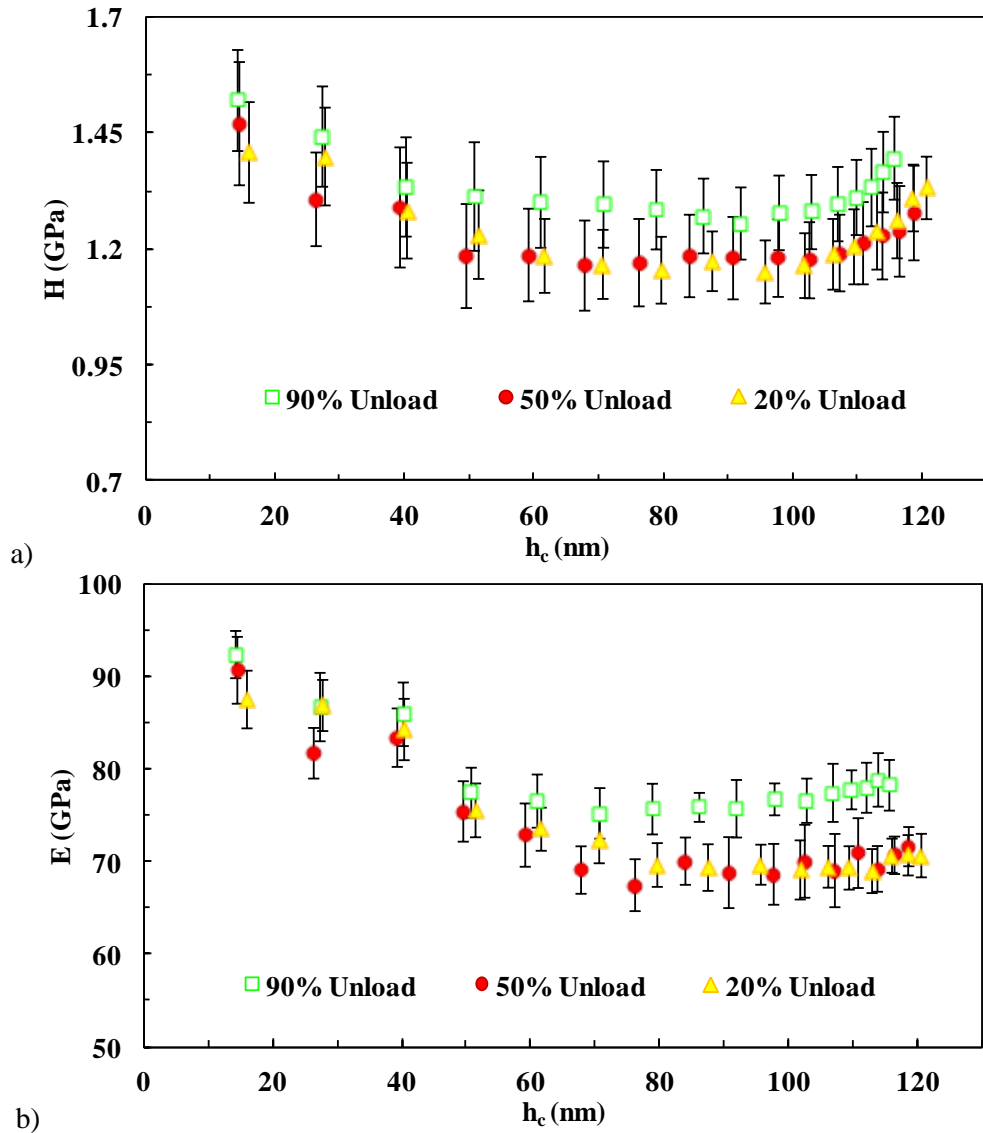


**Figure 5-7. (a) hardness and (b) Young's modulus versus contact depth under multi-cycling tests for the Au thin film.**

Similar to the Cu thin films, the hardness graphs shown in Figure 5-7 can be divided into three regions; the contact depths of less than 40 nm, the depths between 40 nm and 100 nm and the final region is the contact depths greater than 100 nm. It can be seen that due to the indentation size effect, the hardness values are higher at the contact depths lower than 40 nm. However, in the second region they remain constant for all three types of test, but the 90% unloading condition values are higher. Finally, the hardness rises up for the contact depths of more than 100 nm due to the fact that the influence of the pile-up is much larger and therefore significant in this region. The Young's modulus data decreases when the contact depth increases despite the higher modulus of the substrate; this will be discussed in more detail later in this chapter.

### 5.2.2.2 Comparison with Tungsten

To compare the results for anisotropic metals such as Cu under different multi-cycling indentation conditions to a body centre cubic (bcc) structured metal with very little anisotropic behaviour, work was carried out on a standard tungsten (W) sample that had been used for the calibration of the indentation instrument. Figure 5-8 illustrates the average hardness and Young's modulus values for W obtained from 25 multi-cycling indentation tests with the calculated standard deviation.

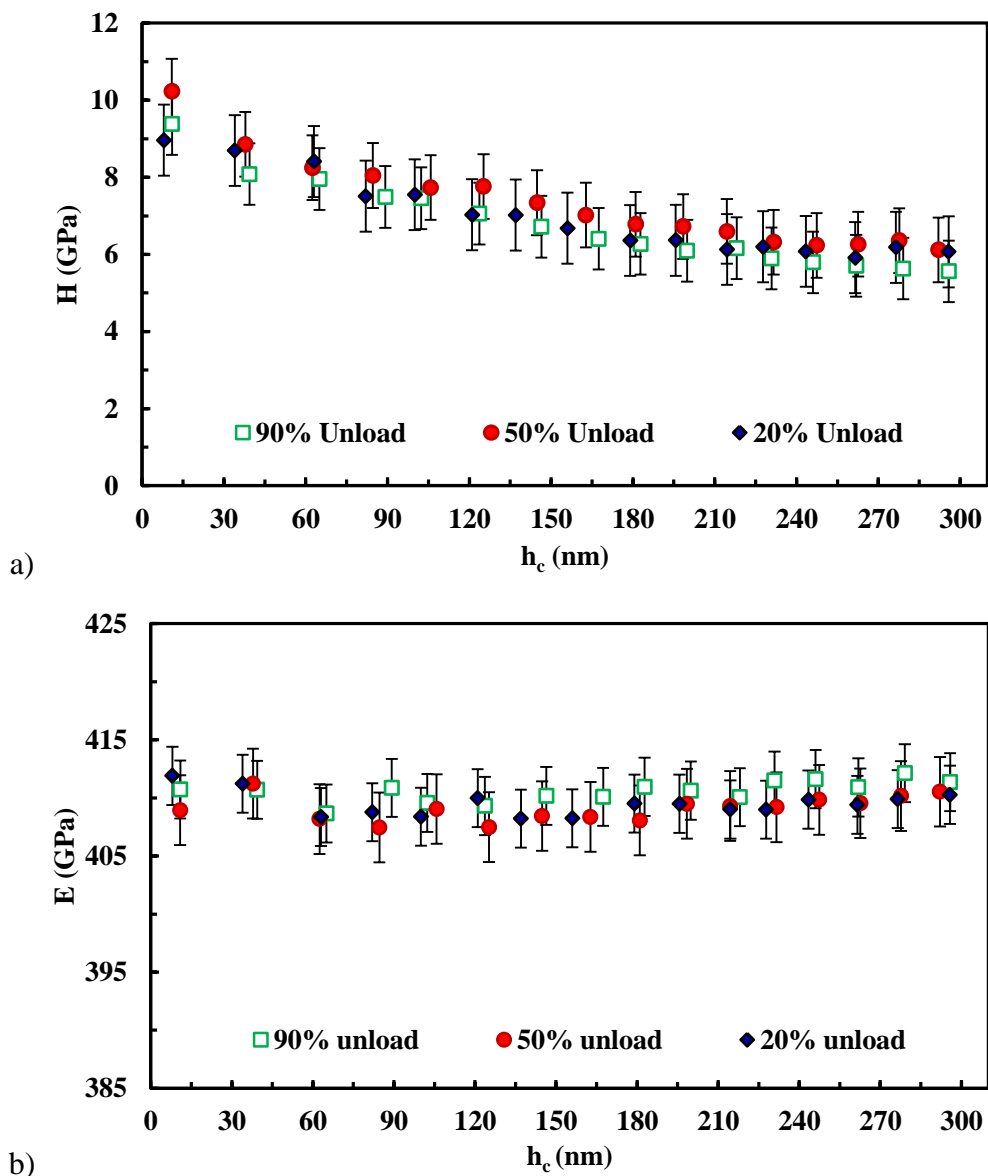


**Figure 5-8. (a) hardness and (b) Young's modulus of W obtained from nanoindentation test under multi-cycling tests.**

The only difference between these tests is that the indentation tests were carried out at higher loads for the W sample because the W sample has no substrate and

consequently there is no substrate effect on the high load values. As mentioned previously, W is elastically isotropic under indentation tests and has a low  $H/E_r$  ratio. Therefore W can minimise the area function error at high contact depths. As can be seen from Figure 5-8 the hardness and modulus values are almost the same for all three different unloading conditions. Hardness decreases slightly through the increase in contact depth, which is in agreement with results reported in the literature (Tymiak *et al.*, 2001). According to Oliver and Pharr (1992), this can be due to the surface-localised cold work hardening resulting from polishing. However, the observed modulus remains nearly constant with an average value of  $409 \pm 2 \text{ GPa}$  which compares well with the known modulus of W of around  $411 \text{ GPa}$ .

### 5.2.3 Annealing Effect

As mentioned previously, the elastic and plastic properties of Cu depend on the crystallographic orientation of its grains. Cu, with its good atomic mobility, allows grain growth during deposition or annealing. Therefore, further studies were carried out on two different annealed Cu thin films to analyse and investigate the effect of annealing on the mechanical properties of Cu. The obtained data were compared to that of a non-annealed sample. To investigate the effect of annealing in the mechanical properties of Cu thin films, the work was carried out using both the single and multi-cycling tests at different contact depths. Initially, this was performed under displacement control to a maximum contact depth of  $120 \text{ nm}$  to ascertain the Young's modulus and hardness values of different Cu thin films. Figure 5-9 compares the hardness and Young's modulus data obtained from three different Cu thin films under displacement control at different contact depths. Each data point represents the average values obtained from 25 single indentations at the same contact depth. As can be seen from Figure 5-9, for all three thin films both the hardness and modulus values decrease as the contact depth increases. In general, the average hardness values for the sample annealed at  $100 \text{ }^\circ\text{C}$  for 60 minutes are slightly higher than both the sample annealed at  $350 \text{ }^\circ\text{C}$  for 1 minute and the non-annealed (as deposited) sample. There is some variation at contact depths lower than  $40 \text{ nm}$  which can be explained by the anisotropy of the Cu and its crystallographic orientation.

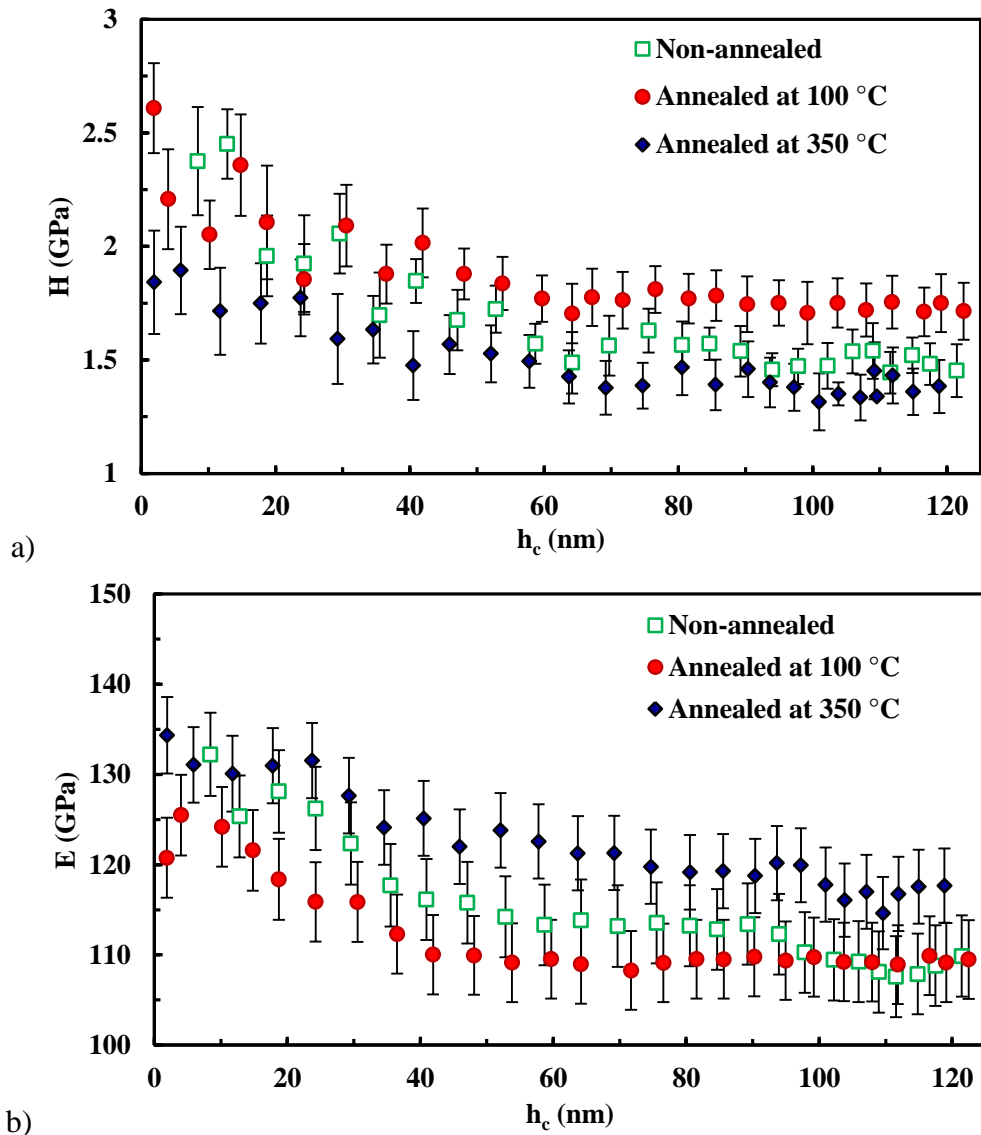


**Figure 5-9. (a) hardness and (b) Young's modulus data obtained from three different Cu thin films.**

However, the variation in modulus data at the same contact depth for different thin films is due to the effect of annealing. Prior to investigating the effect of annealing in the texture of the Cu thin films by use of EBSD and XRD analysis methods, the hardness and modulus data obtained for the Cu thin films under the multi-cycling indentation method were compared. One of the main reasons for using different test protocols to detect the mechanical properties is to minimise and also predict the effect of the substrate on the obtained data. The effect of pile-up, especially at higher contact depths, is another important factor which needs to be considered for thin films during nanoindentation tests. As it was observed previously, the obtained hardness and modulus values from 90% partial unloading of maximum load shows different behaviour. In general the data obtained from 90% unloading is higher than

the two other protocols (20% and 50% partial unload) for thin films. Therefore as the thickness of the films is 800 nm, the effect of the substrate should be identical for all the test protocols. In these circumstances the effect of pile-up in the obtained data is considerable. Consequently, to further investigate the effect of annealing in the mechanical properties of the thin film annealed at 350 °C, work was carried out using the multi-cycling test method (see Figure 5-1 (b) to (d)) with the same conditions as the non-annealed and annealed at 100 °C thin films. In Figure 5-10 the hardness and modulus values for the Cu thin film annealed at 350 °C are plotted against the contact depth.

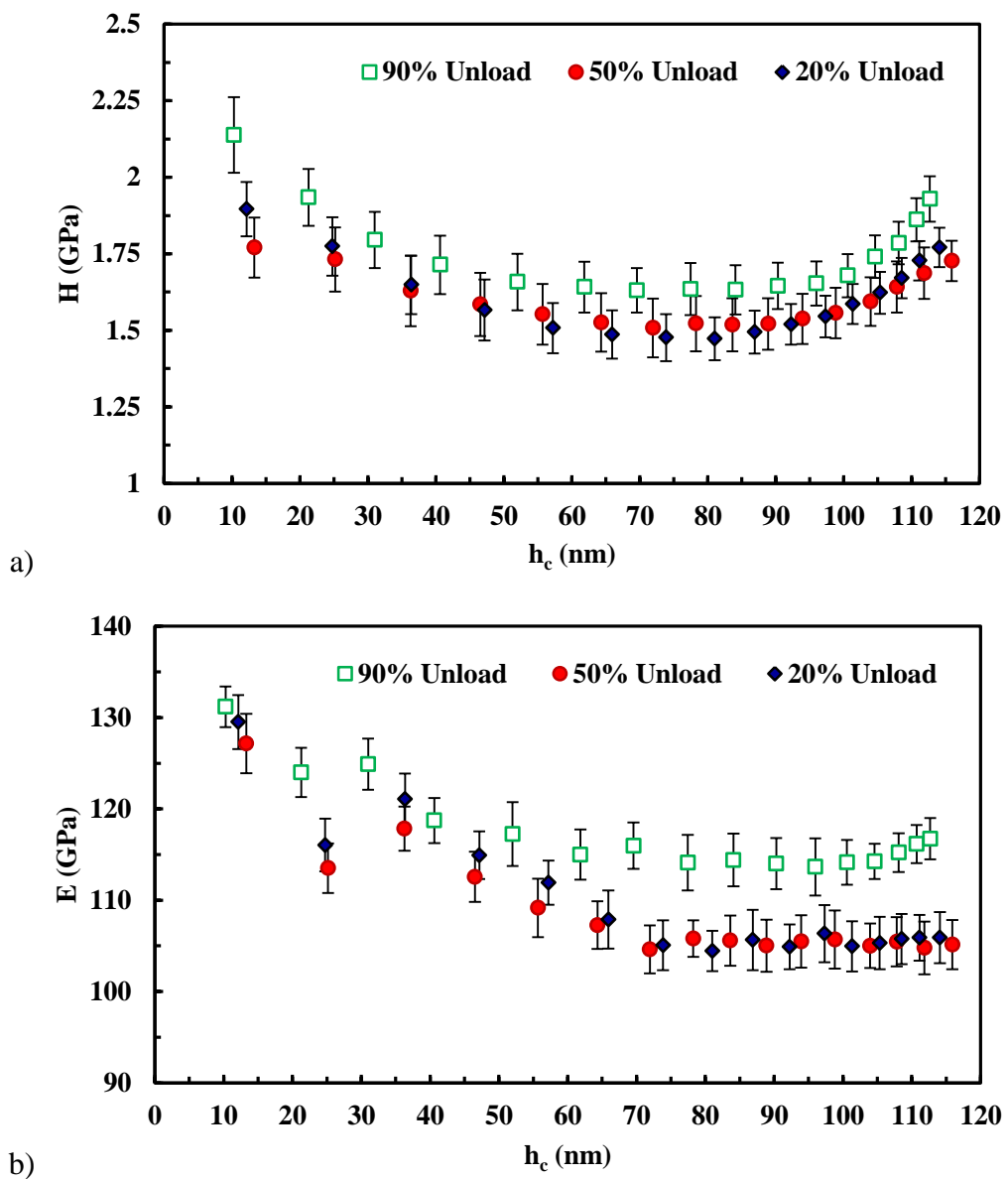


**Figure 5-10. (a) hardness and (b) Young's modulus values versus contact depth in multi-cycling tests for annealed Cu thin film at 350 °C l unloading of the maximum load.**

It is seen that for all three Cu thin films in the multi-cycling indentation, the hardness is higher at lower contact depths due to the indentation size effect but it is relatively constant at intermediate contact depths and increases at high penetration depths. This can be due to pile-up effects or due to the effect of the substrate. The 10% penetration rule (Buckle, 1973) would imply that the substrate effect starts at a 80 nm contact depth, which suggests that the substrate effect dominates over the effect of pile-up (Suresh *et al.*, 1999). However, Equation (2-13) which was described in section 2.2.1 (shown below) can be used to assess whether a substrate contributes to the measured hardness by setting  $R_p = 800 \text{ nm}$  and using the measured  $H/E_r$  ratio for Cu determined at low contact depths.

$$\frac{R_p}{h_{\max}} = -12.907 \frac{H}{E_r} + 4.5451$$

The maximum displacement determined is the largest where no substrate contribution to hardness is expected and may be compared to measured data at higher loads. However, it should be considered that there will always be a contribution from the elastic properties of the substrate in the measured  $E_r$ . This equation calculates that the contact depth at which the substrate effect dominates over the effect of pile-up actually occurs at a higher contact depth. As an example, the maximum indenter displacement measured using the hardness ( $H=1.7 \text{ GPa}$ ) and contact modulus ( $E_r=116 \text{ GPa}$ ) values obtained from the Cu thin film annealed at 350 °C is 183 nm. This is much greater than the largest indentation displacement in this work which is less than 120 nm depth. This was obtained for all three thin films tested in this work.

To further investigate the effect of annealing in the mechanical properties of thin films and also for comparison, the average hardness and Young's modulus with the calculated standard deviation were collected in Table 5-1 for both the single and multi-cycling test methods. It has been found that there is some scatter for the obtained data at the contact depths lower than 40 nm and also the hardness data showed an increase in values at contact depths greater than 100 nm. Therefore to compare the average obtained data, for all three Cu thin films, the table is divided into three regions: contact depths lower than 40 nm, intermediate contact depths which are between 40 to 100 nm and high contact depths which are more than 100 nm.

Cu Thin Film	Indentation Type	Below 40 nm		40 to 100 nm		Above 100 nm	
		H (GPa)	E (GPa)	H (GPa)	E (GPa)	H (GPa)	E (GPa)
Non-annealed	Single	2.1±0.2	125±5	1.6±0.1	113±1	1.5±0.03	108±0.9
	Multi-cycle	2.3±0.2	114±5	2.0±0.05	105±1	2.2±0.01	101±1
Annealed at 100 °C	Single	2.1±0.2	119±4	1.8±0.08	109±0.5	1.7±0.02	109±0.3
	Multi-cycle	2.2±0.1	110±3	2.0±0.04	102±3	2.2±0.06	104±1
Annealed at 350 °C	Single	1.5±0.1	129±4	1.4±0.06	121±2	1.4±0.04	116±1
	Multi-cycle	1.9±0.2	124±5	1.6±0.01	115±1	1.8±0.1	115±1

**Table 5-1. Hardness and Young’s modulus values obtained from Cu thin films under single and multi-cycling (90% unload) tests for various contact depths.**

Moreover, when comparing the data obtained from both single indentations and multi-cycling tests, there is a noticeable difference between the sample annealed at 350 °C and two other samples. This difference can be due to the annealing of defects or grain growth/recrystallisation. The contact modulus determined at contact depths greater than 40 nm is relatively constant for all samples but it is increased in a statistically considerable manner for the sample annealed at 350 °C. These results support the observation that both the elastic and plastic properties of Cu depend on the crystallographic orientation of its grains (Perez-Prado and Vlassak, 2002). The effect of the grain size, grain orientations and grain size distributions are examined using XRD and EBSD analysis in the next sections.

#### **5.2.4 Texture Analysis in Copper Thin Films**

Electron backscatter diffraction (EBSD) and X-ray diffraction (XRD) are the most common techniques used to characterise and analyse the crystallographic texture of materials. Previously, XRD had been used to study the crystallographic orientation of the grains present in the material however, EBSD is an alternative analytical method to locally measure these properties on a nano-scale level (Engler and Randle, 2010; Schwartz, 2010). It should be noted that there are fundamental differences between the two techniques which are due to the penetration depth of each technique; XRD collects data from large penetration depths (Vanasupa *et al.*, 1999) while EBSD detects backscatter electrons from only the uppermost 10 to 50 nm of the sample (Baba-Kishi, 1998). Consequently there is a possibility that the results obtained from

the XRD and EBSD analyses differ and that they are not necessarily in agreement with each other (Mueller *et al.*, 2006).

#### 5.2.4.1 EBSD Analysis

As mentioned previously in section 3.2, EBSD is one of the powerful techniques that have been used to identify the crystallographic orientations of several materials such as metals, ceramics, minerals and semiconductors. When a preferred orientation is required, EBSD can be used to characterise the grain orientation, texture, grain size and its distribution as well as identifying existent phases (Schwartz, 2010). Prior to presenting the EBSD orientation maps of the grains in the Cu thin films, SEM images obtained using the EBSD detector are shown in Figure 5-11.

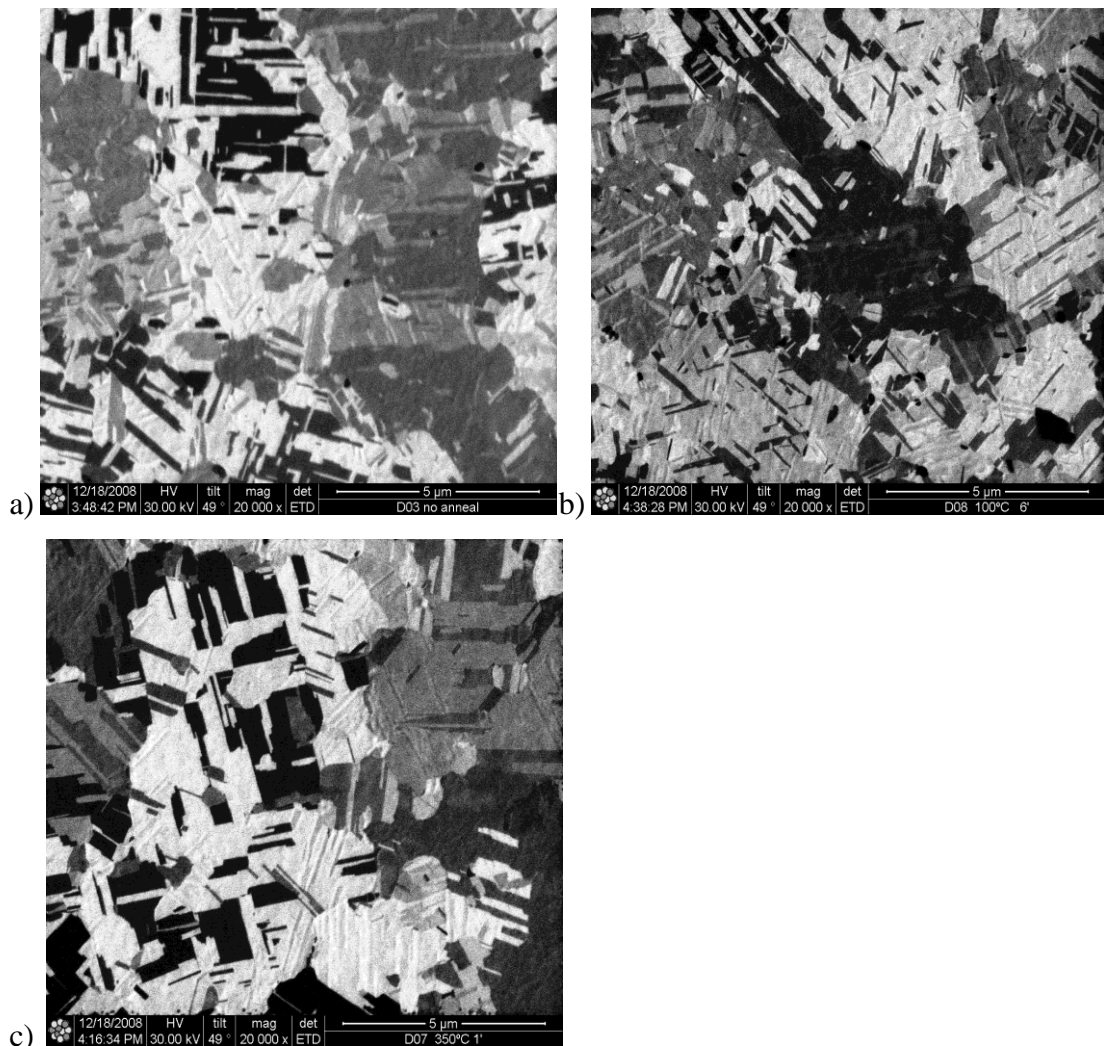


**Figure 5-11. SEM images of Cu thin films obtained using the EBSD detector representing (a) non-annealed sample, (b) annealed at 100°C and (c) annealed at 350°C.**

The diverse orientation of the grains in the annealed samples using the colour coded inverse pole figure maps are shown in Figure 5-12. The (001), (101) and (111) orientations are denoted by RGB (red, green and blue) colours respectively.

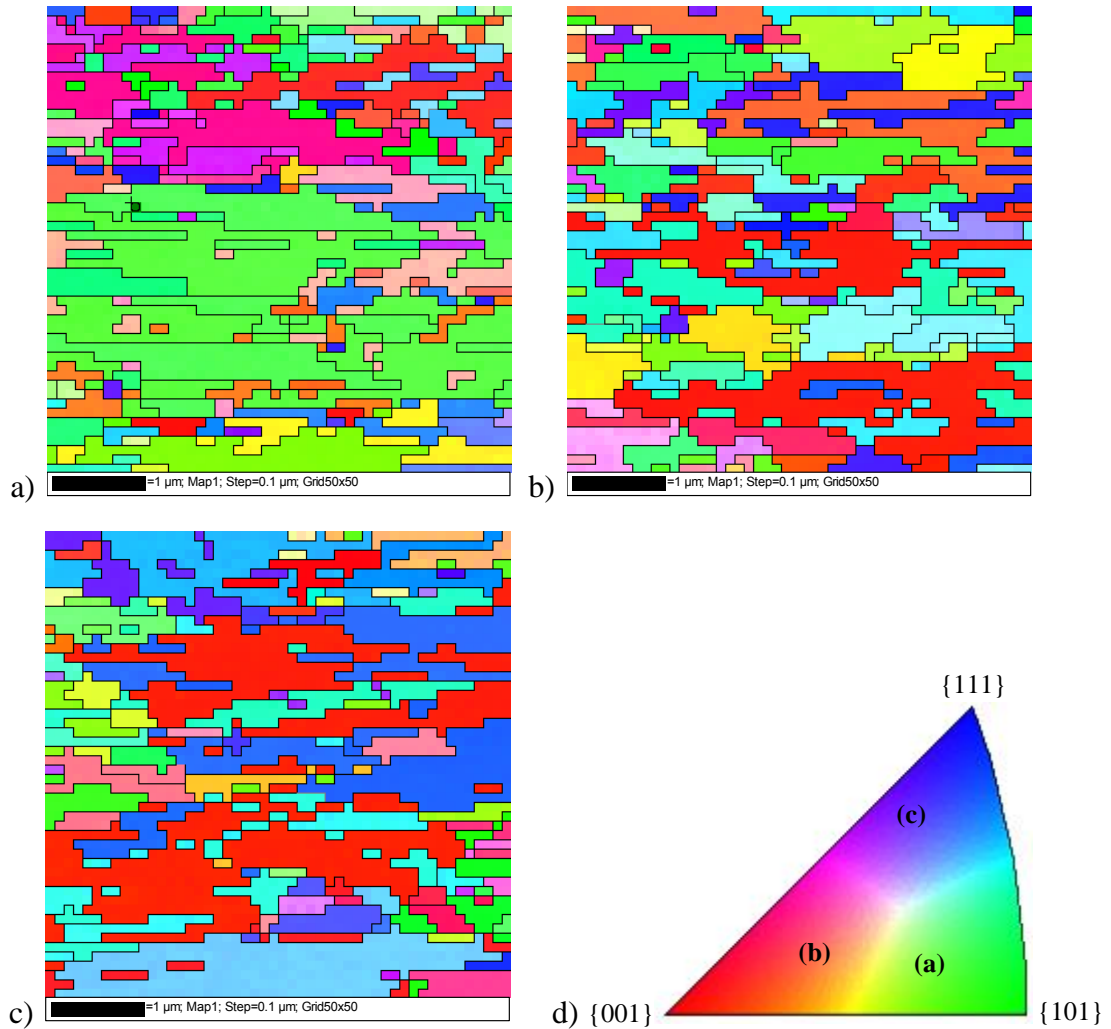


**Figure 5-12. Experimental pole-figure maps of Cu thin films obtained by EBSD test ( $5 \mu\text{m}^2$ ): (a) non-annealed (b) annealed at  $100 \text{ }^\circ\text{C}$  for 60 minutes (c) annealed at  $350 \text{ }^\circ\text{C}$  for 1 minute and (d) inverse pole figure maps colour bar.**

As the blanket Cu thin films were subjected to different post deposition annealing conditions to vary the film texture, EBSD analysis was used to identify any deviation of Cu texture in the films that could be attributed to the annealing process. It should be noted that for all quantitative grain measurements, several regions of  $5 \mu\text{m} \times 5 \mu\text{m}$  area were used and the pole figure orientation maps shown in Figure 5-12 are typical examples of each individual deposited thin film. However, the points (a), (b) and (c) shown in the colour bar in Figure 5-12 (d) are representative of to the average

orientations for the non-annealed, annealed at 100 °C and 350 °C deposited Cu thin films respectively.

The EBSD results confirm that the texture moves towards the (111) orientation as the annealing temperature increases. The Young's modulus values obtained from nanoindentation tests for the sample annealed at 350 °C for both the single and multi-cycling tests were considerably higher than the two other thin film samples. Moreover, the EBSD analysis confirmed that the sample annealed at 350 °C is the most dominant in the (111) orientation compared to the other samples. When comparing the results obtained from both the EBSD analysis and nanoindentation tests, it can be confirmed that the annealing process has a significant effect on the mechanical properties of Cu thin films. Cu is an elastically anisotropic material and any changes in its crystallographic texture can influence the stiffness of the film (Vlassak and Nix, 1993; Xiang *et al.*, 2002). The <111> Cu orientation shows the highest elastic modulus whereas the <100> is the lowest.

At the low annealing temperature, a reduction in the amount of fine-grained material and the growth of the (111) texture is observed, as shown in Figure 5-13. Due to the surface energy of the small grains, it is more energetically favourable for the small grains to disappear first. However, the longer annealing at 350 °C generates some recrystallisation and a significant increase in the growth of the (111) texture was observed in Figure 5-13.

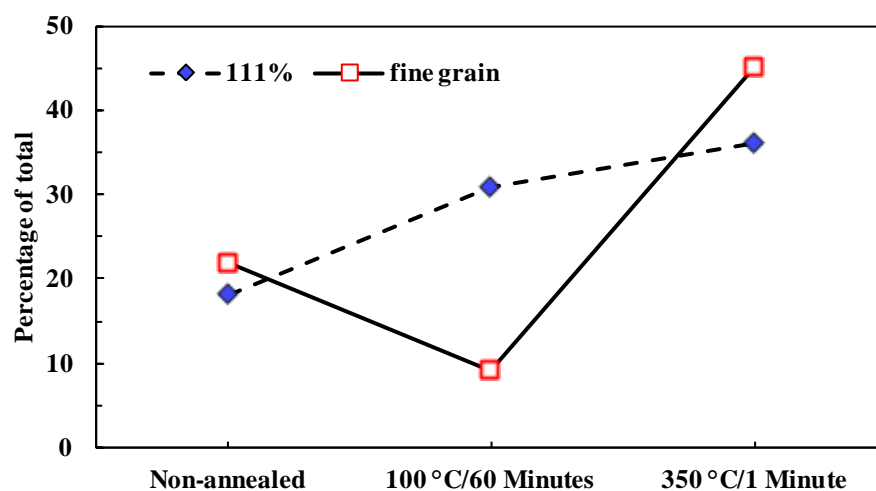


**Figure 5-13. Variation of the amount of (111) oriented grains and fine grained material (<100 nm diameter) as a function of annealing conditions determined from the EBSD results.**

The obtained grains size distributions using the EBSD analysis are represented in Figure 5-14. The mean grain size for Cu thin films for the non-annealed, annealed at 100 °C and annealed at 350 °C are approximately 290, 330 and 280 nm respectively.

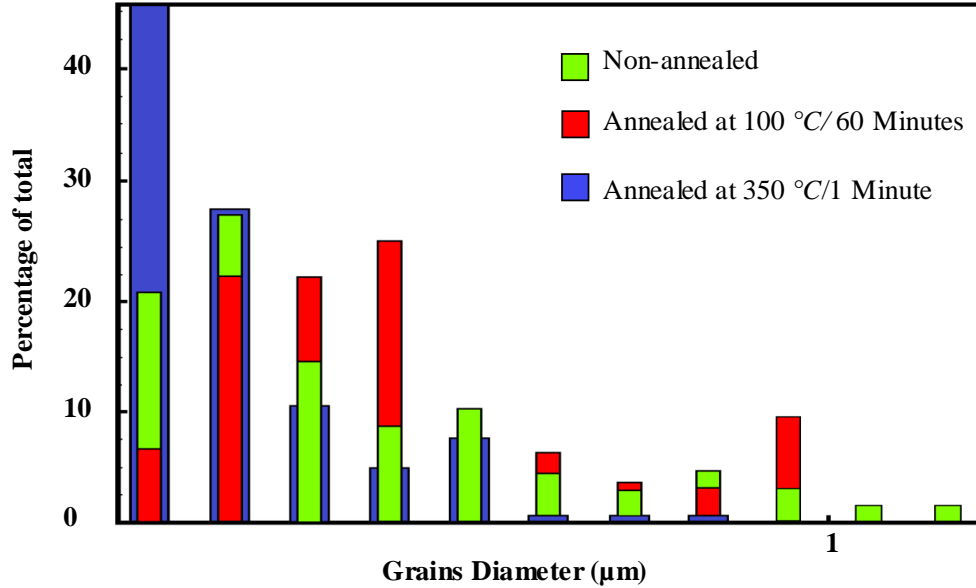


**Figure 5-14.** The grain size distribution for Cu thin films obtained from EBSD.

As mentioned previously, the penetration depth of the EBSD measurement is limited to the upper few nano-metres of the sample but data collected is of a high resolution. However to collect the information at considerably higher penetration depths (deeper into the sample) from a large volume, work was carried out using XRD texture analysis.

#### 5.2.4.2 XRD Analysis

To further investigate and characterise the effect of annealing in the texture of the thin films and also to identify any oxidation taking place on the surface of the thin films work was carried out using XRD analysis. The results obtained for all three thin films are shown in Figure 5-15. To compare the XRD results with the EBSD analysis, the average crystallite size ( $t$ ) was calculated using the Scherrer equation (Pecharsky and Zavalij, 2008) as below:

$$t = \frac{K \times \lambda}{B \times \cos\theta_B} \quad (5-1)$$

where  $K$  is a constant shape factor for which in this work the crystallite shape was assumed to be spherical (producing a value of 0.9),  $\lambda$  is the X-ray wavelength used

which in this work for Cu radiation is  $1.5418 \text{ \AA}$ ,  $B$  is the instrument broadening described by the FWHM (full width at half maximum) of the relevant peak which is  $B_{structural} = B_{observed} - B_{standard}$  and finally  $\theta_B$  is the Bragg angle.

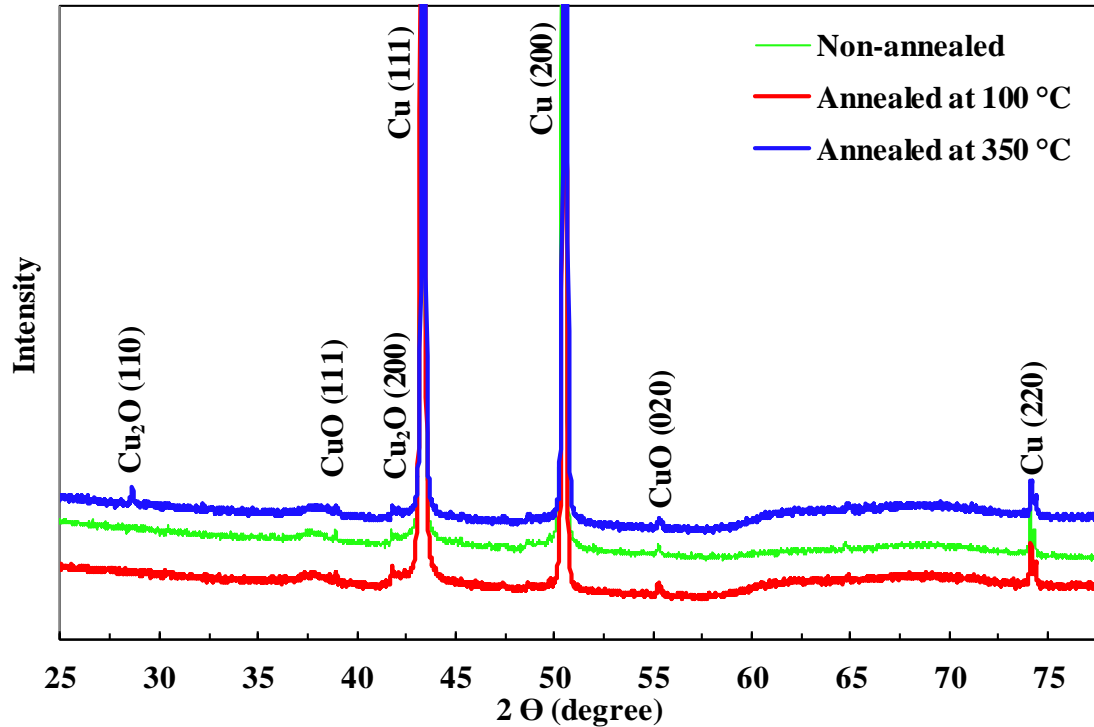


**Figure 5-15.** XRD patterns for Cu thin films.

The average crystallite sizes obtained from the Scherrer equation for the non-annealed sample and samples annealed at 100 and 350 °C are 369, 395 and 312  $nm$  respectively. Although the calculated crystallite size using the XRD analysis is 20 % to 30 % higher than EBSD analysis results, it should be noted that the margin of error of the Scherrer equation is about 20% to 30% (Palosz *et al.*, 2003).

Furthermore, XRD analysis was used to compare and measure the quantity of each orientation for the Cu thin films using the relative intensities of the Bragg reflections (Matthews, 2012). The variation in the amount of (111) oriented grains as well as the fine grained materials are shown in Figure 5-16 for all three thin films. As can be seen from Figure 5-16 for the thin film annealed at 100 °C the amount of fine-grained material is reduced and the growth of (111) texture is observed which is in agreement with the data obtained from EBSD analysis. Moreover, the growth of (111) texture was also obtained for the sample annealed at 350 °C.

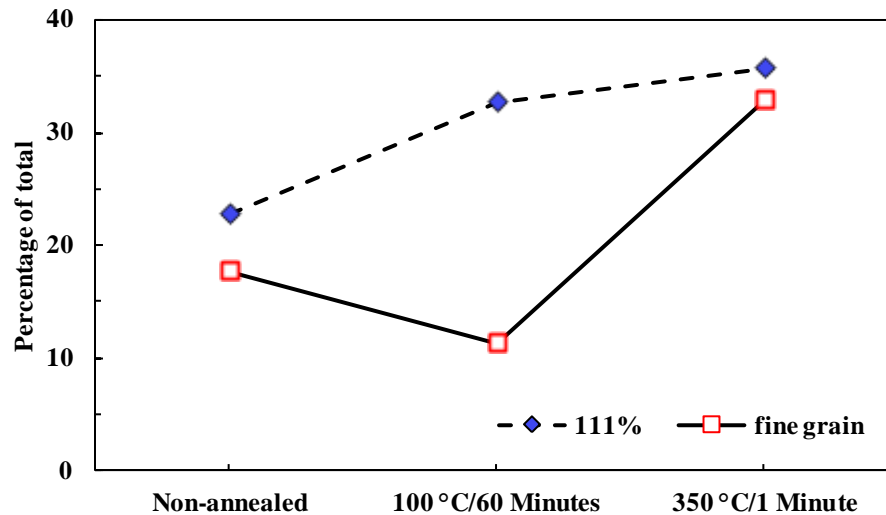


**Figure 5-16. Variation of the amount of (111) oriented grains and fine grained material (<100 nm diameter) as a function of annealing conditions determined from the XRD results.**

The growth of the (111) texture by increasing the annealing temperature implies that the modulus values of the thin films should also increase (Dub *et al.*, 2010). However, the data obtained from the nanoindentation tests show that the non-annealed sample has a higher Young’s modulus than the sample annealed at 100 °C. This means that grain size as well as the presence of the other textures, such as (001) and (101), participate significantly in the obtained modulus data. Closer observation of at the XRD and EBSD results indicate that the growth of the (200) and/or (100) texture for the sample annealed at 100 °C is considerable. Consequently, the obtained Young’s modulus can be lower due to the significant growth of (200) oriented grains. It should be noted that, using the bulk Cu single crystal elastic constant, the theoretical plane-strain modulus values for the (111), (110) and (100) fibre textures are 181, 156 and 99 *GPa* respectively (Xiang *et al.*, 2006).

Initially, when nanoindentation tests were undertaken, the EDX and ion beam analyses were used to detect the presence of oxygen and, as a result, Cu oxide on the surface of the thin films however none was observed. As mentioned before, the thin films were passivated by a TiW layer to prevent oxidation. However, due to the long storage of the samples and presence of only a very thin passivated layer, when reviewing the XRD data some surface oxidation (Cu oxides) was observed. As it can be seen from Figure 5-15, for the  $2\theta$  angles greater than  $60^\circ$  Cu oxide is not observed, however for the  $2\theta$  angles lower than  $60^\circ$  there are several peaks in the

XRD patterns for all thin films which represent two different types of Cu oxide with reasonable intensity. To detect the amount of oxygen on the surface of the thin films, the EDX analysis was repeated and some oxygen (approximately 11 to 20 atomic %) was detected at the surfaces of all the Cu thin films. According to Li et al., 1991, during the annealing of Cu, there are two types of Cu oxides which are most likely to appear. At the annealing temperature of 200 °C, near the surface of the Cu thin films, Cu was oxidised to Cu<sub>2</sub>O (Cuprite). Moreover, they reported that at the higher annealing temperature of 300 °C, Cu was oxidised to CuO (Tenorite) (Li *et al.*, 1991). Both the EDX and XRD analyses results show that the Cu was oxidised to both oxides during storage. To further study the effect of annealing in addition to Cu oxidation on the Cu thin films, Raman spectroscopy analysis was used.

#### 5.2.4.3 Raman Spectroscopy

Raman spectroscopy is another non-destructive optical technique that has been used in this work to characterise the surface oxidation of the thin films as well as the effect of annealing. The data were obtained for wavenumbers less than 1000  $cm^{-1}$ . The lower range was chosen as the fingerprint regions for Si, Cu and its oxides are in the wavenumbers ranging from 200 to 1000  $cm^{-1}$ . The results obtained from Raman spectroscopy for the wavenumbers between 100 and 1000  $cm^{-1}$  (using green laser (514.5 nm) at room temperature) are shown in Figure 5-17.

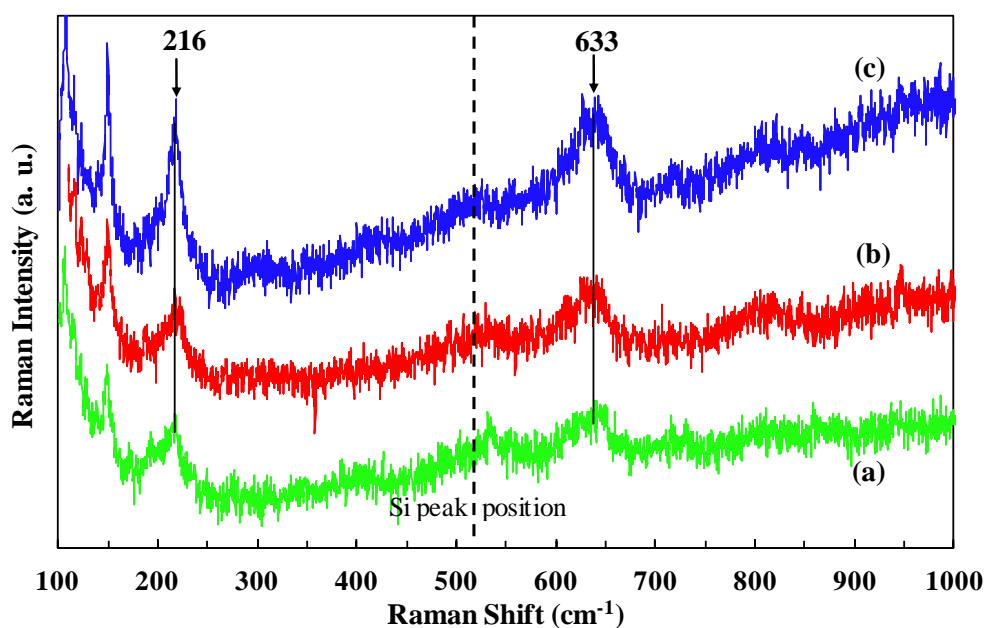


**Figure 5-17.** Raman spectra obtained from Cu thin films (a) non-annealed sample, (b) annealed at 100 °C and (c) annealed at 350 °C.

The black dashed line shown in Figure 5-17 represents the silicon peak position at frequency of  $520.7\text{ cm}^{-1}$  used to calibrate the Raman spectrometer. The peaks present at wavenumbers of 216 and  $633\text{ cm}^{-1}$  for all three thin films are reported in literature as CuO and Cu<sub>2</sub>O (Hamilton *et al.*, 1986; Chrzanowski and Irwin, 1989; Gong *et al.*, 1995; Perez-Robles *et al.*, 1999). The wavenumbers that define a Raman spectrum represent the differences between the incident, exciting and the reflected, shifted frequencies. The shape and position of the peaks of Raman spectra are independent of the frequency of the exciting radiation but critically depend on the bonding and crystal structure of the irradiated material. The intensity, however, is not only strongly dependent on the frequency and power of this radiation, but also on the volume of scattering material.

Crystalline materials show a much greater Raman response than amorphous materials and the intensity of the signal from different phases is proportional to the amount of each phase present in a sample. Consequently, the intensity of the peaks in the Raman spectra obtained from Cu thin films can indicate the quantity of the present Cu oxides. As can be seen from Figure 5-17, as the annealing temperature increases, the intensity of both previously mentioned Cu oxide peaks increases, however the differences are not very significant.

The surface morphology for transition metals also known as non-Raman active metals (Wang *et al.*, 2012), is an important factor which needs to be considered to obtain the Raman signals. However, surface roughness for the Raman active metals can also play a significant role in the detection of the Raman signals and an average surface roughness above 50~200 nm can be crucial (Tian *et al.*, 2002). Consequently, to certify the accuracy of the obtained Raman peaks, the surface roughness was measured for all thin films.

### **5.2.5 Surface Roughness Effect**

Surface roughness is an additional factor that can influence the data obtained from Raman spectroscopy and, more importantly, the calculated Young's modulus and hardness data from small indentations. Bobji et al. (Bobji and Biswas, 1999) reviewed the effects of roughness on the surface mechanical properties obtained using nanoindentation. They concluded that when the penetration depth is more than

3 times the root mean-square (RMS) roughness of the surface, the effect of roughness on hardness and elastic modulus estimation is negligible.

In this work, before and after each indentation test, AFM images of the surface around the impression were produced with the indenter probe to assess the surface roughness and contact area for pile-up correction. The non-annealed, annealed at 100 and 350°C samples have an average surface roughness of 0.18, 0.1 and 0.16 nm respectively, thus the roughness effects can be neglected in their results. Any roughness errors will be confined to the range of contact depths (<10 nm) where the tip calibration is in doubt.

### 5.2.6 Pile-up Effect

Pile-up is the other important factor which influences nanoindentation test results. As mentioned previously in section 2.3.4, pile-up normally occurs for soft metals with residual compressive stress and appears as shown in Figure 5-18.

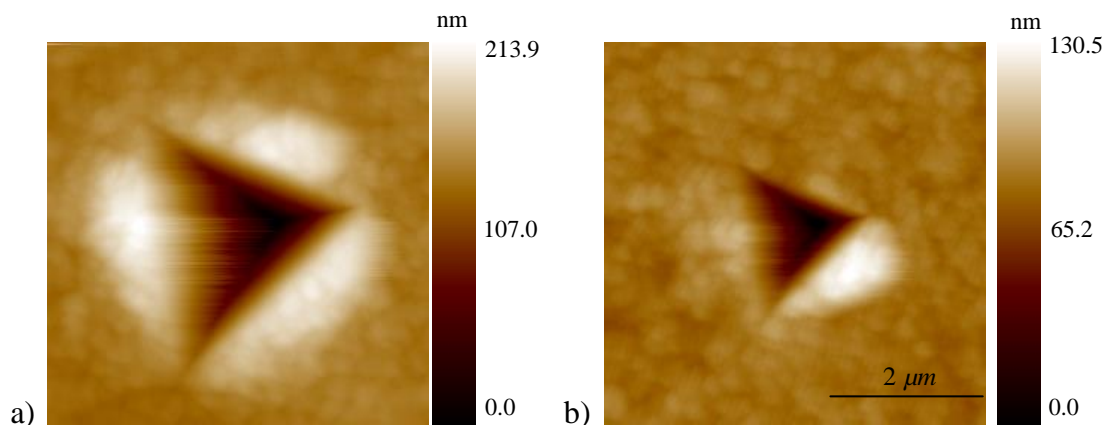


**Figure 5-18. AFM images (90% unload multicycling test) of indentations in a non-annealed Cu thin film which show reduction in pile-up from (a) high (1.5 mN) to (b) low load (0.5 mN).**

Pile-ups are normally symmetrical for polycrystalline materials where the grain size is much smaller than the plastic zone size, but may be very anisotropic when single grains are tested due to the orientation of slip systems with respect to the indentation axis. As fewer grains are sampled the pile-up becomes increasingly anisotropic as illustrated in Figure 5-18 (b). Residual stress and work hardening can also affect the amount of pile-up appearance. The pile-up effect on hardness and contact modulus is observed at high contact depths, such as in Figure 5-18 (a).

For the 90% unload tests discussed here, the pile-up is only significant at high loads where the substrate influences the plastic zone shape and size. In general, the increase in hardness above contact depths of 100 nm is due to enhanced pile-up around the indentation leading to inaccuracies in the hardness determined by the Oliver and Pharr method rather than the effect of plastic deformation of the substrate which does not occur until the contact depth is more than 50% of the coating thickness. For tests with contact depths less than about 80 nm the effect of pile-up can be ignored. Pile-up and its effect on the mechanical properties obtained from the nanoindentation technique will be discussed in greater detail in Chapter 7.

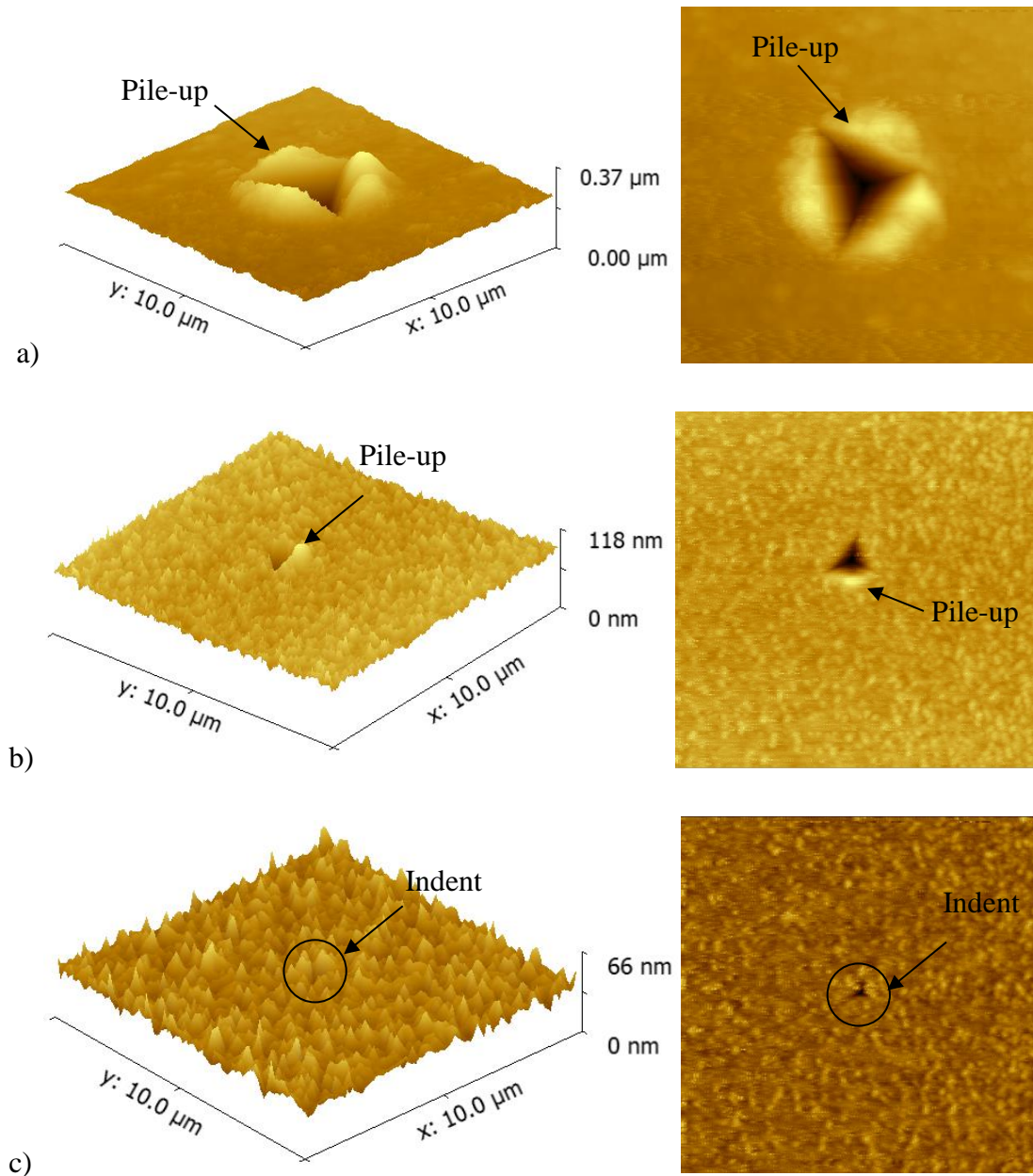
### ***5.2.7 Transition from Single Grain to Continuum Behaviour***

The transition from scattered to smooth modulus data in Figure 5-3 occurs at a contact depth of 40 nm which corresponds to a maximum displacement of 45 nm. For hardness, the transition to smoother continuum behaviour occurs at a much higher contact depth. For this sample (non-annealed Cu thin film) at this contact scale  $H=1.8 \text{ GPa}$  and  $E_r=100 \text{ GPa}$ . Hence, Equation (2-13) as mentioned previously, predicts that the plastic zone radius is 194 nm, which is slightly less than the mean grain sizes measured by EBSD. This is consistent with plastic deformation initiating in a single grain at low indentation loads and then propagating into neighbouring grains as the load increases (Kim *et al.*, 2001). This is in agreement with the observations of Suresh *et al.* (Suresh *et al.*, 1999) that dislocation bursts (pop-in events corresponding to the initiation of plastic deformation) were produced in Cu films on Si at displacements of the order of 10 nm. When the contact depth reaches 80 nm, the plastic zone radius has doubled and is larger than the majority of the grains measured by EBSD, thus continuum behaviour is observed. Elasticity is a longer range process and the transition to continuum behaviour occurs at a much lower contact depth.

Au with low resistivity has been also played a significant role in IC metallisation for many years. The work was carried out on the Au thin films to identify and also confirm the potential issues of nanoindentation tests under diverse loading and unloading conditions and to compare the results with single indentations and bulk mechanical properties.

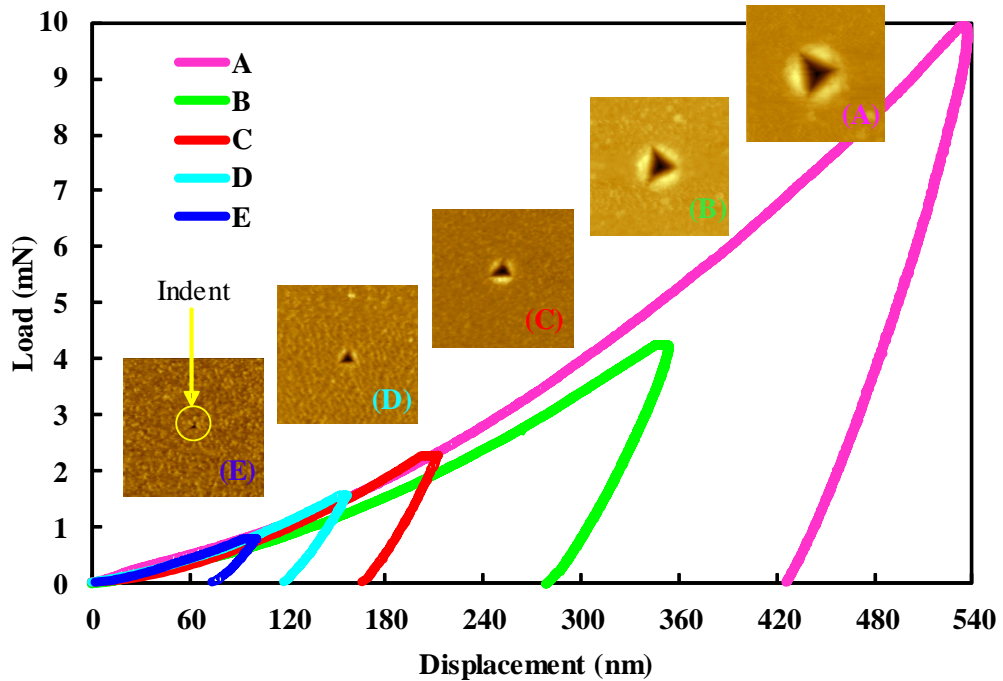
### 5.3 Extracting Mechanical Properties of Gold Thin Films

Figure 5-19 shows three different AFM images (3D views and top-down views) obtained from typical indentation tests carried out on a Au thin film. These example images illustrate that the test took place on a smooth surface with good adhesion. The appearance of pile-up for Au films is clear from the AFM images under the range of loads tested, even at low loads.



**Figure 5-19.** AFM images for typical indentations on Au thin film, three dimensional views and top-down views of (a) high load (10 mN), (b) medium load (1.5 mN) and (c) very low load (0.4 mN).

For example, a large formed pile-up is shown in Figure 5-19 (a) around the indented area at a 10 *mN* load. The obtained results from the indentation tests are therefore consequently affected by pile-up. For comparison, some typical examples of the load-displacement curves obtained from Au thin film as well as the associated AFM images at the same loads are shown in Figure 5-20.



**Figure 5-20. Load-displacement curves and AFM images obtained from Au thin film demonstrating a good adhesion condition between the film and substrate under different applied loads.**

The AFM images illustrate that pile-up occurs even at very small indentations and the effect on the hardness and modulus values can be larger than that from samples with a small amount of pile-up. However, during the indentation test failures such as adhesion can have a significant effect on the observed data. To determine the failure mechanism and its effect on the obtained mechanical properties, the AFM images, as well as the load-displacement curves, from different positions in the films under diverse load ranges were studied to investigate the behaviour of the films.

### 5.3.1 Adhesion

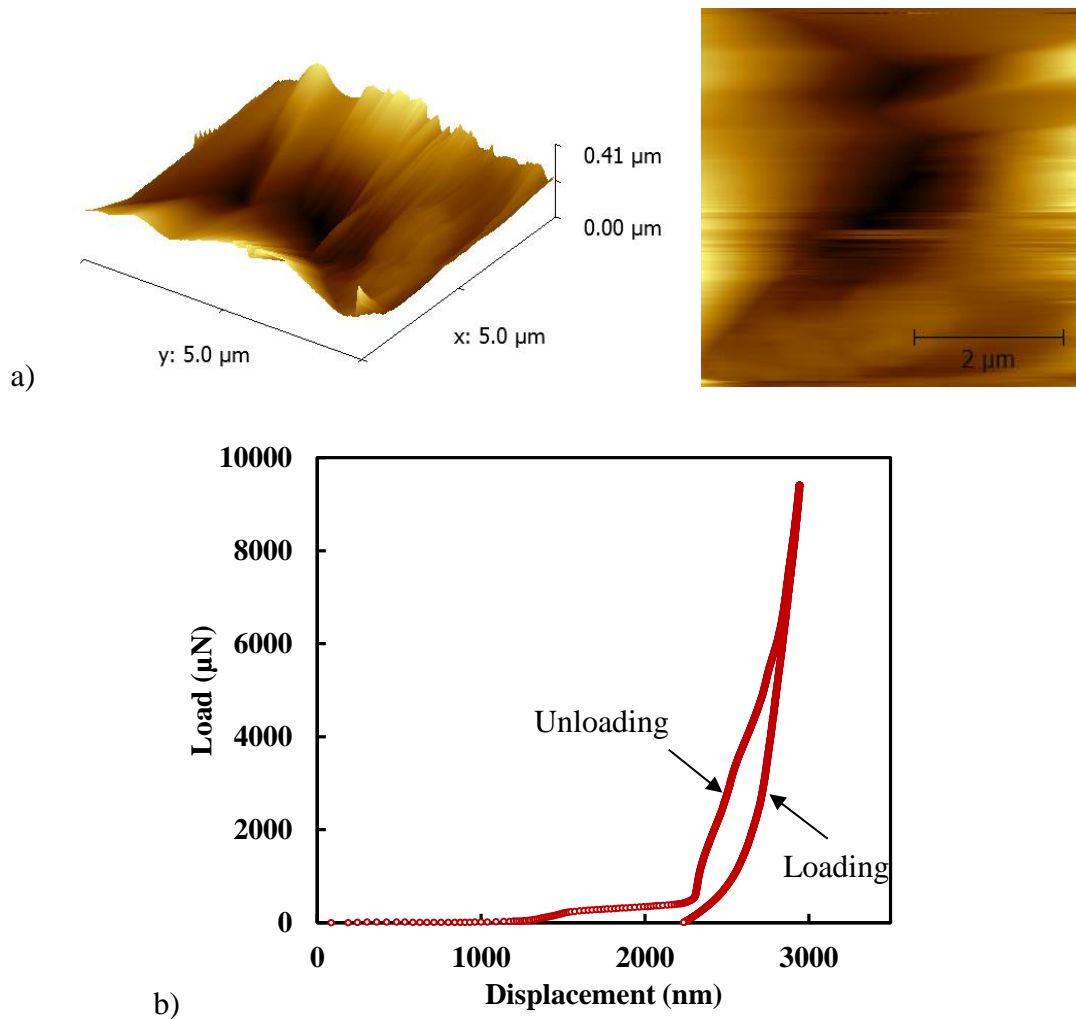
As mentioned in section 4.1.2, one of the main challenges in microelectronic devices is the adhesion between the thin film layer and the barrier layer. This can massively affect device performance both mechanically and electrically. To investigate the

effect of adhesion on mechanical properties and to additionally understand the potential for nanoindentation testing to be used to monitor adhesion performance, the work was again carried out on Au thin films. Samples were divided in two different categories; samples with and without good adhesion.

Screening tests were initially carried out on both types of samples to find out at which load the adhesion failure occurs. During these tests, each sample was subjected to 100 single cycle indentations under open loop mode. To determine the minimum load that fracture or detachment could be produced in the experiment, the load started from the maximum peak load of 10 *mN* and was decreased gradually by 0.1 *mN* in each successive indent. In all cases a 4 seconds peak load hold was used before unloading to allow creep run-out. To fully understand and characterise the film behaviour under the indenter probe, AFM images were obtained over 10  $\mu\text{m} \times 10 \mu\text{m}$  areas. The average roughness value obtained from the AFM images before the indentation tests at 20 different locations on the surface of the sample is approximately 0.51 *nm* which shows that the effect of surface roughness is negligible.

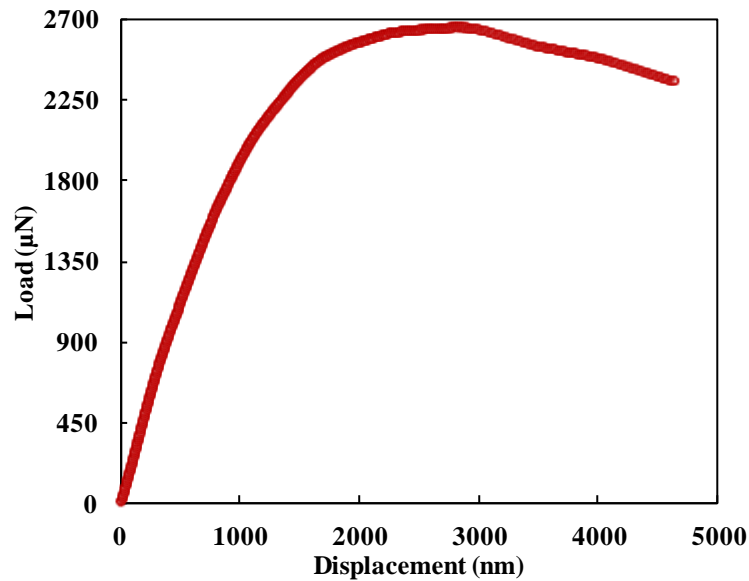
A total of 20 indentations were made in each of the tested samples. The applied loads were based on the 'failure' load found during the screening tests as different failure loads could occur on the different samples due to the variations in their respective metal stacks. Six samples were tested in total.

Figure 5-21 shows an example of adhesion failure. The film surface, under a load of around 10 *mN*, fails and multiple cracks in the film are diverted to the interface causing delamination. It is known that in general loading curves are in a lower displacement range than unloading curves. However, the load-displacement curve obtained from the indentation area shown in Figure 5-21 (b) illustrates that the loading and unloading curves are reversed. This behaviour is due to the failure of the coated system. The detached coating relaxes its residual stress and pushes the indent away from the surface during unloading.



**Figure 5-21. (a) three dimensional and top view of the AFM image for a failed coated system and (b) the load-displacement curve obtained from the same indentation test.**

Upon observation of the obtained load-displacement curves it can be seen that there are a variety of failure mechanisms which exhibit themselves in the load-displacement curves. Each failure mechanism has a characteristic load-displacement curve which allows identification of the type of failure. Figure 5-22 shows another example of the failed load-displacement curve for the load set at 5 *mN*. However when the load reached around 2.7 *mN*, failure occurred. The large indenter penetration implies that either there is a soft layer beneath the top coating or the coating has been detached in the indentation loading cycle. Given the residual depths of the indent in Figure 5-22, it could be visible by light microscopy if the indent was produced by plastic deformation only. Reflected light microscopy and AFM images confirmed that the coating had been completely detached during the indentation loading cycle.



**Figure 5-22. Failed load-displacement curve for the load originally set at 5 mN.**

Two examples of complete detachment of coatings during the indentation test are shown in Figure 5-23 at high loads.

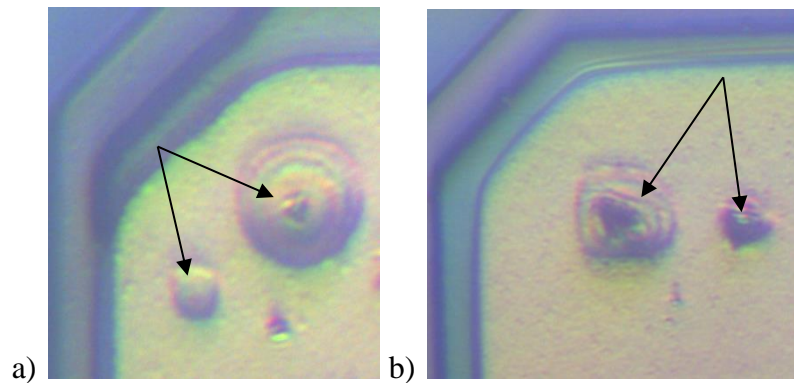


**Figure 5-23. Microscopic images of two different pads with adhesion failure during the nanoindentation test (arrows indicate nanoindentation).**

One of the important features that necessitates consideration during the coating process is consistency of the coating properties across the coated surface. In any electronic devices, similar to other coating applications, it is important to have consistent properties, such as stiffness, all the way through the sample and device performance is highly dependent on this. To fully understand the effect of non-consistency of the coating on the mechanical properties, nanoindentation tests were carried out on both the failed and non-failed samples in different areas, such as at the edge of the coatings. The test results showed that the stiffness of the coatings were not identical across the sample surfaces. Reductions in stiffness are associated with

cracking in the coatings and large visible indentation imprints. For example, the reflected light microscopy image in Figure 5-24 shows that in the load range between 5 and 1 mN, there are 8 indents observable through use of the microscope and the other indents were too small to be seen by the microscope at 600X magnification.

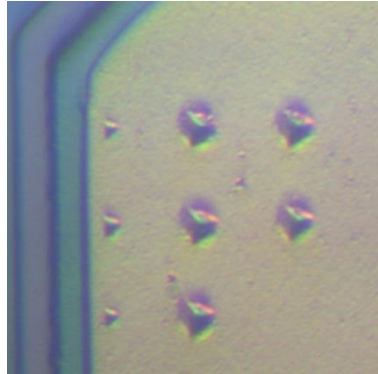


**Figure 5-24. Microscopic image of the Au thin film, presenting visible large indentations illustrating reduction in stiffness.**

Another important factor that needs to be considered during the nanoindentation data analysis is the appearance of cracks on the surface of the sample. A single crack observed from the experiment on the sample having weak adhesion is shown in Figure 5-25. The combination of the AFM image and the load-displacement curve shown in Figure 5-25 illustrate that the single crack in the coating deflects to the interface to cause delamination and crack growth through the film.

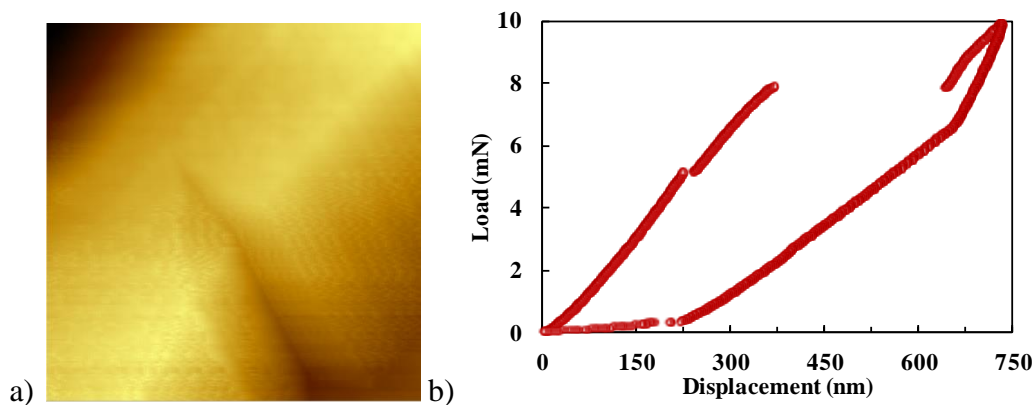


**Figure 5-25. (a) AFM image and (b) the load-displacement curve obtained from the same indentation position.**

### 5.3.2 Thin Film and Bulk Gold Comparison

The nanoindentation tests were carried out on the bulk Au single crystal to compare the results from thin films with bulk Au under the same test conditions for pile-up

correction. Au single crystals were chosen for comparison, due to the simple structure of the material and the removal of the grain boundary effect on the experimental results. The average hardness and modulus values obtained from single crystal Au are  $1.05 \pm 0.2$  and  $84.91 \pm 1$  GPa respectively. The average values are higher than the expected results. The corresponding AFM images confirmed that the appearance of pile-up for Au even at low loads is considerably large, however, as the pile-ups are more symmetrical, pile-up correction is more practical. Using the Gwyddion software to calculate the true contact area from the obtained AFM images, the hardness and modulus values were reduced to  $0.65 \pm 0.1$  GPa and  $80 \pm 1$  GPa which are more in agreement with the results previously reported (Volinsky *et al.*, 2004; Siller *et al.*, 2005; Jahromi, 2008). In comparison to the bulk Au, the thin films are more likely to have even larger pile-ups. The average hardness and contact modulus results determined from 10 single cycle nanoindentation tests on Au thin films after pile-up correction are shown in Figure 5-26.

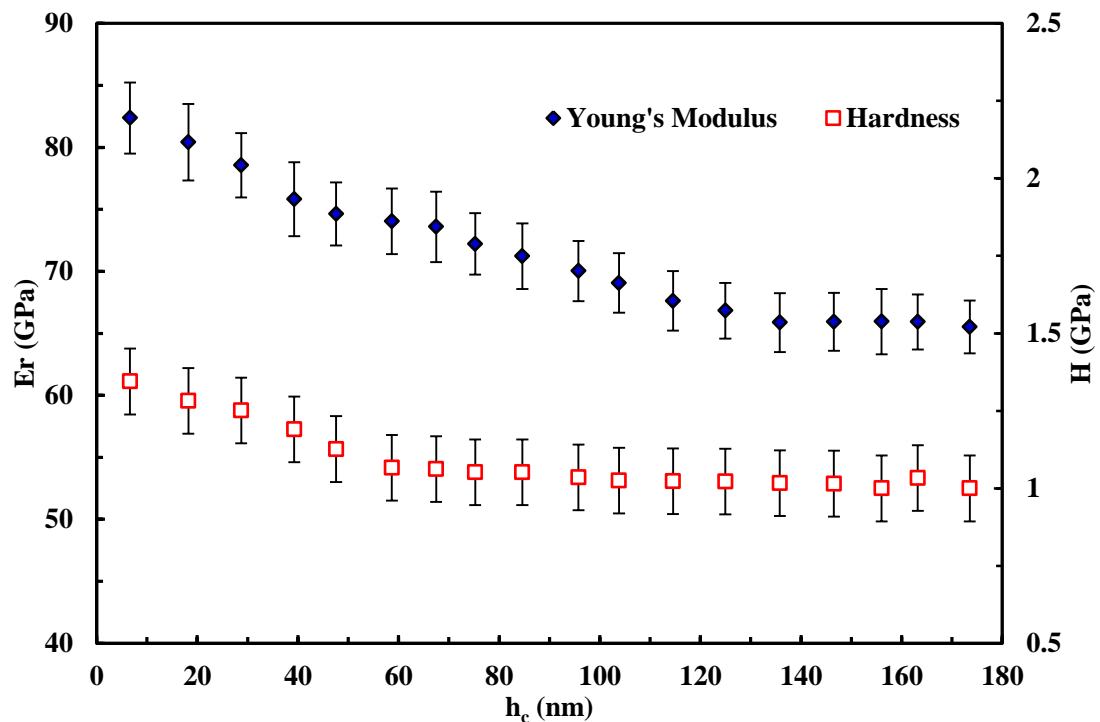


**Figure 5-26. Obtained Young's modulus (left) and hardness (right) results for Au thin film after pile-up correction with standard deviations.**

The average hardness value obtained from single indentation tests is  $1.08 \pm 0.2$  GPa after pile-up correction and the average modulus value is  $71.45 \pm 5$  GPa which is lower than that of bulk Au. As the Au thin films were deposited on a Si/SiO<sub>2</sub>

substrate, the effect of the substrate can influence the obtained modulus values. Thin Au films with 1.08 *GPa* hardness values are harder than pure bulk Au with a hardness of 0.65 *GPa* which can be effected by the substrate, the indentation size effect, strain gradient plasticity phenomena, dislocation straightening and different microstructures (grain sizes). Thin films have smaller grain sizes and consequently lower dislocation movements when compared to that of bulk materials which are harder. However, it should be noted that the cooling rates as well as built-in structural defects during deposition can also have significant effects on the mechanical properties of thin films.

#### 5.4 Why does $E_r$ Decrease with Penetration for Coatings on Silicon?

For the bulk Cu and Au tested in this work, the contact modulus determined from both single indentations and multi-cycling tests are constant with contact depth except at low loads for bulk Cu where surface oxidation influences behaviour. However, for all the Cu and Au coatings on Si the contact modulus decreases as the contact depth increases. Since the Si substrate has a Young's modulus which is greater than Cu and Au, this is a surprising result. However, it should be noted that the Cu and Au coatings were deposited on 1 and 2.3  $\mu m$  thick Si oxide layers respectively which needs to be taken into consideration.

The substrate effect on the obtained data, especially in greater contact depths can be examined using a simple model proposed by Bull (Bull, 2012). This model, which is based on a truncated cone of load support beneath the coating, helps to study the variation of contact modulus with contact depth for a coating/substrate system. In this model:

$$E = \frac{P}{2a_0(\partial_c + \partial_s)} \quad (5-2)$$

In this equation,  $P$  is the applied indentation load and  $a_0$  is the contact circle radius which has a relationship with the contact depth. The displacements in the coating and substrate under the indenter are given by:

$$\partial_c = \frac{P}{\pi E_c} \left[ \frac{1}{a_0 \tan \alpha} - \frac{1}{a_0 \tan \alpha + t_c \tan^2 \alpha} \right] \quad (5-3)$$

and

$$\partial_s = \frac{P}{\pi E_s} \left[ \frac{1}{a_0 \tan \alpha + t_c \tan^2 \alpha} - \frac{1}{a_0 \tan \alpha + (t_c + t_s) \tan^2 \alpha} \right] \quad (5-4)$$

$E_c$  and  $E_s$  represent the Young's Modulus of the coating and substrate respectively,  $t_c$  and  $t_s$  are the thickness of the coating and substrate and  $\alpha$  is the semi angle of the cone of material which supports the load. In this work  $\alpha$  was found to be  $32.48^\circ$  through measurement on the bulk materials and also using the obtained SEM image (Figure 3-5, Chapter 3) for the Berkovich tip. If the indenter geometry is known, the contact depth ( $h_c$ ) determined by the Oliver and Pharr method (Oliver and Pharr, 1992) can be related to the contact radius. For the Berkovich indenter:

$$h_c = \sqrt{\pi/k} a_0 \quad (5-5)$$

where  $k$  is 24.5. Equations (5-2) and (5-4) can be modified for a coating with two or more layers. In the case of the Cu and Au layer on a silica intermediate layer on Si, Equation (5-3) remains valid for the coating contribution but, for an interlayer of thickness  $t_i$  and modulus  $E_i$ , Equation (5-4) becomes:

$$\partial_i = \frac{P}{\pi E_i} \left[ \frac{1}{a_0 \tan \alpha + t_c \tan^2 \alpha} - \frac{1}{a_0 \tan \alpha + (t_c + t_i) \tan^2 \alpha} \right] \quad (5-6)$$

and for the substrate:

$$\partial_s = \frac{P}{\pi E_s} \left[ \frac{1}{a_0 \tan \alpha + (t_c + t_i) \tan^2 \alpha} - \frac{1}{a_0 \tan \alpha + (t_c + t_i + t_s) \tan^2 \alpha} \right] \quad (5-7)$$

In Equation (5-2),  $\partial_c + \partial_s$  is replaced by  $\partial_c + \partial_i + \partial_s$ . Predictions for this bilayer model and the single layer model for 800 nm Cu on Si with a 1  $\mu m$  intermediate silica layer are shown in Figure 5-27. The predicted contact modulus from the bilayer model and the experimentally measured values decrease as contact depth increases whereas the single layer model shows an increase as expected from a coating on a stiffer substrate.

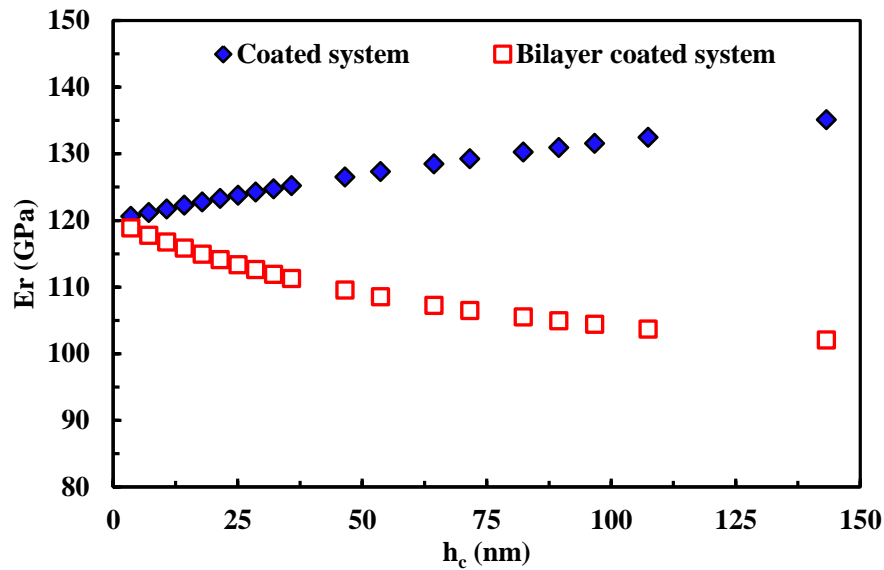


**Figure 5-27. Predicted variation of contact modulus with contact depth for 800 nm Cu on Si with and without a 1  $\mu\text{m}$  silica intermediate layer.**

Similar behaviour was obtained using the model for a 1  $\mu\text{m}$  Au thin film deposited on Si substrate with a 2.3  $\mu\text{m}$  intermediate silica layer. Since the system acts as a series of springs where the reciprocals of the spring constants are added to get the effective spring constant the lowest modulus layer dominates behaviour if it is sufficiently close to the contact surface.

## 5.5 Summary

In the measurement of the mechanical properties of materials such as hardness and Young's modulus, nanoindentation is one of the most commonly used techniques. However, the potential measurement errors caused by factors such as surface roughness, density of the material, pile-up and surface oxidation can be crucial when testing both bulk materials and thin films. To expose the potential measurement errors caused by surface roughness, as well as the effect of porosity on the measurements, work was carried out on Cu, Sn and CuSn coatings with low density and rough surfaces.

Initially in next chapter, the effects of porosity and surface roughness on the mechanical properties measured by nanoindentation are explained. An analysis of the comparison of indentation data obtained from fully dense copper coatings and coatings with porosity is provided. Afterwards, the effects of surface roughness, grain size distribution and the indentation location on the obtained indentation results

are described. These analyses are of interest as the accuracy of indentation data is highly dependent on the surface morphology.

The variation in the obtained results between the porous coatings and fully dense materials are examined using the obtained load-displacement curves along with the corresponding AFM images. Moreover, the scatter within the obtained hardness and modulus values from a time dependent material, tin, for both thin film and bulk samples is analysed. Finally, a comparison between the obtained experimental data for porous coatings and the data obtained from the finite element analysis method using OOF2 are presented. The aim of this analysis was to understand the response of the material to the indenter without the influence of any factors such as pile-up, cracking, detachment and fragmentation of the surface.

## **Chapter 6. The Effect of Density and Surface Roughness on the Mechanical Properties Obtained from Nanoindentation**

*This section details the surface mechanical response obtained using the nanoindentation technique on bulk materials along with thin coatings. The effects of density and surface roughness on the mechanical properties obtained using the nanoindentation technique are described. The hardness and Young's modulus values obtained from low density materials with rough surfaces are compared to these of denser samples with smooth surfaces. The morphology and structure of samples were characterised using scanning electron microscopy and atomic force microscopy.*

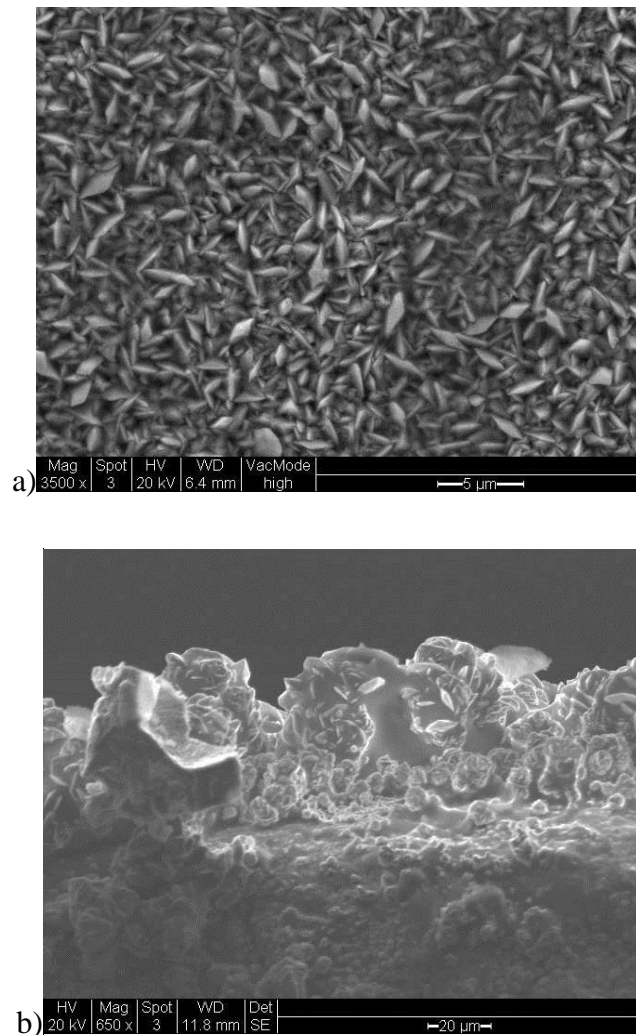
### **6.1 Nanoindentation Testing**

Over the past few years, the nanoindentation technique has been used to probe and identify the mechanical properties of solids (Doerner and Nix, 1986; Loubet *et al.*, 1986a). However, variations in the obtained hardness values in comparison to that of bulk properties have been reported at ultra-low loads and low penetration depths (Oliver *et al.*, 1986; Bhagavat and Kao, 2005). Recent developments of the nanoindentation technique and the use of nano-indenter probes to measure the topography of materials down to atomic scales using atomic force microscopy (AFM) have facilitated a better understanding of the scatter in the mechanical properties and materials behaviour at extremely low contact depths (Pollock *et al.*, 1986; Bobji and Biswas, 1999). The scatter of the nanoindentation results can be due to a surface chemical effect, the variation in the properties with depth, surface roughness, errors in the experimental data, indentation size effects and various other reasons (Yost, 1983; Zhang and Xu, 2002b; Voyiadjis and Peters, 2010). This chapter highlights the effect of sample density as well as surface roughness on the mechanical properties measured by nanoindentation.

### **6.2 Copper**

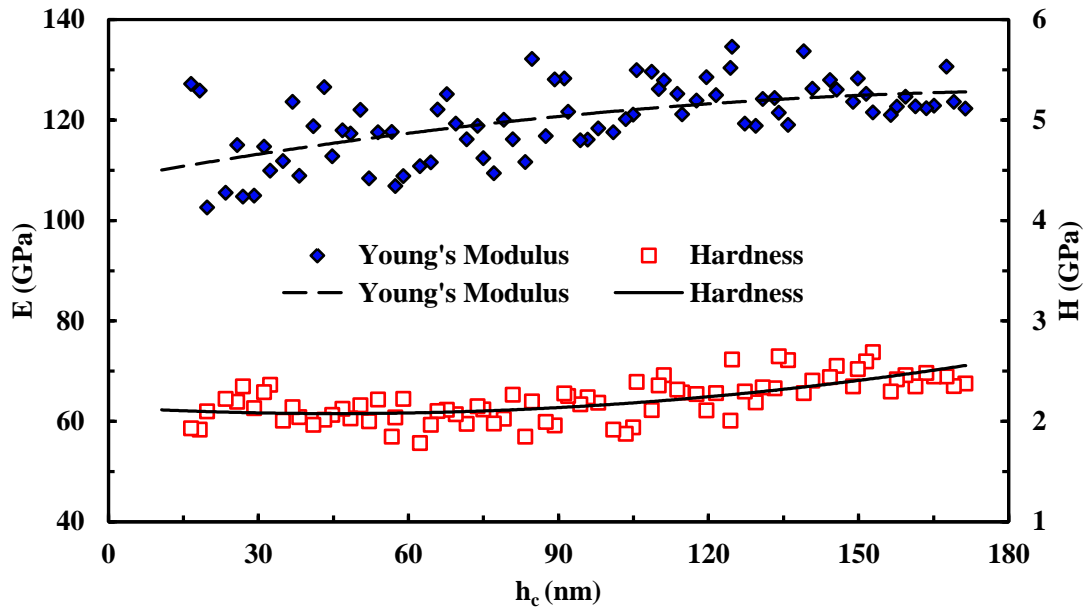
To investigate the effect of roughness on the hardness and Young's modulus data, work was carried out on Cu coatings deposited from a room temperature ionic liquid (RTIL) on a Cu substrate (referred to as a 'rough' surface in this section). A Cu substrate was chosen to minimise the effect of the substrate on the obtained results.

Figure 6-1 shows SEM images of the top and cross-sectional views of the deposited Cu which illustrates the surface roughness of the tested sample.



**Figure 6-1. SEM images of Cu deposited sample on Cu substrate using the RTIL technique (a) top view and (b) cross-sectional view.**

To compare the hardness and Young's modulus data for both the smooth and rough surfaces, sets of single indentations were initially performed in different locations on typical grains under displacement control. To understand the mechanical properties a bulk Cu with a mirror polished surface (referred to as a 'smooth' surface in this section) was used for comparison. Indentations were carried out in different displacements ranging from 10 to 170 *nm* under displacement control. The average roughness obtained from 10  $\mu\text{m} \times 10 \mu\text{m}$  AFM images for at least 10 different locations on the sample for the mirror polished Cu sample was approximately 0.4 *nm*. Figure 6-2 illustrates the hardness and Young's modulus values versus contact depth obtained from (111) bulk Cu having a smooth surface.



**Figure 6-2.** Comparison of nanoindentation tests performed on smooth surfaces of Cu samples showing the Young's modulus (left) and hardness (right) under displacement control.

As can be seen from Figure 6-2, both the hardness and Young's modulus values increase to some extent as the contact depth is increased. This is due to the effect of pile-up at larger depths. However, the obtained values are close to that of nanoindentation results for bulk Cu reported in literature (Draissia *et al.*, 2004; Pellicer *et al.*, 2012). Additionally, by reviewing the AFM images and also the load-displacement curves, a fixed displacement with minimum pile-up appearance was chosen. This can help to minimise the effects of pile-up and isolate the surface roughness effect on the obtained data. To measure the mechanical properties of Cu for both the rough and smooth surfaces under displacement control at the contact depth of 40 nm, 75 single indentations were performed as a line crossing the centre of the sample approximately 3 mm long. This can identify the differences between the indentations that were performed in a valley or on a peak using the load-displacement curves and the AFM images. Figure 6-3 compares the hardness and Young's modulus data obtained from the rough Cu coating with the smooth bulk Cu at a 40 nm contact depth.

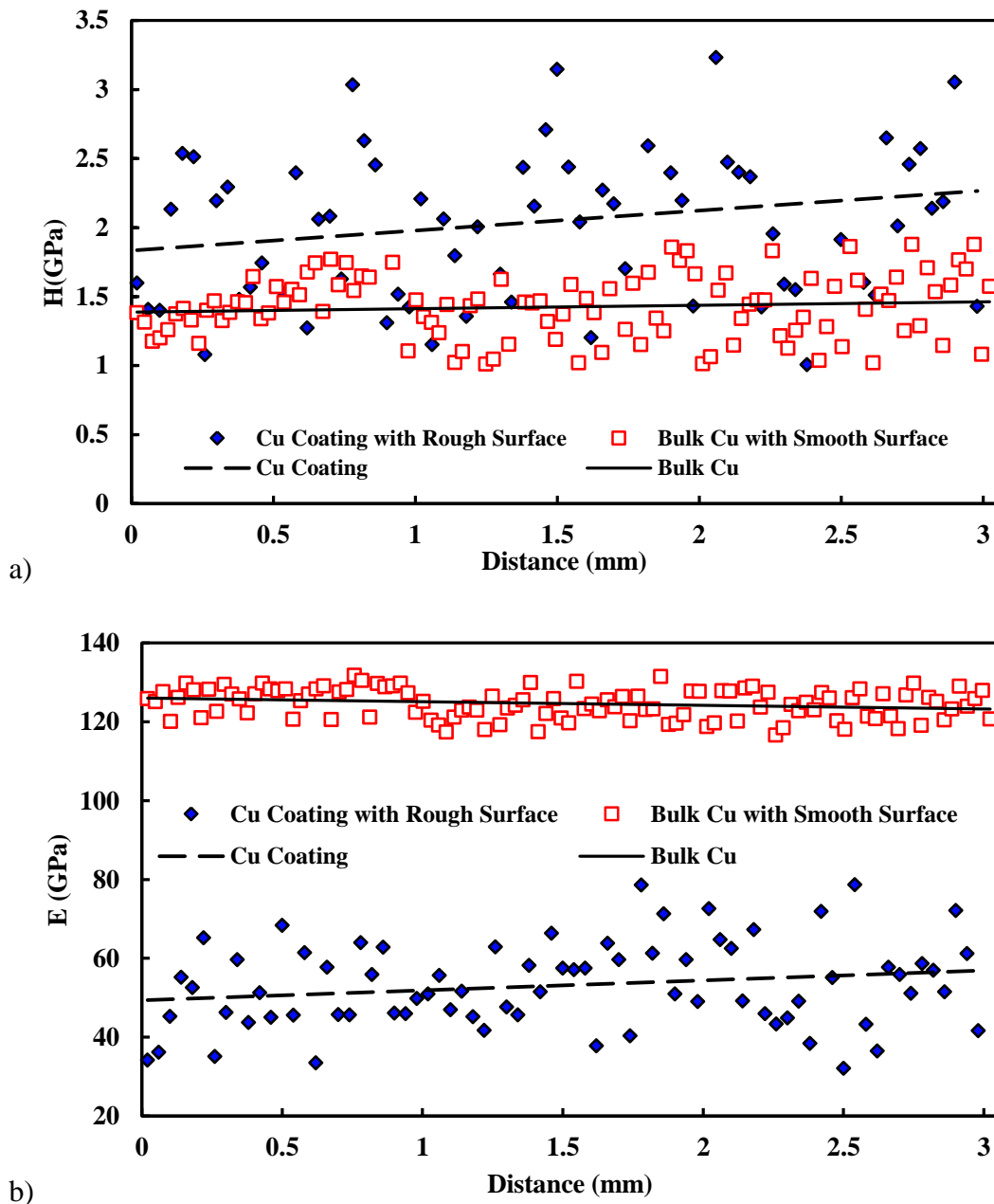


**Figure 6-3. Comparison of nanoindentation tests performed on smooth and rough surfaces of Cu samples showing (a) the hardness and (b) Young's modulus under displacement control at 40 nm contact depth.**

The hardness values obtained from the smooth surface are relatively constant at the same contact depth at  $1.4 \pm 0.2$  GPa. However, there is some scatter in the hardness results obtained from the Cu coating with a rough surface. The hardness data were sometimes overestimated and sometimes underestimated in comparison with the average values of 2.01 GPa with 0.7 GPa standard deviation, nearly three times greater than that of the smooth surface. The average contact modulus for the rough surface is  $54 \pm 14$  GPa which is about 43% lower than the smooth surface value of

124±4 GPa. To further investigate the roughness effect on the mechanical properties and explain the scatter in the obtained results from the rough surfaces, the AFM images were analysed in detail.

### 6.2.1 Potential Issues of Indentation Location

Prior to analysing the AFM images, potential issues of the indentation location such as grain size and its distribution, grain boundaries and surface pores were expected to have an effect on the mechanical properties as shown in Figure 6-4.

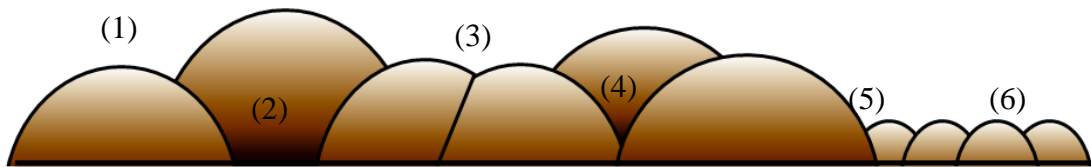


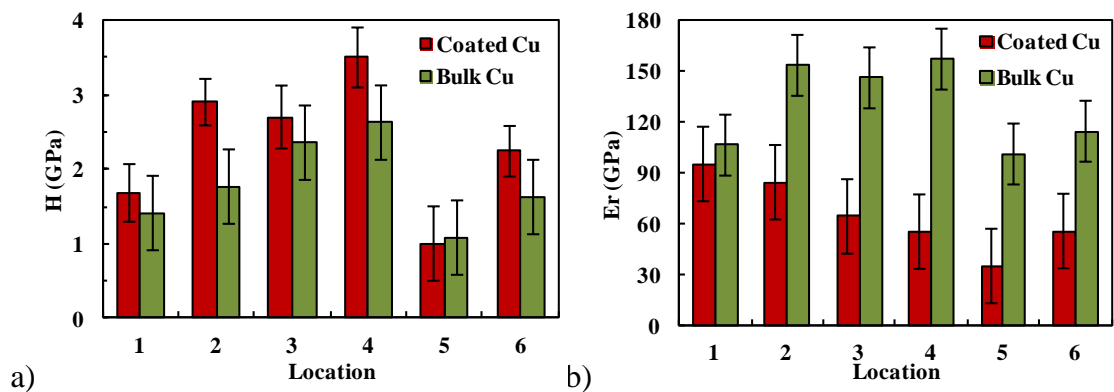
**Figure 6-4. Diagram of a rough surface with various grain sizes illustrating different numbered locations at which the indenter can be seated during an indentation test.**

It is known that materials such as Cu contain a diverse range of grain sizes. As mentioned in Chapter 5, grain size and distribution as well as texture can have a significant effect on the observed hardness and modulus values. Also with regards to the surface roughness effect on the obtained mechanical properties, the location at which the indentation takes place can also cause significant variation. Figure 6-4 shows some examples of the different locations at which the indenter can be seated during the indentation test. It should be noted that this diagram gives an idea about a hypothetical sample with a rough surface containing a range of different grain sizes possessing some surface. If during the indentation test the indenter sits on location number (1) and the combined size of the indenter and the indentation size are smaller than that of the grain size, the obtained hardness and modulus values depend on the single grain and its preferred orientation. Alternatively, if the indentation takes place in locations similar to number (5) or (6) the obtained values are subject to multiple grain effects. However, according to Vlassak and Nix (Vlassak and Nix, 1994), it is important to consider that the size and shape of the elastic zone around the indentation area, as well as the stress state produced by indentation, varies strongly and depends on the position at which that indentation takes place. Consequently, the obtained modulus values are the average of the different effective crystal orientations (Armstrong *et al.*, 2009). Additionally, another important factor which can influence

the obtained mechanical properties (particularly the hardness) is the porosity of the sample. The mechanical properties calculated from the Oliver and Pharr method rely on the measured contact area which can vary due to the porosity. The size of pores and the density of the sample can have a considerable influence on the observed data. As an example, locations such as (2) at which the pores on the surface of the sample are bigger than the indenter can have different effects on the hardness and modulus values observed from location (4), which shows smaller pores on the surface. To support these hypotheses, the AFM images collected from the sample surface before and after indentation tests were analysed.

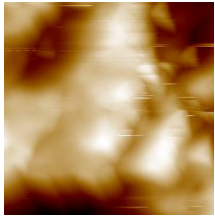
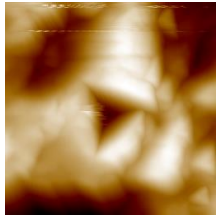
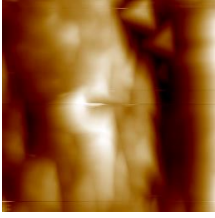
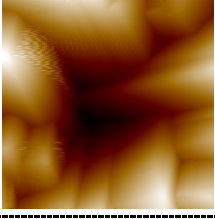
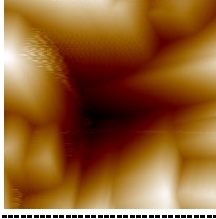
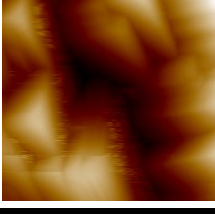
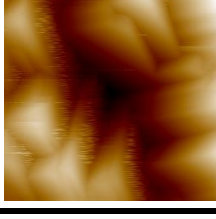
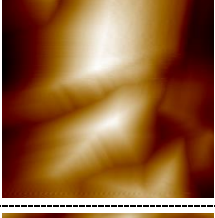
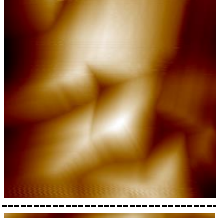
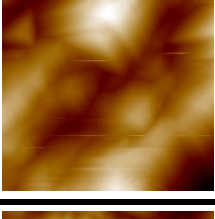
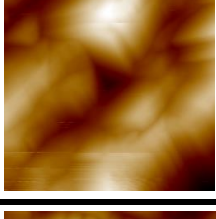
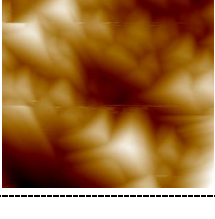
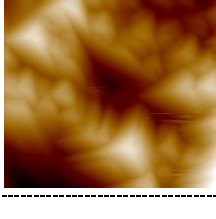
### 6.2.2 AFM Image Analysis

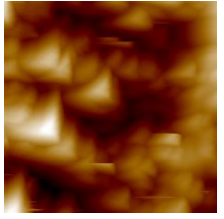
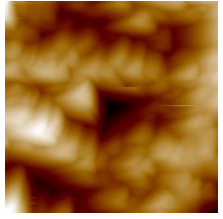
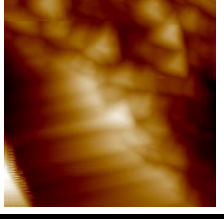
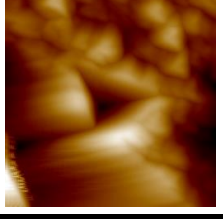
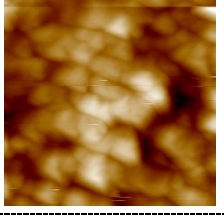
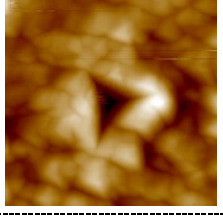
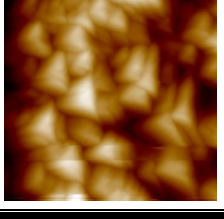
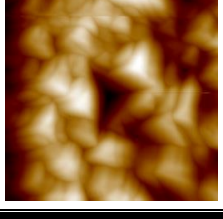
To compare the effect of roughness on the mechanical properties, two Cu samples, bulk Cu and deposited Cu, were examined. The distribution of the average values of the hardness and Young's modulus obtained from different areas on the two Cu samples with rough surfaces is shown in Figure 6-5. It can be seen that there is considerable variation in the obtained values between different areas when using the same indentation conditions. Each location number refers to the position shown in Figure 6-4 for comparison.



**Figure 6-5. Distributions of the (a) hardness and (b) Young's modulus values obtained from bulk and coated Cu with rough surfaces for different locations at which the indenter tip can be seated.**

Table 6-1 shows various AFM images that were obtained over  $5 \mu\text{m} \times 5 \mu\text{m}$  areas from the bulk (111) Cu with a rough surface and compares the hardness and Young's modulus values for the different locations shown in Figure 6-4.

Locations	AFM Images		E(GPa)	H (GPa)	h <sub>c</sub> (nm)	P (μN)
	Before Indentation	After Indentation				
(1)			106	1.30	132	919
			106	1.52	120	924
(2)			142	1.75	110	922
			163	1.78	108	922
(3)			148	2.33	91	926
			143	2.38	90	927
(4)			176	3.12	75	929

			136	2.13	96	924
(5)			98	1.16	141	914
			103	1.00	155	913
(6)			111	1.75	110	922
			116	1.55	118	920

**Table 6-1. Comparison of hardness and Young's modulus values obtained from different locations on the rough Cu surface.**

When the results for different locations were compared using the AFM images shown in Table 6-1, it was found that when the indentation takes place on a single, large mound-like grain, both the hardness and modulus values are lower than for the other areas. For example, location number 1 has the lowest values. This was also true for the location number 5, and although there are small grain contributions in the obtained values, the larger grain acts like a single grain and takes more of the indentation impression. However, in contrast the higher hardness and modulus values were obtained when the indentation occurred within a hole such as location numbers 2 and 4. It was also found that when the indentation was carried out on a number of grains that are smaller than the indentation size, the hardness and modulus values are

closer to that of the smooth surface results with less variation, such as location number 6. Locations such as that shown in number 3 can be assumed as both grain boundary effect and small hole as the grains around the indentation are higher than the indented area therefore the high hardness and modulus values can be explained by both the contact area effect and grain boundary energy. Therefore, the results can be explained by the variation of the true contact area.

During the indentation tests on the rough surfaces, there are two possible locations at which the indentation can take place: on a peak or in a valley. Figure 6-6 illustrates these two locations at which indentation can take place as well as a smooth normal surface for comparison.

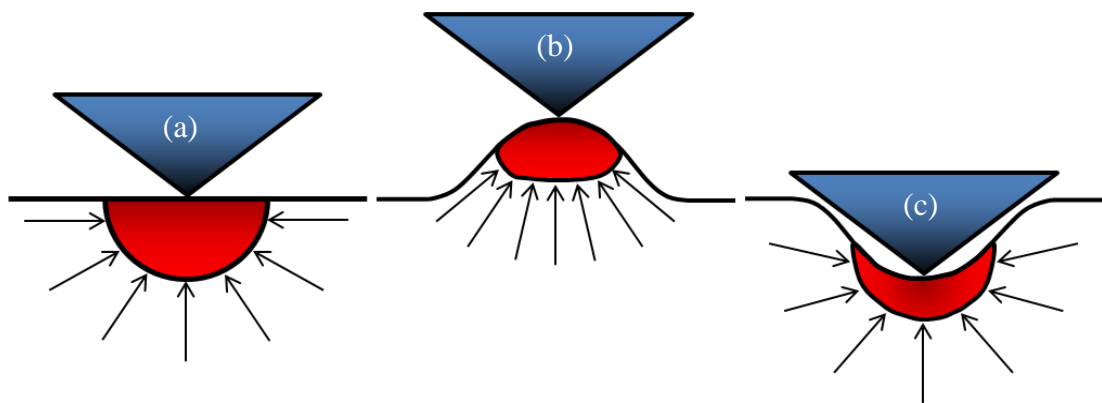


**Figure 6-6. Schematic representation of the stress produced at the contact point between the indenter and sample for (a) normally constrained contact surface, (b) reduced constraint on a peak and (c) increased constraint in a valley.**

If the indentation takes place on a peak Figure 6-6 (b), the localised stress at the contact point between the tip and the sample surface will be increased due to the non-uniform contact area. This implements high contact depths at lower loads and so the calculated hardness will be lower than the true hardness value. On the contrary, if the indentation takes place in a valley Figure 6-6 (c), the calculated hardness will be higher than the true value since the determined contact area is lower than true contact area. Furthermore, the variation on the modulus can be explained by the anisotropy of Cu. It is known that Cu is an anisotropic material and contains combinations of orientations. Therefore, each individual grain, depending on its crystallographic orientation, can have a different Young's modulus value (Armstrong *et al.*, 2009). Consequently, the obtained values can vary even at the same surface feature due to

effects from the grain orientation, grain boundary and its distribution as well as the elastic zone and stress state under the indentation test.

The distribution shown in Figure 6-5 also confirms that the average hardness and modulus results vary in a similar manner for both the bulk and coating Cu samples. The average hardness and modulus values obtained from (111) bulk Cu having rough and relatively smooth surfaces and also the results obtained from rough Cu coating with a smooth thin film (non-annealed Cu thin film) are shown in Table 6-2.

Cu Samples		H (GPa)	E (GPa)
Smooth	Bulk	1.4±0.2	124±4
	Thin Film	1.7±0.3	115±3
Rough	Bulk	2.19±0.6	121±21
	Coating	2.01±0.4	59±14

**Table 6-2. Average hardness and modulus values obtained from Cu samples with smooth and rough surfaces.**

A comparison of the average modulus values between the rough and smooth bulk Cu shows that the scatter in the results obtained from the smooth surface is considerably smaller than the rough surface and shows around a 17% decrease in standard deviation. However, comparing the results between the two Cu coatings demonstrates that the modulus of the smooth surface is about twice as large as the rough surface with porosity in the sample. There is therefore an additional key factor that needs to be considered with regards to the Cu coatings obtained from RTIL other than the roughness; the nucleation density of the tested sample which can have a significant effect on the observed hardness and modulus data since it leads to porosity within the coating.

The expected coating thickness for the Cu samples using RTIL method for deposition was around 15  $\mu\text{m}$ , however the thickness measurements from the SEM images shows that the coatings are 35±5  $\mu\text{m}$  thick which is approximately twice the expected value. The obtained SEM images and the AFM images show that the density of the coated surface varies from point to point. These images also confirmed that the Cu coatings have a lower density that of the bulk material due to the presence of pores. To further investigate the effect of the density on the obtained

mechanical properties, the load-displacement curves were analysed. Figure 6-7 illustrates two typical load-displacement curves at high loads obtained from a dense bulk Cu and the deposited Cu coating with a lower density.

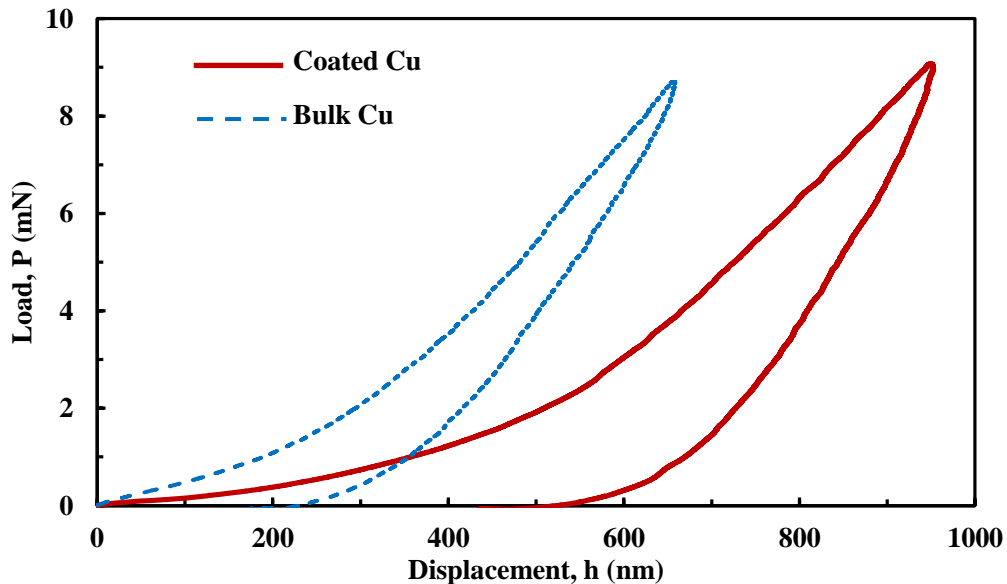


**Figure 6-7. Load-displacement curves obtained under nanoindentation tests on dense bulk Cu and deposited low density Cu on Cu substrate.**

As can be seen from the load-displacement curve obtained from the Cu coating, there is a low rate of load increase at the beginning of the loading below the contact depth of 400 nm and this rapidly increases towards the end. This behaviour shows that the indenter is in contact with a soft layer at the surface which becomes harder or stiffer as the indentation process proceeds. The displacement difference between the two curves in Figure 6-7 can be explained by an initial densification of the coating followed by measurement of a dense material. In the early stages of loading, the roughness and porosity under the indenter collapse causing the aforementioned densification and then dense material behaviour is observed. This is due to the low initial density of the coating which can be observed from the SEM image shown in Figure 6-1.

### 6.3 Tin

To identify the effects of density as well as roughness, further investigations were carried out on bulk Sn samples and also Sn coatings with relatively smooth and rough surfaces. Initially the work was carried out on a pure bulk Sn sample to identify the potential issues such as creep that can have an effect on the obtained

mechanical properties. Figure 6-8 shows the hardness and Young's modulus values of 99.9% pure bulk Sn with a smooth surface obtained from 40 single indentations under displacement control.

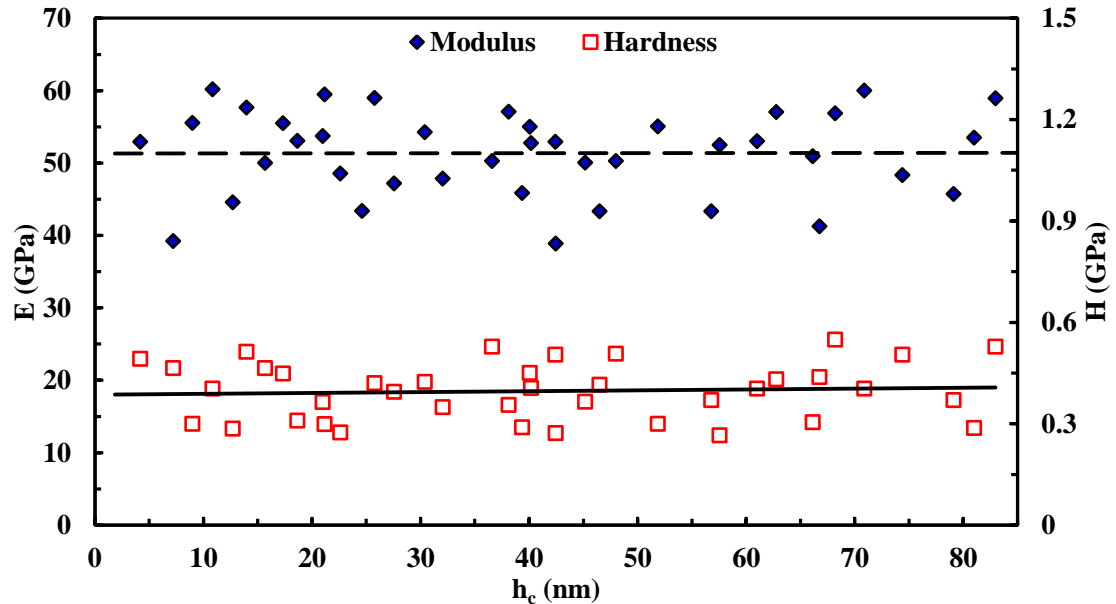


**Figure 6-8. Nanoindentation test results performed on bulk Sn, Young's modulus (left) and hardness (right) with smooth surface under displacement control.**

The average hardness and Young's modulus values obtained from the smooth bulk Sn with high density are  $0.4 \pm 0.1$  and  $51 \pm 6$  GPa respectively. The average Young's modulus value is in agreement with the data reported in literature for bulk Sn at around 47 GPa (Howatson *et al.*, 1972; Li *et al.*, 2012) and nanoindentation test results reported by Sahin *et al.* (Sahin *et al.*, 2008). There is however some scatter in both the hardness and modulus values but this is within a reasonable error margin for the nanoindentation tests. One of the most important factors that needs to be considered during the nanoindentation tests for soft metals with time dependent behaviour and low melting point such as Sn is creep. At the beginning of the unloading process of the indentation test, the penetration depth can increase as a result of creep. As the Oliver and Pharr analysis method is highly dependent on the unloading sections of the load-displacement curves, any change in the displacement can therefore have an influence on the hardness and modulus values. To verify that the data was not affected by creep, two tactics were used. Firstly, the work was carried out under displacement control with a quick holding period at the maximum load. Secondly, after the indentation tests, all of the load-displacement curves were

analysed to identify any potential creep effect on the initial part of the unloading curves. It should be noted that if creep is obvious, there is a noticeable nose at the beginning of the unloading curve. Figure 6-9 shows three different load-displacement curves obtained under open loop mode and displacement control.

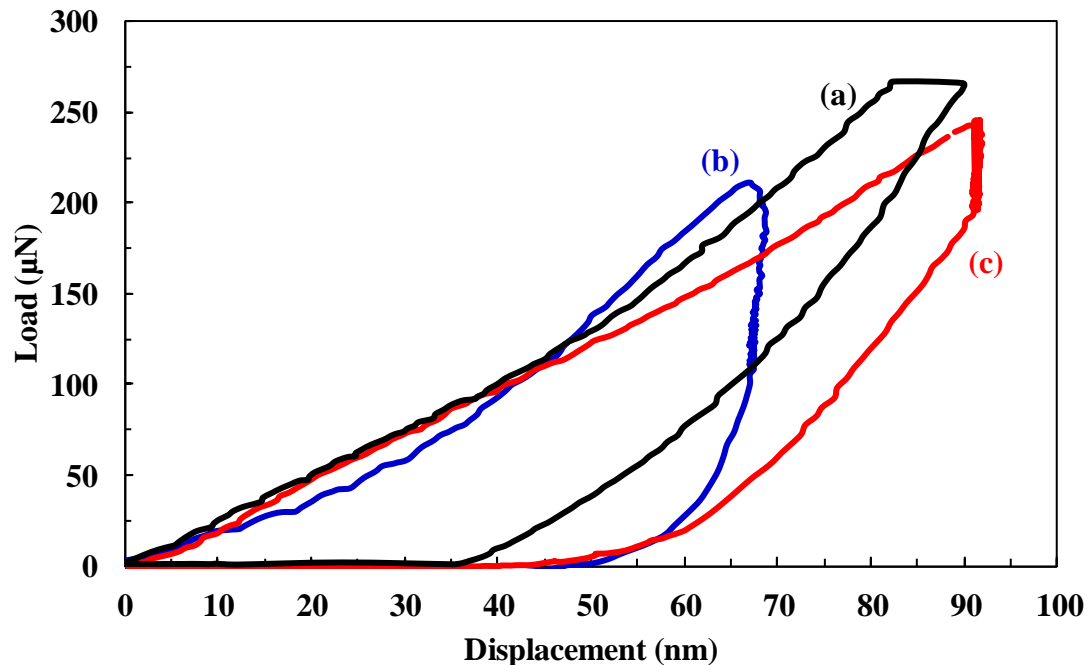


**Figure 6-9. Load-displacement curves obtained from bulk Sn sample under (a) open loop mode without appearance of nose due to the creep, (b) open loop mode with appearance of nose due to the creep and (c) displacement control.**

As can be seen, the load-displacement curve for the displacement control protocol shows no nose in the initial part of the unloading curve and also there is no change in the displacement due to the holding period at the maximum load; for this reason, displacement control was used in this part of the work. However, open loop mode shows an obvious nose at the beginning of the unloading curve due to the creep. To minimise the creep effect on the open loop mode, the rate of the indentation loading and unloading should be chosen correctly and also a sufficient holding period at maximum load is required. Creep and its effect on the mechanical properties obtained from nanoindentation tests will be discussed in more detail in Chapter 7. Finally, the power-law fitting was set between the 20% lower fit and 95% upper fit boundaries to minimise the effect of creep on the calculated results.

To further study the effect of roughness as well as coating density on the mechanical properties, the tests were carried out on two Sn coatings with different densities and

surfaces roughness. To avoid any substrate effect on the obtained results both the coatings were deposited on a Cu substrate. Initially the tests were carried out under displacement control by indenting 200 single indentations in different displacements, ranging from 1 to 85 *nm* on a smooth and dense Sn coating. This test was applied to identify the differences between the bulk Sn and thin coated Sn at different depth ranges. The hardness and modulus values obtained from the nanoindentation tests for the film with high density are shown in Figure 6-10.

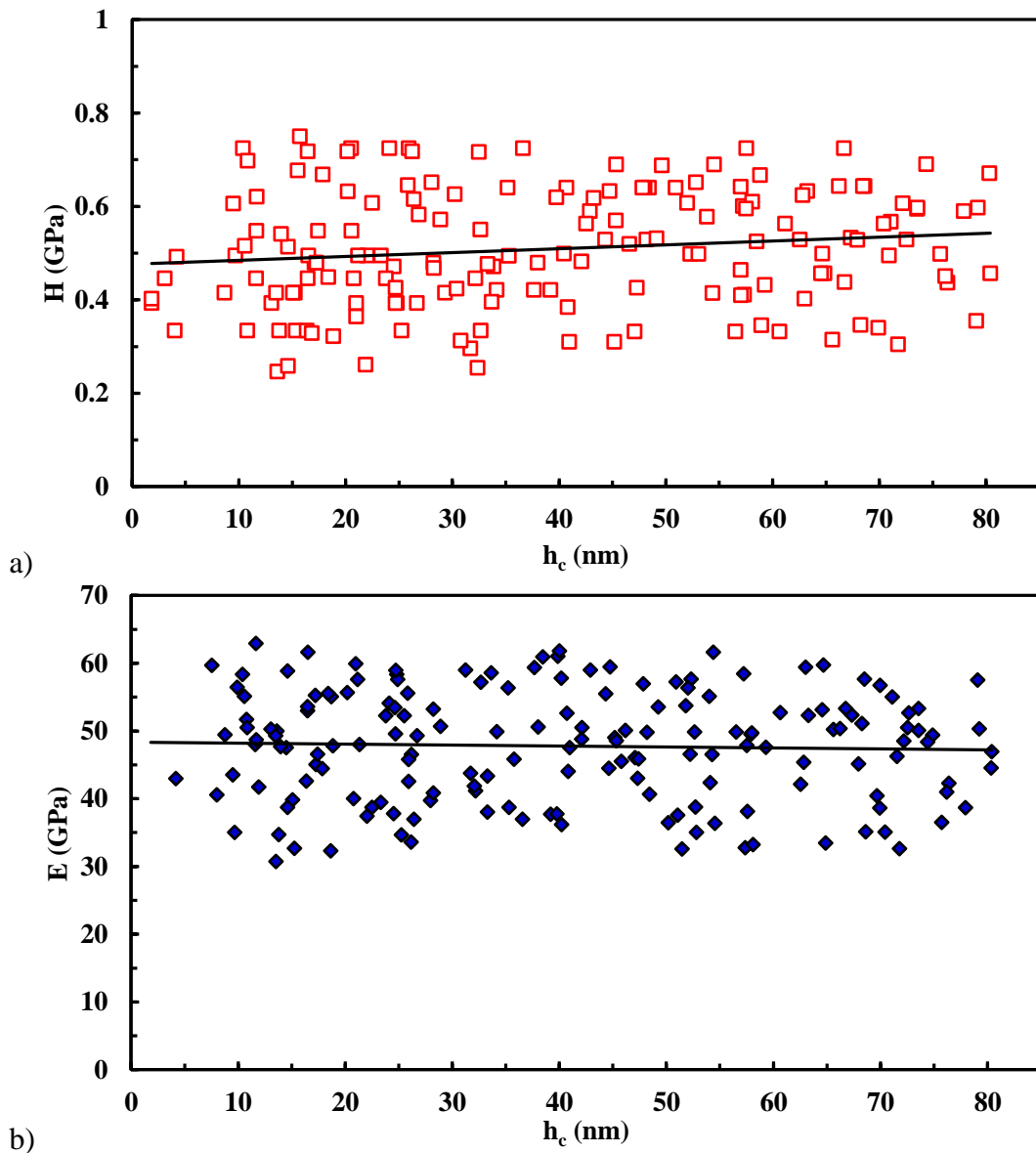


**Figure 6-10. Nanoindentation test results showing (a) the hardness and (b) Young's modulus performed on a dense Sn coating with smooth surface under displacement control.**

The average hardness and contact modulus values obtained from the nanoindentation tests shown in Figure 6-10 are  $0.5 \pm 0.1$  and  $47 \pm 8$  *GPa* respectively. For comparison, the average hardness value obtained from nanoindentation tests is approximately the same for both the coated and bulk Sn samples with a small increase from  $0.4$  *GPa* for the bulk sample to  $0.5$  *GPa* for the dense Sn coating. However, the average modulus value decreases from  $51$  *GPa* for the bulk sample to  $47$  *GPa* for the Sn coating.

To compare the mechanical properties of the coatings with high and low density and also to determine the effect of roughness on the soft metals like Sn, further work was carried out on the Sn coating with a low density. The cross-sectional and top view SEM images obtained from the rough Sn coating with low density are shown in Figure 6-11.

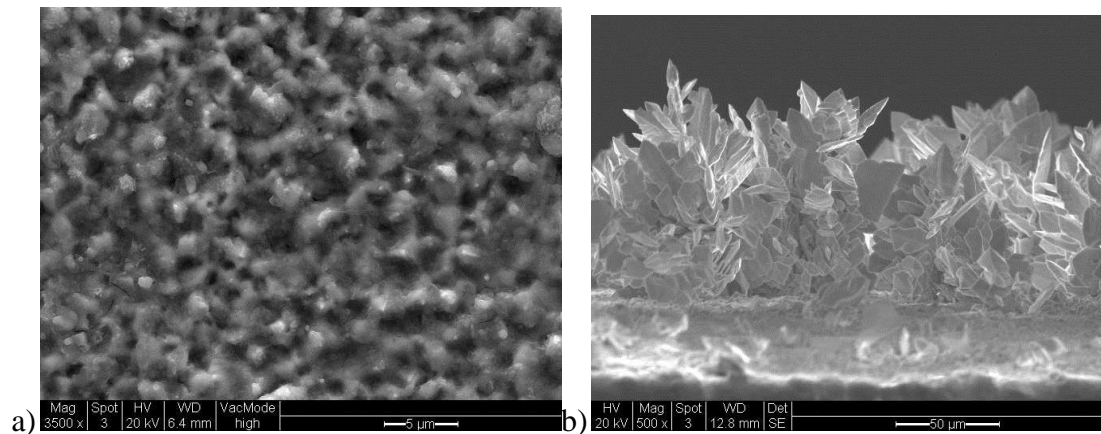


**Figure 6-11. SEM images from the Sn coating on a Cu substrate (a) top view and (b) cross-sectional view.**

The SEM images shown in Figure 6-11 illustrate that the sample has low density and that the surface of the sample is occupied by pores. If the coatings were dense, the thickness of the deposition was expected to be  $11$   $\mu\text{m}$ . However, the SEM images as well as the light microscopy analysis confirm that the average deposition thickness is  $35 \pm 10$   $\mu\text{m}$  which is approximately 3 times more than the expected value. The hardness and modulus values obtained from the nanoindentation tests for the low density Sn coating using displacement control under the same conditions as the high density film are shown in Figure 6-12.

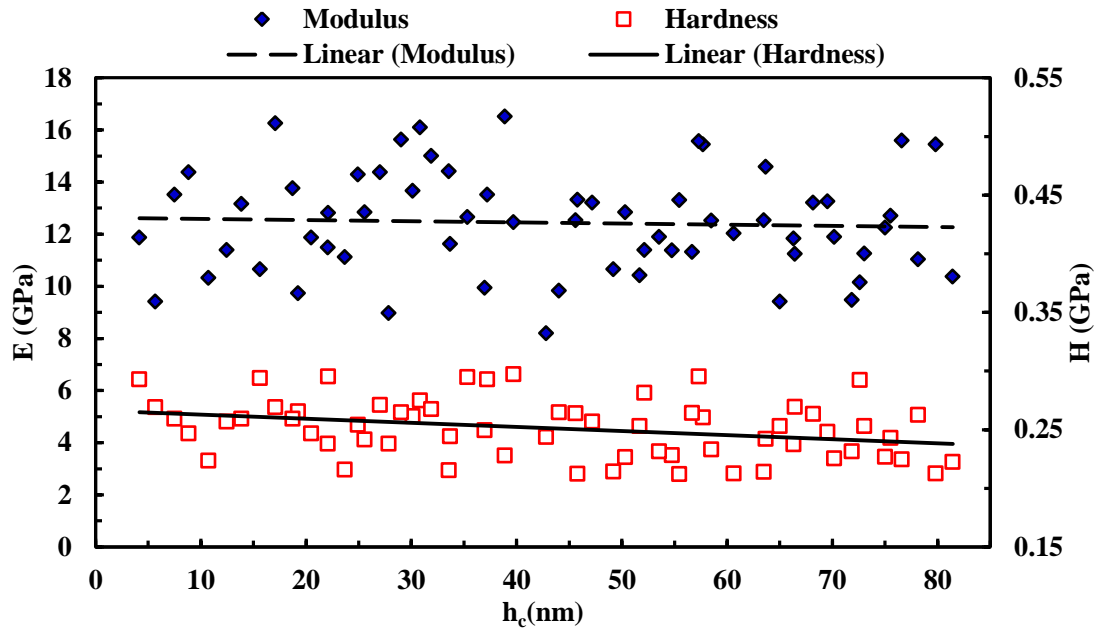


**Figure 6-12.** Nanoindentation test results showing the Young’s modulus (left) and hardness (right) performed on low dense Sn coating with rough surface under displacement control.

The average hardness and modulus values for the Sn coating with low density are  $0.25\pm0.05$  and  $12\pm3$  GPa respectively. The modulus value is approximately 25% of the value observed from both the bulk Sn and the thin Sn film with high density. Table 6-3 compares the hardness and modulus results of the three different types of Sn sample used in this study.

Sn Samples		H (GPa)	E <sub>r</sub> (GPa)
Smooth	Bulk	$0.4\pm0.08$	$51\pm6$
	Thin Film	$0.5\pm0.1$	$47\pm8$
Rough	Coating	$0.25\pm0.05$	$12\pm3$

**Table 6-3.** Nanoindentation test results obtained for Sn samples.

The mechanical property values obtained for the Cu and Sn coatings deposited using the RTIL method are roughly 50% and 30% of the obtained Young’s modulus results for thin films under the same nanoindentation test condition respectively. This shows that the density of the sample as well as the roughness can have a significant effect on the mechanical properties. As it is known, there are numerous different factors that can fundamentally influence the obtained mechanical properties, but it is clear that the porosity in the coatings is controlling the measured behaviour.

## 6.4 Copper-Tin Coating

To further investigate the effect of density and the relationship between the mechanical properties and density, work was carried out on the Cu-Sn coatings with different densities. The first set of experiment was carried out on the Cu-Sn coating deposited from a RTIL on two different substrates; stainless steel and Cu. The approximate thickness of the samples calculated using the current flow during the deposition process for both the coatings was around  $12\ \mu\text{m}$ . However, the average thickness of the coatings measured with SEM image analysis was found to be  $24\pm 4\ \mu\text{m}$ , which confirms that the density of the coatings is lower than the predicted value. The SEM image obtained from the Cu-Sn alloy deposited on the stainless steel substrate is shown in Figure 6-13.

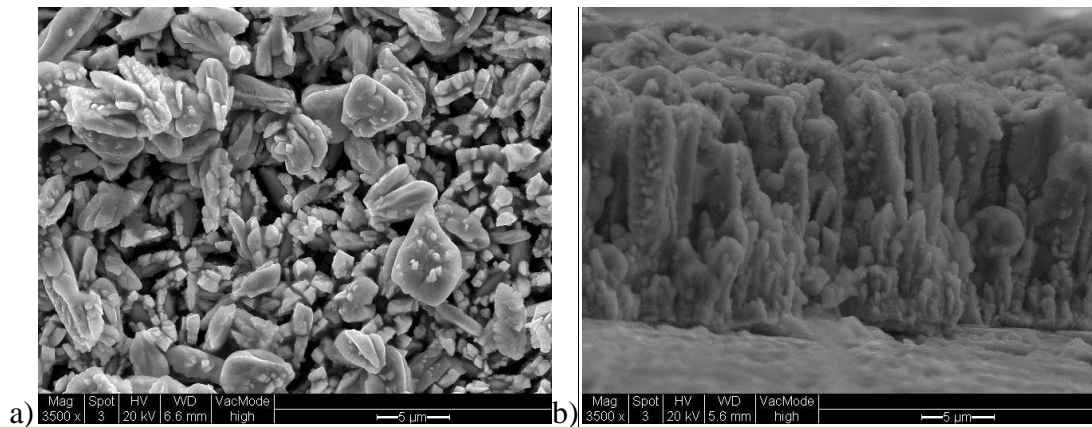


**Figure 6-13.** SEM images obtained from the Cu-Sn alloy showing the density and also the thickness of the coating (a) top view and (b) cross-sectional view.

The SEM images for the Cu-Sn coating confirm that, there are large pores on the surface of the sample. Moreover, there are some smaller holes or pores beneath the surface. To study the effect of the density in addition to the porosity of the sample on the mechanical properties, the nanoindentation test was carried out under open loop mode. The test was set using a force ranging from  $0.1\ \text{mN}$  to  $10\ \text{mN}$ . The hardness and modulus data obtained from Cu-Sn coatings on both Cu and stainless steel substrates under the open loop mode are shown in Figure 6-14.

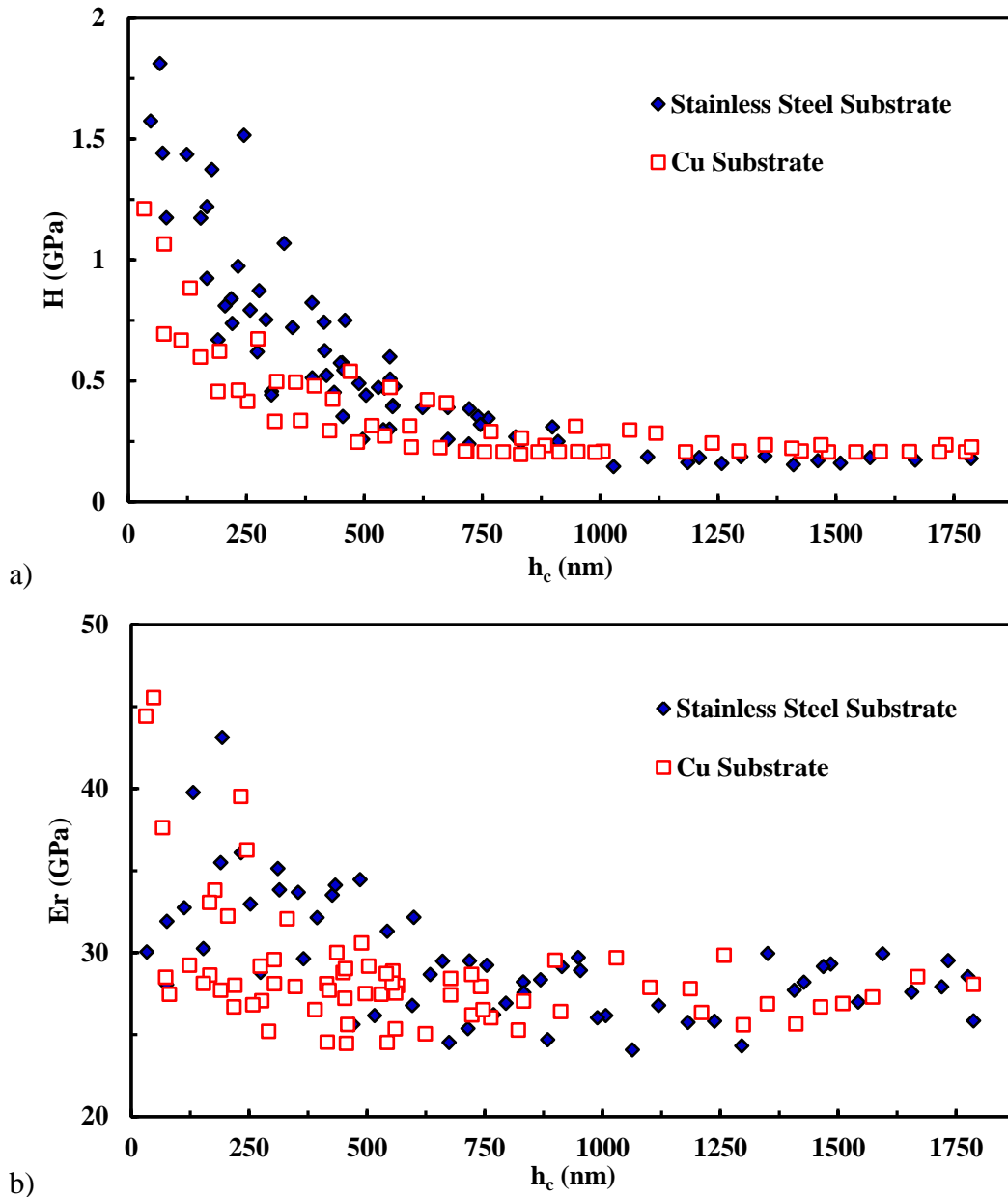


**Figure 6-14.** Nanoindentation test results showing (a) the hardness and (b) contact modulus performed on Cu-Sn coatings on Cu and stainless steel substrates under open loop mode.

The results obtained from both samples in Figure 6-14 (a) illustrate that the hardness value decreases while the contact depth increases. There is some scatter in the obtained hardness values for the depths lower than 600 nm which is  $1.1 \pm 0.15$  GPa. However, for the contact depth greater than 600 nm the obtained hardness values are relatively constant at  $0.2 \pm 0.05$  GPa. As can be seen from Figure 6-14 (b), there is also some scatter in the obtained modulus results. The average modulus value from the open loop mode on both substrates is  $26 \pm 6$  GPa. As confirmed previously by the SEM image shown in Figure 6-13, there are some holes or pores in the coatings. The

obtained AFM images confirm the hypothesis that the porosity on the surface has a significant role in affecting the obtained mechanical properties.

#### **6.4.1 AFM Images and Load-displacement Curves Analysis**

When analysing the nanoindentation test results, there are some other factors that need to be considered. Crack growth, fragmentation and detachment of the coating are some of the important factors that can cause the scatter in the data. To discover the major cause of the large scatter in the obtained modulus data for Cu-Sn coatings, the AFM images as well as the load-displacement curves were analysed.

Figure 6-15 shows an example of the AFM images before and after an indentation test with the associated load-displacement curve obtained from the same test for a Cu-Sn coating under open loop mode. The AFM images shown in Figure 6-15 (a) and (b), which were obtained before and after nanoindentation test respectively, illustrate that there are three cracks indicated after indentation on the coating at all three corners of the Berkovich indenter. Moreover, the load-displacement curve obtained from the same indentation shown in Figure 6-15 (c) exhibits two discontinuities known as ‘pop-in’ during the loading part of the curve. The shape of the load-displacement curve depends on the geometry of the tip, and the elastic and plastic flow behavior of the material.

Usually for brittle materials pop-in occurs due to the generation of dislocations during the nanoindentation test. However, if pop-in occurs at the beginning of the loading part of the load-displacement curve, which occurs mostly for metals, it can be explained by the indenter breaking through the native oxide layer on the surface (Navamathavan *et al.*, 2008).

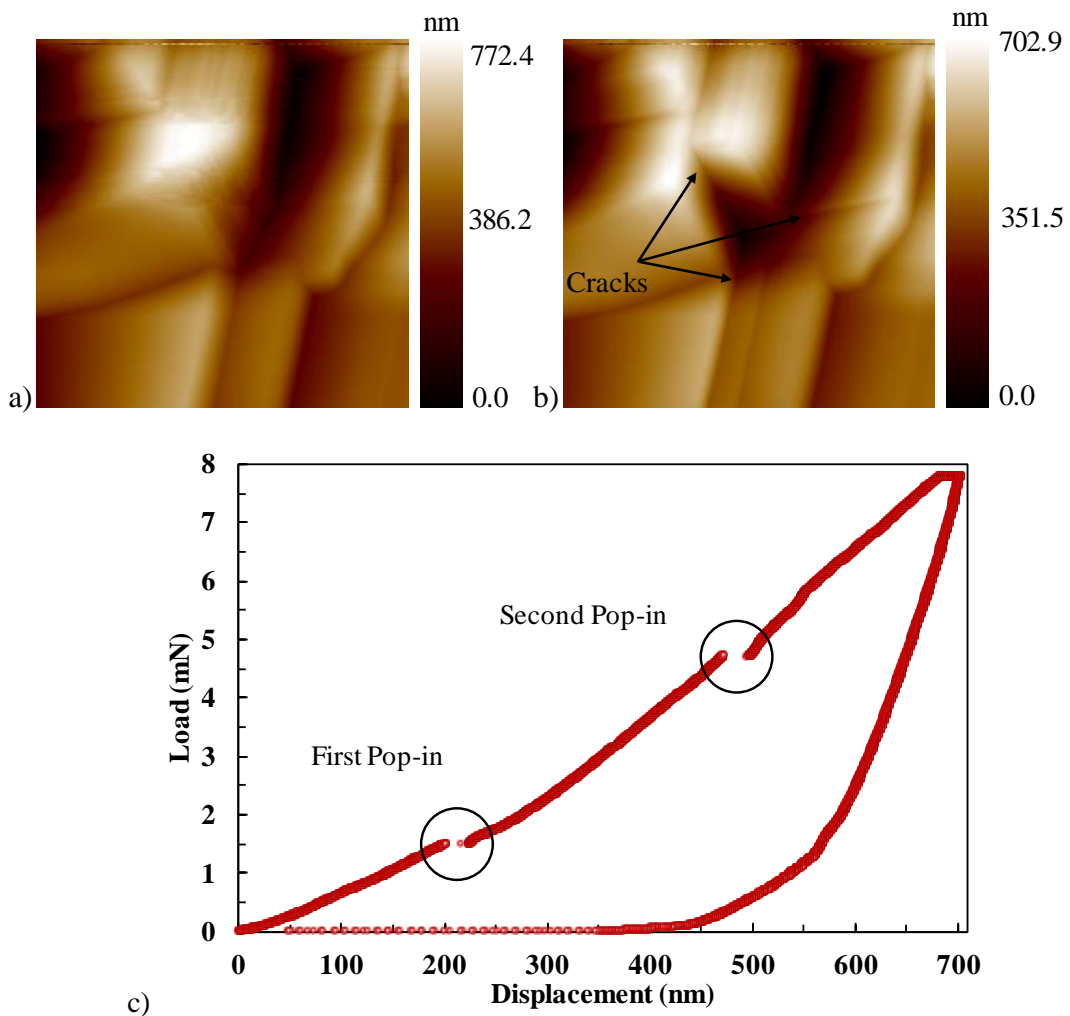


**Figure 6-15.** AFM images obtained from Cu-Sn coating (a) before and (b) after a nanoindentation test as well as (c) load-displacement curve.

In this case illustrated in Figure 6-15, the first pop-in took place at a contact depth of 200 nm with a load of around 1.5 mN and the secondary pop-in occurred when the load was around 4.7 mN, at a contact depth of 470 nm. These discontinuities on the load-displacement curve indicate that the cracks grew in a stepwise manner during the loading part of the indentation cycle (Jungk *et al.*, 2006). The combination of the load-displacement curve shape and the AFM image corroborate the appearance of several cracks during the indentation cycle. Crack growth on the coating surface and roughness of the surface mutually can both influence the obtained mechanical properties. Table 6-4 shows a series of indentation tests into the Cu-Sn coating under open loop mode at various applied load ranges. Each load-displacement curve and the associated AFM images obtained from the same indentation test are shown in the same row of the table.

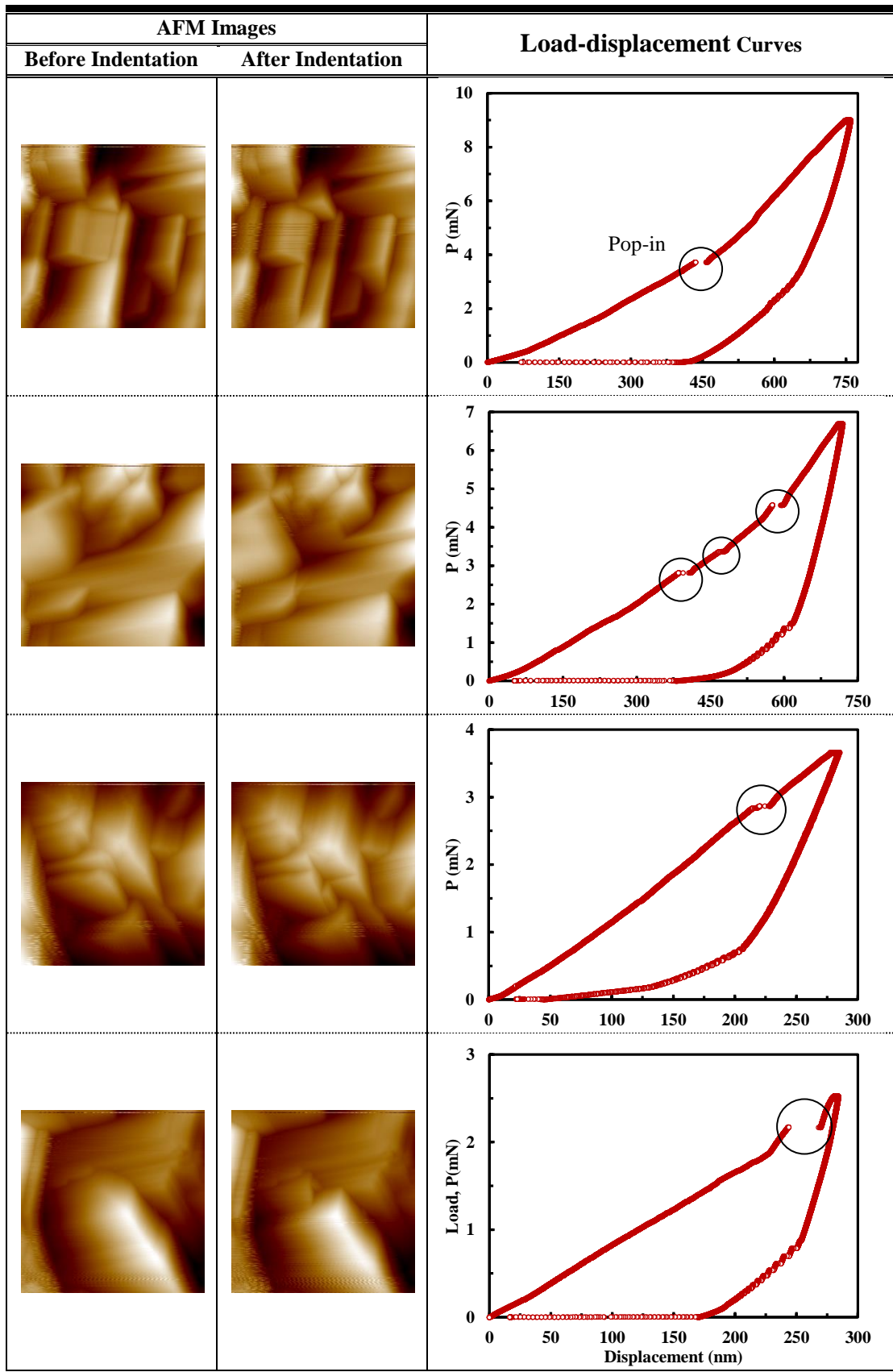
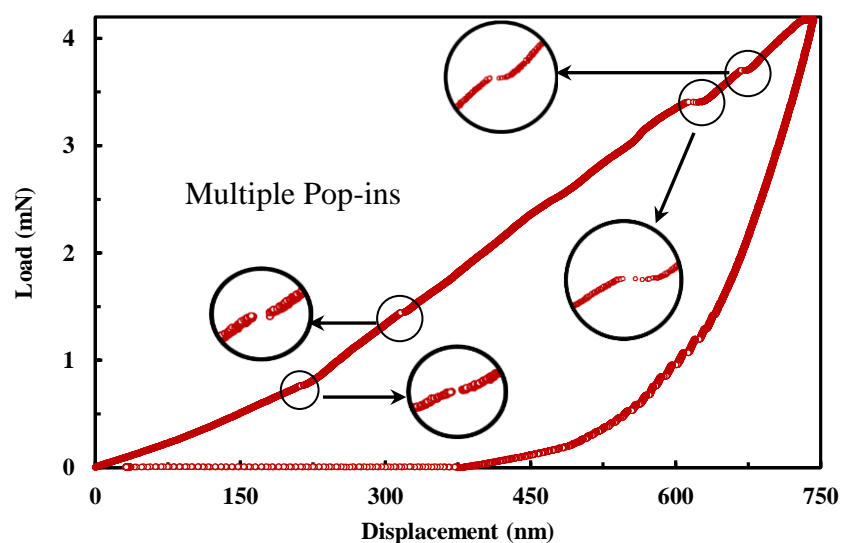
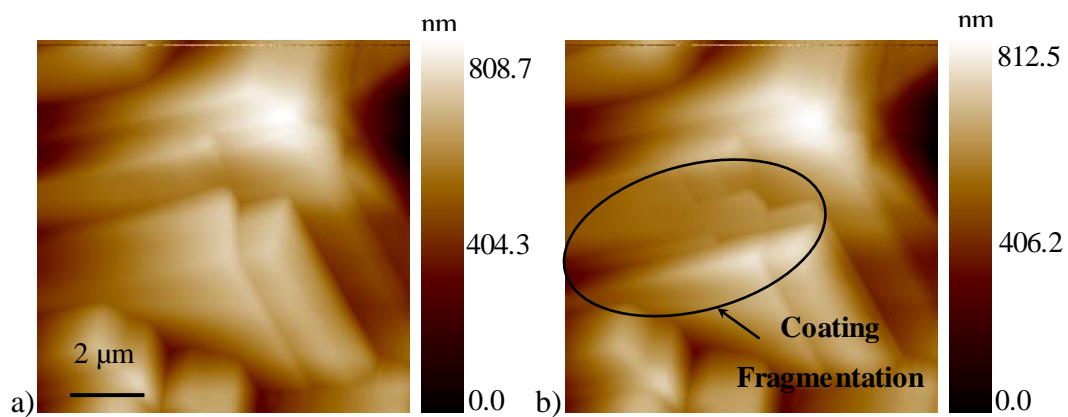


Table 6-4. The AFM images and load-displacement curves obtained from Cu-Sn coatings. The large circles in the load-displacement curves correspond to the pop-in phenomena.

As can be seen from load-displacement curves, the numbers of discontinuities as well as width of the pop-ins are different for each individual indentation test. This can be due to the grain size effect or, in the single grains, it can be due to the local interaction between dislocations and grain boundaries. Clearly from the AFM images and the shape of the load-displacement curves shown in Table 6-4, the roughness of the surface and porosity of the coating, along with crack growth, control the observed hardness and modulus data and can cause the variation in the results.

In addition to crack growth during the nanoindentation test, pop-in can emerge due to fragmentation of the coating. Figure 6-16 shows an example of an indentation test with coating fragmentation. The AFM image obtained after the nanoindentation test shown in Figure 6-16 (b) indicates that during the indentation cycle, part of the coating was detached.



c)

**Figure 6-16.** AFM images (a) before and (b) after indentation as well as (c) the load-displacement curve obtained from the Cu-Sn coating.

Moreover, the obtained load-displacement curve shows multiple pop-ins during the loading part of the indentation cycle. The loading curves obtained from Cu-Sn coatings at a displacement lower than about 200 nm are linear and there is no evidence of discontinuity or pop-ins. Subsequently the curves show pop-in behaviour when the loading section of the curve is at greater displacements. In the unloading part of the load-displacement curves the variations in the last part of the curves prior to complete unloading are due to elastic recovery. This type of behaviour is often enhanced by the detachment of the coating (Chen and Bull, 2011).

As the load-displacement curves obtained from open loop mode for Cu-Sn coatings are linear at the contact depths lower than 200 nm, the test was carried out under displacement control for the displacement range of 200 to 5 nm. The obtained hardness and modulus values under displacement control are shown in Figure 6-17.

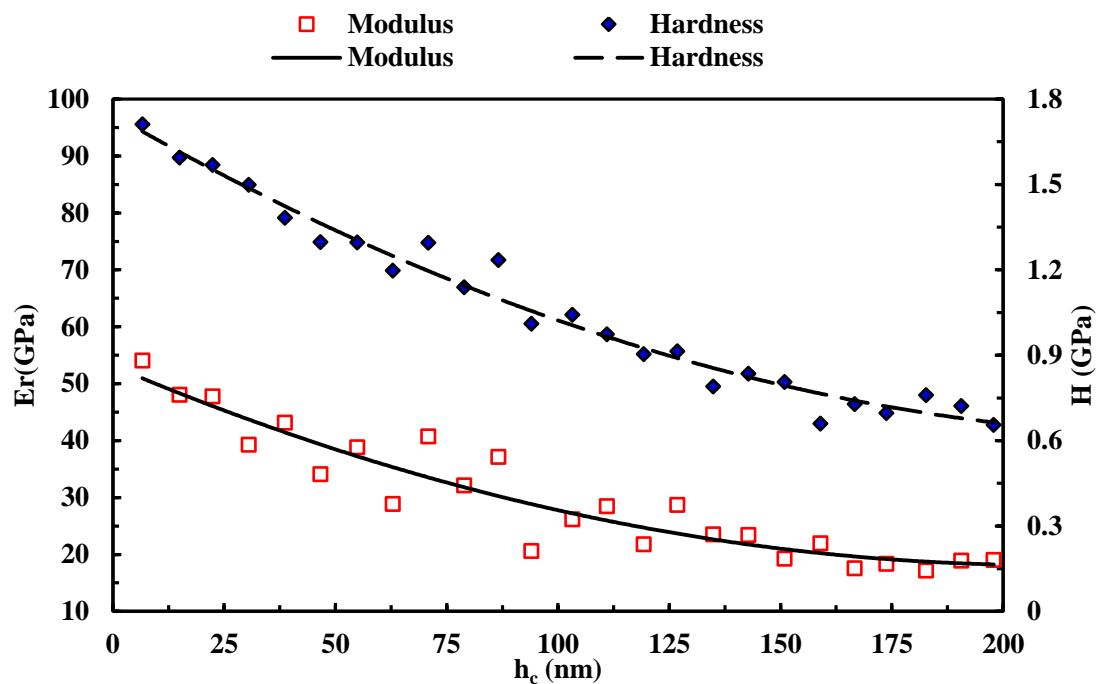


**Figure 6-17. Nanoindentation test results performed on Cu-Sn coating deposited on Cu substrate with low density showing the contact modulus (left) and hardness (right) under displacement control.**

As can be seen from Figure 6-17, there is large scatter in the obtained modulus values for the contact depth lower than 100 nm depth with average value of  $38 \pm 9$  GPa. However at contact depths greater than 100 nm, both the scatter and the modulus value are decreasing with increasing contact depth with an average of  $21 \pm 4$  GPa. Moreover, the obtained hardness results with an average of  $1.35 \pm 0.2$  GPa for

contact depths lower than  $100\text{ nm}$ , decrease to an average value of  $0.8\pm 0.1\text{ GPa}$  when the contact depth increases. To further investigate the mechanical properties of Cu-Sn coatings with low density at a specific contact depth across the surface of the sample, additional work was carried out under displacement control. The hardness and contact modulus results obtained under displacement control for the contact depth of  $65\text{ nm}$  are  $1.8\pm 0.48$  and  $46\pm 11\text{ GPa}$  respectively. However, the hardness and modulus values for the contact depth of  $150\text{ nm}$  are  $1.05\pm 0.8$  and  $36\pm 8\text{ GPa}$  respectively. The obtained standard deviation values for the nanoindentation tests at the same contact depths under both the open loop mode and displacement control mode illustrate that the mechanical properties of materials are highly dependent on the density of the sample and surface roughness.

The decrease in hardness and modulus as the contact depth increases is a consequence of the deforming volume sampling more grains and local porosity as the contact scale increases, rather than a traditional indentation size effect which only affects the hardness data. Figure 6-18 illustrates schematic of (a) a single grain indentation at low contact depth consequently with less porosity effect and (b) the effect of many grains behaviour and consequently higher local porosity at high contact depths on the measured hardness and modulus values.

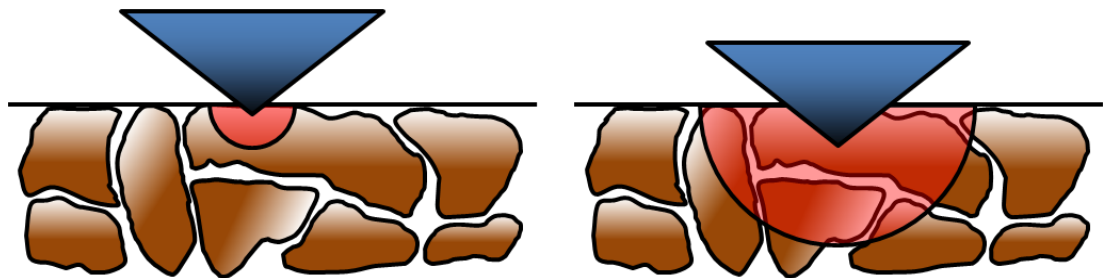


**Figure 6-18. Schematic representation of the deforming volume sampling at (a) low contact depth and consequently high values due reduced porosity effect and (b) high contact depth and consequently lower values due to the higher porosity influence.**

To further investigate the effect of density on the mechanical properties, Cu-Sn coatings were annealed to have approximately the same surface roughness with higher densities.

#### 6.4.2 Annealing Study

To improve the nucleation density of the Cu-Sn coatings the samples were annealed at 400 °C for 30 minutes using a nitrogen atmosphere to prevent the oxidation of the coating during the annealing process. Annealing improved the density of the coatings but fully dense coatings without pores and spaces between grains were not achieved. It should be noted both that as the samples were deposited on the Cu or stainless steel substrates and that the substrate will have an effect on the density measurements using a density bottle on attempting to remove the coating from the substrate to remove this substrate effect the coating fragmented so no density measurement was possible. The consequence of this is that a comparison between the pre and post annealing densities of each sample was not possible. Figure 6-19 shows the cross-sectional SEM image of the annealed Cu-Sn coating. As can be seen in the SEM images, there are still some pores on the surface of the coating in addition to the continuing presence of pores beneath the surface. However, a quantitative comparison with the sample before annealing is not possible as it is impossible to locate the same region for comparison in the SEM.

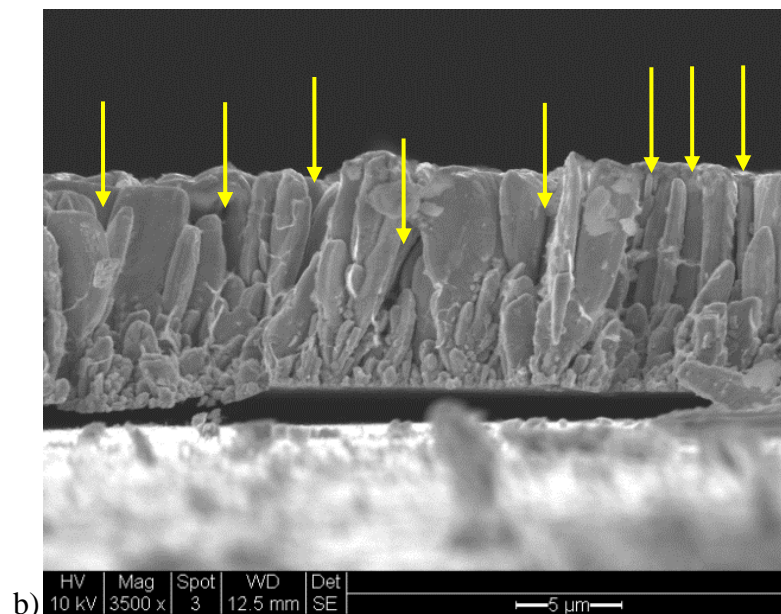


**Figure 6-19. Cross-sectional SEM image of the annealed Cu-Sn coating. The yellow arrows identify the pores on the coating.**

After annealing, the nanoindentation test was carried out under the same conditions as the coatings without annealing. Annealing did not improve the hardness of the coating as the hardness remained constant. However, the obtained modulus values

are higher than the non-annealed coatings at  $46 \pm 18$  GPa. Table 6-5 compiles all the hardness and modulus values obtained under displacement control for Cu, Sn and Cu-Sn coatings and compares the results with bulk and thin film samples.

Samples		H (GPa)		E <sub>r</sub> (GPa)		
Material	Type	Smooth	Rough	Smooth	Rough	
Cu	Bulk	1.4±0.2	2.19±0.6	124±4	121±21	
	Thin Film	1.7±0.3	-	115±3	-	
	Coating	-	2.01±0.4	-	59±14	
Sn	Bulk	0.39±0.1	-	51±6	-	
	Thin Film	0.5±0.1	-	40±8	-	
	Coating	-	0.24±0.05	-	12±3	
Cu-Sn Coating	Copper Substrate		-	0.36±0.2	-	25±12
	Stainless steel Substrate	Non-annealed	-	0.57±0.3	-	27±19
		Annealed	-	0.47±0.3	-	46±12

**Table 6-5. Average nanoindentation test results obtained from different coatings, thin films and bulk samples.**

When comparing the modulus values obtained from same materials with different surfaces, it is clear that the porosity in the coatings is controlling the measured mechanical properties. Therefore, to further investigate the effect of porosity on the mechanical properties, the annealed Cu-Sn coating was used as a case study for modelling the response of the material to the indenter. A finite element analysis program, called Object Oriented Finite 2 (OOF2), shows the response of the material to the indenter without the influence of any other factors such as cracking, pile-up, detachment and fragmentation of the surface.

## 6.5 Modelling of the Indentation Response of Porous Coatings

In this study, the OOF2 element analysis was used to simulate and analyse the effect of density on the elastic modulus results obtained by indentation. OOF2 can use micrographic images, such as SEM images, as an input to the model. In the current work, the SEM image of the cross-section of the deposited annealed Cu-Sn coating with the diamond indenter tip was used to simulate the microstructure in the finite element grids. Figure 6-20 shows the SEM image of the Berkovich tip used in this work to perform the experimental indentation tests, from which the dimensions for

the simulated tip have been extracted. This ensures a geometric similarity between the tip used in the experimental and simulation sections of this work.

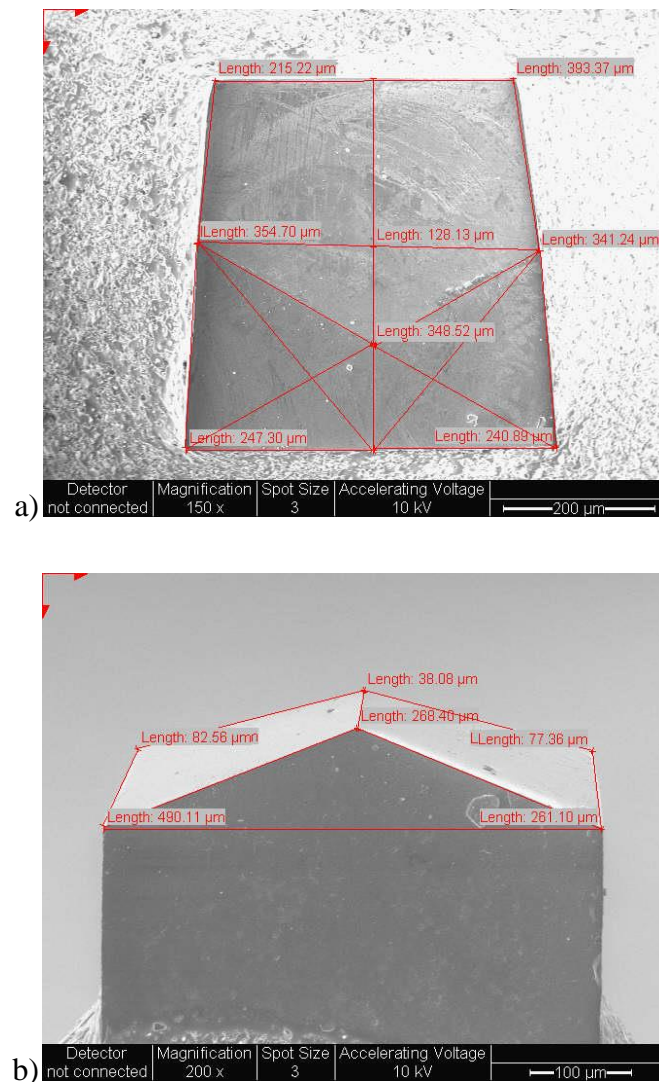


**Figure 6-20. SEM images of the indenter tip (a) top view and (b) cross-sectional view having the geometries of the tip.**

Initially, features in the SEM image were selected and subsequently assigned the appropriate materials properties. The assigned Poisson ratio and elastic modulus for the diamond tip were 0.07 and 1140 *GPa* respectively. Moreover, the Poisson ratio for the Cu-Sn alloy was assumed as 0.3 and an experimental elastic modulus of 46 *GPa* were the materials properties used in OOF2. To measure and visualise the internal stress and determine the elastic modulus of the sample, meshes were created for both the sample and indenter tip which are shown in Figure 6-21.

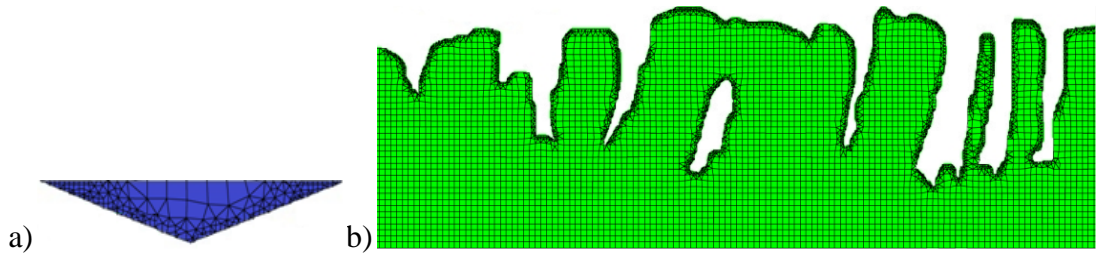


**Figure 6-21. Meshes produced by OOF2 modelling (a) diamond indenter and (b) annealed Cu-Sn coating with low density.**

To determine the variation in the elastic modulus of the coating, the indenter was situated in different horizontal positions across the surface. Three examples of these positions are shown in Figure 6-22 by triangular markers which represent the indenter tip in the different simulations. In each individual position, the straight down displacement of the indenter tip ranged from 1 to 5  $\mu m$  with a step size of 0.5  $\mu m$ . At each increment, both the average stress and strain generated beneath the indenter in the simulated sample were recorded to calculate the elastic modulus of the position by using the slope of the obtained stress-strain curve.

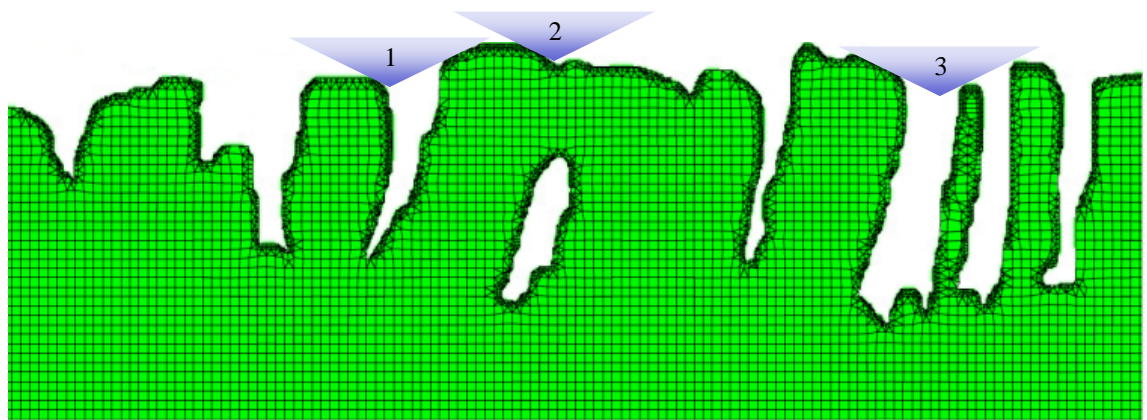


**Figure 6-22. Simulated microstructure of annealed Cu-Sn coating with different indentation positions shown with numbers 1, 2 and 3.**

As an example, the simulated microstructures for position 2 under four different applied displacements are shown in Figure 6-23. The green coloured areas show the original material shape and the mesh gives the distorted shape after the displacement by harder indenter.

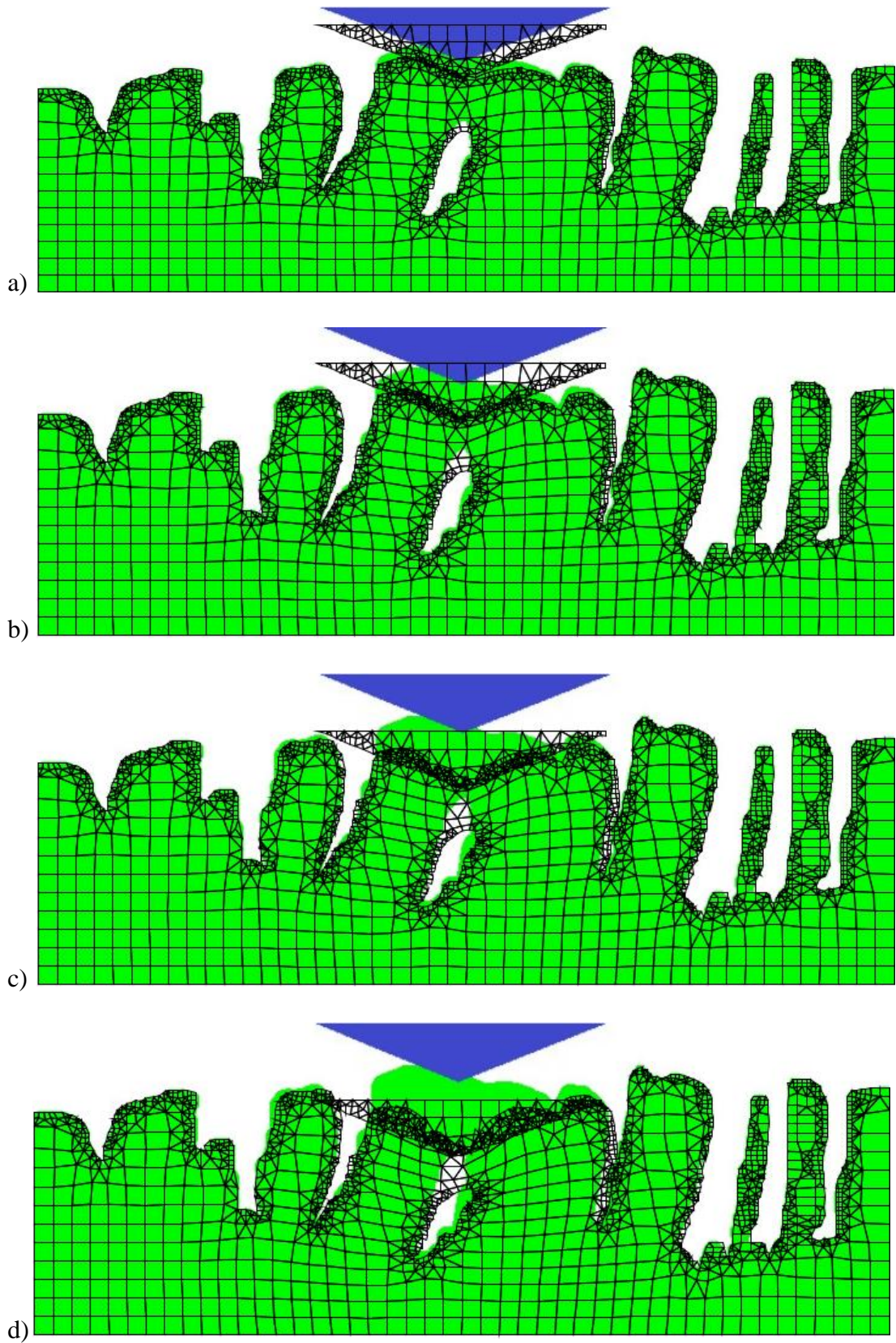


**Figure 6-23. Simulated microstructure of position 4 under different displacement (a) 1, (b) 2, (c) 3 and (d) 4  $\mu\text{m}$ .**

Figure 6-24 shows examples of the stress-strain curves obtained from positions 1, 2, 3 and the fully dense simulated Cu-Sn coating. The slopes of the curves produced from the simulation are the elastic modulus of the aforementioned positions which is

$$E = \frac{\text{stress}}{\text{strain}}.$$

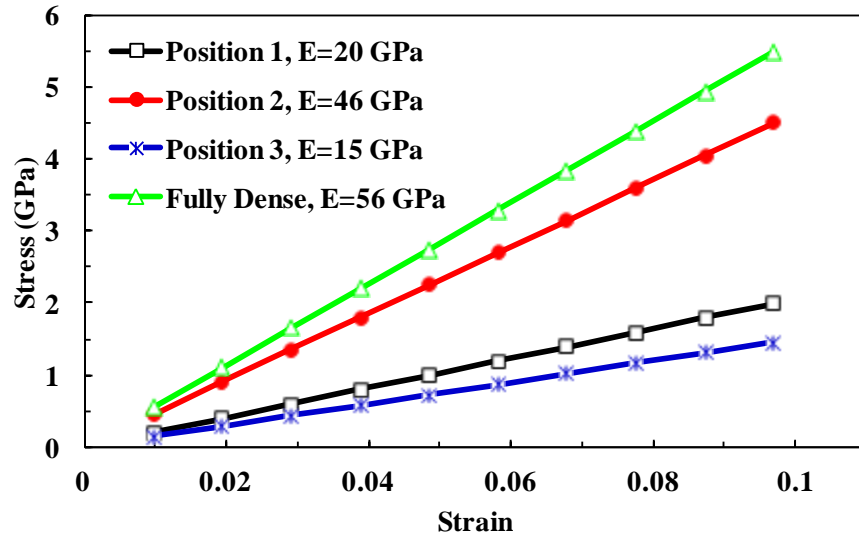


**Figure 6-24. Stress-strain curves obtained from simulated Cu-Sn coating with obtained elastic modulus values at different positions of the coating using OOF2.**

As illustrated in Figure 6-24 the elastic modulus differs based on the position of the indenter tip and also crucially, low values of elastic modulus are determined in test locations where only small initial contact areas are observed (for example, position 1 and position 3) and the material around the point of contact is easily pushed laterally by the wedging action of the indenter. The precise position of the indenter with respect to the surface structure is therefore critical. The average value for the elastic modulus calculated from the simulations is  $36 \pm 13 \text{ GPa}$  which is in reasonable agreement with  $46 \pm 12 \text{ GPa}$ , the average value observed from nanoindentation tests. Within the model, the lateral stiffness is infinite and so there will be no lateral sliding of the indenter which is not the case in the experimental data, as distorted triangular impressions are often observed.

An additional factor that requires investigation is subsurface porosity which can also influence the results in the simulations. To further study the effect of pores underneath the surface on the simulated results, simulations were carried out at position 2. Two different scenarios were explored; one in which a hole was present

under the surface of the coating and one without the hole. The responses of both types of coatings to the indenter tip are shown in Figure 6-25.

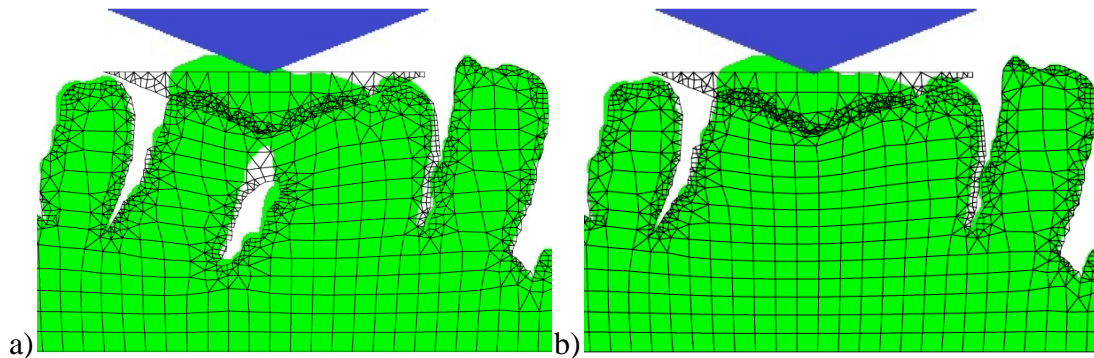


**Figure 6-25. Simulated samples (a) with and (b) without the hole beneath the sample surface.**

The modulus values calculated for the samples with and without a hole beneath the surface are 46 and 45 *GPa* respectively. These results suggest that the sample with the hole is apparently stiffer than that without. In this case, the lateral expansion of the indented microstructural unit into the adjacent free space is larger when there is no hole as some of the elastic movement of material under the indenter is taken up in distorting the hole. The varying constraint from the surrounding material will thus considerably affect the mechanical properties obtained from indentation testing of such porous materials.

To further investigate the effect of surrounding materials and pores on the mechanical properties, work was carried out on the fully dense simulated sample with the same properties as the previous simulation. Figure 6-26 shows the simulated microstructure and subsequent dislocation of the fully dense sample under different applied loads. The average modulus value obtained from the fully dense simulated sample is 56 *GPa* which is higher than the average modulus value obtained from position 2 without the presence of the hole in the sample. The obtained values for the samples in Figure 6-25 are approximately 20% lower than the fully dense sample, showing a similar relationship with the experimental nanoindentation results. This highlights the importance of maintaining a sufficient distance from any porous feature in or on the sample when performing nanoindentation tests unless the scale of the indentation is very much larger than the pores size in the material being tested.

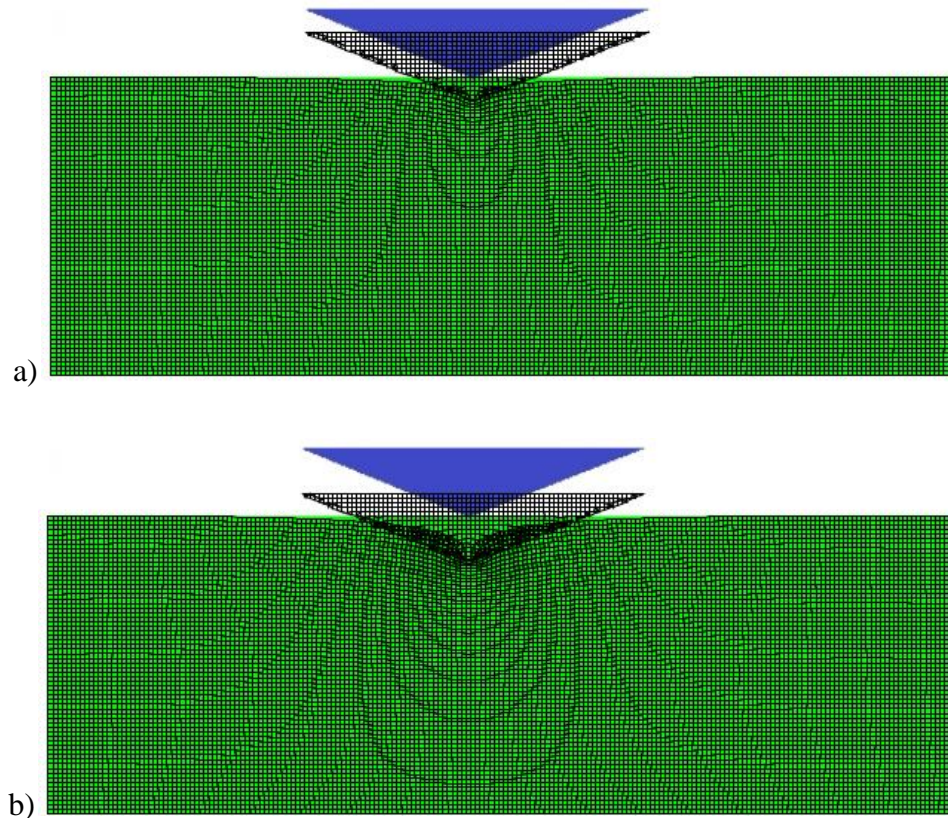


**Figure 6-26. Simulated microstructure of fully dense sample under (a) 1 and (b) 2  $\mu\text{m}$  displacement.**

The importance of the surrounding porous features on indentation results is clear from the modulus results at the different positions shown in Figure 6-22 and Figure 6-24. In nanoindentation tests, factors such as surface roughness and porosity have a significant effect on the results. The columnar growth mode of these coatings results in large intercolumn gaps which give space for elastic expansion of the column during indentation and reduced constriction. This leads to a considerable reduction in the measured properties of the coating in indentation tests, even if the columnar grains themselves may be fully dense. There are some techniques available, such as polishing, that can be used to mitigate the surface roughness. However, the large intercolumnar gaps and pores beneath the surface cannot be removed from the coating by polishing or short term annealing, and the data obtained from such open porous coatings where the pores size is of a similar scale to the impression must be regarded as questionable. Modelling can help to understand these effects and assess the reliability of the produced experimental data.

## 6.6 Summary

The surface roughness as well as the porosity of the samples can have significant effects on the obtained hardness and modulus values and requires consideration during the measurement of mechanical properties using the nanoindentation technique. The scatter in the obtained data can be verified by AFM image analysis in addition to the use of load-displacement curve analysis. The material's behaviour during the indentation tests can be seen using the loading curve of the load-displacement curves and phenomena such as pop-ins can be explained with the corresponding AFM images. All of these phenomena can cause variation in the nanoindentation hardness and modulus results. However, these are not the only causes of scatter in the results and there are other important factors such as pile-up and creep.

The next chapter highlights the importance of pile-up and creep effects on the nanoindentation test results using the Oliver and Pharr analysis method. A comparison of pile-up formation for bulk and thin film copper is provided. Subsequently, the effect of annealing copper thin films in the formation of pile-ups is presented. Following this, the pile-up appearance for bulk and thin aluminium films deposited on glass substrates are compared to those of the copper samples. Afterwards, general information with regards to creep and its effect on the load-displacement curves is provided. Finally, the scatter seen in the obtained Young's modulus values of zinc due to anisotropy is discussed.

## **Chapter 7. The Potential Measurement Errors of Mechanical Properties using Nanoindentation Techniques**

*This chapter covers the potential sources of error in the obtained data. Pile-up and its effect on the obtained data is described. The amount of pile-up formation in the bulk materials is compared to those of thin films under the same indentation conditions. Afterwards, the effect of annealing in the appearance of pile-up is discussed. Low melting point materials are compared to high melting point materials in terms of creep and its effect on the changes of indenter displacement and consequently the obtained mechanical properties. Different test protocols are compared to detect and minimise the creep effect on the hardness and Young's modulus values. Finally, anisotropy of the materials and its influence on the scatter obtained in Young's modulus values is described.*

### **7.1 Potential Sources of Data Distortion**

As nanoindentation with its high accuracy for measuring the mechanical properties of materials at very small scales becomes a more commonly used technique, there are some potential issues that need to be considered when testing both bulk materials and thin films, with the reliability of the obtained hardness and modulus results being dependent on these issues. With regards to thin films for example, when the thickness of the film is less than 1  $\mu\text{m}$  there are some errors, especially at greater depths, on the obtained mechanical properties due to the influence of the substrate on the results, consequently affecting the load-displacement curve (Tsui *et al.*, 1997b). Furthermore, when dealing with soft coatings on hard substrates, such as Au on a Si substrate, issues such as pile-up appearance are clear and the obtained results are usually overestimated. This is because the Oliver and Pharr method cannot account for the effect of pile-up on the obtained data at greater depths, the method is most accurate when materials sink-in rather than pile-up.

Another important factor which requires consideration during nanoindentation tests is creep. Creep, which is defined as time-dependent plasticity at a constant load, can influence the maximum depth at maximum force and consequently can have a significant effect on the data obtained. The errors on the extracted values can be

sometimes greater than 20% (Chudoba and Richter, 2001). In this chapter the most common issues with the data from nanoindentation test will be covered.

## **7.2 Changes in Contact Area**

One of the main issues in determining the hardness and modulus of materials is the accurate measurement of the contact area, as any miscalculation of the contact area can heavily influence the obtained data. The deformation behaviour of different materials during indentation tests can be different. Consequently, when subjected to loading, some materials tend to pile-up around the indenter which leads to a significant increase in the contact area and therefore a miscalculation in the contact area. Conversely however, there are materials that show sink-in behaviour during indentation, meaning that when undergoing indentation, material collapses from the area surrounding the indenter. There are further issues when dealing with the accuracy of contact area measurement such as surface roughness in nano-scale testing, which was addressed previously in Chapter 6.

### **7.2.1 The Importance of Pile-up**

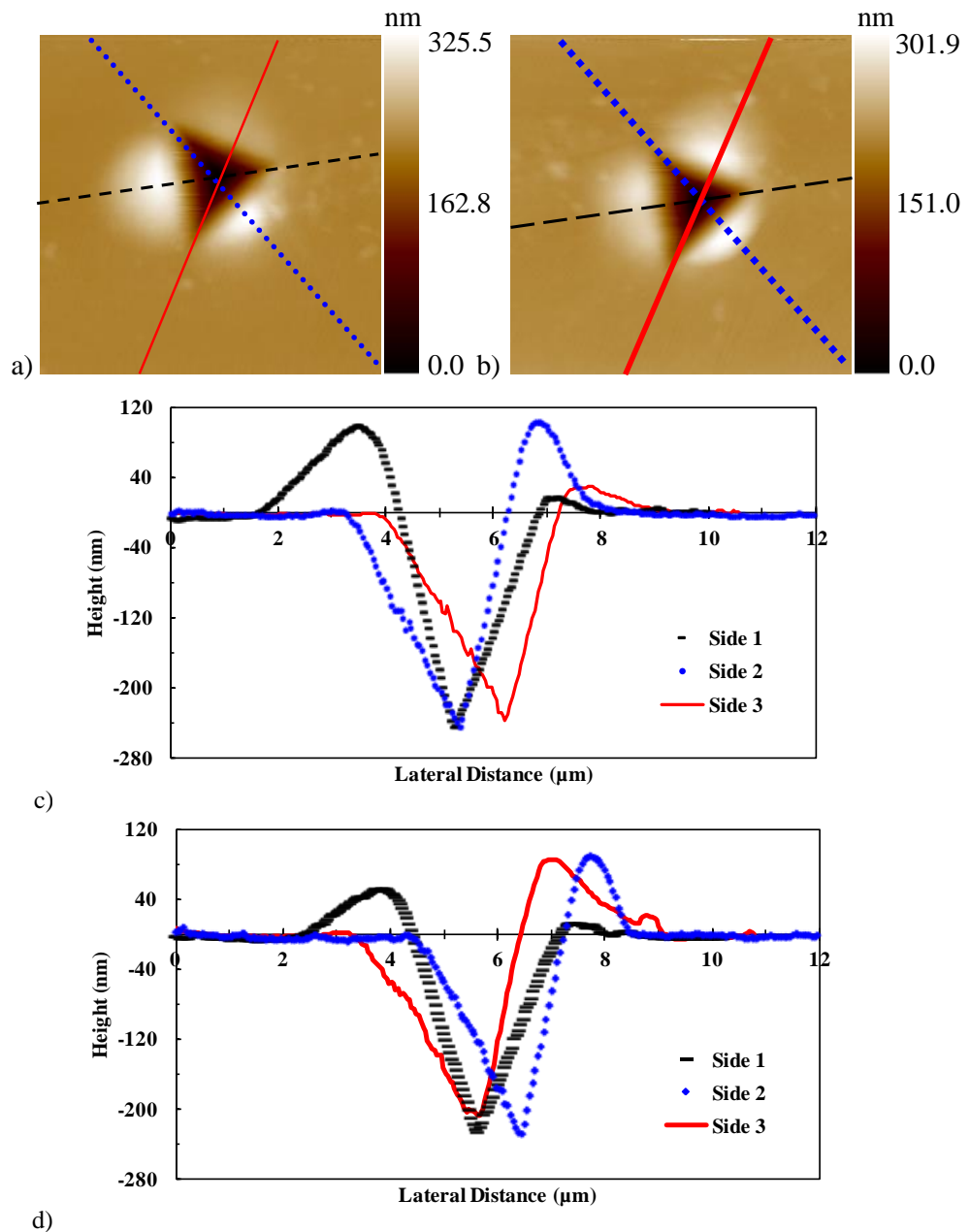
As mentioned previously, the appearance of pile-up around the edges of the contact area results in an underestimation of the contact area and therefore an overestimation of the Young's modulus and hardness values. As mentioned in Chapter 2, based on the Oliver and Pharr, method the hardness is inversely proportional to the contact area and the Young's modulus is inversely proportional to the square root of the contact area.

During nanoindentation tests for both thin films and bulk materials, the deformation mechanisms, and therefore the governing of dislocations nucleation events, are complex and not fully understood (Suresh *et al.*, 1999; Soare *et al.*, 2004). Work from Cheng and Cheng (Cheng and Cheng, 2004) shows that pile-up depends on work hardening behaviour and  $E/H$ . Soft easily hardened materials sink-in whereas harder work hardened materials pile-up (Cheng and Cheng, 2000). Therefore, the volume of the pile-ups is not always proportional to the indentation load and the true measurements of the Young's modulus and hardness values require the calculation of the contact area from the nanoindentation load-displacement curves as well as AFM or SEM images. For that reason, in this work, the AFM images were obtained after

each indentation to accurately measure the true contact area and apply the pile-up correction to the obtained data for comparison.

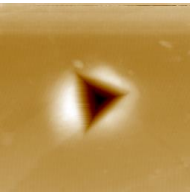
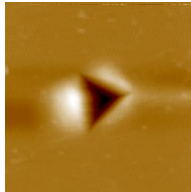
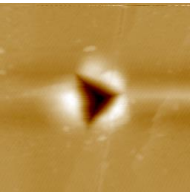
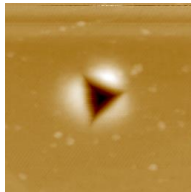
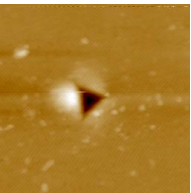
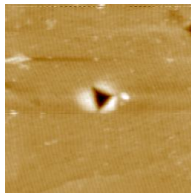
### 7.2.2 Comparison of Pile-up Appearance between Bulk and Thin Film Copper

Initially, the effect of pile-up on the hardness and modulus values obtained from the nanoindentation tests on bulk Cu was investigated. Figure 7-1 (a) and (b) illustrate two AFM images ( $10\ \mu\text{m} \times 10\ \mu\text{m}$  areas) obtained from a polished bulk Cu sample after nanoindentation tests in open loop mode under 10 and 9 mN loads respectively.



**Figure 7-1.** (a) and (b) AFM images as well as respective (c) and (d) cross-sectional curves of the drawn lines in the images obtained from bulk Cu after indentation tests under 10 and 9 mN loads for open loop mode.

Additionally, the cross-sectional curves obtained from the three different sides of the indentation edges are shown in Figure 7-1 (c) and (d), corresponding to the AFM images shown in (a) and (b) respectively. The cross-sectional curves assist in measuring the amount of pile-up, as well as its height and width around the indentation edges. The combination of AFM images and cross-sectional curves confirms both that the pile-ups are not symmetrical around the indentation edges and that the height and width of the pile-ups differ from each other at the three different sides of the indentations. They also confirm that during the formation of pile-ups, the material protrudes upwards in proximity to the indentation edges, building narrow but high pile-ups. Table 7-1 presents examples of various AFM images obtained under open loop mode from high load indentation tests, with applied loads ranging from 1 to 10 *mN*. It should be noted that these tests were performed under very high loads to observe the magnified effects of pile-ups on the hardness and Young's modulus values of bulk Cu obtained from nanoindentation tests. In addition to this, the tests were also carried out at high loads to allow for a comparison of the pile-up shapes of harder bulk Cu samples with softer Al bulk samples, which will be discussed later in this chapter.

AFM Image	P ( <i>mN</i> )	Height			AFM Image	P ( <i>mN</i> )	Height		
		0.0	133.3	266.6			0.0	115.5	231.0
	7	0.0	133.3	266.6		6	0.0	115.5	231.0
	5	0.0	97.1	194.3		4	0.0	105.5	211.1
	3	0.0	64.3	128.5		2	0.0	43.3	86.7

**Table 7-1. AFM images obtained from bulk Cu sample under open loop mode at high loads.**

The hardness and Young's modulus values obtained before and after pile-up correction for high load indentation tests on bulk Cu under open loop mode are shown in Figure 7-2.

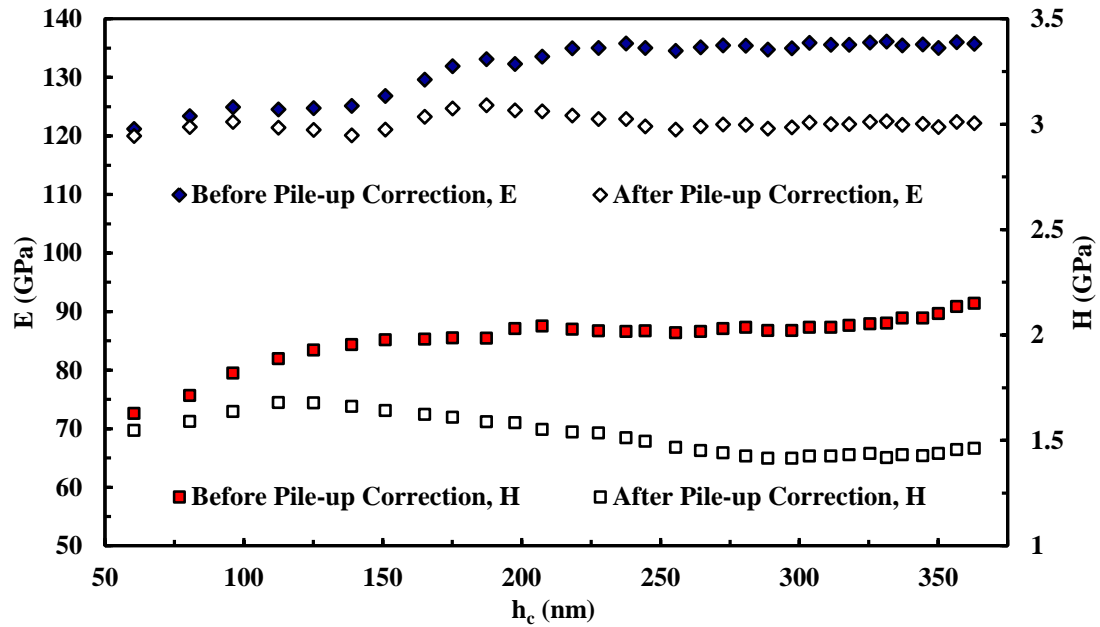


**Figure 7-2. Young's modulus (left) and hardness (right) values obtained under high load indentation tests for bulk Cu using open loop mode showing data before and after pile-up correction.**

It was observed that as the indentation size is increased, the pile-ups show a greater influence on the obtained hardness and modulus values. When quantifying the effect of pile-up from lower loads to higher loads it was found that the effect on the obtained data increased from 5 to 15% for the Young's modulus and 10 to 35% for the hardness values.

To determine the relationship between the pile-up appearance and contact depth as well as the effect of pile-up on the obtained data for lower loads, the height and width of the pile-ups were measured using the AFM images. The measured height and width of the pile-ups obtained from 100 nanoindentation tests applied on bulk Cu for open loop mode under low ranges of load are shown in Figure 7-3. As can be seen from Figure 7-3 (a) and (b), both the pile-up heights and widths increase as the contact depth increases. The effect of pile-up height on the measured contact area is important when using the Oliver and Pharr method as it can modify the calculated hardness and modulus values. Moreover, the width of the pile-up can represent the plastic radius zone around the indentation contact radius. For the indentations with

contact depths of less than 50 *nm* the pile-ups were extremely small and not even observable.

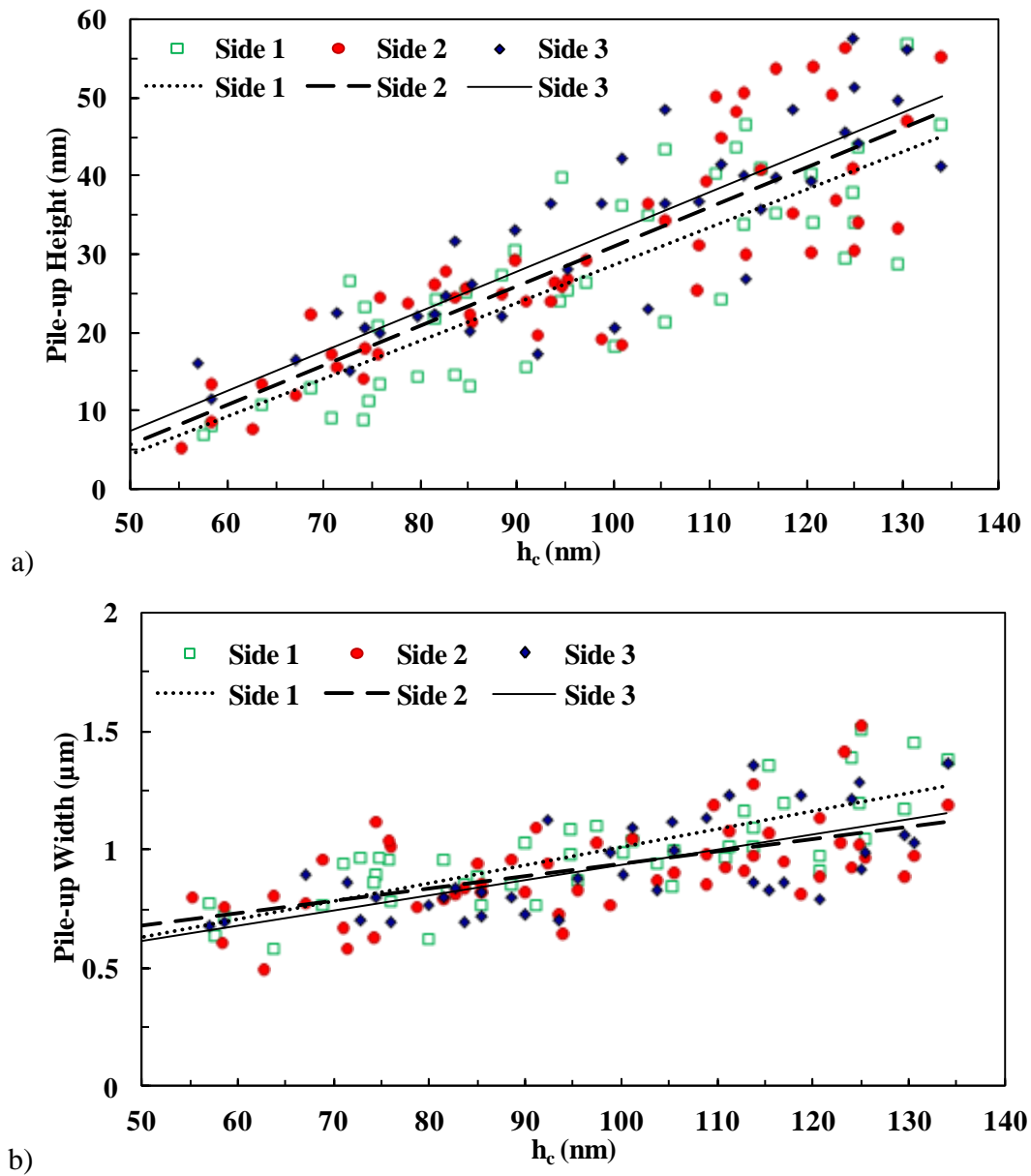


**Figure 7-3. (a) height and (b) width of the pile-ups obtained from a single cycle nanoindentation test under open loop mode from bulk Cu.**

When pile-up heights and widths obtained from bulk Cu were compared to the thin films under the same indentation conditions, it was observed that the amount of pile-up that appeared in the thin films was considerably higher than in the bulk Cu. Thin films such as Cu, Au or Al with low hardness values deposited on substrates such as glass ( $H=5$  to  $8$  *GPa*) and silicon ( $H=12$  *GPa*), which are harder than the deposited materials by nearly one order of magnitude, show a different plastic deformation under the impression of the hard indenter (Tsui *et al.*, 1997b). During the indentation

tests, the harder substrate does not deform to the same extent as the softer deposited coating and consequently it has an extreme effect on the degree of pile-up formation on the thin film. For comparison, the height and width of pile-ups obtained from non-annealed Cu thin film deposited on a silicon substrate are shown in Figure 7-4. The non-annealed sample was compared to the bulk Cu to avoid any annealing effect in the comparison of the obtained data.

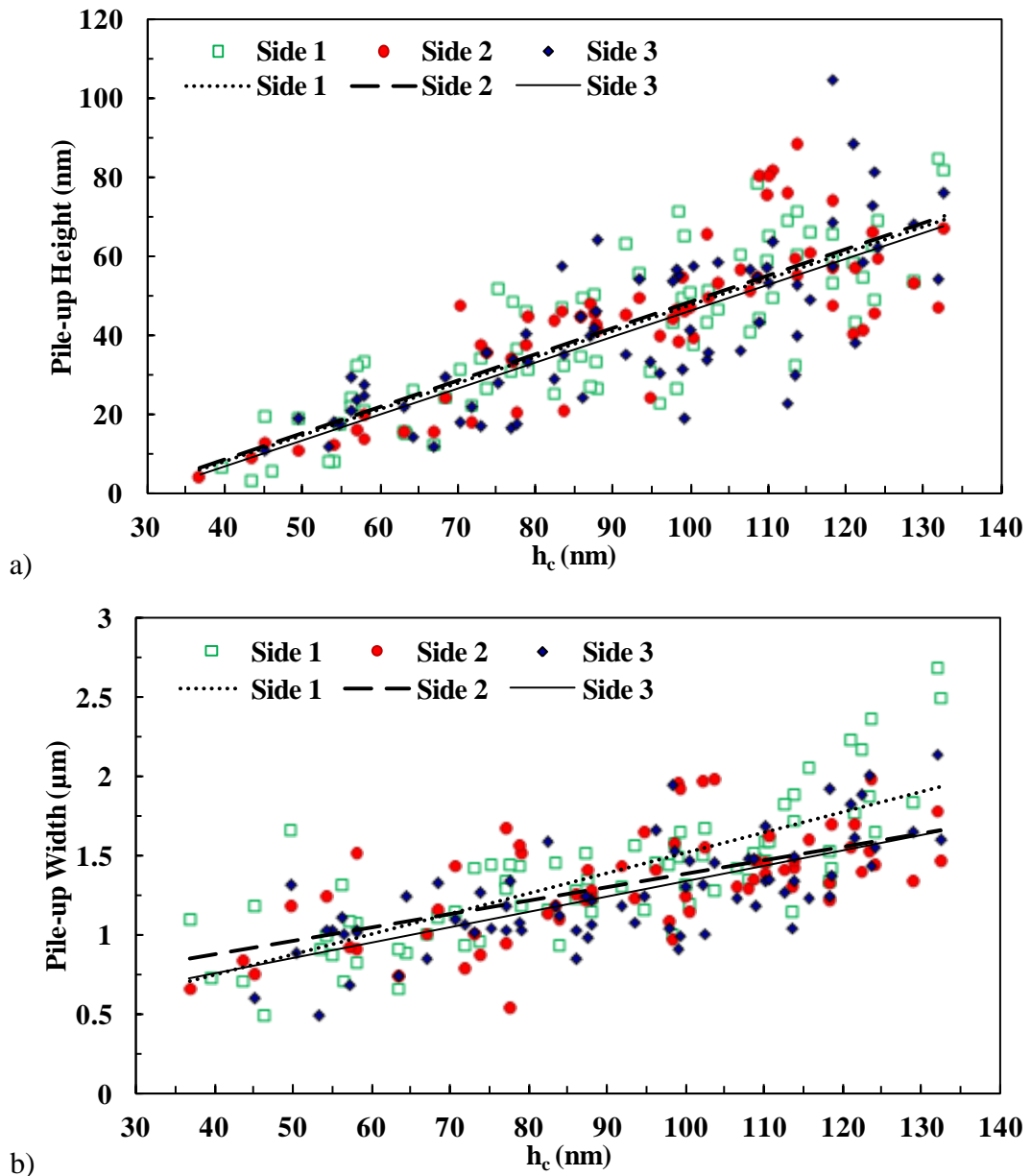


**Figure 7-4. (a) height and (b) width of the pile-ups obtained from single cycle nanoindentation test under open loop mode on non-annealed Cu thin film.**

It should be noted that although the effect of pile-up in the hardness and modulus values is important, it is also important to understand when this effect starts.

Sometimes the effect is minor and the actual area in contact with indenter tip is not related to the measured pile-up height directly. For example, the pile-up influence in the obtained data for the non-annealed Cu thin film at contact depths less than 50 *nm* did not have any effect on the measured contact area, but for the depths greater than 85 *nm*, the effect is significant. Figure 7-5 shows schematic example of a formed pile-up around the indenter tip with (a) and (c) illustrating top views and (b) and (d) illustrating cross-sectional images of the respective top views. Both images demonstrate that pile-up partially supports some of the applied load and therefore changes the projected contact area.

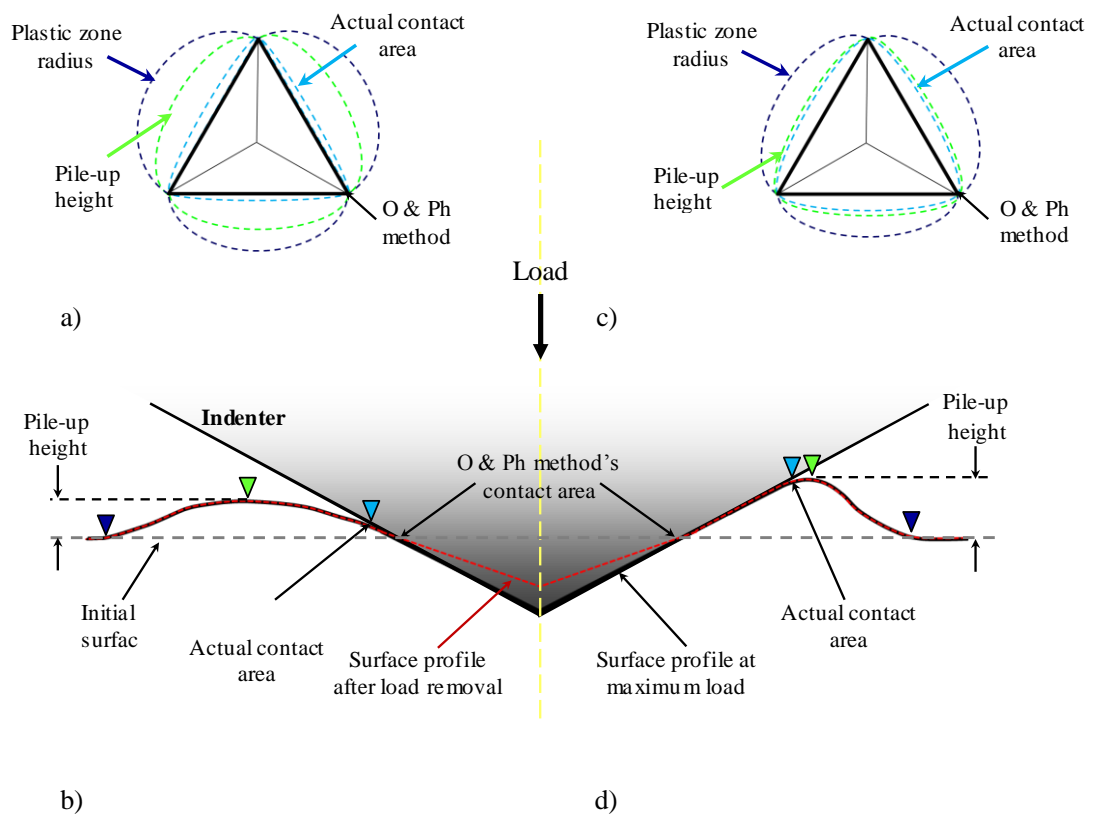


**Figure 7-5. Schematic representation of the physical indentation process: (a) and (c) top views of the indentation, (b) and (d) the cross-sectional views of the same indentations respectively.**

These diagrams represent two different types of pile-up based on their heights and widths; (b) short but wide and (d) tall but narrow. The dashed yellow line in the centre of the diagram separates these two pile-up scenarios. As can be seen from left side of the image (Figure 7-5 (a) and (b)), when the pile-up is broad the difference between the actual contact area and the contact area measured by the Oliver and Pharr method (labelled as O & Ph in Figure 7-5) is very small. Consequently, the

change in the contact area caused by pile-up does not greatly influence the hardness and modulus values obtained using the Oliver and Pharr method. This situation was obtained mostly for bulk Al, which will be discussed later in this chapter. The right hand side of the image (Figure 7-5 (c) and (d)) illustrates a pile-up appearance with great height and narrow width, which greatly effects the contact area measurement. When the pile-up is tall, the actual contact area during the indentation test is much larger than the area measured by the Oliver and Pharr method. This mainly occurred in this work for the majority of the thin film samples during the indentation process.

The AFM images obtained from the Cu thin films confirmed that the pile-up was increasing as the contact depth increased. However, as the Cu thin films were annealed at different temperatures, work was carried out to investigate the effect of annealing on the shape and also the amount of pile-up appearance during the nanoindentation tests.

### 7.2.3 Annealing Effect on Pile-up Height and Width

As was seen in Chapter 5, annealing influences the mechanical properties of Cu thin films. Therefore, there is a possibility that the dislocation nucleation changes through annealing. The average heights and widths of pile-up obtained from the single cycle indentation tests under open loop mode at a 1 mN load and contact depths of less than 120 nm for the non-annealed, annealed at 100 °C and annealed at 350 °C Cu thin films are shown in Figure 7-6.

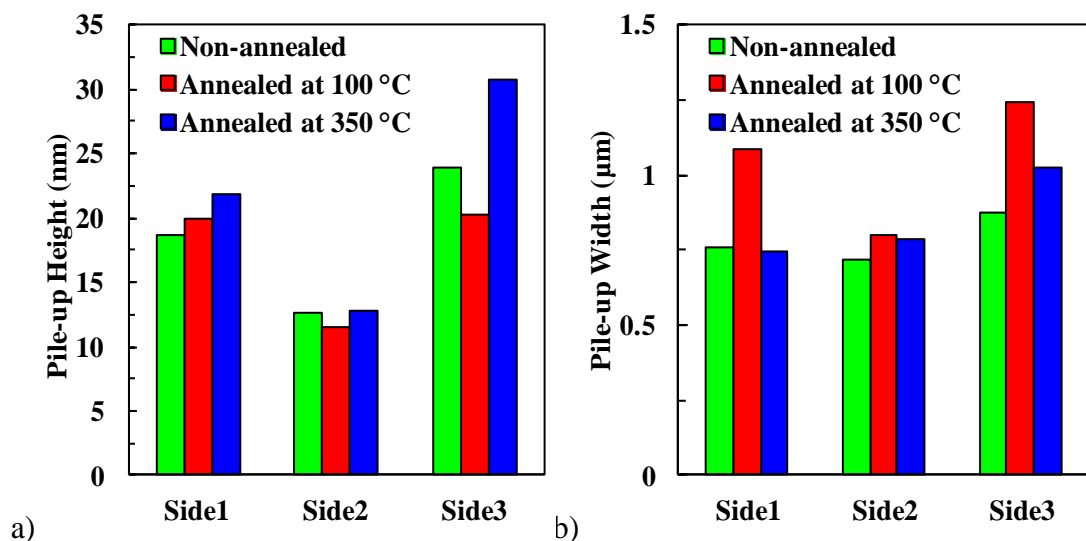


Figure 7-6. Average pile-up (a) height and (b) width obtained from the single cycle indentation tests under open loop mode for the Cu thin films.

As can be seen from Figure 7-6, the average pile-up height obtained from the sample annealed at 350 °C is higher than both of the other thin film samples. This can be due to recrystallisation and grain growth which occurs during the annealing process at 350 °C. Both the EBSD and XRD results obtained from Cu thin films (see Chapter 5) confirmed that the average grain size for the thin film annealed at 350 °C is smaller than both other thin films. Fine grain growth and the prevalence of the dominant (111) orientation were also confirmed by EBSD and XRD analyses for this sample. Consequently, all of these sources can have an influence on governing the nucleation of dislocations under the nano-indenter during the indentation tests.

A more detailed inspection of the data obtained from the sample annealed at 100 °C shows that the pile-up widths are higher for this sample in all three sides compared to the other samples. This confirms that the grain size, as well as its orientation, plays a considerable role in forming the pile-up. Therefore when using the Oliver and Pharr method to extract the mechanical properties of materials, the accuracy of the obtained data, especially at greater contact depths, highly depends on the mechanisms by which dislocations nucleate and pile-up appears.

For the single indentation method there is the opportunity to measure the contact area using AFM images and correct the obtained data for pile-up. However, when dealing with multi-cycling tests pile-up corrections are only applicable for the last segment when complete unloading occurs. Additionally, for multi-cycling tests, the AFM image is obtained when the indentation test cycle finishes.

Consequently, to further understand the quantity of pile-up that appears at different stages (each segment) of partial unloading during multi-cycling tests, work was carried out on Cu thin films under multi-cycling tests at different peak loads. The first set of data were obtained for the partial 90% unloading of maximum load for the peak loads ranging from 0.1 *mN* to 1 *mN* with a 60  $\mu$ *N* decrease in each indentation test. The height and width of pile-ups were measured using the AFM images for all three sides of the indenter edges. As an example, the results from the pile-ups obtained through 25 multi-cycling indentations for 90% partial unloading for the non-annealed sample are shown in Figure 7-7.

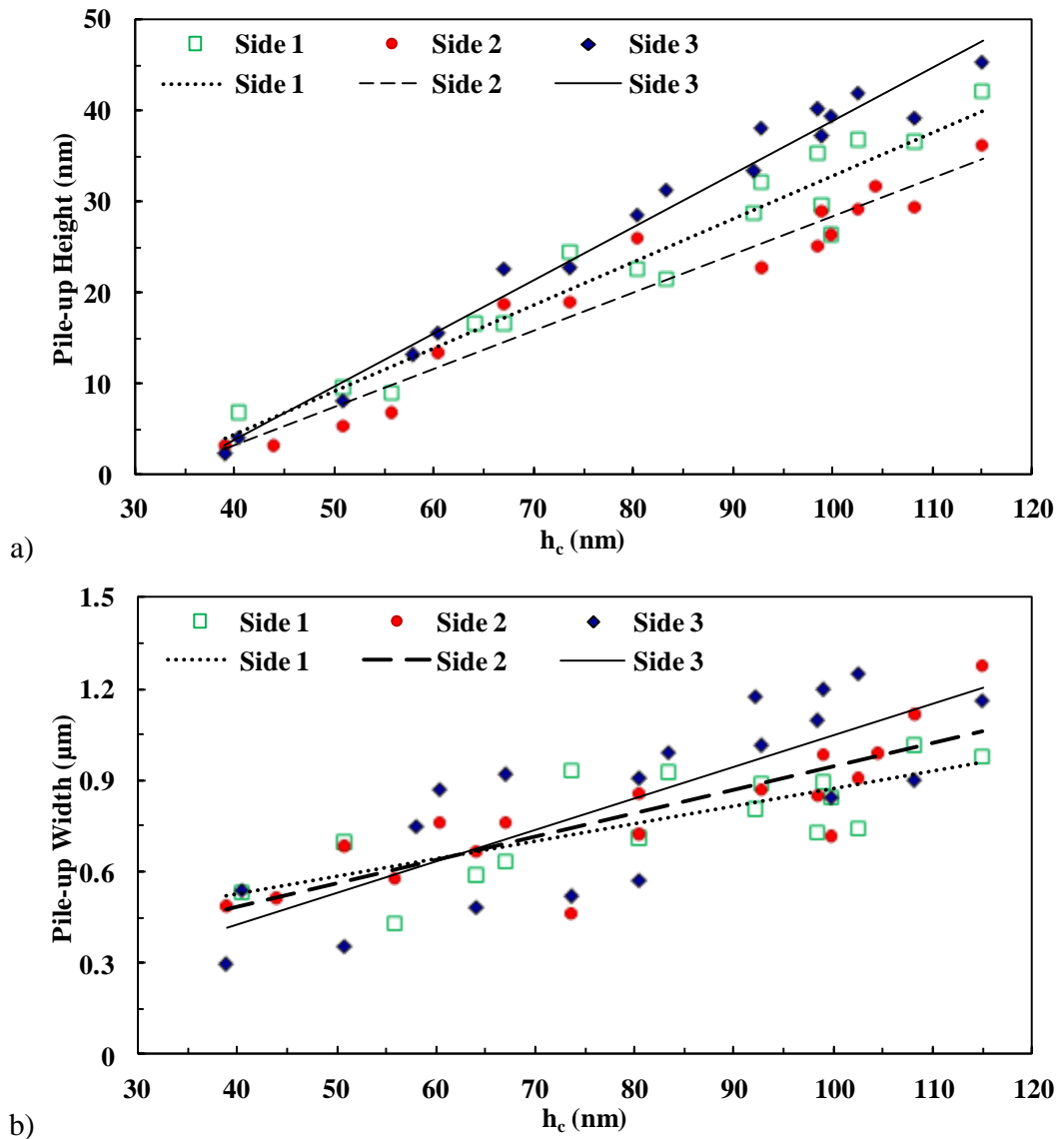
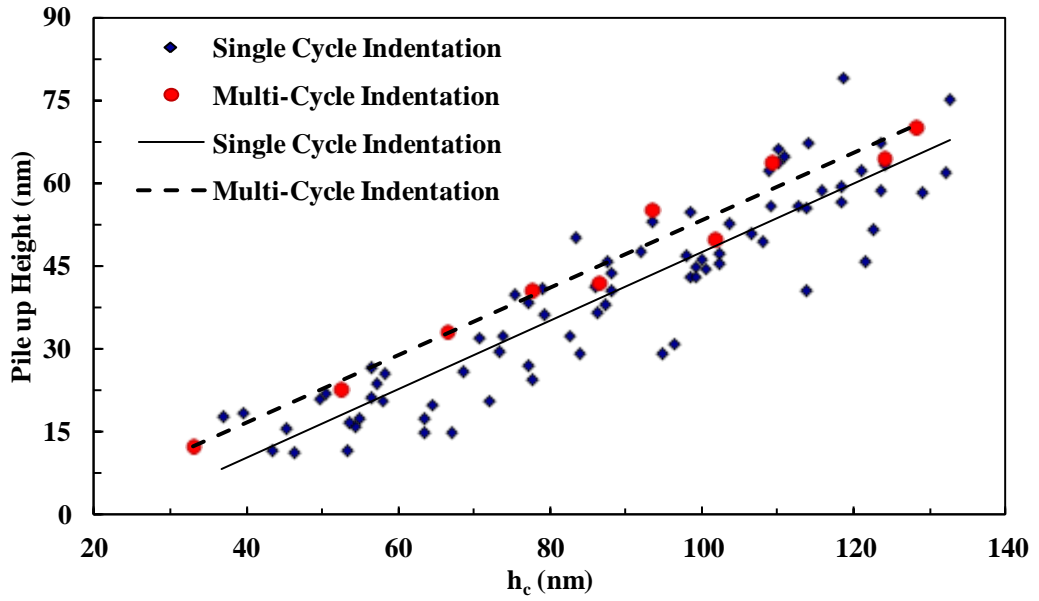
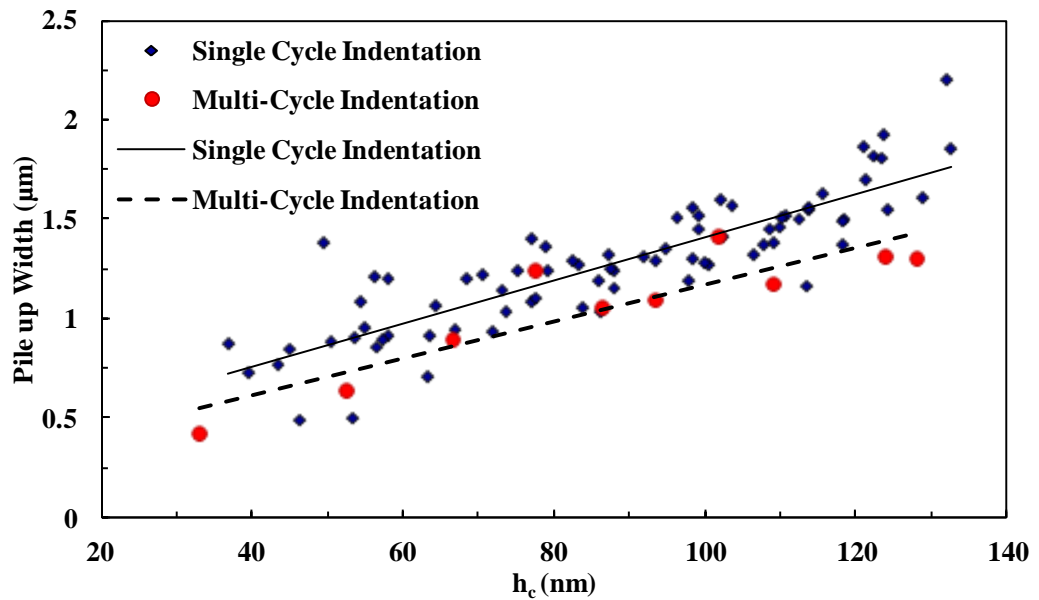


**Figure 7-7. (a) heights and (b) widths of pile-ups measured using the AFM images from nanoindentation tests for non-annealed Cu thin film under the multi-cycling test (90% unload).**

It has been observed that pile-up occurs for multi-cycling tests in the same manner as for single indentations, meaning that larger penetration depths, results in greater pile-ups. However, when using approximately identical contact depths, the average pile-up height for the multi-cycling tests is slightly higher than that from the single indentations. This can be attributed to the relaxation process which occurs during the unloading cycle in a multi-cycling test. As an example, the height and width of pile-ups obtained from non-annealed Cu thin film for the single and multi-cycling indentations are compared in Figure 7-8. For both the single and multi-cycling indentations, the applied peak loads were started at 2  $mN$  and reduced by 50  $\mu N$  at each indentation site.



a)



b)

**Figure 7-8. Pile-up (a) heights and (b) widths obtained from non-annealed Cu thin film under single and multi-cycling indentation tests (90% unload).**

The data shown in Figure 7-8 are the average pile-up heights and widths obtained from all three sides of the indentation edges. The same behaviour was obtained for the other Cu thin film samples. As was shown in Chapter 5, the hardness and modulus values obtained from nanoindentation tests for three different multi-cycling protocols (20, 50 and 90% partial unloading of the maximum load) showed some variation from each other. Subsequently, work was carried out under multi-cycling tests at different peak loads (high to low loads) to investigate and also compare the appearance of pile-up during each protocols.

#### 7.2.4 Further Investigation of Pile-up for Different Multi-cycling Tests

When comparing the results obtained using the Oliver and Pharr method on multi-cycling data using 20% and 50% unloading for both the bulk Cu and thin films, the results were almost constant and there were no significant differences in the hardness and Young's modulus values. However, at 90% partial unloading of the maximum load, both the hardness and modulus data were higher, with this difference becoming more pronounced at greater depths and additionally, the pile-up effects were magnified. During 90% unloading, the dislocations can untangle due to back stresses and form new interactions. This increases the extent of pile-up and also increases the measured hardness and contact modulus at higher contact depths where pile-up effects are significant. Figure 7-9 illustrates two examples of AFM images ( $5 \mu\text{m} \times 5 \mu\text{m}$  area) obtained from non-annealed Cu thin film for the same peak load ( $1.5 \text{ mN}$ ) but using two different partial unloading protocols 20% and 90% partial unloading. It can be seen that, the unloading scheme changes the appearance of the pile-up with narrower but higher pile-up regions being produced at 90% unload.

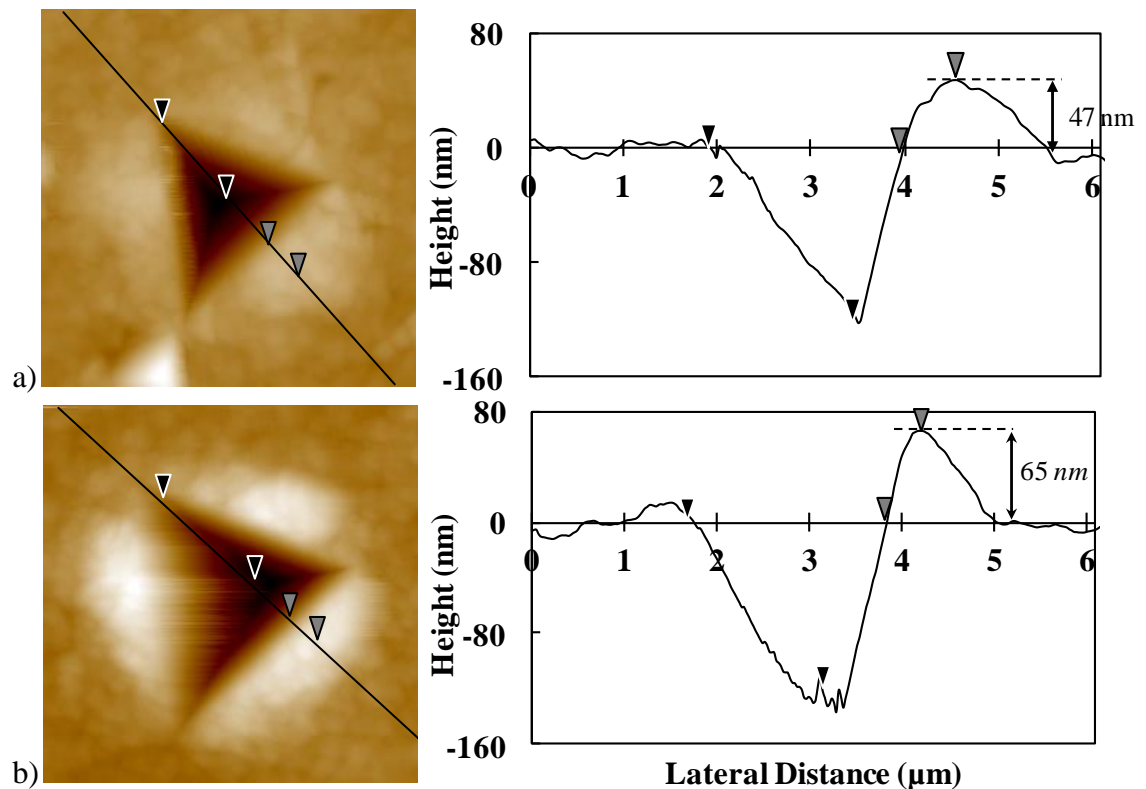


**Figure 7-9.** AFM images of high load ( $1.5 \text{ mN}$  peak load) multi-cycling indentations in the non-annealed Cu coating (a) 20% unload and (b) 90% unload as well as the cross-sectional curves obtained from the drawn lines at AFM images.

As previously acknowledged, the pile-up height plays significant role in the miscalculation of the projected contact area. Therefore, as the 90% unloading method produces greater pile-up heights than two other protocols, the calculated hardness and modulus values will consequently be higher. This situation was also observed when using lower loads. Figure 7-10 compares the average pile-up heights and widths for all three sides of the indentation edges obtained under different test protocols using multi-cycling tests for the non-annealed Cu thin film.

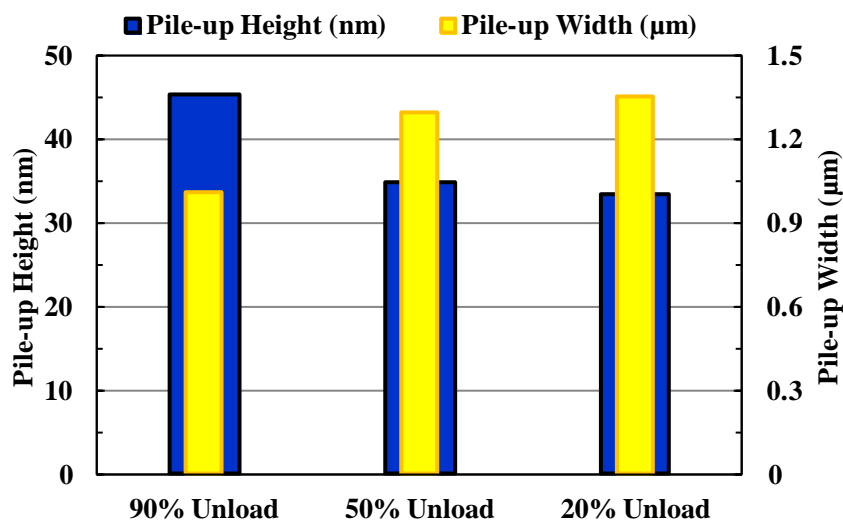


**Figure 7-10. Average pile-up heights and widths obtained from all three sides of the indentation edges for non-annealed Cu thin film under different multi-cycling test protocols.**

As can be seen, the measured pile-up heights obtained from 20% and 50% partial unloading are approximately same, with this also being applicable to the measured pile-up widths. There is however a substantial difference when comparing these two protocols to 90% unloading and the obtained height is considerably higher. This confirms both the effect of pile-up on the obtained data and that when using the same material with different loading and unloading protocols, the nature of the obtained pile-up can be different. Consequently, the correct selection of the load function can be essential and also can have a significant influence on the hardness and modulus values obtained from the nanoindentation technique using the Oliver and Pharr method.

Although the AFM images confirmed the appearance of pile-ups and their effect in the obtained mechanical properties, the load-displacement curves can also be used to observe the effect of loading and unloading under various conditions in multi-cycling

tests on the obtained data. This is possible because the hardness and modulus values obtained from nanoindentation tests are highly dependent on the obtained load-displacement curves. Figure 7-11 shows the average of 25 load-displacement curves obtained for three different indentation protocols using multi-cycling tests for the non-annealed Cu thin film at a 1 mN peak load.

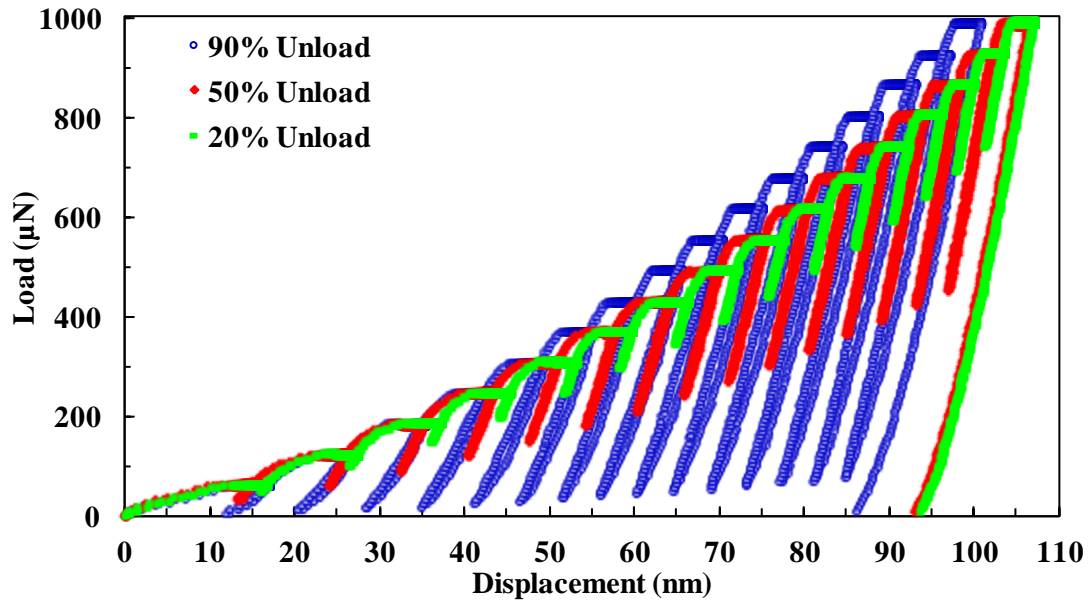


**Figure 7-11. Partial load-displacement curves in multi-cycling test for 20, 50 and 90% unloading of maximum load.**

It can be observed that for three different protocols, the obtained load-displacement curves have almost the same contact depth when comparing identical peak loads in the lower load sections of the curves. However, in the higher load sections of the curves there is a considerable difference when comparing the 20% and 50% partial unloading data with the 90% data. When using the same load, the maximum contact depth obtained from 90% is lower than that from 20% and 50%. This is due to the appearance of higher pile-ups for 90% partial unloading, which change the measured contact depths.

### ***7.2.5 Effect of Pile-up on the Mechanical Properties of Aluminium***

To further investigate the effect of pile-up in the mechanical properties obtained from nanoindentation tests, work was carried out on an Al single crystal (100) sample. High purity bulk Al was chosen as it has a well-known modulus value of 70 GPa and a low hardness value. These properties make Al one of the ideal materials

used for area function calibration and load frame compliance calibration of nanoindentation machines. Moreover, Al is nearly elastically isotropic and its modulus value is independent of indentation depth (Bhushan and Li, 2003). Therefore, Al can be used to identify any changes in the modulus value due to the effect of pile-up.

To investigate the difference in pile-up appearance as well as its effect on the hardness and modulus values of thin films with different thicknesses, Al films were deposited on a hard glass substrate. A glass substrate was chosen as the Young's modulus of the glass and Al are relatively similar, thereby ensuring that any unusual behaviour in the obtained data cannot be related to the substrate effect. This consequently means that any unexpected behaviour can be attributed to differences in the plastic flow characteristics only. Also, despite the modulus values of these two components being approximately the same, the great difference in the hardness values (approximately 0.5 to 1 *GPa* for Al thin films compared with 7 *GPa* for glass (Saha and Nix, 2002)) makes them an ideal example system of a soft coating on a hard substrate.

#### *7.2.5.1 Bulk Aluminium*

A series of indentations were applied on the Al bulk sample under open loop mode for loads ranging from 0.1 to 4 *mN* and also displacement control for contact depths of less than 130 *nm*. The obtained hardness and modulus values for the Al bulk sample are shown in Figure 7-12. These tests were applied to investigate the hardness and Young's modulus of Al under different loads and contact depths and compare these results to those of Al thin films. The average hardness and Young's modulus values obtained from both tests for bulk Al are 0.45 *GPa* and 70.2 *GPa* respectively. The slight increases in the obtained data at shallow depths can be due to the thin layer of Al oxide near the surface for modulus data and the indentation size effect with regards to the hardness values.

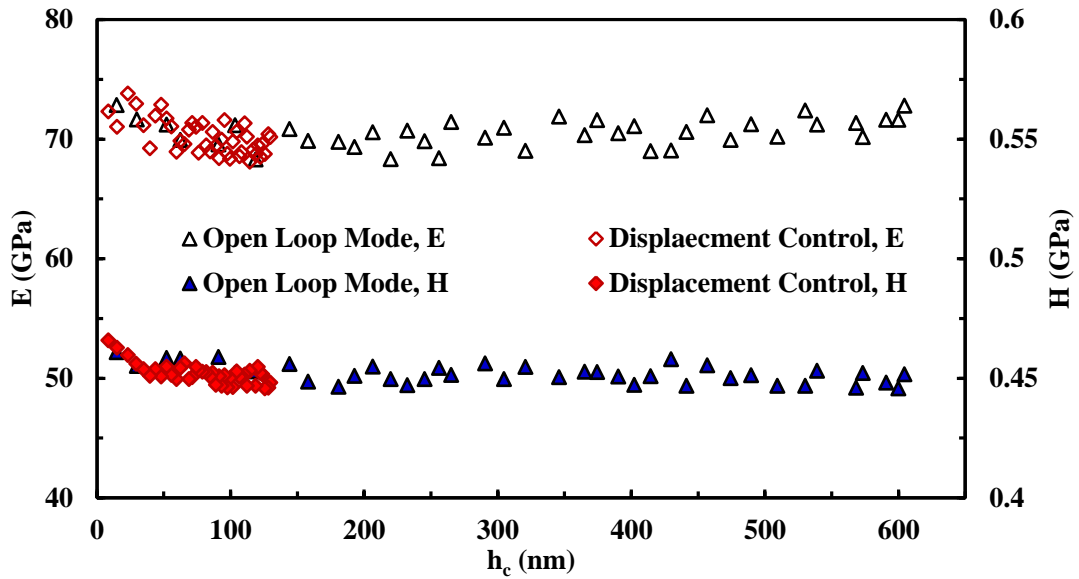


**Figure 7-12. Young's modulus (left) and hardness (right) values of bulk Al obtained under open loop mode and displacement control.**

The displacement control data were obtained for the contact depths less than 130 nm, and it was confirmed through the obtained AFM images that appreciable pile-up did not occur. Al has a low hardness value and consequently the aforementioned contact depths can be produced at very low loads. However, for the data obtained under open loop mode, it was expected that some pile-ups would be observed around the indenter imprint edges when the applied load is high. However, the hardness and Young's modulus values obtained from open loop mode are almost constant even at very high loads. When the AFM images were reviewed, it was observed that there were some evident, broad pile-ups around the indentation impressions at high loads. However, the shapes of pile-ups were different from those found on the bulk Cu samples and the effect on the hardness and Young's modulus values was extremely small.

The pile-up shapes (heights and widths) are shown in Figure 7-13 which illustrates several AFM images and the associated cross-sectional curves obtained from the single crystal Al sample indented at high loads. These are similar to the high load indentation tests undertaken on the bulk Cu sample and were performed to magnify the pile-up appearance and its effect on the hardness and modulus values of the bulk Al. These images, when compared to the bulk Cu AFM images (Table 7-1), confirm that the dislocation movements under the indentation tests are different from each other.

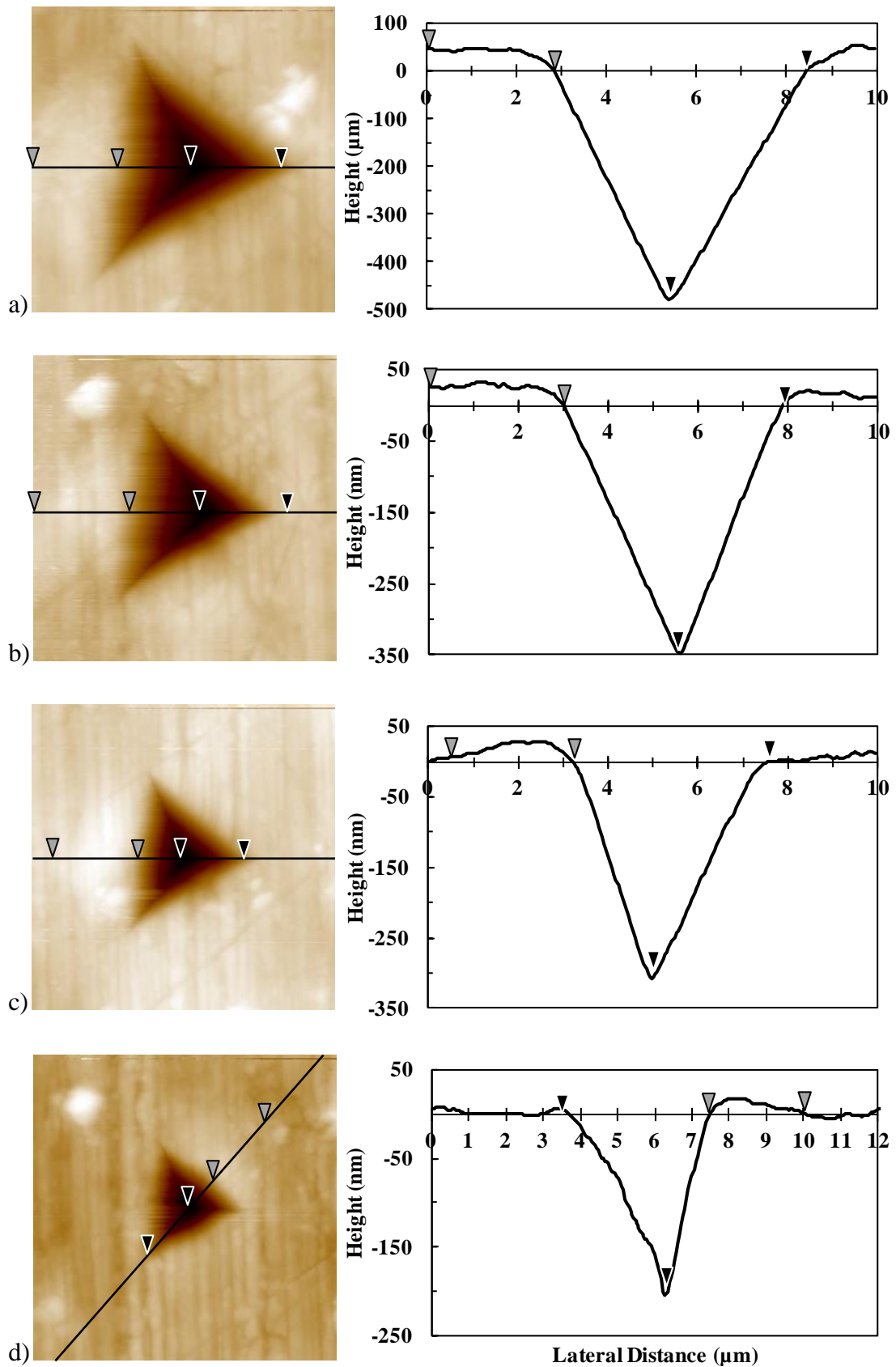


**Figure 7-13.** AFM images (left) and cross sectional information (right) of the drawn line in the image obtained from bulk Al after indentation tests under (a) 10 (b) 8 (c) 5 and (d) 2 *mN* loads for open loop mode.

Consequently, the pile-up effects for the obtained Al data differ from those associated with Cu. It should be noted that the volume of the pile-ups is related to the indentation volume for both materials, however the height and width characteristics of the pile-ups cause the differences in the effect of pile-up on the obtained values.

Since pile-up formation and its effect on the accuracy of the contact area measurement has been shown to have considerable influence on the obtained data, further work was carried out on the Al thin films to detect the presence of any substrate-induced enhancement of pile-up and to investigate its influence on the accuracy of the mechanical properties measured from thin films.

#### 7.2.5.2 Aluminium Thin Film

Two different high purity Al thin films with 375 nm and 1400 nm thickness, deposited on glass substrate, were investigated under open loop mode to detect the substrate and pile-up effects on the hardness and Young's modulus values obtained using nanoindentation tests. These two films were chosen to study the effect of the substrate on the appearance of pile-up in two different situations. The first situation is when the indentation penetrates greater than the film thickness (using the 375 nm thick film) and the second is when the indentation remains in the thin film but is affected by the harder substrate (using the 1400 nm thick film).

A series of indentations were conducted under open loop mode at very high loads for both thin films using the same indentation conditions. The hardness and Young's modulus values of the 1400 nm Al film obtained from both the Oliver and Pharr method and the actual contact area determined using the AFM images are shown in Figure 7-14 as a function of penetration depth. The obtained hardness values from the Oliver and Pharr method (shown with open circles in Figure 7-14) at small depths are around 0.7 GPa and increase to 1.8 GPa as the contact depth increases. The Young's modulus calculated using the Oliver and Pharr method also increases from 65 GPa at small contact depths to 112 GPa at higher contact depths. However, the results measured using the actual contact areas obtained from AFM images (shown in Figure 7-14 with filled circles) are much lower than those from the Oliver and Pharr method.

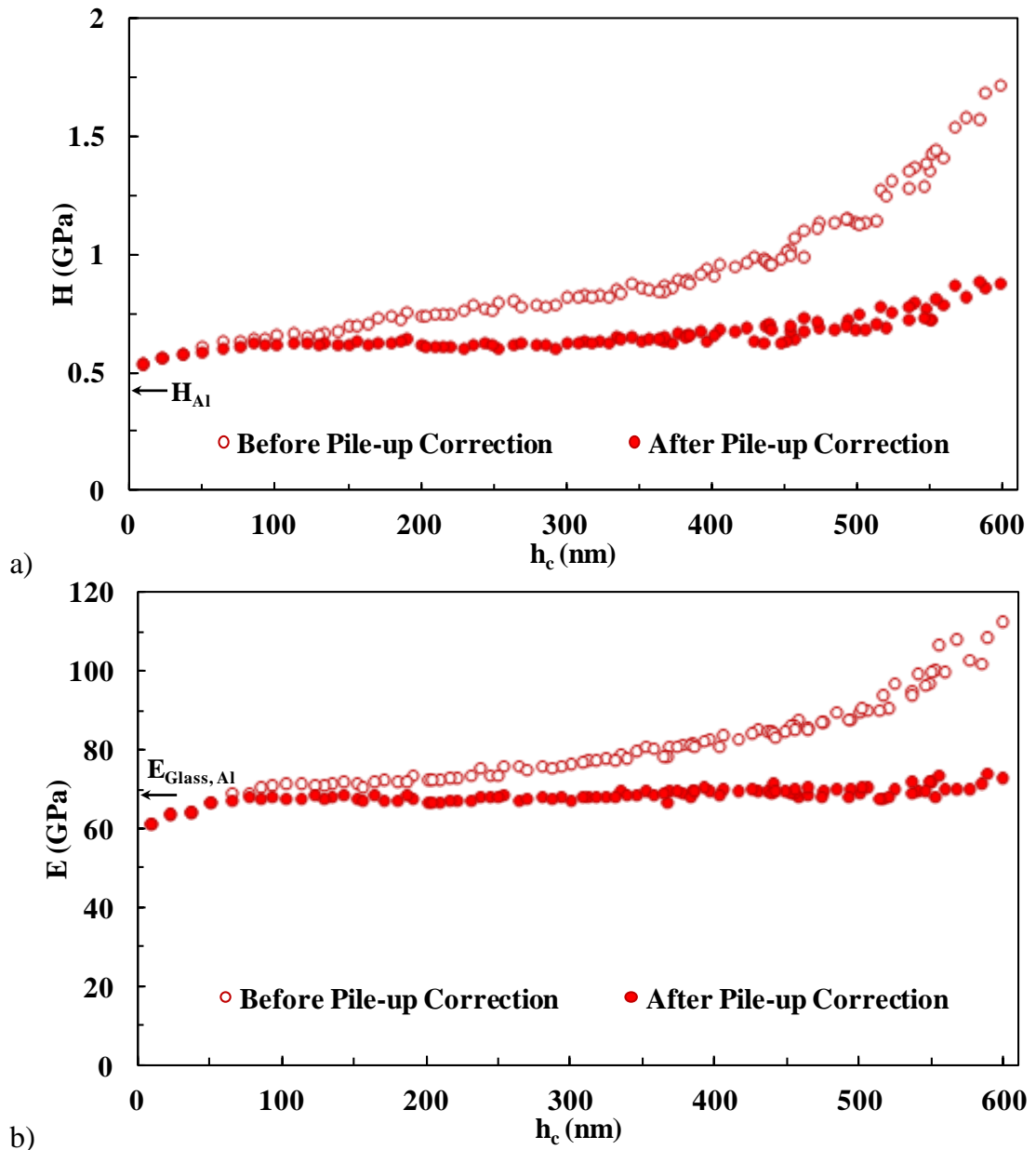


**Figure 7-14. (a) hardness and (b) Young's modulus values of 1400 nm thick Al film for before pile-up correction (measured using the Oliver and Pharr method) and after pile-up correction (measured using the actual contact area).**

These results show that the effects of pile-up on the Young's modulus and hardness values can alter the results from 5 to 30% and 10 to 45% respectively, depending on the contact depth. The average values of hardness and Young's modulus measured from actual contact area were almost constant at  $0.81 \pm 0.07$  GPa and  $69 \pm 2$  GPa respectively. These results are in agreement with nanoindentation measurements of thin Al films on a glass substrate reported by Tsui and Pharr (Tsui and Pharr, 1999). When data was compared to that of 375 nm Al film shown in Figure 7-15, it was observed that the hardness values are higher than the 1400 nm film even at very

small indentation depths and that they increase as the contact depth increases. This is in good agreement with the hardness and Young's modulus measurements of Al films deposited on glass substrate stated by Saha and Nix (Saha and Nix, 2002). This increase is due to the influence of the hard glass substrate beneath the Al film. However, the increase in the hardness values for the contact depths of less than 300 nm is almost steady and is mainly due to the pile-up effects on the actual contact area measurement.

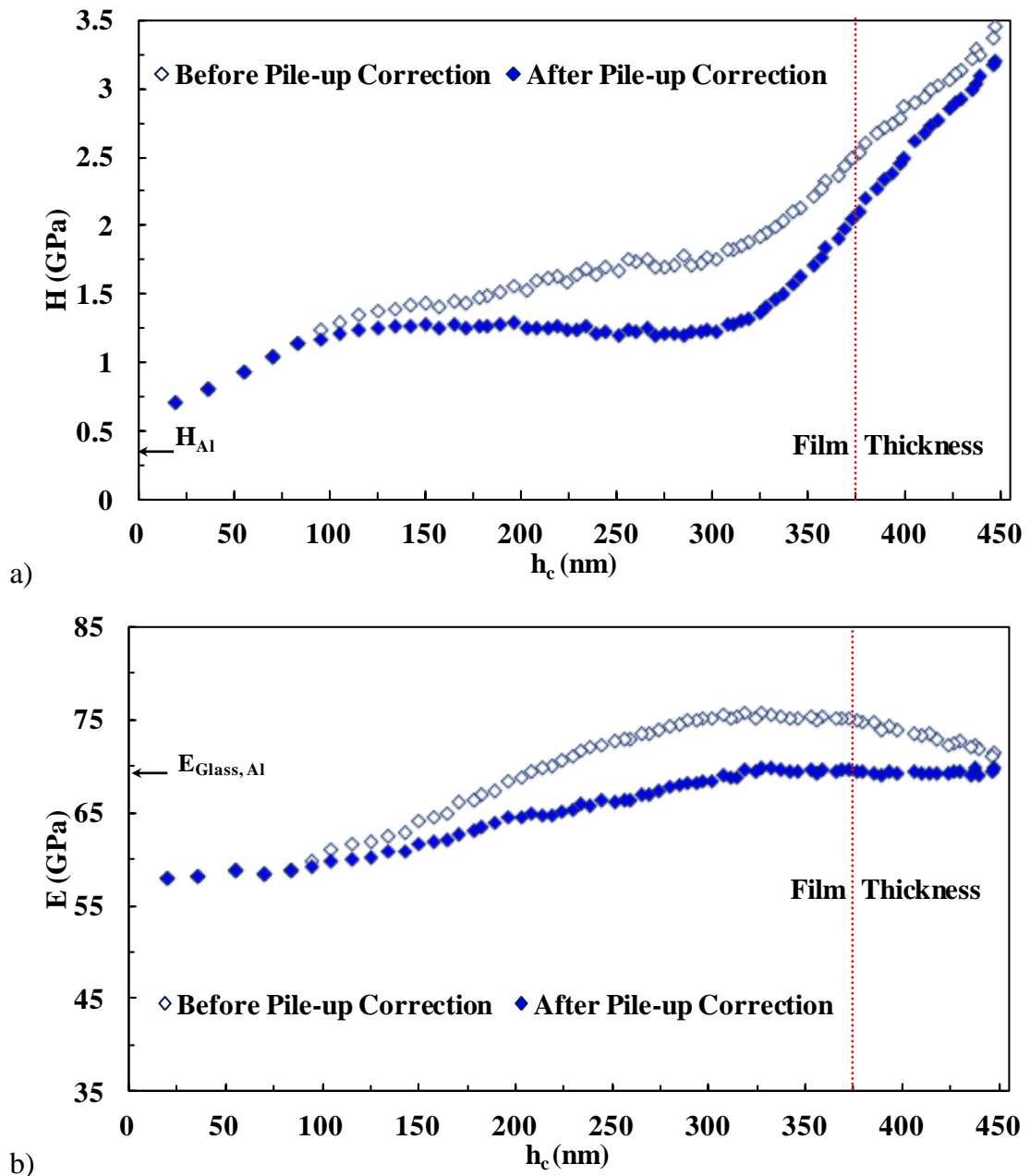


**Figure 7-15. (a) hardness and (b) Young's modulus values of 375 nm thick Al film, before pile-up correction (measured using the Oliver and Pharr method) and after pile-up correction (measured using the actual contact area).**

At a contact depth of approximately 300 nm, which is approximately a maximum indentation depth of 325 nm, the hardness increases rapidly while the pile-ups get slightly smaller and the effect on the actual contact area reduces. When approaching the film thickness, the glass substrate begins to have an even bigger effect on the obtained data and suddenly start to control the dislocation movements.

Similar behaviour is also observable in the Young's modulus results. For the contact depths lower than 300 nm, the obtained Young's modulus data increases with increasing contact depths and is similar to that of the 1400 nm Al film. However, the obtained values start to plateau for about 40 nm after this and eventually decrease when the substrate influence dominates over the pile-up effect. This is due to the residual contact impression as well as a transition in the characteristic profile from indentations in the soft Al film with straight-sides to indentations in the hard bulk glass with a cusp-like shape at the bottom of the unloading curve (Tsui and Pharr, 1999).

Although both the thin film and glass have similar Young's moduli, the glass has a higher hardness value, requiring a higher contact pressure and consequently a greater fraction of the total displacement is elastic. Therefore, during the indentation, the elastic displacement recovery of the Al is much smaller than that of the glass. Figure 7-16 illustrates a schematic representation of the physical indentation process for a soft thin film deposited on a hard substrate in which the maximum contact depth ( $h_{max}$ ) is (a) less than the film thickness ( $h_f$ )  $h_{max} < h_f$ , (b) similar to the film thickness  $h_{max} \approx h_f$  and finally (c) penetrating in to the glass substrate  $h_{max} > h_f$ .

As can be seen from Figure 7-16 (a), the loading and unloading of the indentation tip is entirely reliant on the Al film and its displacement recovery. However, as there is a hard glass substrate, the quantity of pile-up appearing around the indenter is higher than when examining bulk Al. The obtained results are therefore highly dependent on the degree of pile-up appearance. When the indenter is closer to the substrate but still remaining in the film (b), the hardness and modulus values depend on the thin film's elastic recovery with influences from the hard substrate and pile-up. However, in the scenario in which the indentation penetrates deeper than film thickness (c), both the film and the substrate affect the loading and unloading parts of the load-displacement curve.

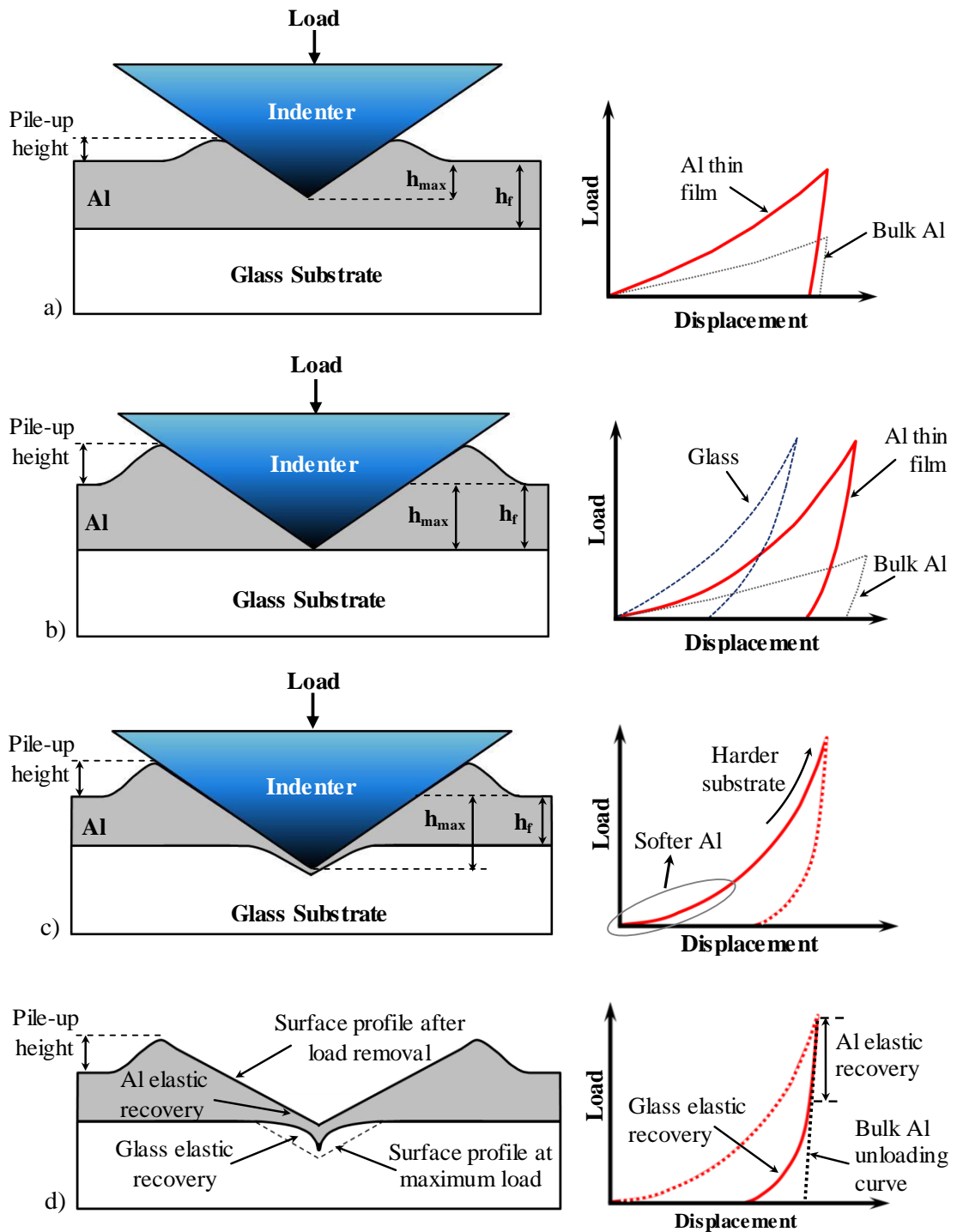


**Figure 7-16.** Schematic representation of the physical indentation process and relative load-displacement curves for the soft Al thin film deposited on a hard glass substrate showing the following scenarios: (a)  $h_{max} < h_f$ , (b)  $h_{max} \approx h_f$ , (c)  $h_{max} > h_f$  and (d) representing elastic recovery for both Al and glass for the position (c) when the indenter is removed.

As the Oliver and Pharr method relies on the unloading part of the load-displacement curve, it is important to understand what physically occurs during the unloading of the indentation. As shown in Figure 7-16 (d), after a small amount of unloading, the

indenter comes out of the contact with the Al thin film around the edges of the indenter as Al has less elastic recovery than glass. Consequently, the subsequent elastic recovery is controlled by the harder glass substrate that quickly dominates the unloading curve. As the glass substrate has a greater elastic recovery than the Al, the unloading curve is different to that obtained from bulk Al. As the contact stiffness is obtained from the unloading part of the load-displacement curve and the obtained mechanical properties are strongly dependent on the measured stiffness, any changes in the curve can have an effect on the obtained data when using the Oliver and Pharr method. To investigate how the variations on the bottom part of the unloading curves affect the obtained data, the power-law fittings were studied for the Al, Au and Cu thin films. This is described in more detail in next section.

### **7.3 The Importance of Power-law Fitting**

As mentioned previously, the mechanical properties obtained from nanoindentation tests using the Oliver and Pharr method rely on the power-law relation ( $P = \alpha (h-h_f)^m$ ), which was described in detail in section 2.1.2. A soft material, Al for instance, with a very small elastic recovery during the unloading segment of the indentation test, has a nearly vertical unloading curve. Therefore, during the analysis of the obtained load-displacement curves, the unloading data fits very effectively to the power-law relationship, even at the very bottom of the unloading curve. However, for hard materials such as glass, there is a greater elastic recovery during the unloading segment. These differences between the materials with regards to their elastic recoveries can have a significant influence on the unloading part of the indentation test. Therefore, the ISO standard (ISO/FDIS, 2002) in the fitting procedure for nanoindentation testing specifies that the upper 80% of the unloading data be used. However, when testing soft thin films such as Al, Au or Cu on hard substrates such as glass or silicon, the differences in the elastic recovery can influence the unloading curve and consequently the obtained data. To observe the effect of the power-law fitting on the Young's modulus values obtained from the thin films, the power-law fitting was set to different percentages of the unloading segment of the load-displacement curves. The upper limit of the fit was set at 95% for all the obtained data to minimise the effect of creep on the obtained data. Creep and its effect on the nanoindentation test results will be discussed later in this chapter. The lower limit of

the power-law fitting was set to between 10% and 50% of the unloading curves. The average Young's modulus results obtained from the Au and non-annealed Cu thin films deposited on the silicon substrate and the Al thin films deposited on glass substrate are shown in Figure 7-17. It should be noted that after measuring the contact stiffness at different percentages of the power-law fit, the actual contact areas obtained from AFM images were used to measure the reduced modulus and consequently Young's modulus.

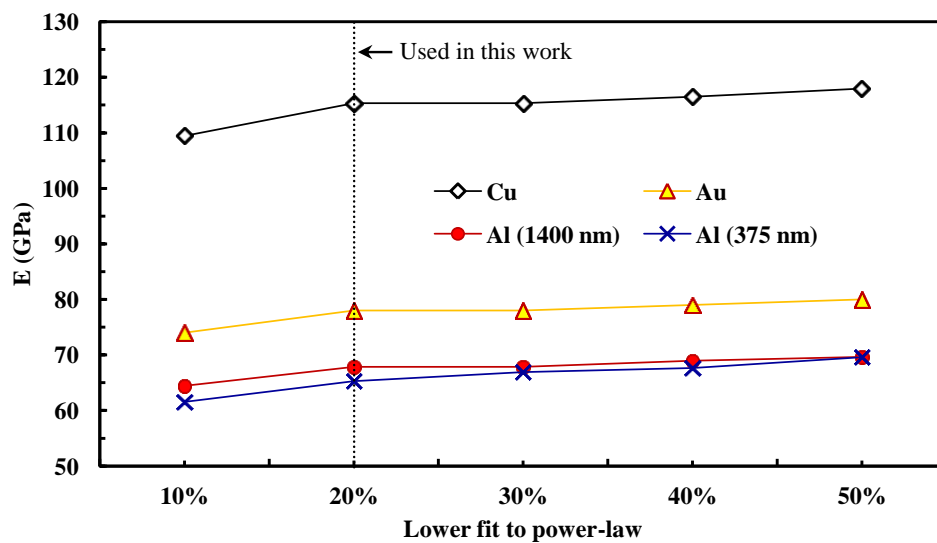


**Figure 7-17. Young's modulus data obtained by the Oliver and Pharr method for the single indentations using different percentages of the power-law fitting to the unloading curves for various thin films.**

The black dashed line in the figure shows the power-law fit used in this study which indicates that the lower and upper limits for fitting were 20% and 95% of the unloading curve of the load-displacement curves respectively. It can be seen that the obtained data for all four thin films at the 10% fit were smaller than at higher fit limits. The change from 10% to 20% lower fit increased the obtained modulus values by nearly 5% for all of the thin film values. This is due to the bend on the unloading curve near the end of indentation unloading due to the elastic recovery of the materials. However, when the fits were increased to 30% and 40% of the lower part of the curves, the Au, Cu and 1400 nm Al films did not show any significant variation. Additionally, the obtained values were increased slightly by less than 2% from the upper 45% of the total fit to the unloading curves (50% lower fit and 95% upper fit).

However, the modulus values obtained from the 375 nm Al thin film act differently to some extent and were found to increase consistently when raising the lower fit limits. The result was increased by 6.1% when the limit was changed from 20% to 50%. The increases in the modulus values are due to the use of very high loads and contact depths for the 375 nm Al film. As a result, at the maximum contact depths, which are larger than the film thickness, the substrate influences the unloading displacement by changing the elastic recovery in the obtained curve from being controlled by Al to being controlled by glass. Therefore, the effect of the substrate on the unloading part of the load-displacement curve is much bigger than in the other thin films. As mentioned before, this is due to the bend on the unloading curves caused by the elastic recovery of the glass substrate. Therefore, the fit underestimates the slope of the curve from which the stiffness is derived due to the change in the lower portion of the curve and as a result, causes a decrease in the calculated modulus values.

Although the effect of the limit set to the unloading curves for the data obtained from the Au, Cu and 1400 nm Al thin films was minute, the obtained data confirmed there is a 2% increase in Young's modulus when using the upper 45% portion of the unloading curve. One of the causes for these slight differences on the results for all thin films can be the effect creep deformation in the films during the indentation tests. A solution to minimise the effect of creep on the obtained data was to set the upper fit to 95% of the unloading curve; this can minimise but not remove the effect. Creep and its effect on the mechanical properties obtained from nanoindentation tests are described in more detail in next section.

#### **7.4 Creep**

One of the potential problems with extracting the mechanical properties of metals at room temperature using indentation tests is creep. As mentioned previously in section 2.3.1, creep takes place because of time-dependent plastic flow with extreme effects occurring for soft and low melting point materials. Creep can occur during the nanoindentation test as it is characterised as deformation under the influence of mechanical stress. In most cases indentation creep is different from the creep that occurs in bulk mechanical tests at high temperature and is akin to the primary creep rather than steady-state creep which is usually measured.

At high temperatures, it should be noted that there are two different mechanisms through which creep occurs in materials under stress; diffusion creep and dislocation creep. Diffusion creep takes place by material transport by the diffusion of atoms within a grain which is driven by a gradient of free energy created by stress. Atoms within a material can move inside grains, along grain boundaries or in pore spaces. Therefore, diffusion creep can be divided into two different types which depend on the diffusion paths. If the diffusion paths are predominantly through the grain boundaries and diffusion occurs along the grain boundaries, diffusion creep is Coble creep or grain boundary diffusion. However, if the diffusion paths are through the grains themselves and diffusion occurs within the main body of the grain, diffusion creep is bulk diffusion (volume-diffusion) called Nabarro-Herring (NH) creep. In both types of diffusion creep, the rate of creep can be reduced by increasing the grain size.

Dislocation creep is a creep mechanism which is controlled by the movements of dislocations and tends to dominate at high stresses and comparatively low temperatures. Dislocation creep can occur at low temperatures as the dislocations can move by gliding in a slip plane which requires low thermal activity. During the nanoindentation test a highly stressed region is created beneath the indenter after loading. Dislocations in the stressed volume can move in response to this stress if there is sufficient thermal activation and will migrate to lower stress regions. Thus initially there will be some creep but this will drop to zero after a short time, so-called exhaustion creep. For low melting point materials it is possible that some steady-state creep is observed even at room temperature but mostly this is small.

Creep can have a remarkable influence on both the hardness and modulus results if it is not taken into consideration. The effect can however be made much smaller if the load hold at peak load before unloading the indentation is chosen carefully (Baker *et al.*, 1991; Feng and Ngan, 2002). According to Chudoba and Richter, the holding time at the maximum load is correctly chosen if the loading period at the maximum load is sufficiently long that the depth increase in one minute is reduced to less than 1% of the indentation depth. The significance of the creep effects on the hardness and modulus values is dependent on the creep rates of the material as well as the loading and unloading rates of the indentation (Chudoba and Richter, 2001).

#### 7.4.1 High Melting Point Materials

When materials with high melting points ( $T_{mp}$ ) such as Cu (1085 °C) and Au (1064 °C) are tested at room temperature ( $T$ ), the homologous temperatures ( $T_H$ ) are sufficiently low that the creep rate is not expected to be significant. Due to their high melting temperature, insufficient thermal activation is available at room temperature to assist diffusion (Shen *et al.*, 2012). However, creep does occur and the effect must be dealt with as part of the test protocol. When creep is high, a distinct nose can be seen in the unloading portion of the load-displacement curves (Feng and Ngan, 2002). This is nonetheless not always the case and sometimes creep will change the maximum depth during the hold period at maximum peak load; this is more likely to occur under open loop mode. No noses were observed in the load-displacement curves for Cu and Au thin films using open loop mode in this study, due to the 4 second hold time before unloading. Moreover, the tests conducted under displacement control do not show this feature as the feedback parameters were correctly set and creep was minimised. Some examples of load-displacement curves obtained from the bulk Cu under displacement control are shown in Figure 7-18.

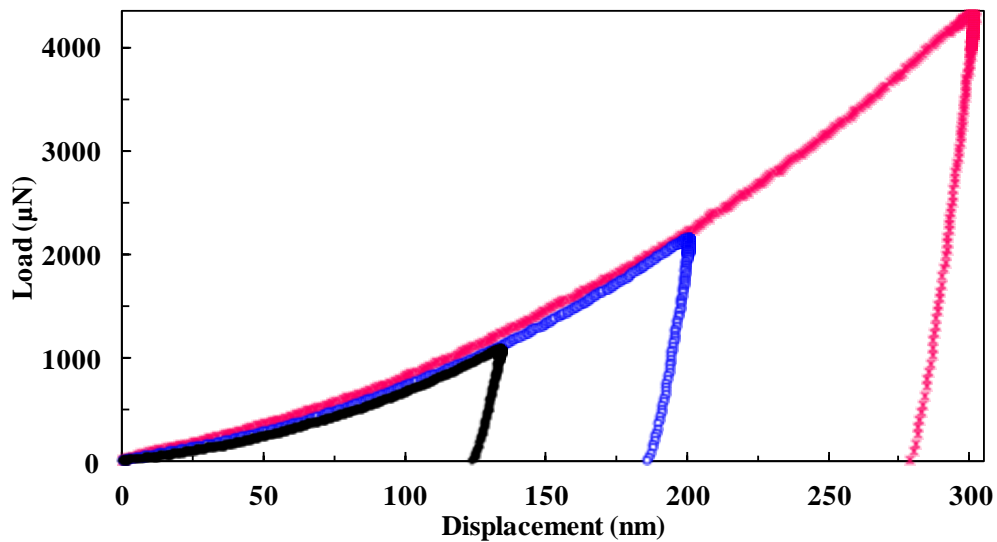


**Figure 7-18. Load-displacement curves obtained from bulk Cu under displacement control showing no creep effect on the curves at three different peak loads.**

As can be seen from Figure 7-18, the unloading curves decrease linearly and the power-law was fitted to the unloading curves very effectively. Additionally, the holding period at the maximum displacement (peak load) did not modify the maximum depth of the indentation. With regards to the open loop mode, there are

two different techniques to confirm the presence of creep from the load-displacement curves. The first technique is based on examining the consistency of the applied peak load from several indentation tests using the same load. Figure 7-19 presents several examples of the load-displacement curves obtained under open loop mode with peak loads that were expected to be  $500 \mu N$ . However, it can be seen that the loads differ from each other and that they did not reach the expected maximum load. Although the discrepancies between the maximum loads for the curves are minute, they need to be considered when the precision of the data is on the nanoscopic scale.

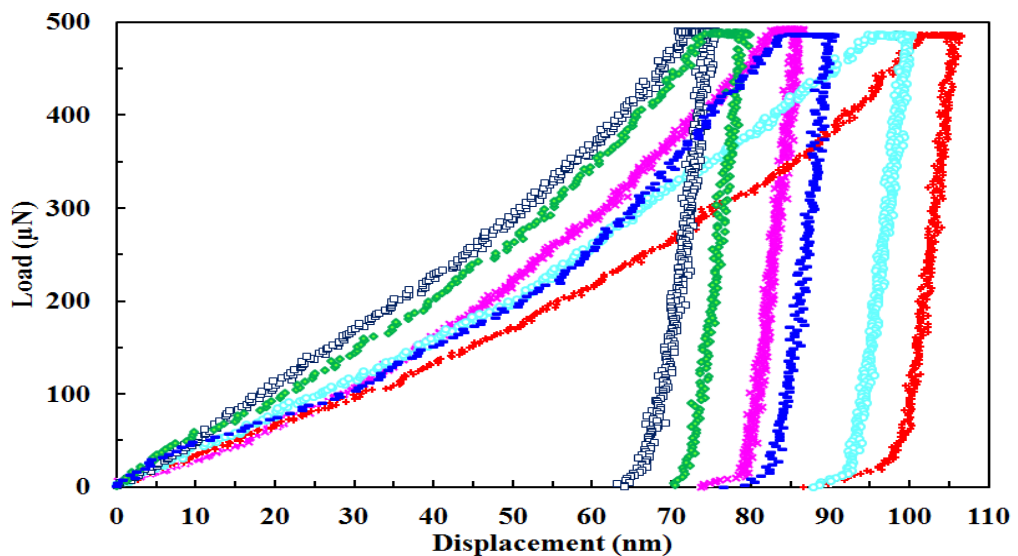


**Figure 7-19. Examples of load-displacement curves obtained under open loop mode for bulk Cu presenting creep behaviour at the maximum load and failure to attain the preferred load.**

The second method is based on the holding period at the maximum load before unloading. The hold at the maximum peak load can change the maximum penetration depth which increases the contact stiffness and consequently changes the obtained data. Figure 7-20 illustrates some examples of load-displacement curves obtained for bulk Cu under open loop mode with a 20 second holding period at the maximum load before unloading.

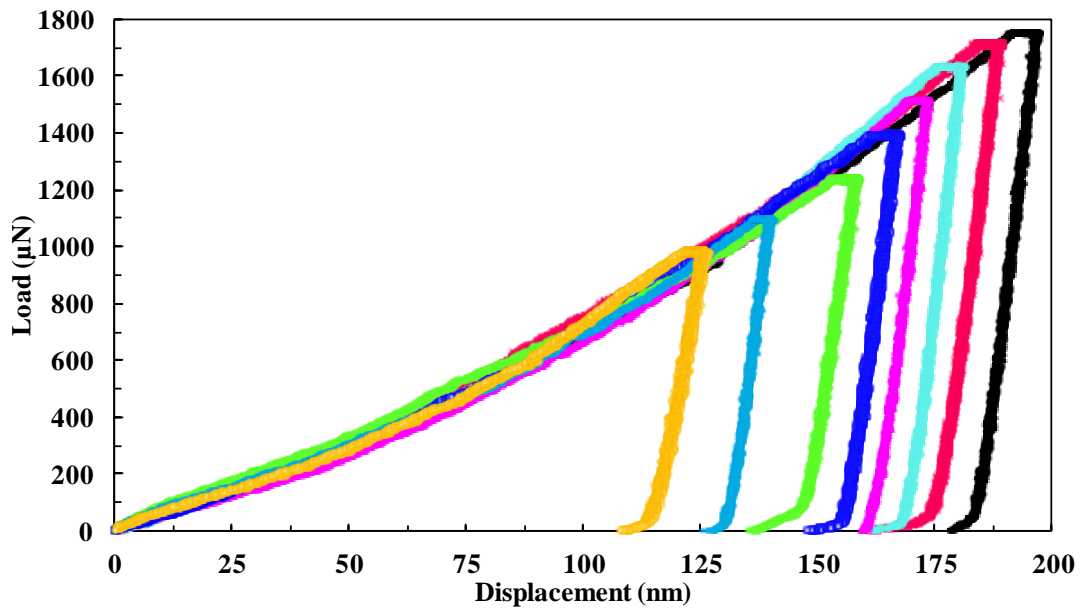


**Figure 7-20. Examples of load-displacement curves obtained for bulk Cu under open loop mode that illustrate the changes in the maximum contact depths due to creep occurrence.**

As can be seen, there are no obvious noses at the beginning of the unloading curves and by setting the upper fit of the power law to 95%, the effect of the creep can be minimised. However, the change in the displacement at the maximum load of a few nanometres can have an effect on the obtained contact stiffness and therefore the obtained modulus values. This also can modify the measured contact area consequently affecting the obtained hardness values. This confirms that choosing an appropriate holding time at the peak load before unloading is important to minimise creep. To identify the appropriate holding period for minimising creep and its effect on the obtained data, both the bulk and thin film Cu samples were investigated under open loop mode and displacement control using a range of holding periods at peak loads.

It was observed that the modulus values for both types of sample using hold periods of less than 30 second were relatively constant. However, the data obtained for Cu thin films when using a holding period of greater than 30 s shows some variation in the modulus results. Depending on the film thickness and indentation depth, this can be caused by the substrate influencing the appearance of the creep and its consequent effect on the obtained data for thin films. As an example, contact modulus values obtained from non-annealed Cu thin film and (111) bulk Cu under displacement

control at a 40 nm contact depth are shown in Figure 7-21. A contact depth of 40 nm was chosen to avoid any pile-up effects.

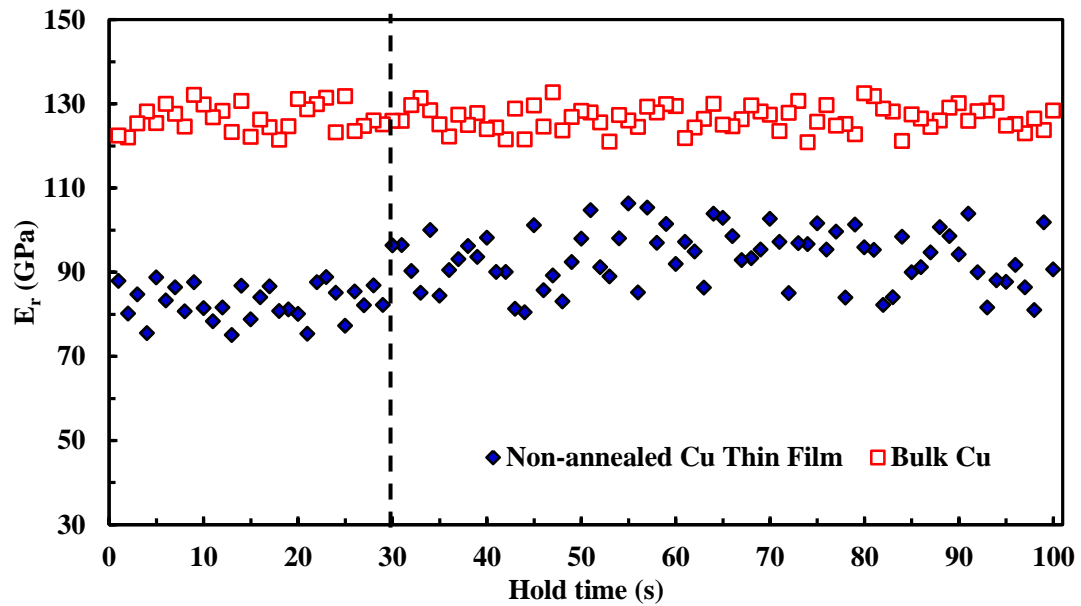


**Figure 7-21. Contact modulus values obtained from non-annealed Cu thin film and (111) bulk Cu under displacement control at 40 nm contact depth.**

The average contact modulus values for non-annealed Cu thin film increased from  $83 \pm 4$  GPa to  $93 \pm 6$  GPa for the data obtained when using more than a 30 second hold at peak load. The black dashed line shown in the figure shows where this variation starts. Although there is some variation in the obtained data that needs to be considered, it is very small in comparison to that found in the results of materials that show a significant creep effect. The creep effects for materials with low melting points such as Sn or zinc (Zn) when tested at room temperature can be as large as 20%. Additionally, when the load hold period is of a sufficiently long duration, thermal drift correction also starts to show some variation. The Hysitron Triboindenter corrects the obtained data for thermal drift using a linear fit, but the temperature variation in the lab shows a sinusoidal behaviour as the heater is repeatedly switched on and off to maintain a constant average temperature. The obtained data shown in Figure 7-21 illustrates to some extent this behaviour. It is therefore important to choose an appropriate load function which has a correctly selected loading rate, holding period and unloading rate when using nanoindentation tests.

Regulating the displacement rate under displacement control is another way of controlling creep which can control and detect the potential errors on the obtained hardness and modulus values. Furthermore, in open loop mode, creep effects can be minimised by controlling the loading and unloading rate of the indentation. To detect and also investigate the effects of loading, unloading and displacement rates on the obtained modulus values on Cu, work was carried out using both open loop mode and displacement control. To identify the creep effect under open loop mode, 100 single indentations were applied to both the bulk Cu and the non-annealed thin film at different loading and unloading rates ranging from 20 to 2000  $\mu\text{N/s}$ . Both the hardness and Young's modulus values obtained from the open loop mode are shown in Figure 7-22 for bulk Cu. Similar behaviour was found for the non-annealed Cu thin film. The maximum applied load was set at 500  $\mu\text{N}$  as the previously obtained results for Cu samples confirmed that pile-up and consequently its effect is negligible on the obtained data when using this condition.

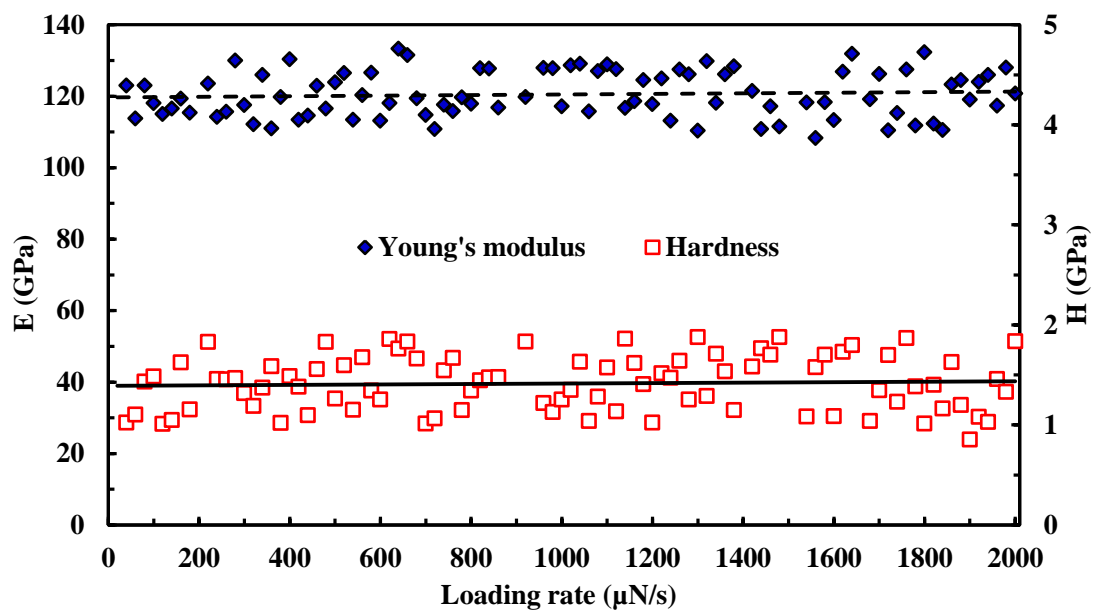


**Figure 7-22. Hardness and Young's modulus values obtained from bulk Cu under open loop mode using a 500  $\mu\text{N}$  load at diverse loading rates.**

These results confirm that the loading and unloading rates do not show a significant effect on the obtained data under open loop mode for materials with high melting points, such as Cu, when tested at room temperature. Additionally it has been confirmed that the obtained results are satisfactorily close to the expected values for both bulk and thin film Cu. To further identify any creep effect on the data obtained under displacement control, work was carried out at a 40 *nm* displacement using

different displacement rates ranging from 5 to 500 *nm/s*. The hardness and Young's modulus values obtained from different displacement rates on bulk Cu are shown in Figure 7-23. The results from the thin Cu film are not shown as they displayed similar behaviour to that of bulk Cu.

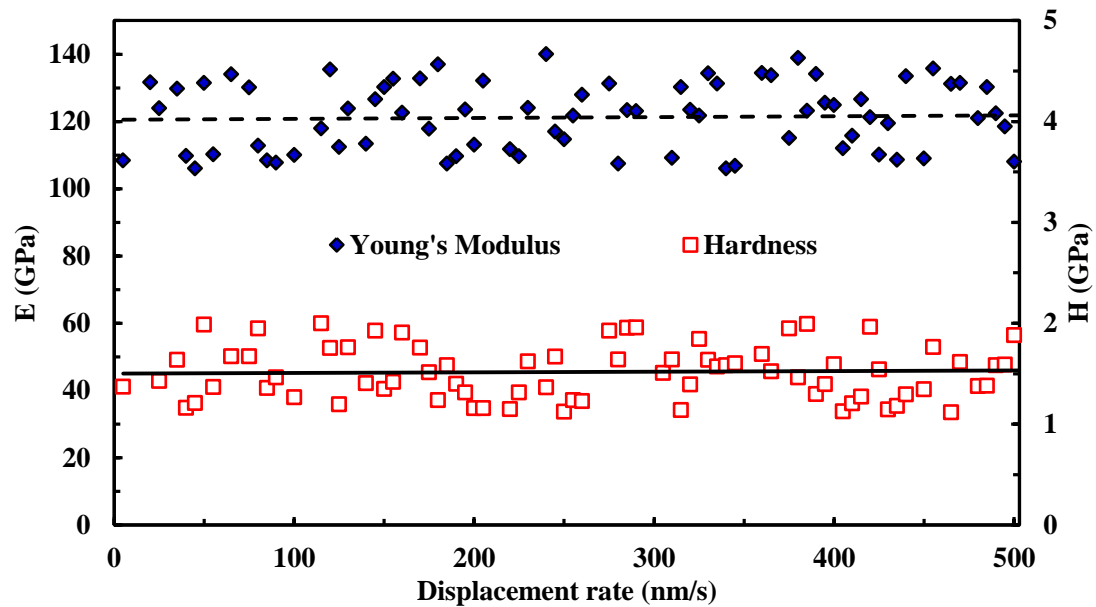


**Figure 7-23.** Hardness and Young's modulus values obtained from bulk Cu under displacement control at a 40 *nm* contact depth at diverse displacement rates.

As shown in Figure 7-23, for bulk Cu there is slight scatter in the hardness data when using displacement rate control however, the Young's Modulus values are almost constant at 120 *GPa*, which is the expected value for polycrystalline Cu. As mentioned previously, the creep effect, which modifies the data obtained for materials with low melting points such as Sn, is significant. Therefore it is important to understand how to minimise the creep effect on the data obtained from nanoindentation techniques. Hence, further investigation was carried out on the bulk Sn sample to justify the choice of the operating mode applied to obtain the hardness and Young's modulus values in this work.

#### **7.4.2 Low Melting Point Materials**

As mentioned in Chapter 6, to obtain the mechanical properties of Sn samples in this work the data was obtained under displacement control rather than open loop mode. This was chosen because when testing soft metals such as Sn and Zn with time dependent properties and low melting points (231.9 °C and 419.5 °C respectively) at

room temperature, they show faster creep rates under the indentation tests. Therefore, extracting mechanical properties using nanoindentation techniques with minimised creep effects on the data is a big challenge for such materials. The test protocols consequently need to be correctly set in order to minimise or, even in some cases, to avoid the creep effect on the obtained data.

As mentioned earlier, as the feedback parameters were correctly set for the tests conducted under displacement control, there probability of changes in the contact depths and contact stiffness caused by creep was reduced. The obtained data for the Sn samples demonstrated in this work in section 6.3 were all collected under displacement control to keep the creep effect at a minimum level. However, under open loop mode for different protocols, the appearance of a nose was confirmed in the obtained load-displacement curves. Therefore the first step in creep correction was to remove the nose in the unloading curves. It was for this reason that displacement control mode was chosen. Three different load-displacement curves obtained under open loop mode and displacement control from a bulk Zn sample are shown as examples for comparison in Figure 7-24. All three curves were obtained using loading and unloading rates of  $50 \mu\text{N/s}$  with different hold periods at the maximum load.

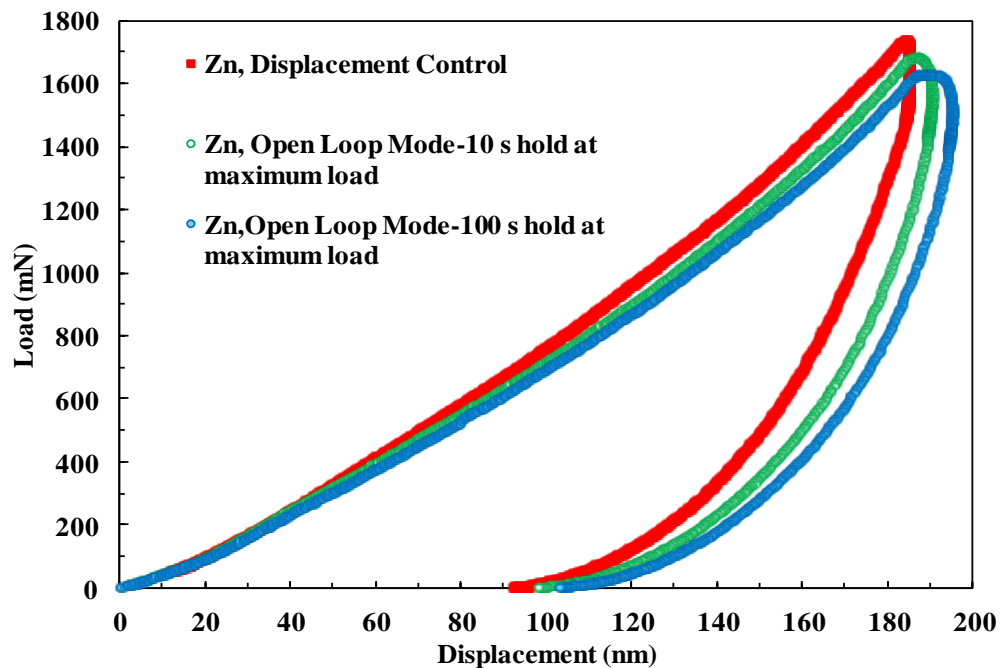


**Figure 7-24.** Load-displacement curves obtained using open loop mode with two different holding periods at the maximum load and displacement control from bulk Zn samples.

As can be seen from Figure 7-24, the load-displacement curves obtained from open loop mode for both curves show an obvious nose at the beginning of the unloading part of the curve. However, under the same conditions, the load-displacement curves obtained from displacement control do not show any nose. Similar behaviour was obtained for the Sn sample tested in this work and examples of the load-displacement curves obtained using both protocols were shown in Figure 6-9 in Chapter 6.

When the data obtained from the bulk Zn and Sn samples under both open loop mode and displacement control were examined, it was found that there was considerable scatter on both the hardness and modulus values, however the hardness values show less scatter than the Young's modulus data. To illustrate this, the obtained hardness and modulus values under displacement control for bulk Zn sample are shown in Figure 7-25.

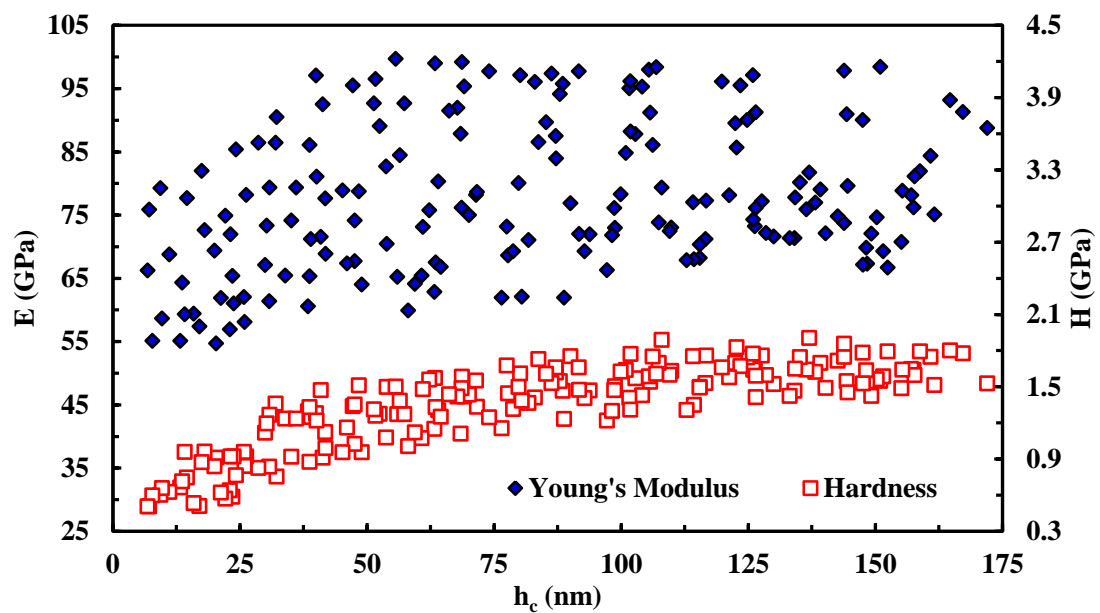


**Figure 7-25. Comparison of nanoindentation tests performed on bulk Zn sample showing the Young's modulus (left) and hardness (right) under displacement control.**

There are two important reasons to explain the large scatter in the obtained modulus data. Firstly, polycrystalline Zn has a close packed hexagonal structure and is an anisotropic material. Therefore, the crystallographic orientation of Zn can have a significant effect on the obtained data and as the bulk Zn sample used in this study contains large grains, the orientation of individual grains can consequently massively influence the obtained modulus values. However, extracting mechanical properties from Zn with a high creep rate requires a load function that minimises the creep

effect and provides accurate results. The slight reduction at the beginning of the graph can be attributed to the indentation size effect.

To detect the anisotropy effect on the modulus data for bulk Zn, 4 different large grains were identified. In each individual grain, 4 single indentations were applied under displacement control at displacements ranging from a 50 to 80 nm contact depth. The modulus values from these indentations are shown in Figure 7-26.

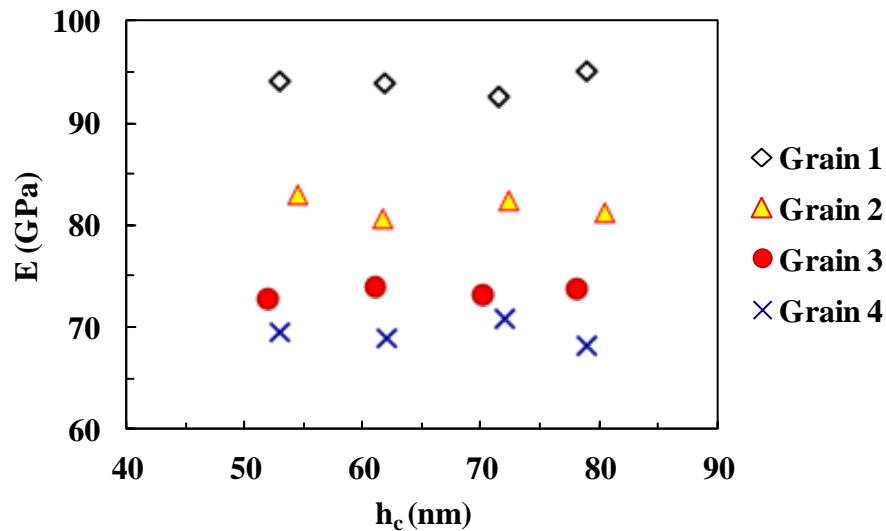


**Figure 7-26. Young's modulus values of bulk Zn obtained under displacement control from different large grains.**

When dealing with anisotropic materials such as Zn it therefore needs to be considered that the scatter in the results can be due to the crystallographic orientation of individual grains rather than experimental variability. Consequently, to detect the effect of creep on the obtained data, two different methods were used. The first method was based on the Feng and Ngan method (Feng and Ngan, 2002) which is dependent on the total displacement rate and the second method was based on the indentation strain using the obtained displacements. Both methods will be described in greater detail.

Feng and Ngan provide a method to detect any creep effect during the indentation cycle and if detected, they provide a correction method to remove the effect from the obtained data. In their method they present an equation for the creep factor ( $C$ ), based on the total displacement rate recorded at the end of the load hold ( $\dot{h}_h$ ) to

measure the importance of creep over the elasticity. This equation defines the creep factor as:

$$C = \frac{\dot{h}_h^c S}{|\dot{P}|} \quad (7-1)$$

In this equation,  $S$  is the contact stiffness,  $\dot{P}$  is the unload rate at the onset of unload and  $\dot{h}_h^c$  can be calculated from the difference between total displacement rate ( $\dot{h}_h$ ) and thermal drift rate ( $\dot{h}^t$ ) as  $\dot{h}_h^c = \dot{h}_h - \dot{h}^t$ . Therefore, for comparison, the data obtained from the bulk Sn sample under both open loop mode and displacement control was checked for creep using Equation (7-1). The creep factor using Equation (7-1) for data obtained under displacement control was 0.0135, which is an order of magnitude smaller than that of open loop mode with a creep factor of 0.24. This method was used to obtain the creep factor for different materials used in this work. The obtained creep factors for these materials are plotted against their homologous temperature ( $T_H = T/T_{mp}$ ) in Figure 7-27 for a comparison between the open loop mode (shown with open symbols) and displacement control (shown with filled symbols). It should be noted that to determine the homologous temperature, room temperature was assumed to be 298 K.

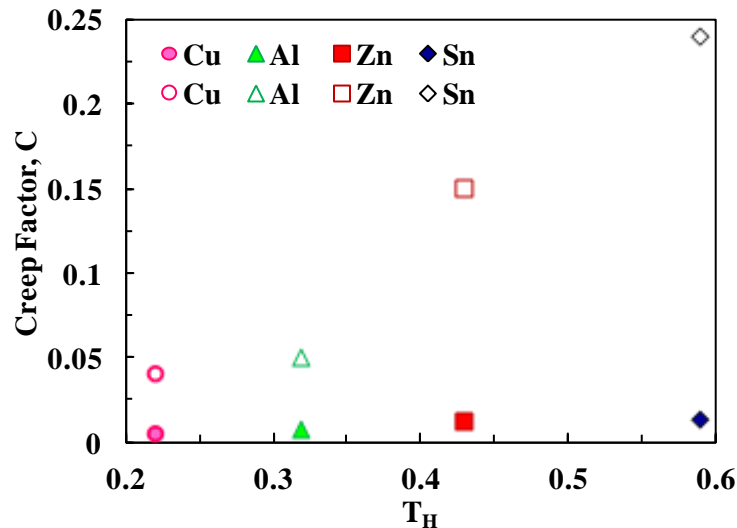


**Figure 7-27. Creep factor obtained from Fang and Ngan method for four different materials versus their homologous temperature ( $T_H$ ); open symbols represent the open loop mode data and filled symbols represent the displacement control.**

The calculated data shows that under displacement control the creep effect can be minimised to an acceptable error margin, even when using materials with high creep

rates. However, when using open loop mode for materials such as Sn and Zn with high creep rates, the creep factors are much bigger than that of Cu and Al which have lower creep rates due to their high melting points. There are however some creep effects for both Cu and Al, but both are less than 5%. It was expected to observe even larger creep factors under open loop mode for bulk Sn and Zn samples, however the obtained data confirmed that the effects are measured at 24% and 15% respectively.

This data illustrates that even under displacement control creep does occur during the indentation tests, but the effect can be minimised by choosing the correct load function. Consequently, in this work during the indentation tests, displacement control was predominantly used to produce a negligible creep effect on the obtained data, especially for materials with a high creep rate, such as Sn.

The obtained data can be also examined for any creep effect by studying the creep strain data plotted against the holding time at the maximum load. The creep strain or indentation strain can be calculated by dividing the change in displacement by the displacement at the start of the hold period at maximum load. The typical calculated behaviours of the materials with different creep rates used in this work under nanoindentation tests are shown in Figure 7-28.

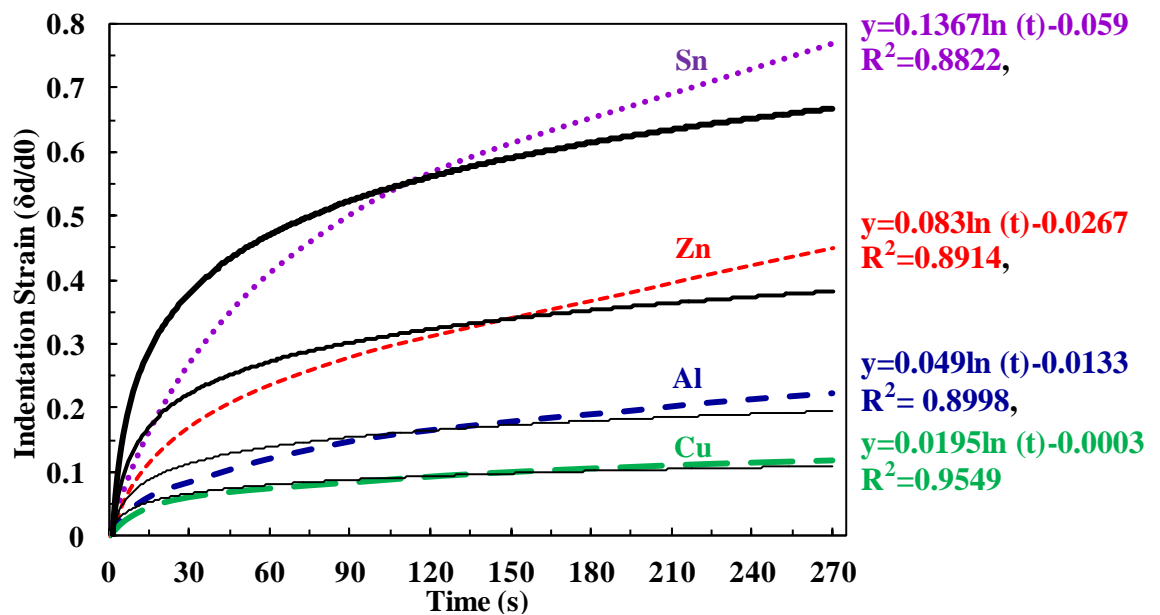
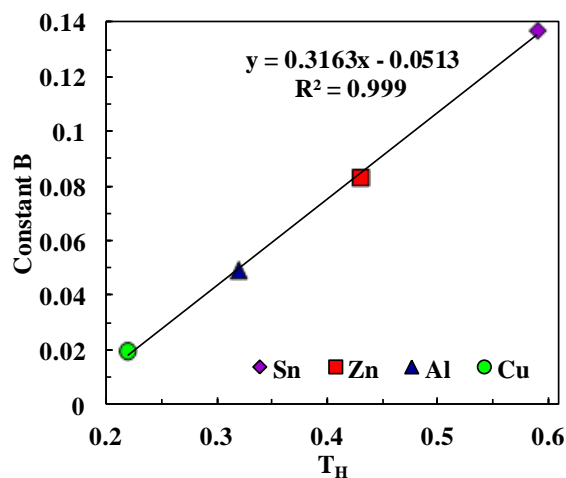


Figure 7-28. Creep behaviour comparison of bulk Sn, Zn, Al and Cu under the same loading and unloading conditions.

For all four samples shown in Figure 7-28 there are initial sharp rises in the displacement at the early stages of the creep segments with a diverse range of rates. Afterwards this sharp rise changes to a lower rate of increase of displacement with time for Cu and Al samples, but much higher rates are obtained for Sn and Zn. Because diffusion processes are significant for both Sn and Zn due to their lower melting point, creep rates are expected to be higher than those from Cu and Al. When comparing the indentation creep measurements for all the materials used in this work, it was observed that for the materials with similar melting points, and consequently similar homologous temperatures such as Cu and Au, the creep rates are similarly low, with an acceptable error margin (less than 1%). However, it is evident that materials with lower melting points demonstrate higher creep rates. Sn, for example, has a melting point nearly half of that of Zn, but shows a creep strain that is approximately double. This data confirms that the effect of creep in the obtained nanoindentation data critically depends on the homologous temperature of the material being tested. For all four samples, the logarithmic trend-lines shown as solid black lines in Figure 7-28 were used to investigate the  $B$  constant in the equation  $\varepsilon = A+B \ln (t)$ . In this equation which was proposed by Chudoba and Richter (Chudoba and Richter, 2001),  $\varepsilon$  is the increase in depth at maximum load and  $t$  is the loading time. This equation was developed for primary creep (also known as transient creep) and fits the creep strain line if there is no secondary or steady-state creep. Figure 7-29 illustrates the obtained constant  $B$  for all four samples versus their homologous temperature.



**Figure 7-29.** Comparison between the constant  $B$  and homologous temperatures for the creep behaviour of bulk Sn, Zn, Al and Cu obtained from indentation strain versus time curves.

The obtained data confirms that the constant ( $B$ ) from the equation  $\varepsilon = A + B \ln(t)$  increases linearly with the homologous temperature confirming that even at room temperature the creep rate is highly dependent on the diffusion process and consequently the melting point. Moreover,  $R^2$  values can be obtained from the logarithmic trend line fits in Figure 7-28 and used to show how precisely the trend lines fit to the curves. When the obtained  $R^2$  values were compared, it was found that the logarithmic trend line is relatively accurate for the Cu sample ( $R^2 = 0.95$ ) but less so for the Al sample ( $R^2 = 0.9$ ). The trend lines for the Sn and Zn samples are also less accurate than that of Cu, with  $R^2$  values equal to 0.88 and 0.89 respectively. This is due to the appearance of secondary creep (steady-state creep) in materials with a high homologous temperature combined with the use of an equation that was originally developed for primary creep. These data are in good agreement with the results reported by Tohid and Bull (Tohid and Bull, 2007).

Therefore, this illustrates that the hold at maximum load is crucial for materials such as Sn and Zn in which secondary creep appears even at room temperature. The use of longer holding periods at the maximum load failed to remove creep and additionally resulted in a change in the contact area. The secondary creep state and the changes it causes to the indentation depth due to the longer indentation tests were also clearly noticeable from the obtained load-displacement curves.

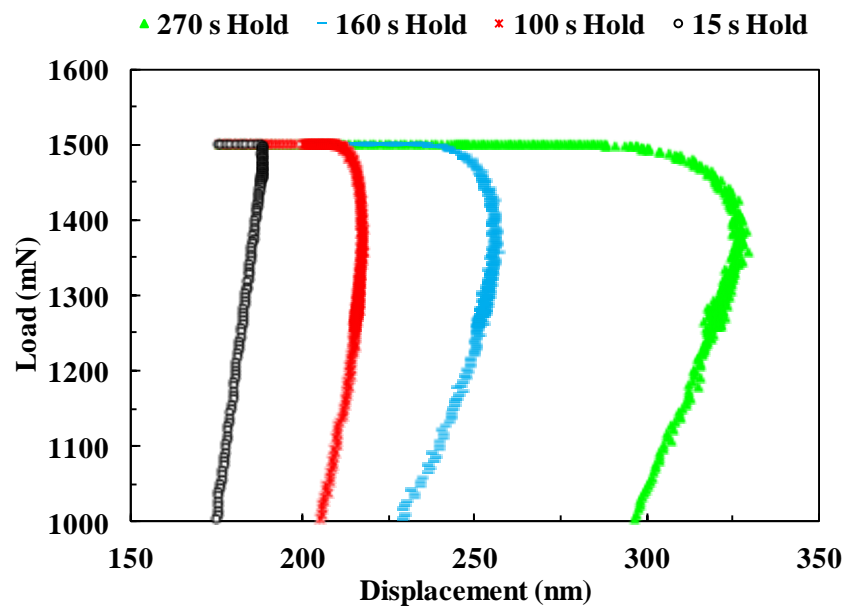


**Figure 7-30. The hold-unload sections of four different load-displacement curves obtained from bulk Sn using the open loop mode at very similar loads with different holding periods at the maximum load before unloading.**

Figure 7-30 illustrates the unloading sections of four different load-displacement curves obtained from the bulk Sn sample close to the maximum load and displacement using open loop mode. The hold periods at the maximum load shown in this figure are 15, 100, 160 and 260 seconds. This can be concluded that the hold period at the maximum load of the indentation tests is necessary to assist in the run out of primary creep in materials such as Cu, Au and Al. However, for materials with low melting points, such as Sn and Zn which even at room temperature can show secondary creep during the nanoindentation tests, the use of longer period holding is not the solution and these materials necessitate the use of displacement control protocols to minimise the creep effect on the obtained data.

## **7.5 Summary**

The pile-up, substrate and creep can have significant effects on the obtained hardness and modulus values and requires consideration during the measurement of mechanical properties using the nanoindentation technique. However, the effect of each phenomenon can be minimised. For example, the effect of pile-up can be corrected for by measuring the true contact area using the AFM or SEM images. The influence of the substrate on the measured data can be found by measuring the plastic radius using the AFM images. Finally, creep and its effect on the nanoindentation results can be removed by the correct selection of the load function, including the loading and unloading rates and a sufficient hold at the maximum load. Moreover, the type of testing protocol can help to remove the effect of creep as well.

All of these phenomena can cause variation in the nanoindentation test results. However, these are not the only causes of variation in the results and there is another important factor that can change the hardness and modulus values dramatically; the oxidation of the sample surface. The next chapter highlights the importance of the surface oxide on the mechanical properties of the materials.

This work was performed on titanium-based and cobalt-chrome alloys used in orthopaedic applications. The longevity of these materials is highly influenced by their mechanical properties. This work was carried out due to the interest in the oxidation appearance in vivo and the changes that may occur in the mechanical properties of materials due to their oxidation. Initially some background information on titanium and cobalt-chromium based alloys is introduced, followed by a brief

literature review with regards to the effect that the human body can have on their performance and longevity. The results are compared for samples before being used in the body, to account for surface mechanical response due to implant manufacture, and after, to consider the material's response to long-term cyclic loads. The effects of oxidation on the mechanical properties of the alloys treated electrochemically with a sodium chloride (NaCl) solution at body temperature are presented. Sample characterisation as well as the surface morphology is presented using various characterisation techniques.

## **Chapter 8. Influence of Oxidation on the Materials Mechanical Properties**

*In this chapter a basic overview of the importance of oxidation of materials on their performance in their intended environment is provided. This is put into context with regards to the failure of hip implants in vivo focussing on the titanium and cobalt-chromium alloys which are the most common implantation materials. The mechanical properties of these alloys are discussed followed by comparison to that of the alloys that have been oxidised both in vivo and electrochemically. The surface characterisation of the materials by means of EDX, XRD and XPS analyses that have been used to better understand the findings from the nanoindentation tests are discussed.*

### **8.1 Oxidation**

Oxidation is an environmental phenomenon and the extent of oxidation, as well as the mechanical properties of the produced oxide, is critical in dictating the performance of a material. For some materials, such as aluminium, the oxide layer can act as a protective barrier to reduce further oxidation of the sample's surface (Akhadejdamrong *et al.*, 2002). However, the formed oxide layer can change the mechanical properties of these materials, such as the hardness, near the surface. It has been suggested by Pethica and Tabor (Pethica and Tabor, 1979) that the indentation size effect is due to the surface oxidation, which alters the hardness of the surface.

Another scenario for consideration is when the produced oxide layer does not remain adhered to the material's surface and continuously spalls off. This will result in the surface of the sample being repeatedly oxidised and then spalling over and over again, consequently resulting in a loss of the metal or alloy.

To prevent surface oxidation, coatings are sometimes used. As an example, stainless steel implants are coated by a chromium oxide layer to prevent oxidation (Charles and Ness, 2006). However, there are always advantages and disadvantages in the use of coated layers and they are not always the best preventative measure for oxidation.

Since the longevity of orthopaedic implants is highly influenced by the chemical and mechanical properties of the incorporated materials, there has been enormous attention focused on the fabrication of implants that are resistant to failure from both chemical and mechanical causes. By achieving this it is possible to significantly enhance the quality of life for the recipient of the implant.

It is for this reason that titanium (Ti) based and cobalt-chromium (Co-Cr) based alloys have been widely used in orthopaedic applications. However, when these two components articulate, for example in the taper connections of stems and femoral heads in modern modular designs implants, damage has been reported. This part of the work attempts to understand and investigate the bulk and surface mechanical properties, such as hardness and Young's modulus, of the Co-Cr and Ti based alloys used as implant materials.

To assess the mechanical properties of the alloys, a number of fully processed hip implants were compared with idealised flat plate samples. To assess the effect of the human body environment on the surface mechanical properties, two types of samples were investigated; samples before use in the body, to account for surface mechanical response due to implant manufacture, and after, to account for the material's response to long-term cyclic loads. This also facilitates the identification of any effects from impurities and surface oxidation in the hardness and modulus values of the implanted materials.

## **8.2 Why Titanium and Cobalt-Chromium Alloys?**

Recently, Ti and Co-Cr based alloys have attracted the most attention for use in metal-on-metal joint replacement implants. One of the main motivations for the selection of Ti and its alloys for the stem portions of most hip implants is that Ti has a lighter weight when compared to the other orthopaedic alloys, such as stainless steel (Imam and Fraker, 1996). The use of Co-Cr based alloys in orthopaedic implants has also been successful, which can be attributed to its biocompatibility, corrosion resistance and hardness (Punt *et al.*, 2008). Nowadays, Co-Cr based alloys are the most commonly used materials as a replacement for knee components and femoral heads.

However, the recent change in the design of the hip implants from fixed-head femoral prostheses (a single piece design) to a modular design (interchangeable parts), which often included a Co-Cr femoral head on a flexible Ti stem (Collier *et al.*, 1992; Cohen, 2012), brought both advantages and disadvantages in the usage of hip implants. When used in combination, the mechanical properties of each alloy play a leading role in determining the longevity of an implant in the highly corrosive human body environment (Navarro *et al.*, 2008). Additionally, biocompatibility and relevant clinical factors of each component where they are connected becomes important factor in the longevity of the implant (Hansen, 2008).

One of the main advantages of Ti alloy femoral stems is their superior biocompatibility in the human body demonstrated by a good tissue tolerance which consequently shows no allergic reaction with the surrounding tissues or blood (Imam and Fraker, 1996; Wang, 1996). Moreover, Ti based alloys have enhanced corrosion resistance properties, a low elastic modulus closer to that of bone (Bischoff *et al.*, 1994) and a high strength-to-weight ratio when compared to stainless steel and Co-Cr alloys. As a result, for many years Ti alloys have been used preferentially in many applications such as dental implants, maxillofacial applications and joint replacement implants (Jinno *et al.*, 1998). In comparison, Co-Cr alloy prosthetic bearings are the most common used type of bearing for metal bearing on a metal surface situations due to the reduced inflammation, less bone loss and more importantly, reduced wear for hip replacements in use today (Brown *et al.*, 2006).

It is due to these superior properties that the use of the combination of Co-Cr alloy bearings and Ti alloy stems has attracted the most attention along with a significant improvement in the long-term behaviour of the implanted devices. Therefore, metal-on-metal hip replacement has become a common total hip replacement with the potential for a low level of wear. Failure has however been reported in some implants, such as wear between the connections of the stems and femoral heads in modern modular designs in which the Ti taper has a rough turned surface. In such cases the Co-Cr unexpectedly shows more wear despite it having a higher hardness than the Ti counter face, and this has been attributed to either a fretting fatigue or tribocorrosion mechanism (Gilbert *et al.*, 1993; Ryu *et al.*, 2007; Hosseinzadeh *et al.*, 2012; Langton *et al.*, 2012).

Therefore, it is of interest to detect the effect of the chemical environment in the body on the surface mechanical properties. Consequently, this will aid in identifying the cause of the failure of the implants by detecting the effects on the mechanical properties such as hardness and Young's modulus of both the head and stem portion of the total replacements as Co-Cr based alloys have higher hardness values than Ti based alloys.

### **8.3 Mechanical Properties of Co-Cr Alloys**

Although Co-Cr alloys with their aforementioned mechanical properties and biocompatibility are suitable candidates for load-bearing implants, their low wear rates and material loss from tribocorrosion processes are becoming more important issues in implant manufacturing. As a result of these processes, ions from the implant are released into the body (Pham *et al.*, 2011).

One significant contribution to the overall wear behaviour in a total joint replacement is microabrasion. An example of this is the removal of UHMWPE debris from an acetabular cup by asperities on the surface of a worn femoral head. A better understanding of the surface hardness to assess the resistance of a surface to abrasive wear becomes a major concern (Lampe *et al.*, 1998). Moreover, evaluating the resistance of asperities to shear damage from adhesive wear also requires a better understanding of hardness.

To assess the mechanical properties of Co-Cr-Mo femoral heads, nanoindentation tests were performed under both displacement control and open loop mode. As it has been seen from previous chapters, the use of displacement control can minimise the effect of creep and provides the hardness and modulus values at specified indentation depths. Therefore, initially, displacement control tests were performed to measure the hardness and modulus values of Co-Cr-Mo samples at indentation depths ranging from 80 *nm* to zero. Afterwards, to detect the mechanical properties at higher contact depths, open loop mode tests were also performed under large loads ranging from 10 *mN* to 100  $\mu$ *N*.

It should be noted that since the tested femoral heads are of a rounded shape, a specific sample holder was built to minimise the slight misalignments between the surface and the indenter tip prior to the commencement of the indentation tests as

any slight tilt in the sample surface can modify the contact area and consequently the obtained hardness and modulus values. Figure 8-1 demonstrates the significance of this by showing two AFM images obtained from the Co-Cr-Mo sample under the same indentation conditions with and without the elimination of the misalignment of the surface.

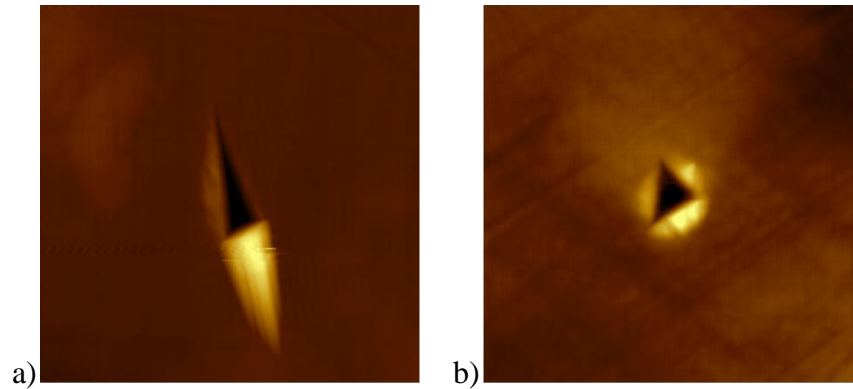


**Figure 8-1. AFM images obtained from Co-Cr alloy femoral head (a) with and (b) without misalignment between the tip and sample surface.**

Initially, the indentation tests were carried out on the sample surface as received of samples that had not been used in the human body. The obtained hardness and modulus values using both displacement control and open loop mode are illustrated in Figure 8-2. Both the displacement control and the open loop mode results from Figure 8-2 confirm that the hardness is lower at shallow depths and therefore closer to the surface, however the hardness increases when contact depth increases.

The obtained data shown in Figure 8-2 can be divided in four different regions; contact depths below 10 *nm*, from 10 to 50 *nm*, and between 50 and 80 *nm* for both open loop mode and displacement control. The final region is for contact depths higher than 80 *nm* which applies just for open loop mode in this test. At contact depths below 10 *nm*, the average hardness value and Young's modulus were found to be  $5.1 \pm 2.0$  *GPa* and  $133 \pm 27$  *GPa* respectively. This demonstrates that the surface of the sample is relatively soft, therefore suggesting a key cause for failure in metal-on-metal hip implants. However, the tip end shape effect should be considered for the contact depths of less than 10 *nm*. The second region from 10 to 50 *nm*, gives average values of  $9.4 \pm 2.0$  *GPa* for hardness and  $167 \pm 11$  *GPa* for modulus, which is relatively close to the bulk property values of cobalt and chromium reported in the literature.

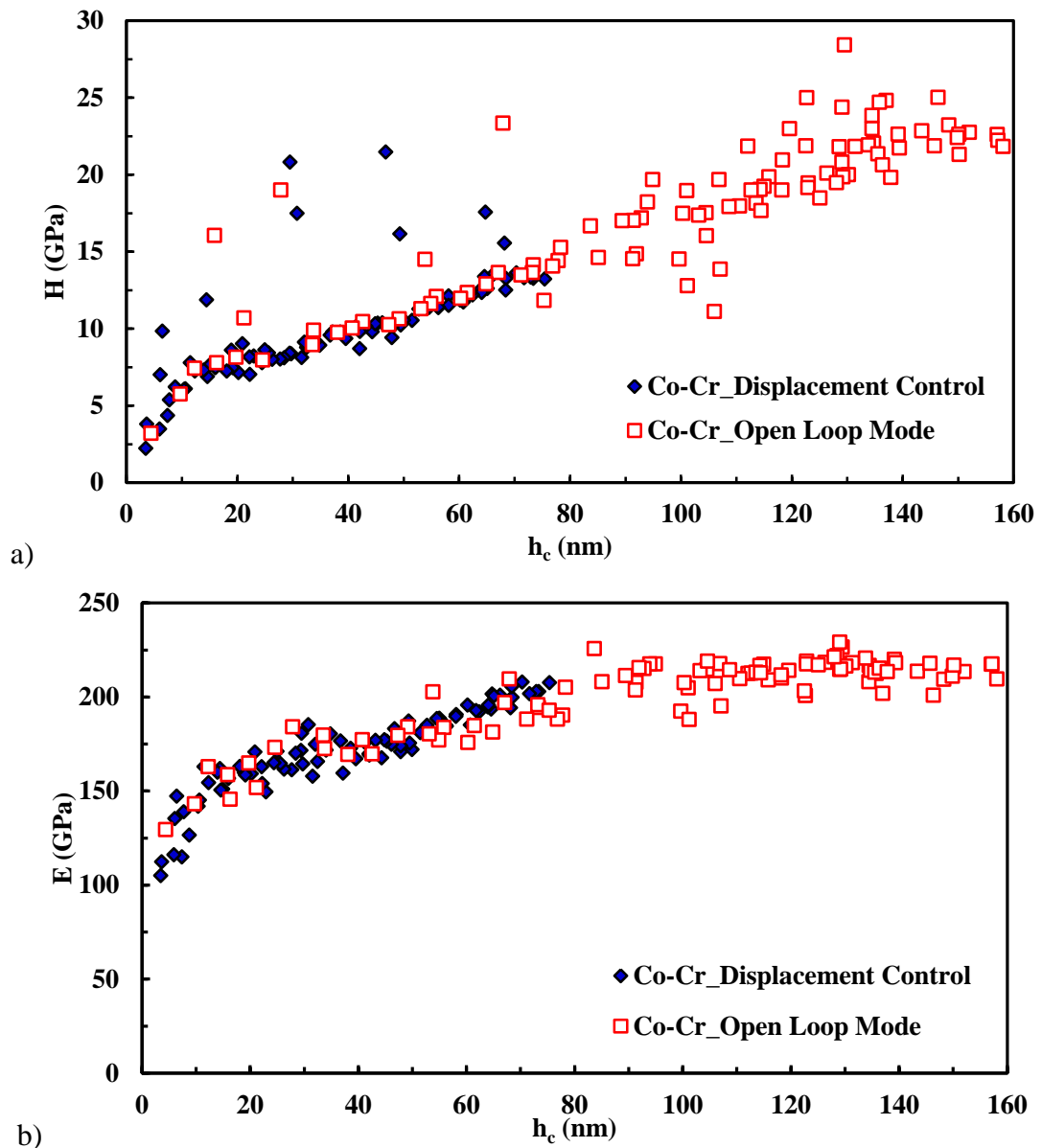


**Figure 8-2. Comparing both the (a) hardness and (b) Young's modulus for Co-Cr alloy under displacement control and open loop mode.**

For contact depths between 50 and 80 nm, both the hardness and Young's modulus results increase to  $13.0 \pm 2.0$  and  $193 \pm 10$  GPa respectively; this is due to the pile-up. For the open loop mode results at contact depths above 80 nm, the average values for both hardness and Young's modulus increase further to  $20.0 \pm 3.0$  and  $213 \pm 7$  GPa.

The recorded AFM images were used to determine the effect of pile-up in the measured values of hardness and modulus at different contact depths. Figure 8-3 illustrates the measured pile-up heights and widths versus the contact depths using the AFM images for all three sides of the indentations produced under displacement control.

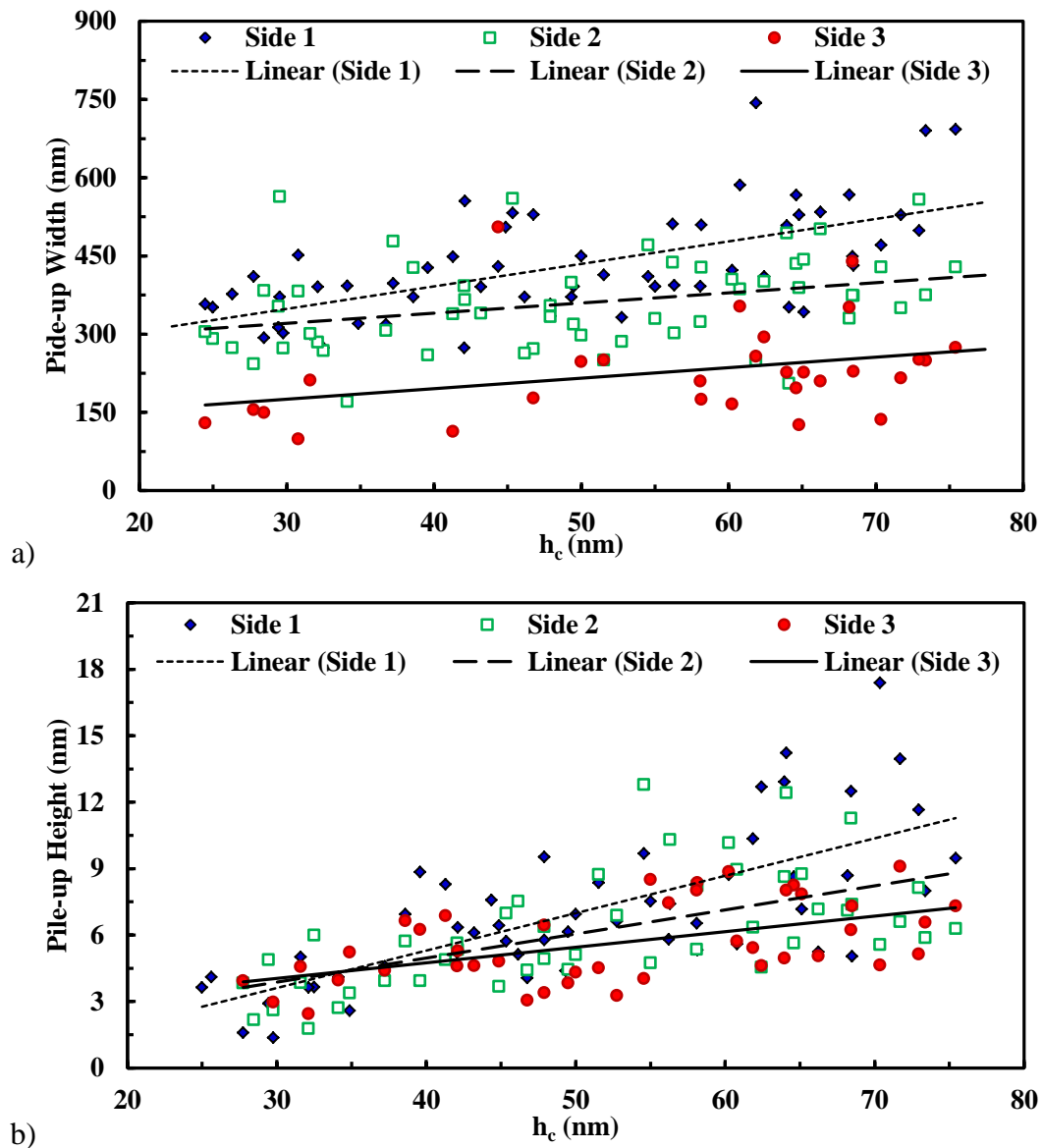


**Figure 8-3. Comparison of all three sides of pile-ups (a) widths and (b) heights for Co-Cr alloy under displacement control.**

It can be seen in Figure 8-3 that as the size and depth of the indentation increases, the height and width of the pile-ups becomes larger. This relationship is observed to be linear with the increase in contact depth, with some degree of scatter in the data points. Consequently, as mentioned in the previous chapter, due to the pile-up appearance, the effective contact area increases and modifies the observed hardness and Young's modulus values. The AFM images obtained for the indentations at contact depths of less than 50 nm show that the pile-ups at all three sides of indentations have reasonably similar heights and widths. However, when the indentation size is larger, the pile-ups tend towards being non-symmetrical and as a result the potential for pile-up correction using any kind of constant is impracticable.

Consequently, to measure the hardness and Young's modulus of the Co-Cr alloy, the nanoindentation tests were carried out at a 50 nm contact depth to minimise the pile-up effect on the obtained data. However, to achieve a 50 nm contact depth in a reasonably hard and stiff material such as Co-Cr alloy, the applied load must be large enough to be capable of being accurately measured within the force resolution of the instrument. Moreover, the tests at lower contact depths facilitate a quick loading and unloading approach, and therefore thermal drift and the effect of the primary creep can be removed from the obtained data. To identify the cause of the scatter seen in the hardness data seen in Figure 8-2, the tests were carried out along a line across a polished flat on the sample using displacement control under the same indentation condition at 50 nm depth and the obtained results are illustrated in Figure 8-4.

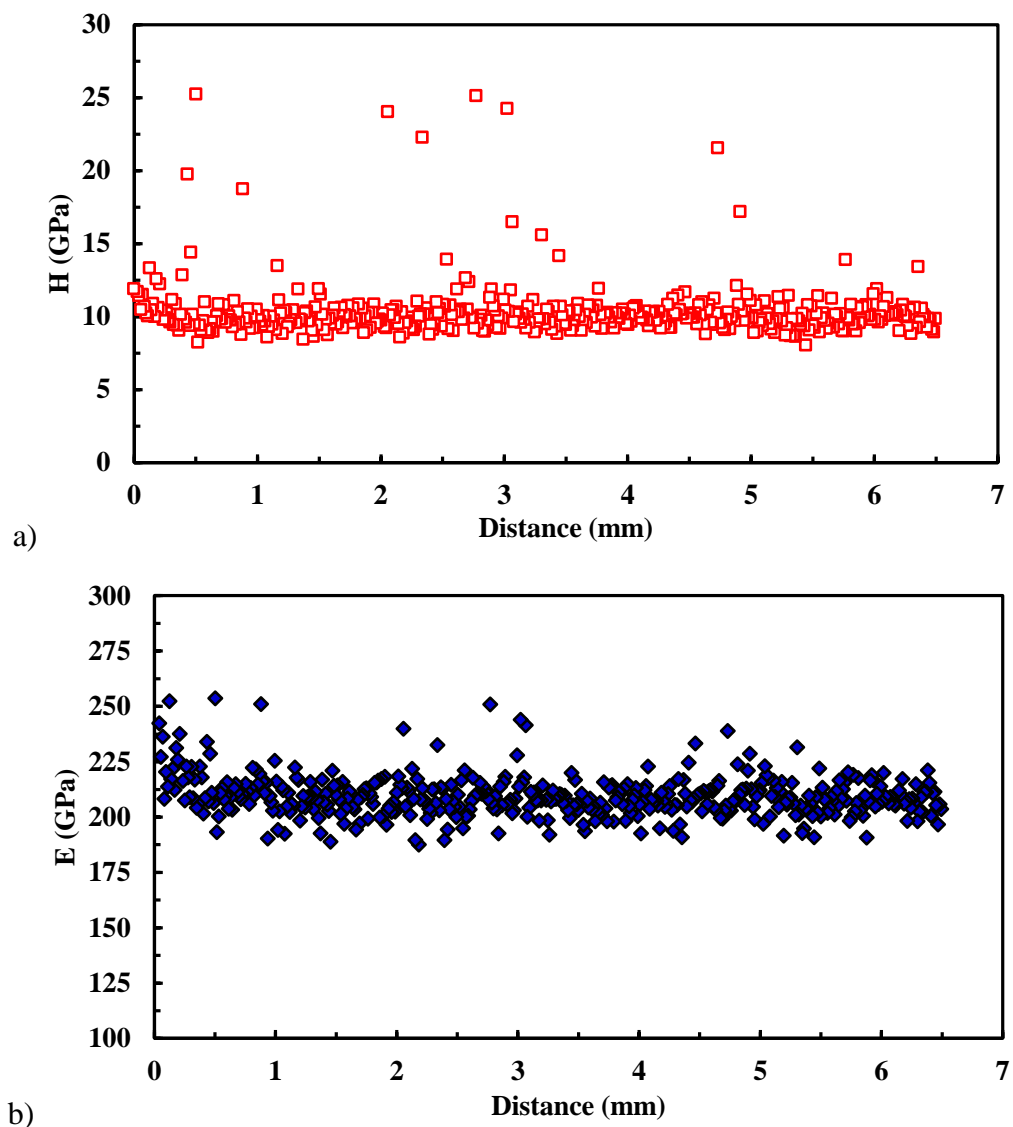


**Figure 8-4. (a) hardness and (b) Young's modulus for Co-Cr alloy under displacement control over a straight line across a polished flat on the sample.**

As can be seen from Figure 8-4, the average hardness value obtained from 500 indentations performed at the same displacement for Co-Cr-Mo alloy is around  $10.5 \pm 2.0 \text{ GPa}$ . The average Young's modulus is  $210 \pm 10 \text{ GPa}$  which is similar to the modulus reported for Co-Cr alloys ( $220 \pm 20 \text{ GPa}$ ) in the literature (Brunette, 2001; Kurtz, 2009; Pham *et al.*, 2011). However, Roy *et al.* (Roy *et al.*, 2010) reported the modulus value for Co-Cr alloy as  $345 \pm 19 \text{ GPa}$ .

Additionally, the hardness values obtained from both the test results shown in Figure 8-2 (a) and Figure 8-4 (b) demonstrate some large values which are noticeably higher than the average hardness values. It should be noted that to increase the strength of the Co-Cr alloys some other metals such as molybdenum and nickel were added and the scatter in the results can be due to the formation of carbide with the chromium or molybdenum during processing.

It should however be taken into consideration that the human body, with a pH of around 7.4, at a temperature of  $37^\circ\text{C}$  and consisting of a saline electrolyte environment, can be a highly oxygenated setting which can have an effect on implanted mixed-metal prosthesis. Consequently, the oxidation of the alloys that could occur in the human body can cause the scatter in the hardness values. To analyse the microstructures of the Co-Cr-Mo samples as well as to characterise and quantify the elemental compositions, analytical techniques such as EDX and XRD are required.

Prior to discussing the results obtained from characterisation techniques, the hardness results obtained from nanoindentation tests for the samples which were treated electrochemically with NaCl solution at body temperature are illustrated in Figure 8-5. These samples were oxidised electrochemically to assess the effects of oxidation on the hardness values. Therefore, for a useful comparison, the indentation tests were carried out under the same conditions as used before the oxidation process, using displacement control.

Additionally, to obtain the hardness values at the greater depths, the indentations were continued to higher contact depths. Figure 8-5 compares the hardness results from the displacement control nanoindentation tests for Co-Cr-Mo alloy before and after the electrochemical oxidation process.

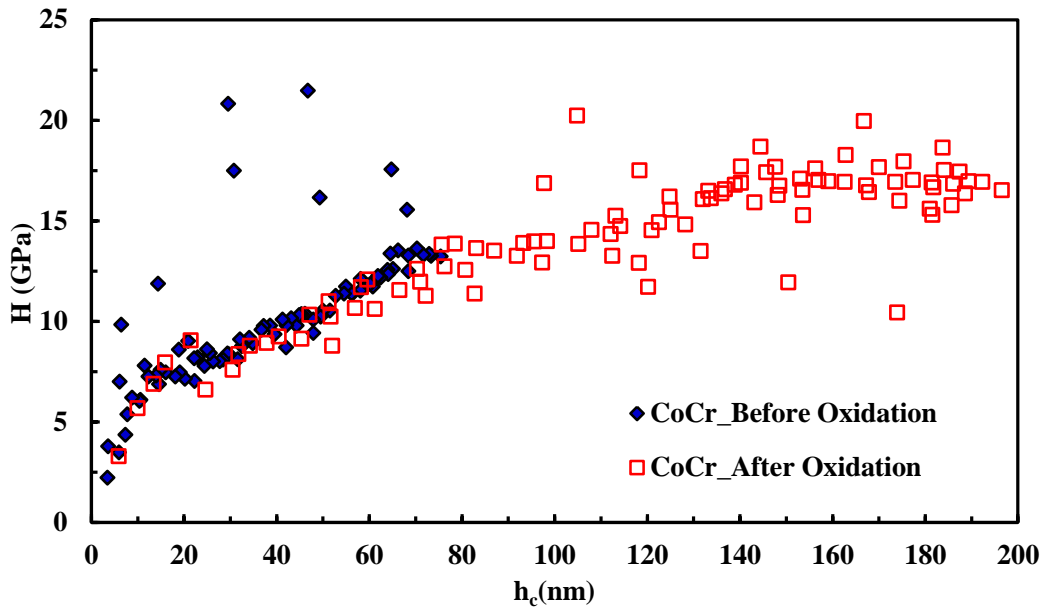


**Figure 8-5. Comparison of the hardness results for Co-Cr-Mo alloy before and after electrochemical oxidation.**

As can be seen from Figure 8-5, the hardness values after oxidation are very similar to the values obtained before the oxidation process. Similar behaviour was found for the samples that had been implanted in the human body. Although this can indicate that significant oxidation did not occur as the hardness values did not change, further analytical methods such as EDX and XRD were used to compare the samples before and after oxidation.

### **8.3.1 EDX and XRD Characterisation Analyses**

As mentioned previously in section 3.2, EDX in the SEM is one of the commonly used characterisation methods for the identification and quantification of elements in materials. However, as the EDX measurement accuracy is limited (Carlton *et al.*, 2004) and there is a possibility that EDX does not detect some elements that are present in low atomic percentages, XRD analysis was used as an additional technique for characterising the sample surfaces.

The EDX results obtained from the Co-Cr-Mo alloy samples are shown in Table 8-1. Results were obtained for samples that had been implanted in the human body and samples that had not been implanted, but were instead oxidised electrochemically. These results can be used as primary confirmation that significant oxidation did not

occur on the surface of the both the implanted and non-implanted samples and that the elemental compositions remain relatively identical for both of the samples.

Elements	Not implanted	Implanted
	Atom. C [at.-%]	Atom. C [at.-%]
Co	60.97	60.24
Cr	33.27	32.83
Mo	3.78	4.39
Si	1.99	2.54

**Table 8-1. EDX results of Co-Cr-Mo alloy samples as received without implantation in the human body and implanted *in vivo*.**

After the EDX analysis, XRD analysis was carried out for both types of sample. The XRD pattern shown in Figure 8-6 was obtained for the implanted sample which also displays no evidence that significant oxidation took place during the use of the implant *in vivo* as the obtained pattern is characteristic for Co-Cr-(Mo, Ni) alloys.

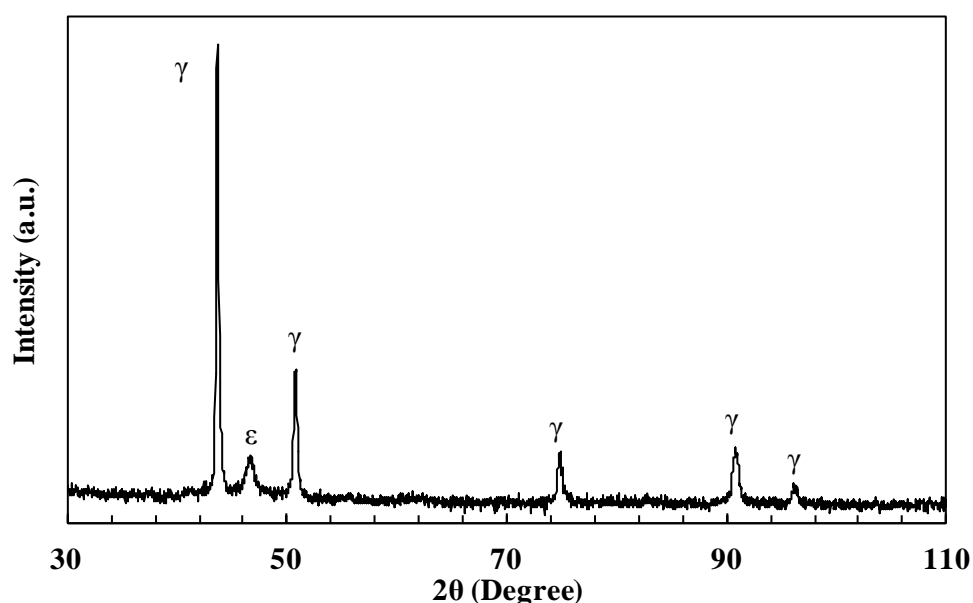


**Figure 8-6. X-ray diffraction pattern for the implanted Co-Cr-Mo alloy.**

It was confirmed from the XRD pattern that the Co-Cr alloy has two different crystal structures referred to as face-centre cubic or fcc ( $\gamma$ ) and hexagonal close packed or hcp ( $\epsilon$ ). The ratio of these two phases has a significant effect on the mechanical properties of the alloys (Kurosu *et al.*, 2006).

It has been detailed in the literature that the presence of the hexagonal phase is essential for wear resistant properties (Buckley, 1976), however the inclusion of the cubic phase is required for plasticity. In the metal-on-metal hip implants, the epsilon ( $\epsilon$ ) phase has been reported as being responsible for a decrease in the extent of metal ions released into the body and superior wear resistance (Kurosu *et al.*, 2005; Saldivar-Garcia and Lopez, 2005). The dominance of the gamma ( $\gamma$ ) phase over the  $\epsilon$  phase is clearly shown in the XRD pattern. Conflicting results on the effect of epsilon on mechanical properties have been reported (Chiba *et al.*, 2007). The wear on Co-Cr-Mo hip implants might be explained by a lack of the  $\epsilon$  phase, resulting in insufficient wear resistance in the implant (López *et al.*, 2000; Yamanaka *et al.*, 2013). The results from the XRD analysis were found to be identical for the samples oxidised electrochemically.

#### **8.4 Mechanical Properties of Ti-6Al-4V Alloy**

Since the design of the implants has been changed to a modular design that allows different components to be combined, Ti has played a significant role in the stem portion of hip implants. As a result of their passive oxide layers (Williams, 1981) and outstanding corrosion resistance for a complete range of oxide states and pH levels, titanium based materials, such as Ti-6Al-4V and Ti-6Al-7Nb alloys, match the requirements for implantation and are well tolerated by the body (Takeuchi *et al.*, 2003; Zhou *et al.*, 2007). Therefore, since the 1950s they have been used as implant materials (Wang, 1996).

In order to investigate why Ti alloy wears Co-Cr alloy despite Ti alloy having a lower bulk hardness and also to examine the effect of oxidation on Ti alloy, experiments on the Ti alloy samples were carried out under the same conditions as the Co-Cr alloys. The hardness and Young's modulus values for the Ti alloy samples before oxidation under open loop mode and displacement control are shown in Figure 8-7.

The average hardness and Young's modulus values at contact depths of less than 80 nm for the Ti alloy samples, under both the displacement control and open loop mode tests, are  $5.4 \pm 1.0$  GPa and  $111 \pm 17$  GPa respectively. These values are similar to the modulus values reported in the literature (Bono, 1999; Majumdar *et al.*, 2008). It

should be noted that Young's modulus is an intrinsic material property and fundamentally related to the nature of the inter-atomic bonding. Adding an alloy or thermal-mechanical processing to change phase composition affects the bond forces and ultimately the Young's modulus (Zhou *et al.*, 2007).

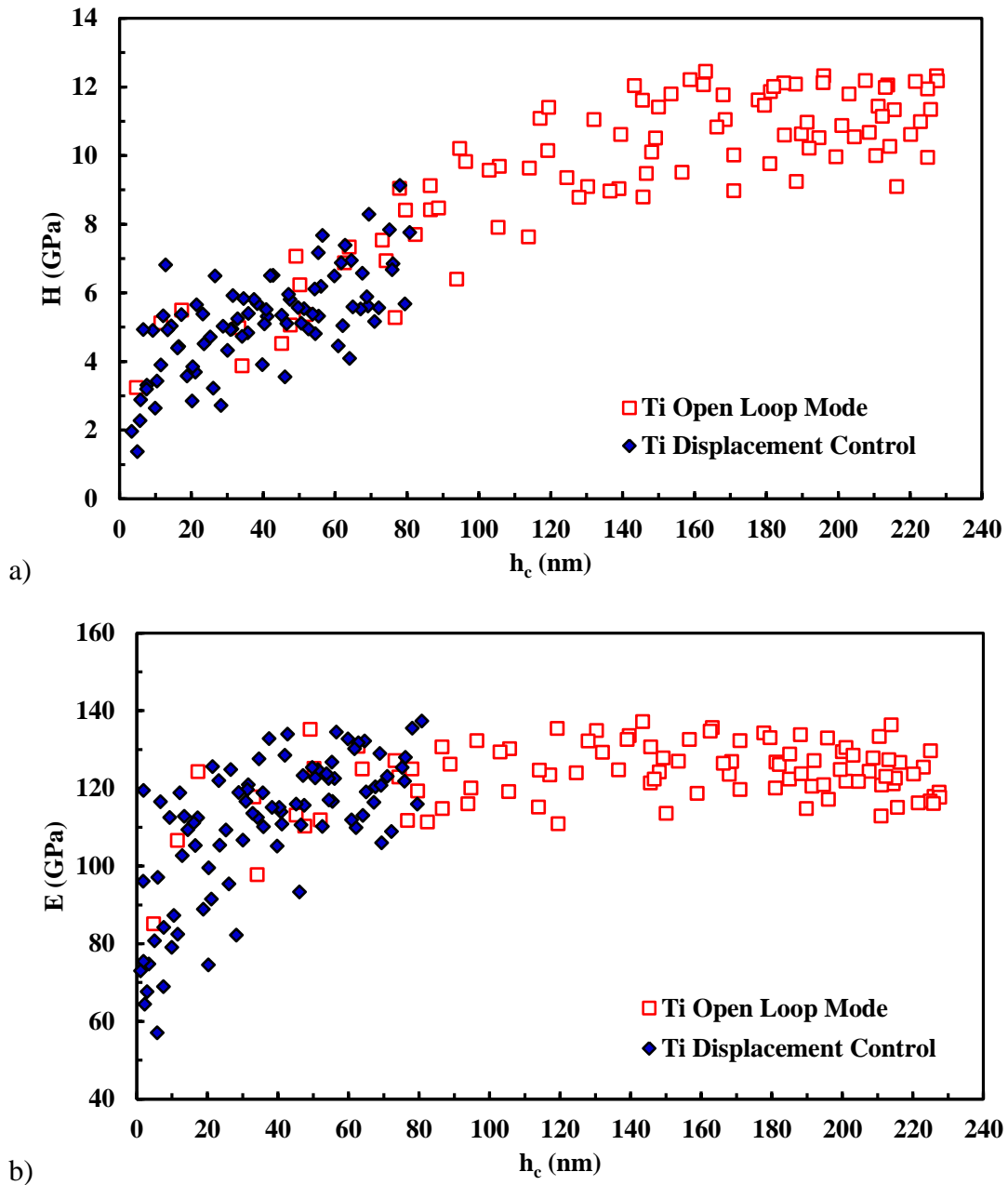


**Figure 8-7. Comparison of both the (a) hardness and (b) Young's modulus for the Ti alloy under displacement control and open loop mode.**

For depths larger than 80 nm, the hardness value increases to  $10.6 \pm 1$  GPa under open loop mode whilst the average Young's modulus remains constant for the larger depths at  $125 \pm 6$  GPa. Similar to the Co-Cr alloy samples, the obtained AFM images

confirmed the appearance of pile-up for the higher contact depths. Figure 8-8 illustrates the width and height of the pile-ups obtained under open loop mode. Only the open loop mode data is presented in Figure 8-8 as the obtained AFM images under displacement control tests for Ti alloy showed no significant evidence of pile-up appearance. This is understandable however, as the open loop mode tests were carried out at higher loads therefore significant pile-up started to form at contact depths more than 70 nm depths.

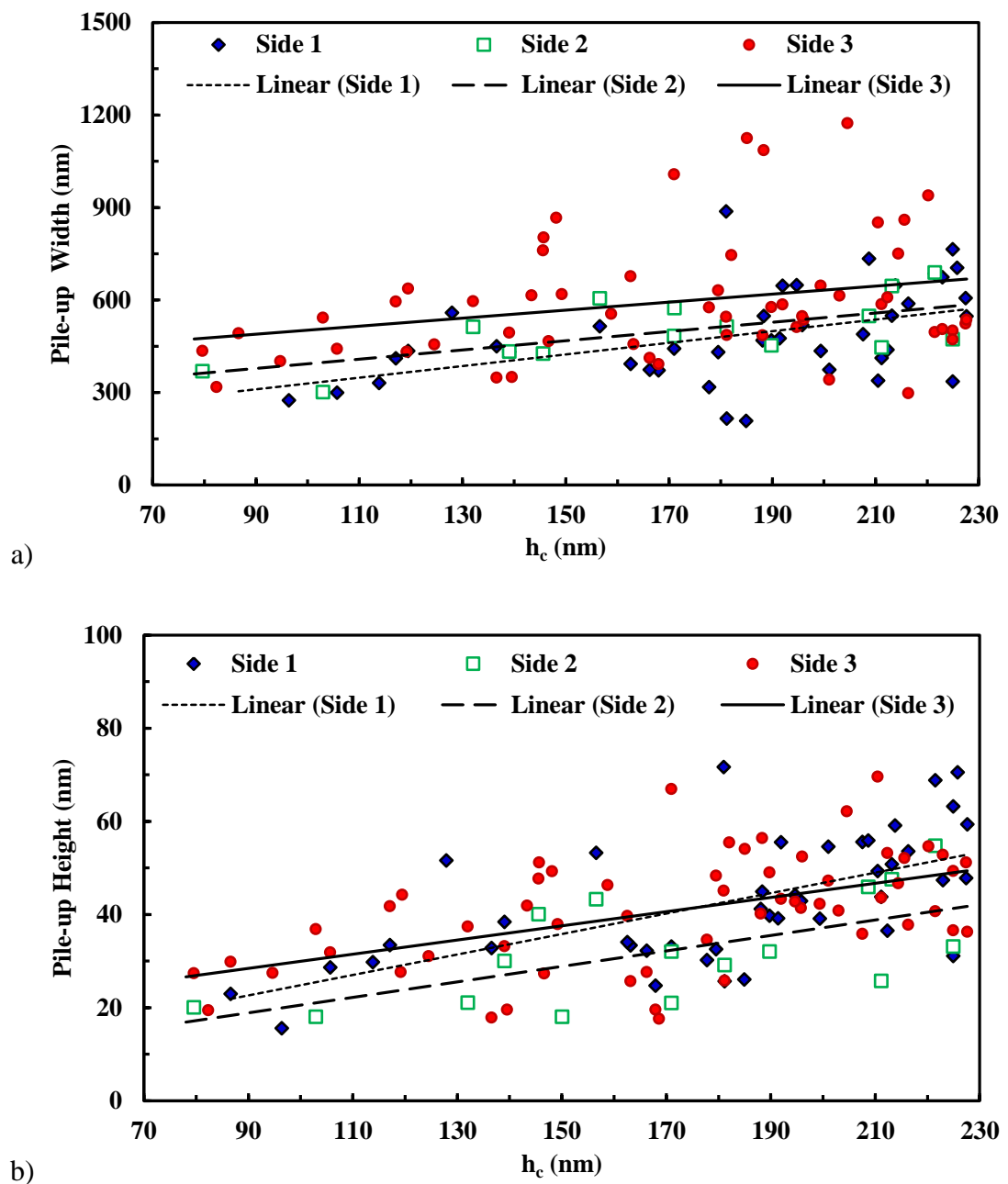
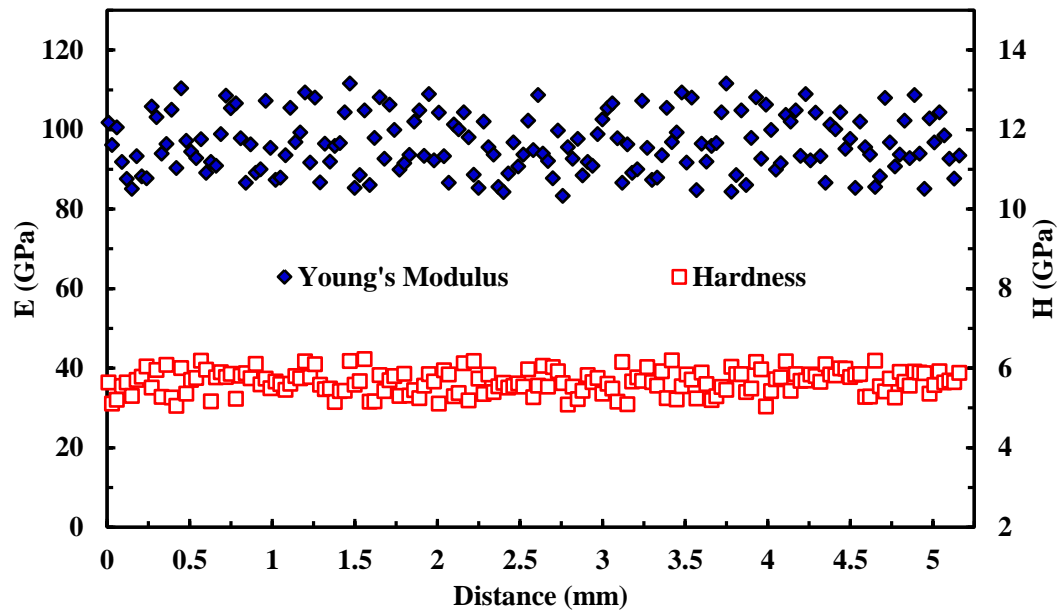


Figure 8-8. Comparison of all three sides of pile-ups (a) widths and (b) heights for Ti alloy using open loop mode.

To compare the hardness and Young's modulus of the Ti alloy samples with the Co-Cr alloys under the same indentation conditions and without influence of the pile-ups on the obtained data, work carried out using displacement control at a 50 nm contact depth. This series of indentations was carried out over a straight line across the sample for idealised flat plate Ti alloy from which the obtained hardness and Young's modulus values are shown in Figure 8-9.



**Figure 8-9.** The Young's modulus (left) and hardness (right) for Ti alloy under displacement control over a straight line across a polished flat on the idealised sample.

The average of the obtained Young's modulus from both the obtained data shown in Figure 8-7 and Figure 8-9 confirm that the Ti alloy has Young's modulus that is approximately half the value of the Co-Cr alloy. Consequently, Ti alloy with a lower Young's modulus, can minimise the stress shielding of the femur and subsequently these smaller stresses reduce the strain between the bone and implant interface (Scales, 1991). Generally the modulus of the metallic biomaterials, such as stainless steel or Co-Cr, is higher when compared to that of human cortical bone tissue (10-40 GPa) (Long and Rack, 1998).

#### 8.4.1 EDX and XRD Characterisation Analyses

Ti occurs in two different phases in the common used alloys, a hexagonal crystal structure known as alpha ( $\alpha$ ) and body centred cubic structure known as beta ( $\beta$ ). The ratio in which these two phases are present can provide different values of Young's

modulus. The beta phase, with a lower Young's modulus closer to that of bone, is the more favourable phase. To stabilise both  $\alpha$  and  $\beta$  phases, the elements Al and vanadium (V) were added in the alloy that has been tested here. The XRD results shown in Figure 8-10 confirm the presence of each phase in the Ti alloy (Geetha *et al.*, 2009).

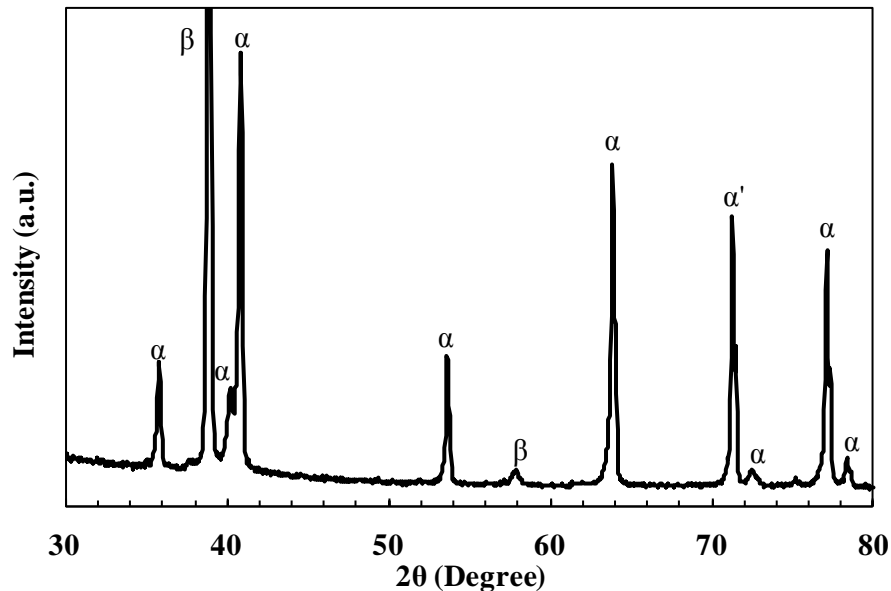


**Figure 8-10. X-ray diffraction pattern for the Ti-6Al-4V before oxidation.**

It has been reported in literature (Hallam *et al.*, 2004) that Ti alloys are corrosion resistant and insoluble due to the compact layer of titanium oxide. In order to investigate the oxidation effect on the mechanical properties, the Ti alloy stems were treated electrochemically with NaCl solution under the same conditions as the Co-Cr alloy. As previously discussed, the experiments were conducted under displacement control for contact depths of less than 80 nm to produce negligible pile-up effects. Figure 8-11 compares the hardness and Young's modulus results for the Ti alloy samples before and after oxidation.

As can be seen in Figure 8-9, there is a significant difference in the hardness results observed before and after oxidation with the average hardness value increasing from  $5.4 \pm 1.0$  to  $12.0 \pm 3.0$  GPa for the sample before and after oxidation respectively. This major change in the hardness values can suggest why the Ti alloy wears the Co-Cr alloy in taper joints, consequently causing failure of the hip implants. The Young's modulus also increases from  $111 \pm 17$  to  $139 \pm 20$  GPa which is closer to the modulus of titanium oxide.

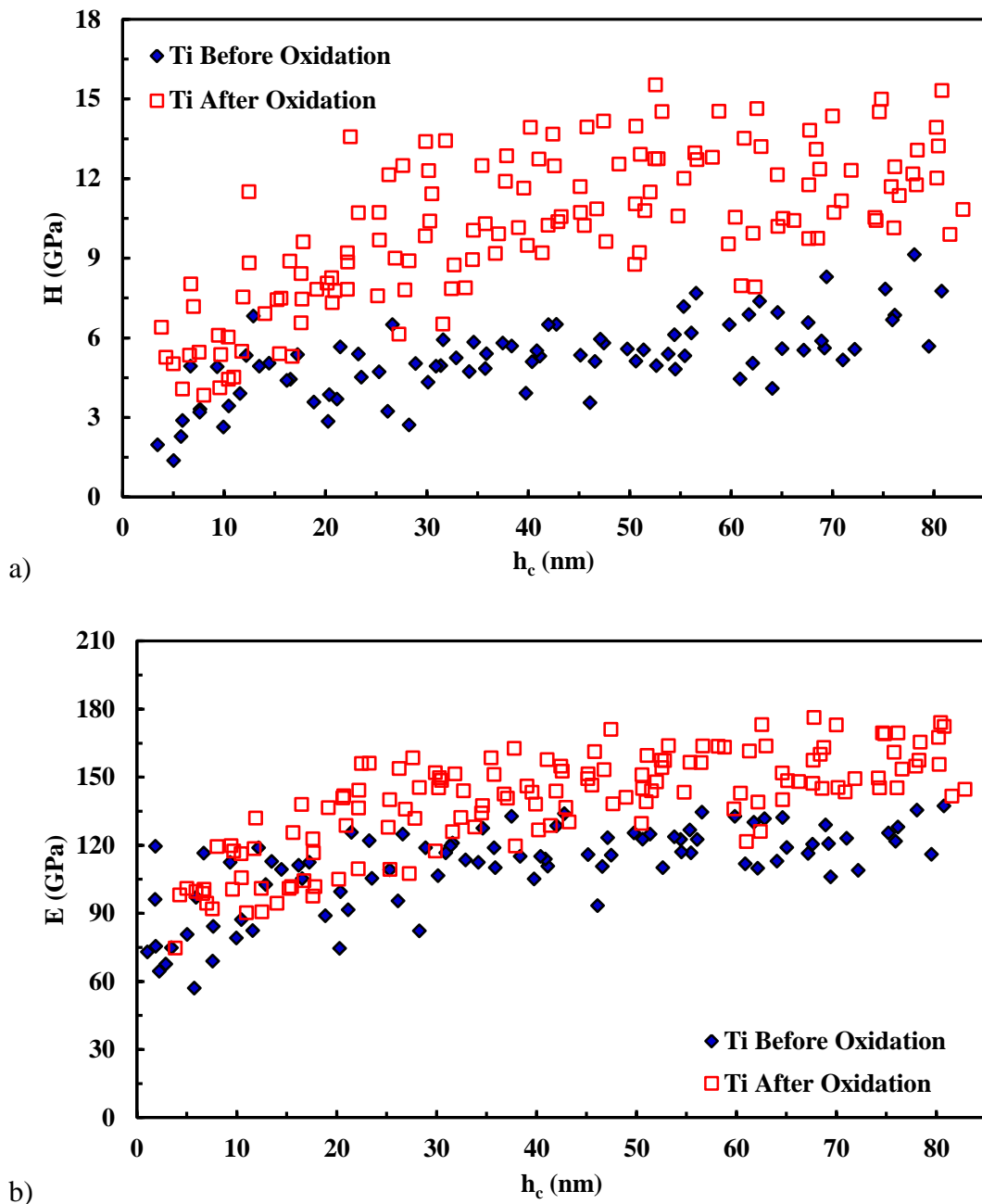


**Figure 8-11. Comparison of the Ti alloy results for (a) hardness and (b) Young's modulus before and after oxidation under displacement control.**

To compare the mechanical properties of the oxidised Ti alloy with the sample used in the body, the nanoindentation tests for the sample used in the body were carried out using the same conditions as for the oxidised sample, under displacement control. Figure 8-12 compares the hardness and Young's modulus results for both tests. Figure 8-12 shows that the average hardness and Young's modulus values for the samples that had been used in the body and those that had been oxidised electrochemically are approximately the same.

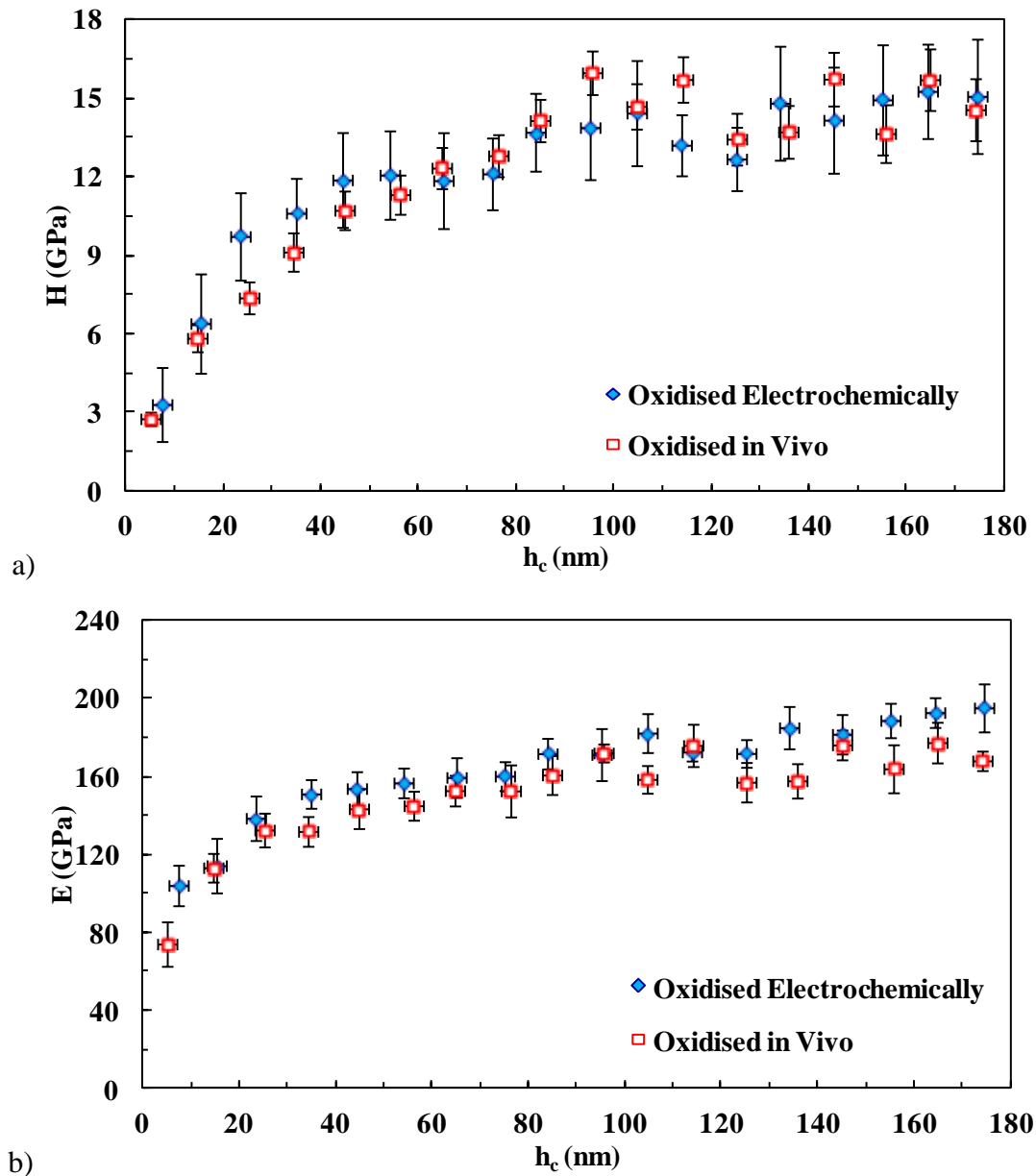


**Figure 8-12.** Comparison of the hardness and Young's modulus values between the oxidised Ti alloy and the sample which was implanted in the body.

When used in the highly corrosive environment of the human body, the stable passive oxide layers of the Ti alloy implants act as an advantageous corrosion resistant barrier (Gilbert *et al.*, 1993; Schenk, 2001; Virtanen *et al.*, 2008). The thickness of this oxide layer continuously increases with time as the implant is constantly in contact with the neighbouring tissues and fluids. This has been demonstrated by the findings of Sundgren *et al.* in which it was shown that the oxide layer on metal implants was considerably thicker for samples that had been subjected to an implantation period of between 6 and 8 years when compared to those from shorter implantation periods (Sundgren *et al.*, 1986). This increase is caused by the

continuous abrasion of the oxide layer and the subsequent repassivation of the surface material that, when occurring for a prolonged period of time, causing the aforementioned thick oxide layer (Grupp *et al.*, 2010). The wear between the implant components that have rough surfaces can also be explained as being a consequence of the fluid that is trapped between the components, in addition to the distribution of contact spots (Hosseinzadeh *et al.*, 2012).

EDX analysis was used to determine the magnitude of oxidation that the Ti alloys had undergone in vivo by quantifying the amount of oxygen on the surface of the samples, as well as identifying the presence of any other key elements. The EDX results shown in Table 8-2 show that the average oxygen content of the sample in the area that was analysed is approximately 19% which implies that a significant amount of oxidation has taken place on the sample. It should be also taken into consideration that the type of oxidation as well as growth rate of the oxide layer is dependent on the location of the implant.

Elements	Not Implanted	Implanted
	Atom. C [at.-%]	Atom. C [at.-%]
Ti	93.35	62.45
Al	6.65	5.88
O	0	19.17
C	0	12.50

**Table 8-2. EDX results for the Ti-6Al-4V alloy samples.**

As mentioned previously, EDX and XRD analysis methods are the most common techniques to characterise the surface structure and identify the elements in materials near the surface. However, as Ti alloys are continually in contact with oxygen, surrounded human tissues and blood when implanted in vivo, an additional method was used to detect the oxidation in Ti alloys for both implanted and electrochemically oxidised samples and also to observe the depth of oxidation.

### **8.5 XPS Characterisation Analysis**

X-ray photoelectron spectroscopy (XPS) characterisation analysis is a surface chemical analysis technique with higher accuracy than the aforementioned methods to not only detect the surface elemental composition of a sample, it can also provide elemental composition as a function of ion beam etching, known as depth profile.

Therefore, XPS analysis was undertaken to identify the depth of the oxide layer in both the Ti and Co-Cr alloys. Since Co-Cr alloy is similar to other metals, it can produce a native oxide layer at the surface however this oxide layer may be too thin and be present in too small a quantity to be detected by other analysis methods such as EDX. Therefore, work was carried out using XPS analysis to detect and measure the presence of oxidation as well as determining the depth of the oxide layer for both of the alloys.

The elemental composition results for the implanted and electrochemically oxidised samples are shown in Table 8-3. As can be seen from the table, the XPS results confirm that oxidation has taken place on both the Co-Cr and Ti alloys. The sample oxidised electrochemically has a slightly lower percentage of oxygen compared to the sample that was oxidised in vivo. This can be due to the long term effect of being exposed to the body's environment and oxidation conditions as the body contains a variety of biomolecules, various cells and compounds (water, sodium chloride, dissolved oxygen, proteins, enzymes, etc.) that interact with the surface (Virtanen *et al.*, 2008).

Sample	Element	Electrochemically oxidised	Implanted in vivo
		Atom. C [at.-%]	Atom. C [at.-%]
Ti-6Al-4V	Ti	16.42	14.71
	O	83.58	85.29
Co-Cr-Mo	Co	17.83	6.19
	Cr	13.64	12.47
	Mo	3.54	2.42
	O	64.99	78.92

**Table 8-3. Elemental compositions obtained from XPS for the Ti and Co-Cr alloys after oxidation.**

Further investigation was carried out using XPS depth profiling analysis to measure the depth of the oxide layer for both alloys oxidised electrochemically and in vivo. Figure 8-13 illustrates an initial set of O 1s XPS spectra corresponding to the oxygen obtained by ion beam etching during the depth profiling experiments for Ti alloy and CO-Cr alloy samples oxidised in body.

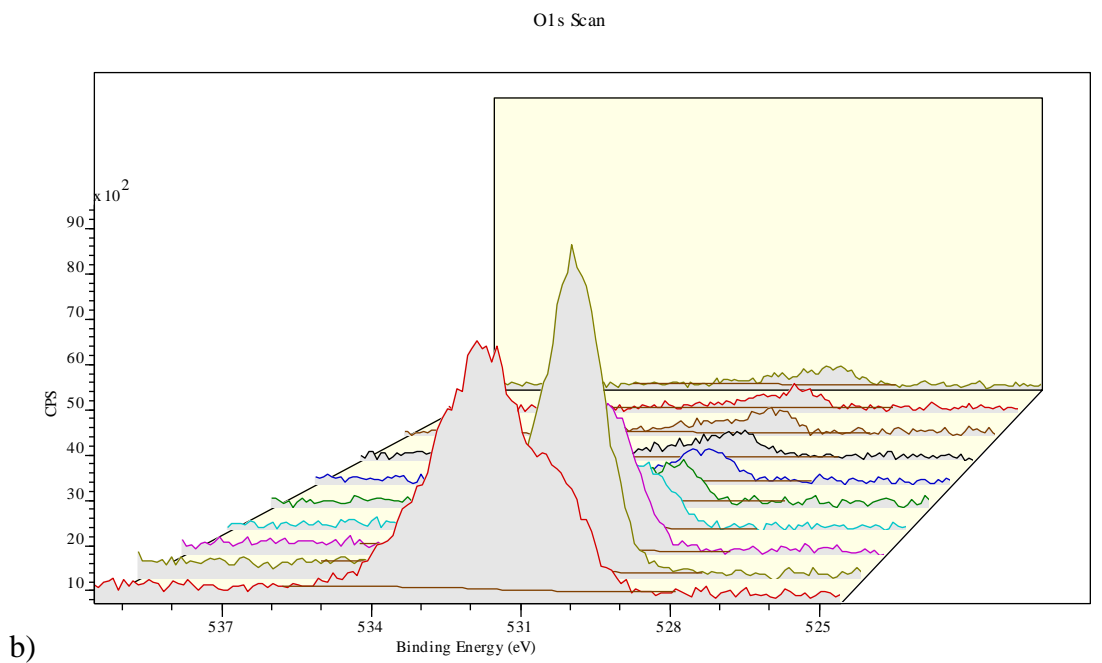
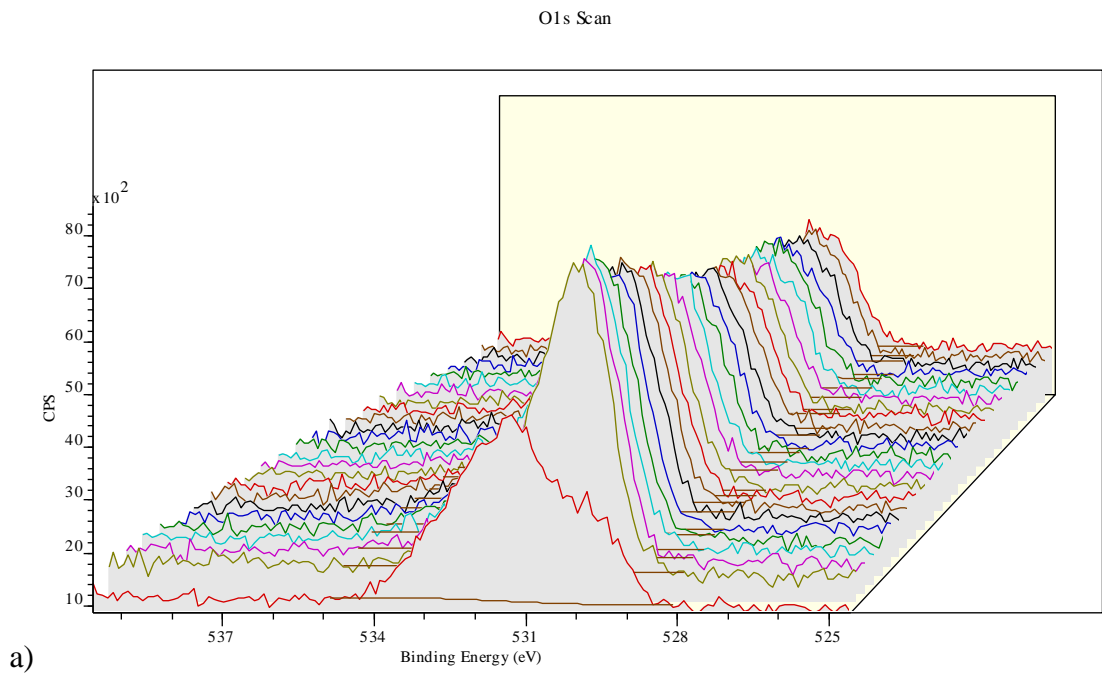


**Figure 8-13. The set of O 1s spectra measured during the depth profiling experiment of the (a)Ti alloy and (b) Co-Cr alloy in vivo.**

The obtained depth profile results using Figure 8-13 are shown in Figure 8-14. The aim of depth profiling experiment was to plot the trend in the quantified composition values as a function of etch-time.

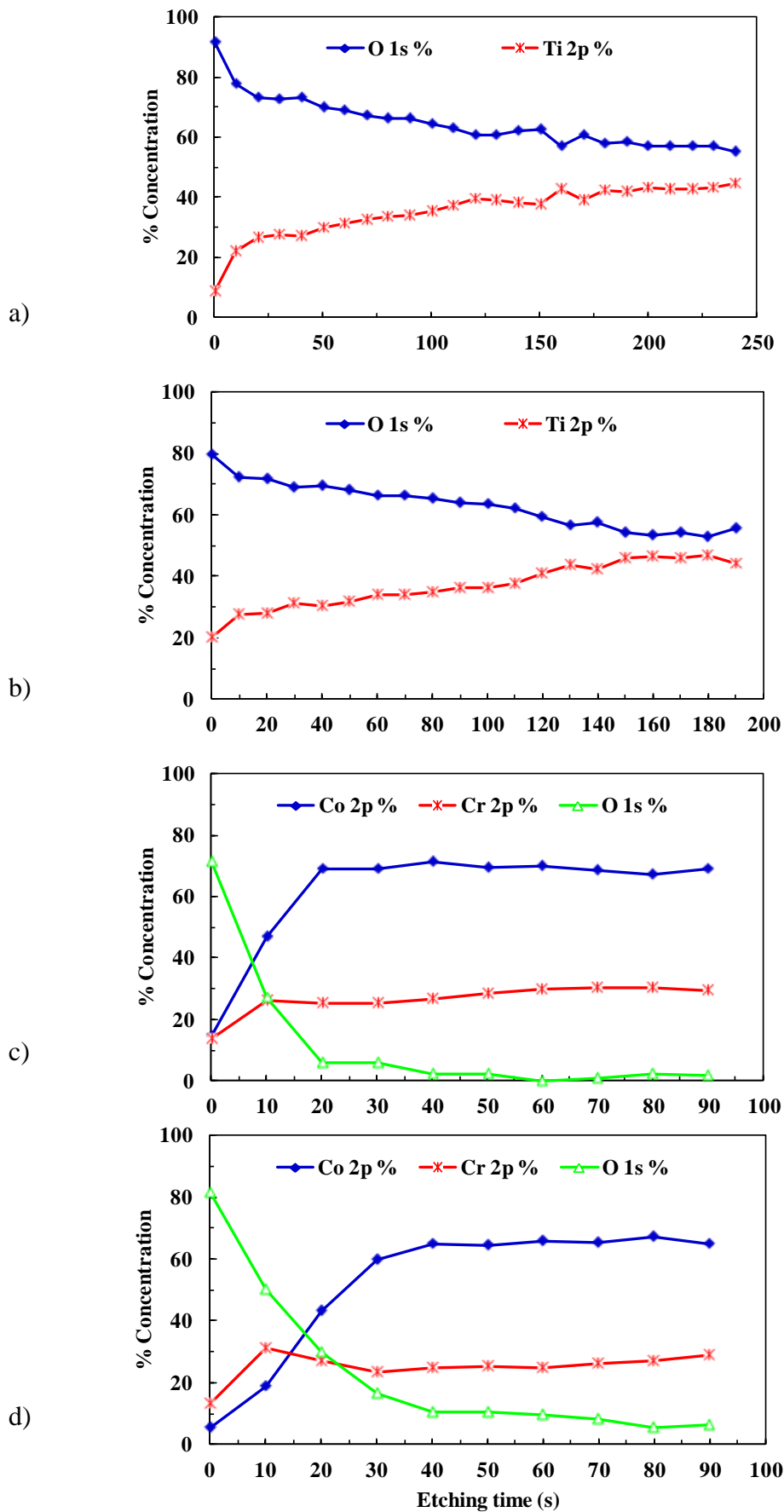


Figure 8-14. XPS depth profile analysis for Ti alloys (a) in vivo, (b) oxidised electrochemically and Co-Cr alloys (c) in vivo and (d) oxidised electrochemically.

It can be clearly seen that there is a very thick oxide layer (more than 150 *nm* based on sputter pit depth measurement) on both Ti alloys regardless of whether the oxidation occurred electrochemically or in the human body. When these results are compared to those from the Co-Cr alloys which were oxidised in an identical manner to the Ti alloy samples, the oxide layers for the Co-Cr alloys are found to be drastically thinner, being only a few nanometres thick, which is representative of the native oxide layer on metals.

The obtained results confirmed that oxidation occurs on both of the implanted metals, and that the produced oxide layer for Ti alloy is much thicker than Co-Cr alloy. Therefore, when considering the implantation of these metals for metal on metal implants, it is important to consider the tribocorrosion mechanisms as well as other important features.

These results suggest that a tribocorrosion mechanism is important in the wear of modular hips composed of Ti and Co-Cr alloy components. In the body, the surfaces of both alloys will oxidise, but the oxide layer produced will be much thicker on the Ti component. Mechanical degradation of these oxides will occur by tribological processes as the joints are loaded during movement, which will produce oxide debris. The thicker remnant oxide on the Ti alloy will protect the underlying metal from abrasive damage whereas the thinner oxide on Co-Cr cannot do this. Therefore more damage will be seen on the Co-Cr due to abrasion from the Ti oxide. As metal is uncovered by oxide fragmentation and detachment, fresh oxide will be created which can be damaged and removed by further movement resulting in a continuous corrosion-assisted wear process.

## **8.6 Summary**

The importance of the effect of oxidation and the changes which occurs due to the oxidation on the mechanical properties of materials has been shown by two important alloys used in hip implantation. These alloys were of interest due to the importance of their role in the quality of the human life. It was found that the nanoindentation technique is an effective method to measure the surface properties and detect the effects that can have an influence on these properties such as impurities, additives and native oxidation.

The accuracy of the obtained data for all of the materials tested in this work can be verified by the method proposed by Hainsworth and colleagues in 1996 which involves analysing the loading portion of the load-displacement curves instead of the unloading portions. Therefore, the results obtained using the Oliver and Pharr method by fitting the power-law relationship to the unloading curve for various materials are compared with the results obtained from the loading curves using the aforementioned method in the next chapter. The reliability of both the loading and unloading curve analyses is then discussed.

## Chapter 9. Loading Curve Analysis

*In this chapter, brief background information on loading curve analysis is provided. The nanoindentation hardness and modulus results using the Oliver and Pharr method for various materials used in this investigation are summarised and used to calculate loading curve behaviour. The results are then compared with the results measured from experimental data.*

### 9.1 Load-displacement Curves

Over the last two decades, nanoindentation tests have been commonly used to measure the mechanical properties of materials using the load-displacement curves by analysing the unloading portion of the curves. However, there was very little attention paid to the loading portion of the load-displacement curves, with the focus being mainly on the unloading portion. This can be due to the difficulties that can occur during indentation tests in the loading portion of the curve, such as discontinuities like pop-ins, during the loading. However, throughout this work, a large number of materials that do not show any discontinuity during the loading stage of the tests were investigated. Therefore, this presented an opportunity to use the loading portion of the load-displacement curves for various materials ranging from polymeric materials (tested with a very high strain rate to reduce viscose effect) to ceramic coatings with extremely high hardness and high modulus values. As some of these materials, such as fused silica, are standard materials with a known elastic modulus, they can be used to determine the accuracy of the loading curve analysis method.

### 9.2 General Background Information of the Method

As mentioned earlier in section 2.1, recording the material's response to the contact deformation continuously during the nanoindentation test provides the material's *mechanical fingerprint*, which is known as a load-displacement curve. Therefore, both the loading and unloading of the load-displacement curves can provide useful information about the material's behaviour, such as elastic and plastic deformation, during the indentation test. Various materials act in different ways and show different elastic and plastic deformations during the indentation tests. Therefore, obtaining mechanical properties for materials with high elastic moduli and indentation

hardness, stiff materials and also inhomogeneous systems can be very difficult with the unloading curve analysis. If the unloading curve does not behave well, the accuracy of the measured data based on the unloading curve and the validity of the obtained data will be an issue, since it strongly depends on the material's elastic recovery during the load removal (Hainsworth *et al.*, 1996). For these materials, measurement of the true contact area is another difficult task. Consequently, to avoid the difficulties in the determination of the true contact area, the loading curve analysis gained attention. In 1996, Hainsworth and colleagues (Hainsworth *et al.*, 1996) published a paper outlining a method of analysing the loading portion of the load-displacement curve rather than the unloading portion. The method was based on the previously developed analysis for the Vicker indenter in 1986 by Loubet and co-workers (Loubet *et al.*, 1986b). The basic principle of the method relies on the Sneddon relationship between the load,  $P$ , and displacement,  $\delta$ . According to the Sneddon analysis for the case of a non-adhesive rigid conical punch on the plane surface of a smooth elastic body load can be defined as below (Sneddon, 1965):

$$P = \frac{2E \tan \theta}{(1 - \nu^2)} \delta^2 \quad (9-1)$$

In this equation  $\theta$  is the half apical angle of the cone. During the loading and unloading, the normal load, calculated using this equation, is proportional to the square of the penetration depth. The elastic parameters (Young's modulus,  $E$ , and Poisson ratio,  $\nu$ ) as well as the geometrical properties of the contact ( $\theta$ ) are the factors that formulate the proportional factor. It was found that if the indentation takes place on uniform and homogeneous elastoplastic materials with perfect plasticity, the relation can be defined as below:

$$P = K_{ep} \delta^2 \quad (9-2)$$

In this equation  $K_{ep}$  depends on the aforementioned elastic parameters as well as the plastic parameter,  $Y$  (yield stress), and geometry of the indenter. Initially, it was assumed that the elastic and plastic behaviour of the materials can be split into two independent parts:

$$P = K_p \delta_p^2 \quad (9-3)$$

and

$$P = K_e \delta_e^2 \quad (9-4)$$

For the plastic part,  $K_p$  is a function of yield stress and for the elastic part,  $K_e$  is a function of  $E$ ,  $\nu$  and  $\theta$ . Another assumption that was made was that  $\delta = \delta_p + \delta_e$ ; therefore:

$$K_{ep} = \left[ (K_e)^{-1/2} + (K_p)^{-1/2} \right] \quad (9-5)$$

According to Loubet and colleagues, this equation can be expressed as follows in terms of the Vickers hardness ( $H_v$ ) (Loubet *et al.*, 1986b):

$$K_{ep} = \left[ 0.92 \left( \frac{1 - \nu^2}{E} \right) \sqrt{H_v} + \frac{0.194}{\sqrt{H_v}} \right]^{-2} \quad (9-6)$$

In 1996 Hainsworth and colleagues (Hainsworth *et al.*, 1996) used the same assumption for the total deformation of material as two components (elastic and plastic components) for the loading curve. Based on their method, if the indented material behaves in a plastic manner, a characteristic contact radius,  $a_c$ , would be presented as:

$$a_c = \sqrt{\frac{P}{H}} \quad (9-7)$$

The plastic indentation depth for both the conical and pyramidal indenters has a direct relationship with the characteristic contact radius, therefore:

$$\delta_p = \phi a_c = \phi \sqrt{\frac{P}{H}} \quad (9-8)$$

In this equation  $P$  is the load,  $H$  is the hardness and  $\phi$  is an empirical constant that depends on the geometry of the used indenter. Moreover, the elastic component developed using dimensional analysis is:

$$\delta_e = \psi \frac{P}{E a_c} = \psi \frac{P}{E} \sqrt{\frac{H}{P}} \quad (9-9)$$

where  $\psi$  is another empirical constant. Therefore, the combined elastic and plastic deformations can be rewritten as below:

$$\delta = \delta_p + \delta_e = \phi \sqrt{\frac{P}{H}} + \psi \frac{P}{E} \sqrt{\frac{H}{P}} \quad (9-10)$$

Therefore:

$$\delta^2 = \frac{P}{E} \left( \phi \sqrt{\frac{E}{H}} + \psi \sqrt{\frac{H}{E}} \right)^2 \quad (9-11)$$

Consequently, the load and displacement relationship can be written as below:

$$P = E \left( \phi \sqrt{\frac{E}{H}} + \psi \sqrt{\frac{H}{E}} \right)^{-2} \delta^2 = K_m \delta^2 \quad (9-12)$$

Therefore, as  $K_m$  is the equivalent of Loubet's elastic-plastic parameter, it can be directly compared to that of  $K_{exp}$  which can be measured from experimental load and displacement curves. Hainsworth et al., also found that  $\phi = 0.194$  and  $\psi = 0.93$  experimentally. These constant values were measured for a blunt Berkovich indenter for a range of materials. However, this research did not use contact or reduced modulus,  $E_r$ , in the calculations. This was justified as it was claimed that any discrepancy would be overcome by using the constants  $\phi$  and  $\psi$ .

However, later in 2000, a similar equation was developed by Malzbender et al. (Malzbender *et al.*, 2000). In this equation, rather than using the Young's modulus, the reduced modulus was introduced to the Equation (9-12). In fact, a physical basis for the empirical constants reported by Hainsworth et al. was presented, which was expressed as below:

$$P = E_r \left( \frac{1}{\sqrt{C}} \sqrt{\frac{E_r}{H}} + \varepsilon \sqrt{\frac{\pi}{4}} \sqrt{\frac{H}{E_r}} \right)^{-2} \delta^2 \quad (9-13)$$

In this equation,  $C$  defines the tip geometry and for a perfect Berkovich tip  $C = 24.5$  and  $\varepsilon = 0.75$ . Therefore, the constant factors  $\phi$  and  $\psi$  can be calculated:

$$\phi = \frac{1}{\sqrt{C}} = \frac{1}{\sqrt{24.5}} = 0.202 \quad \text{and} \quad \psi = \varepsilon \sqrt{\frac{\pi}{4}} = 0.75 \sqrt{\frac{\pi}{4}} = 0.664$$

The constant  $\phi$  value is in a good agreement with the value reported by Hainsworth et al. however the  $\psi$  shows variation with the reported value. It should be noted that the tip end shape of any indenter is not perfect therefore due to the rounding of the tip, a correction factor,  $\xi$ , was added to Equation (9-13). For this reason, the indenter area function can be modified as below (Sun *et al.*, 1999):

$$A_c = C(\delta_c + \xi)^2 \quad (9-14)$$

The  $\gamma$  correction factor described in section 2.1.2 was also added to Equation (9-13) due to non-axial symmetry of the indenter tip.

$$\gamma = \pi \frac{\frac{\pi}{4} + 0.154 \cot \phi \frac{(1-2\nu)}{4(1-\nu)}}{\left(\frac{\pi}{2} - 0.831 \cot \phi \frac{(1-2\nu)}{4(1-\nu)}\right)^2} \quad (9-15)$$

Finally, Equation (9-13) can be rewritten by including both of the correction factors as below:

$$P = E_r \left( \frac{1}{\sqrt{C}} \sqrt{\frac{E_r}{H}} + \frac{\varepsilon}{\gamma} \sqrt{\frac{\pi}{4}} \sqrt{\frac{H}{E_r}} \right)^{-2} (\delta + \xi)^2 \quad (9-16)$$

Similar to the model reported by Hainsworth, et al. this method has the capability of calculating either the hardness or modulus values if the other one is known. One of the major advantages of this technique is that it does not require any treatment of the data to remove the effects of factors including pile-up, sink in and time dependent behaviour. However, there are inherent disadvantages to this technique, one of which is that the calculation requires the occurrence of fully plastic behaviour in the sample material and as a result the technique is not appropriate when the elastic regime is significant. This situation can occur when using either very low loads or very small displacements. Another disadvantage is that any discontinuity in the loading section of the load-displacement curve, caused by events such as pop-ins, will have an effect on the obtained results.

In this work, the loading curve analysis was used to check the accuracy of the data obtained using the Oliver and Pharr method for various materials. Figure 9-1 illustrates examples of the loading portion of the load-displacement curves for several materials that were investigated in this work.

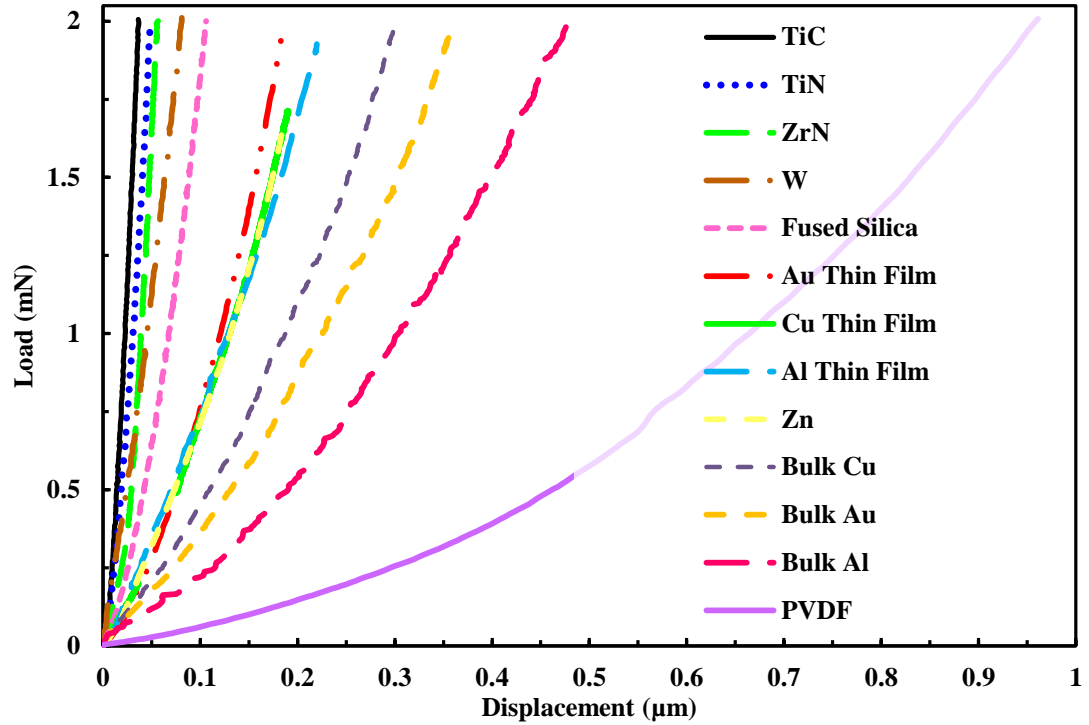


**Figure 9-1. Loading portions of the load-displacement curves for various materials with wide ranges of  $E$  and  $H$  at approximately the same indentation load.**

By assuming  $P = K_m (\delta + \xi)^2$  and using Equation (9-16),  $K_m$  can be calculated from the experimental results obtained in this investigation. For each individual material, the average of 10 hardness and modulus values were used from similar loads. Table 9-1 illustrates the average hardness and contact modulus values as well as the calculated  $K_m$  values from the same materials using Equation (9-16).

Material	H (GPa)	$E_r$ (GPa)	$E$ (GPa)	$\nu$	$\gamma$	$K_m$
TiC	37.17	328	443	0.19	1.0910	506
ZrN	24.96	331	449	0.19	1.0910	409
TiN	25.61	269	329	0.25	1.0787	377
W	7.25	321	411	0.28	1.0718	155
Fused Silica	10.5	70	72	0.17	1.0948	122
Cu thin film	1.7	121	121	0.33	1.0591	38
Bulk Cu	1.4	116	115	0.33	1.0591	32
Au thin film	1.08	80	71	0.42	1.0316	24
Zn	1.02	79	80	0.25	1.0787	23
Al thin film	0.8	74	70	0.33	1.0591	18
Bulk Au	0.65	90	80	0.42	1.0316	15
Bulk Al	0.45	76	73	0.33	1.0591	11
PVDF	0.08	2	2	0.18	1.0929	2

**Table 9-1. Summary of the materials with various  $H$  and  $E$  values used to calculate the  $K_m$  values.**

To compare the measured  $K_m$  with the  $K_{exp}$  and check the accuracy of the data, load ( $P$ ) versus displacement squared ( $\delta^2$ ) curves were plotted for each material to find the line of best fit for each curve that, according to Hainsworth et al., is the  $K_{exp}$ . Hainsworth et al. then used the  $K_{exp}$  to find the constants  $\phi$  and  $\psi$ .

To compare the calculated  $K_m$  values from Equation (9-16) with the  $K_{exp}$  values determined from the  $P$  vs.  $\delta^2$  plots, a graph of  $K_m$  versus  $K_{exp}$  was plotted. Initially these graphs were plotted for individual materials to compare the accuracy of the results for each sample. Afterward, the average  $K_m$  and  $K_{exp}$  for various materials under approximately the same load were drawn. Figure 9-2 shows some examples of the  $K_m$  vs  $K_{exp}$  graphs with the same material in each graph but under different loading conditions.

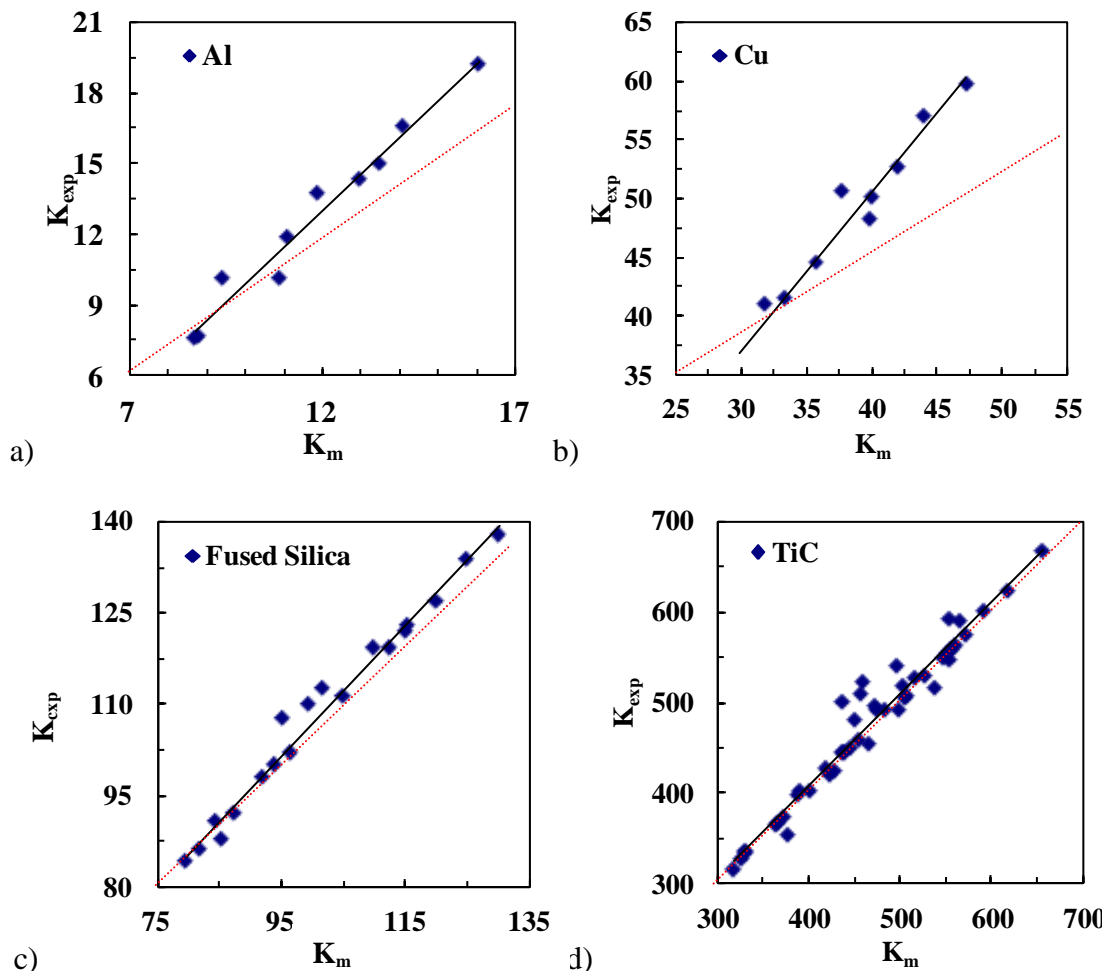


**Figure 9-2.**  $K_{exp}$  versus  $K_m$  plotted for low  $H$  and  $E$  (a) Al and (b) Cu as well as high  $H$  and  $E$  (c) fused silica and (d) TiC. The black solid line in each curve indicates the linear fit to the obtained data and the red dashed line indicates the expected line.

As can be seen, the graphs plotted for both types of materials (materials with low hardness and moduli as well as materials with high hardness and moduli) show that a linear relationship was observed. Although there is small variation in the results, the linearity of the curves can be a good indication of the accuracy of both types of data for low and high loads. Similar behaviour was observed for all the materials investigated in this work. Therefore, to develop an understanding of the relationship between the variety of materials, a graph was plotted for a range of materials under the same indentation conditions for  $K_m$  versus  $K_{exp}$  which is shown in Figure 9-3.

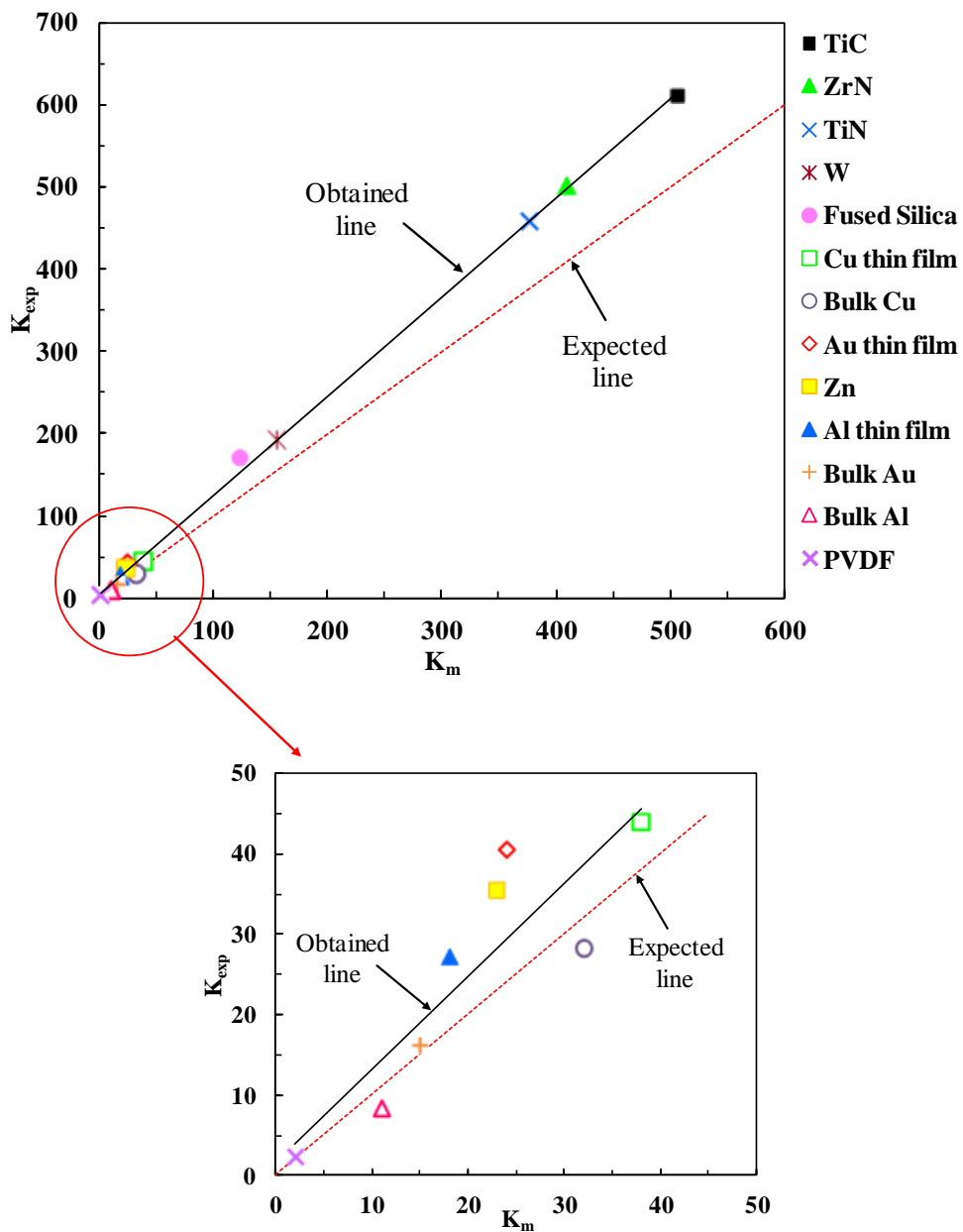


Figure 9-3.  $K_{exp}$  versus  $K_m$  plotted for various types of materials including both high and low hardness and modulus values.

As the range of investigated materials included those with very low hardness and Young's modulus and those with higher values, some of the values were very small in comparison and therefore a magnified graph detailing the lower section of the original graph is also shown in Figure 9-3.

The results shown in Figure 9-3 illustrates that the relationship between the  $K_{exp}$  and  $K_m$  for all types of materials, ranging from soft materials like PVDF, to very hard and stiff materials such as TiC, stays linear if the results are measured accurately. When the graph was magnified for the lower portion of the curve it was clear that the scatter in the data for softer materials is more significant than that of hard and stiff materials, however, they still show a linear relationship.

If Equations (9-12) or (9-16) were a correct description of the loading behaviour, then it is expected that  $K_m$  would be equal to  $K_{exp}$ . In general this has not been observed here, with the best agreement occurring for hard, stiff materials like TiC. Soft metals show a very large deviation which might be due to the effects of time-dependent deformation (creep). However, when all data are plotted together for different materials, there is a linear relationship between  $K_m$  and  $K_{exp}$ . A numerical agreement can be achieved by changing  $\psi$  in Equation (9-12) or the value of  $\varepsilon$  in Equation (9-16). The value of  $\psi$  would need to be 0.25 to make  $K_m$  equal to  $K_{exp}$  and  $\varepsilon$  would need to be 0.28, which is not physically reasonable. Further work is therefore necessary to develop a reliable loading curve equation.

### 9.3 Summary

This chapter can conclude that the loading curve analysis can be a very accurate method to measure the hardness or Young's modulus of very stiff materials with high hardness, if one of these values is known. It can also be used to determine the effects of concepts such as creep and pile-up in the measured data from the Oliver and Pharr method. However, for the softer materials with very low elastic moduli the loading curve analysis results may vary from the results obtained from unloading curve analysis. Therefore, this necessitates using both analysis methods to compare the results instead of determining the result through one method.

It can be concluded that if the loading curve is well behaved there is the potential to verify the measured hardness and Young's modulus of materials for accuracy and

any variation in the results should be checked. The AFM imaging can be helpful to understand the sources of the variation such as surface roughness.

All of the key findings from this investigation are summarised in next chapter and the importance of each phenomena that can have an influence on the mechanical properties of material measured by nanoindentation is listed.

## **Chapter 10. Conclusions and Future Work**

*This chapter summarise all the main factors that need consideration in order to accurately measure the mechanical properties of materials using the nanoindentation technique. The main results determined during this investigation are presented. The importance of effects such as pile-up, oxidation, surface roughness, density and more importantly creep on the mechanical properties obtained using nanoindentation under different test protocols are discussed.*

### **10.1 Mechanical Properties of Thin films**

The hardness and Young's modulus of very thin coatings and bulk materials can be reliably measured at low contact depths where pile-up does not influence the results. Although indentation size effects may influence the measured hardness, the contact modulus is not affected by contact scale. However, when thin coatings such as Cu and Au are deposited on an underlying silicon oxide substrate with a lower modulus than the coating, the contact modulus will tend to decrease as the contact depth increases. This is not an indentation size effect, but instead the consequence of the coating stack being, in essence, a set of springs in series. Thus to understand the indentation behaviour of a multilayer coating stack, all layers must be considered.

#### ***10.1.1 Copper Thin Film***

For thin Cu films at low indentation loads, a transition from single grain to many-grain behaviour was observed. Measurements in different grains at low loads lead to considerable scatter in the measured Young's modulus data. This is due to the possibility that indentation takes place in a single grain and consequently the measured data is that of an individual grain and as Cu is anisotropic, these different grains can have varying orientations and subsequently, different Young's modulus values. When the contact depth increases, this effect is reduced as continuum behaviour (many grains) is achieved. The contact depth at which this occurs was found to be lower for modulus than hardness because of the relatively long range of elastic behaviour.

The annealing of Cu thin films promotes the presence of the (111) texture of the coating, leading to an increase in the contact modulus of the coating and

consequently the obtained Young's modulus. The EBSD and XRD results confirmed that in the Cu thin film annealed at 350 °C, the (111) texture was dominant, resulting in a higher Young's modulus than the sample annealed at 100 °C and the non-annealed Cu thin film. The nanoindentation technique is sensitive enough to be influenced by anisotropy, but the measurements do not show the complete range of single crystal Cu data as deformation is not uniaxial in the indentation test. However, when anisotropic materials, such as Zn, with grains of a large size were tested, the microstructural effects on the Young's modulus data were clearly noticeable. Consequently, it was observed that in anisotropic materials, the scatter in the Young's modulus results can be due to the effect of the orientation of each individual grain during the indentation tests.

When both the single cycle and multi-cycle indentation tests were compared for all Cu thin films, there was a deviation between the two test protocols at higher loads and contact depths. This was due to pile-up appearance and its effect on the measured contact area, consequently causing an overestimation of the Young's modulus and hardness values.

Although the appearance of pile-up was clear for all of the Cu thin films tested in this work based on the AFM images obtained after the indentation tests, it was found that dislocation nucleation changes through annealing. Consequently, the appearance of pile-up and their shapes were dissimilar for different Cu thin films due to the activation of different slip systems during the indentation tests. This was due to the differences in the size and orientations of the grains that were undergoing indentation.

### ***10.1.2 Pile-up Effect***

It was observed that the pile-ups have a significant effect on the accuracy of the hardness and Young's modulus values obtained from the nanoindentation tests, especially for indentation tests carried out on the soft thin films deposited on hard substrates. The importance of pile-up correction for the nanoindentation results was illustrated by the changes in the Young's modulus values of Al thin films deposited on glass substrates. Since Al and glass have similar modulus values, any unusual change in the data was related to the appearance of pile-up. The effect of pile-up on

the Young's modulus and hardness values was quantified and found to range from 5 to 30% and 10 to 45% respectively, depending on the contact depth.

When the appearance of the pile-ups were compared for the bulk Al and Cu, it was found that the dislocation movements under the indentation tests differ for Al and Cu bulk samples, and the effect of pile-up on the mechanical properties of bulk Al is much smaller in comparison to that of bulk Cu under similar indentation conditions.

In general, when the pile-up height and width of the Cu, Au and Al thin films were compared to that of similar bulk materials, it was found that the bulk materials tend to form less pile-up than thin films. This confirmed that thin films show different plastic deformation under the indentation tests due to the substrate effect as well as the work hardening effect. It was also found that the pile-up appears asymmetrically in most of the indentation tests and consequently, the pile-up correction methods using constant factors that are suggested in literature are not practical, unless the AFM or SEM images after indentation tests are available and the true contact area can be measured.

The other important finding was the effect of the loading and unloading test protocols on pile-up formation. It was found that the method by which the load is applied during the indentation tests can change the appearance of the produced pile-ups. For example, the measured pile-up heights for the multi-cycling tests were higher than the single cycle tests under the same indentation conditions. Moreover, the heights of the pile-ups were even greater for the experiments conducted with multi-cycling tests using 90% unloading of the maximum load protocol.

### ***10.1.3 Surface Roughness and Density Effects***

Another important factor which can influence the contact area measurement is the surface roughness. An examination into the effect of surface roughness was performed using various bulk and coating samples for comparison. When the hardness and Young's modulus values were compared for the smooth and rough surfaces, it was found that the best data can be obtained when the indentation size is much bigger than the size of the grains and the roughness of the surface. However, the data demonstrated huge scatter when the surface roughness was larger than the indentation size. This was due to the support of the surrounding surface features on

the indenter tip, thereby modifying the calculated contact area and consequently causing an over or under estimation of the measured hardness and modulus values. Therefore, the location at which the indenter is seated during the indentation tests significantly influences the data.

It was also found that the density of the coatings has an enormous influence in determining mechanical properties from nanoindentation tests, and that the Young's modulus and hardness can be reduced if the density of the material decreases. The reduction in the mechanical properties of materials was found to have a direct relationship with their density. This was also confirmed by modelling the indentation response of porous coatings using the finite element analysis code OOF2. It was found that the effect of density on the elastic modulus is as important as surface roughness because it is of a similar scale to the size of the impression.

#### ***10.1.4 Creep Effect***

It was found that creep occurs for many types of materials, ranging from Cu with a high melting point to Sn with a much lower melting point, and needs to be considered during the indentation process at room temperature. However, the difference between these materials is that for materials such as Cu and Au, only the primary creep needs to be removed from the indentation data. This can be easily achieved by choosing the correct loading and unloading rate, and sufficient holding period at maximum load. In this study it was found that the holding period of 4 to 10 s is enough to allow for creep to run out for both open loop mode and displacement control test protocols, since both of these materials experience only the primary creep stage during the nanoindentation tests. This was determined by carrying out indentation tests at different maximum load hold periods and no differences were obtained in the hardness and modulus values. However, it was found that during the indentation tests for materials with lower melting point such as Zn and Sn, the secondary creep stage was observed in addition to primary creep. Therefore, choosing the correct test protocol was deemed to be essential in being able to measure the mechanical properties of materials without the effect of creep in the data. The indentation tests carried out under open loop mode illustrated noticeable creep effect on the data. The effect was clear enough to be seen from the load-displacement curves in which an obvious nose appeared at the beginning of the

unloading curves. The first step to eliminate the effect of the creep was to remove the nose from the load-displacement curves and it is suggested by literature that this can be accomplished by holding the load at the maximum load for a long period of time. However, it was found that not only did a prolonged holding period at the maximum load fail to remove the effect of creep on the nanoindentation test results, but also allowed the material to reach the secondary creep segment, which is not easily removed under open loop mode. Therefore, if open loop mode is the chosen test protocol, the appropriate selection of the loading rate, the holding period at the maximum load and the unloading rate can all together minimise the effect of creep on the nanoindentation load-displacement curves and consequently the Young's modulus and hardness results. It was found that for both the Zn and Sn samples the best loading and unloading rates to minimise the creep effect were 20 to 50  $\mu\text{m/s}$  and 10 to 50 second holding period at the maximum load. Although these test conditions minimise the effect of the creep on the obtained data, creep nevertheless still occurs at a very minute level.

In this work the best results were obtained under the displacement control protocol. The creep effect was very diminutive even with a quick loading rate, holding period and unloading rate test conditions using displacement control. Therefore this study suggests the use of the displacement control protocol for materials with low melting points and high creep rates such as Sn and Zn.

#### ***10.1.5 Oxidation Effect***

The Cu thin films used in semiconductor devices are passivated with a TiW layer to prevent oxidation however it was found that after prolonged storage the films become oxidised which leads to a decrease in the Young's modulus of the Cu near the surface. The effect of oxidation on the modulus values was also observable from the bulk Cu sample. Most of the metals used in industry have the potential to be oxidised during their performance and therefore a change in the mechanical properties can be obtained during the use of the metals.

In this work the effect that oxidation can have on mechanical properties in the context of its effect on the longevity of materials was studied. It was revealed that one of the major causes of failure in hip implants of the modern modular design is surface oxidation. Through this work it was found, the oxidation of the Ti alloy used

in the stem portion of the implants significantly changes the mechanical properties of the alloy. A harder and stiffer oxidised Ti alloy wears the Co-Cr alloy. Although the Co-Cr alloy undergoes oxidation as well, it was found that the mechanical properties of Co-Cr alloys do not change due to the oxidation. Therefore, the softer Ti alloy becomes harder due to the oxidation and wears the Co-Cr femoral head at the taper connection. This was a clear example of the significance of oxidation taking place and the need for consideration of the environment in which materials are designed to be used.

## **10.2 Loading Curve Analysis**

The accuracy of all the data obtained by means of the unloading curve analysis can be verified by using the loading curve analysis provided the constants in the loading curve prediction equation are accurately known. This method provides a very effective result for the hard and stiff materials however, for the soft materials with a low elastic modulus, there is a small degree of scatter in the data. This variation can be due to the disadvantages of both the loading curve and unloading curve analyses. For the loading curve analysis it was found that the data is less accurate when the load or displacement is very small as the plastic regime of loading is not attained and therefore the fit to the curve is not as accurate. For the unloading curve analysis, the effects of pile-up, sink-in and creep all result in a greater degree of scatter in the obtained data.

## **10.3 Possible Future Work**

In this study the materials of focus have all been metals and therefore there is a need to expand the range of materials to include different types of materials. Some examples of these materials are visco-elastic materials and very soft materials, such as biomaterials. The inclusion of these materials in a future study would allow for verification that all of the conclusions found in this work are applicable to materials other than just metals.

## References

---

- Abadias, G., Dub, S. and Shmegeera, R. (2006) 'Nanoindentation hardness and structure of ion beam sputtered TiN, W and TiN/W multilayer hard coatings', *Surface & Coatings Technology*, 200(22-23), pp. 6538-6543.
- Akhadejdamrong, T., Mitsuo, A., Iwamoto, C., Yamamoto, T., Ikuhara, Y. and Aizawa, T. (2002) 'Formation of protection layer during oxidation of Al-implanted TiN coating', *Materials Transactions*, 43(6), pp. 1291-1297.
- Andricacos, P.C. (1999) 'Copper on-chip interconnections. A breakthrough in electrodeposition to make better chips', *Electrochemical Society Interface*, 8(1), pp. 32-36.
- Andricacos, P.C., Uzoh, C., Dukovic, J.O., Horkans, J. and Deligianni, H. (1998) 'Damascene copper electroplating for chip interconnections', *Ibm Journal of Research and Development*, 42(5), pp. 567-574.
- Armstrong, D.E.J., Wilkinson, A.J. and Roberts, S.G. (2009) 'Measuring anisotropy in Young's modulus of copper using microcantilever testing', *Journal of Materials Research*, 24(11), pp. 3268-3276.
- Aryaei, A. and Jayasuriya, A.C. (2013) 'Mechanical properties of human amniotic fluid stem cells using nanoindentation', *Journal of Biomechanics*, 46(9), pp. 1524-1530.
- Ashby, M.F. and Jones, D.R.H. (2005) *Engineering Materials 1: An Introduction to Properties, Applications and Design*. Elsevier Science, pp. 38.
- Ashby, M.F., Shercliff, H. and Cebon, D. (2013) *Materials: engineering, science, processing and design; North American Edition*. Elsevier Science, pp. 62.
- Asif, S.A.S., Wahl, K.J. and Colton, R.J. (1999) 'Nanoindentation and contact stiffness measurement using force modulation with a capacitive load-displacement transducer', *Review of Scientific Instruments*, 70(5), pp. 2408-2413.
- Baba-Kishi, K.Z. (1998) 'Measurement of crystal parameters on backscatter Kikuchi diffraction patterns', *Scanning*, 20(2), pp. 117-127.
- Bachman, B.J. and Vasile, M.J. (1989) 'Ion-bombardment of polyimide films', *Journal of Vacuum Science & Technology a-Vacuum Surfaces and Films*, 7(4), pp. 2709-2716.
- Baker, S.P., Barbee, T.W. and Nix, W.D. (1991) 'Time-dependent deformation in room-temperature indentation experiments using a nanoindenter', *MRS Proceedings*, 239, pp. 319-325.
- Baker, S.P. and Nix, W.D. (1994) 'Mechanical properties of compositionally modulated Au-Ni thin films - nanoindentation and microcantilever deflection experiments', *Journal of Materials Research*, 9(12), pp. 3131-3145.

- Beake, B.D., Goodes, S.R. and Smith, J.F. (2003) 'Nanoscale materials testing under industrially relevant conditions: high-temperature nanoindentation testing', *Zeitschrift Fur Metallkunde*, 94(7), pp. 798-801.
- Bell, T.J., Bendeli, A., Field, J.S., Swain, M.V. and Thwaite, E.G. (1992a) 'The determination of surface plastic and elastic properties by ultra micro-indentation', *Metrologia*, 28(6), pp. 463-469.
- Bell, T.J., Field, J.S. and Swain, M.V. (1992b) 'Elastic-plastic characterization of thin films with spherical indentation', *Thin Solid Films*, 220(1-2), pp. 289-294.
- Bell, T.J., Field, J.S. and Swain, M.V. (1992c) *Stress-strain behaviour of thin-films using a spherical tipped indenter*, MRS Proceedings, 239, pp. 331-336.
- Bhagavat, S. and Kao, I. (2005) 'Nanoindentation of lithium niobate: hardness anisotropy and pop-in phenomenon', *Materials Science and Engineering a-Structural Materials Properties Microstructure and Processing*, 393(1-2), pp. 327-331.
- Bhushan, B. and Li, X.D. (2003) 'Nanomechanical characterisation of solid surfaces and thin films', *International Materials Reviews*, 48(3), pp. 125-164.
- Bischoff, U.W., Freeman, M.A.R., Smith, D., Tuke, M.A. and Gregson, P.J. (1994) 'Wear induced by motion between bone and titanium or cobalt-chrome alloys', *Journal of Bone and Joint Surgery-British Volume*, 76B(5), pp. 713-716.
- Bobji, M.S. and Biswas, S.K. (1999) 'Deconvolution of hardness from data obtained from nanoindentation of rough surfaces', *Journal of Materials Research*, 14(6), pp. 2259-2268.
- Bolshakov, A., Oliver, W.C. and Pharr, G.M. (1995) 'An explanation for the shape of nanoindentation unloading curves based on finite element simulation', in Baker, S.P., Ross, C.A., Townsend, P.H., Volkert, C.A. and Borgesen, P. (eds.) *Thin Films: Stresses and Mechanical Properties V*.
- Bonin, W.A. and Hysitron Inc. (1996) *Capacitive transducer with electrostatic actuation*. Patent, U.S. 5576483.
- Bonin, W.A. and Hysitron Inc. (1999) *Multi-dimensional capacitive transducer*. Patent, U.S. 5869751.
- Bray, J. (2002) *Innovation and the Communications Revolution: From the Victorian Pioneers to Broadband Internet*. Institution of Engineering and Technology, pp. 109.
- Brinksmeier, E. and Schmutz, J. (1997) 'Generation and texture of surfaces in ultraprecision cutting of copper', *Machining Science and Technology*, 1(2), pp. 185-193.
- Brotzen, F.R. and Moore, S.C. (1994) 'Mechanical testing of thin films', *International Materials Reviews*, 39(1), pp. 24-45.
- Brown, C., Fisher, J. and Ingham, E. (2006) 'Biological effects of clinically relevant wear particles from metal-on-metal hip prostheses', *Proceedings of the Institution of Mechanical Engineers Part H-Journal of Engineering in Medicine*, 220(H2), pp. 355-369.

- Brunette, D.M. (2001) *Titanium in Medicine: Material Science, Surface Science, Engineering, Biological Responses & Medical Applications*. Springer Verlag, pp. 128.
- Buckle, H. (1973) *Science of hardness testing and its research applications*. Metals Park, Ohio: ASM, pp. 453.
- Buckley, D.H. (1976) 'Crystal structure', in Sarker, A.D. (ed.) *Wear of metals*. New York: Pergamon Press, pp. 93.
- Bull, S.J. (2002) 'Extracting hardness and Young's modulus from load-displacement curve', *Zeitschrift Fur Metallkunde*, 93(9), pp. 870-874.
- Bull, S.J. (2003) 'On the origins and mechanisms of the indentation size effect', *Zeitschrift Fur Metallkunde*, 94(7), pp. 787-792.
- Bull, S.J. (2012) 'Mechanical response of atomic layer deposition alumina coatings on stiff and compliant substrates', *Journal of Vacuum Science & Technology A*, 30(1), p. 01A1602.
- Bull, S.J., Page, T.F. and Yoffe, E.H. (1989) 'An explanation of the indentation size effect in ceramics', *Philosophical Magazine Letters*, 59(6), pp. 281-288.
- Bull, S.J., Sanderson, L., Moharrami, N. and Oila, A. (2012) 'Effect of microstructure on hardness of submicrometre thin films and nanostructured devices', *Materials Science and Technology*, 28(9-10), pp. 1177-1185.
- Burnham, N.A. and Colton, R.J. (1989) 'Measuring the nanomechanical properties and surface forces of materials using an atomic force microscope', *Journal of Vacuum Science & Technology a-Vacuum Surfaces and Films*, 7(4), pp. 2906-2913.
- Callister, W.D. and Rethwisch, D.G. (2011) *Fundamentals of Materials Science and Engineering: An Integrated Approach*. Wiley, pp. 261.
- Cardinale, G.F. and Tustison, R.W. (1992) 'Fracture strength and biaxial modulus measurement of plasma silicon-nitride films', *Thin Solid Films*, 207(1-2), pp. 126-130.
- Carlton, R.A., Lyman, C.E. and Roberts, J.E. (2004) 'Accuracy and precision of quantitative energy-dispersive X-ray spectrometry in the environmental scanning electron microscope', *Scanning*, 26(4), pp. 167-174.
- Chakraborty, H., Sinha, A., Mukherjee, N. and Chattopadhyay, P.P. (2012) 'Exfoliated graphite reinforced PMMA composite: A study on nanoindentation and scratch behavior', *Journal of Nanotechnology*.
- Charles, E. A. and Ness, M.G. (2006) 'Crevice corrosion of implants recovered after tibial plateau leveling osteotomy in dogs', *Veterinary Surgery*, 35(5), pp. 438-444.
- Chen, J. and Bull, S.J. (2006a) 'A critical examination of the relationship between plastic deformation zone size and Young's modulus to hardness ratio in indentation testing', *Journal of Materials Research*, 21(10), pp. 2617-2627.

- Chen, J. and Bull, S.J. (2006b) 'On the relationship between plastic zone radius and maximum depth during nanoindentation', *Surface & Coatings Technology*, 201(7), pp. 4289-4293.
- Chen, J. and Bull, S.J. (2008) 'Multi-cycling nanoindentation study on thin optical coatings on glass', *Journal of Physics D-Applied Physics*, 41(7).
- Chen, J. and Bull, S.J. (2011) 'Approaches to investigate delamination and interfacial toughness in coated systems: an overview', *Journal of Physics D-Applied Physics*, 44(3).
- Chen, J., Bull, S.J., Roy, S., Kapoor, A., Mukaibo, H., Nara, H., Momma, T., Osaka, T. and Shacham-Diamand, Y. (2009) 'Nanoindentation and nanowear study of Sn and Ni-Sn coatings', *Tribology International*, 42(6), pp. 779-791.
- Cheng, Y.-T. and Cheng, C.-M. (2000) 'What is indentation hardness?', *Surface and Coatings Technology*, 133-134(0), pp. 417-424.
- Cheng, Y.L., Wang, Y.L., Chen, H.C. and Lin, J.H. (2006) 'Effect of inter-level dielectrics on electromigration in damascene copper interconnect', *Thin Solid Films*, 494(1-2), pp. 315-319.
- Cheng, Y.T. and Cheng, C.M. (2004) 'Scaling, dimensional analysis, and indentation measurements', *Materials Science & Engineering R-Reports*, 44(4-5), pp. 91-149.
- Chiba, A., Kumagai, K., Nomura, N. and Miyakawa, S. (2007) 'Pin-on-disk wear behavior in a like-on-like configuration in a biological environment of high carbon cast and low carbon forged Co–29Cr–6Mo alloys', *Acta Materialia*, 55(4), pp. 1309-1318.
- Chinn, R.E. (2009) 'Hardness, bearings, and the Rockwells', *Advanced Materials & Processes*, 167(10), pp. 29-31.
- Chrzanowski, J. and Irwin, J.C. (1989) 'Raman-scattering from cupric oxide', *Solid State Communications*, 70(1), pp. 11-14.
- Chudoba, T. and Richter, F. (2001) 'Investigation of creep behaviour under load during indentation experiments and its influence on hardness and modulus results', *Surface and Coatings Technology*, 148(2–3), pp. 191-198.
- Cohen, D. (2012) 'How safe are metal-on-metal hip implants?', *British Medical Journal*, 344.
- Collier, J.P., Surprenant, V.A., Jensen, R.E., Mayor, M.B. and Surprenant, H.P. (1992) 'Corrosion between the components of modular femoral hip prostheses', *Journal of Bone and Joint Surgery-British Volume*, 74(4), pp. 511-517.
- Constantinides, G., Silva, E.C.C.M., Blackman, G.S. and Van Vliet, K.J. (2007) 'Dealing with imperfection: Quantifying potential length scale artefacts from nominally spherical indenter probes', *Nanotechnology*, 18(30).
- Constantinides, G., Tweedie, C.A., Holbrook, D.M., Barragan, P., Smith, J.F. and Van Vliet, K.J. (2008) 'Quantifying deformation and energy dissipation of polymeric surfaces under localized impact', *Materials Science and Engineering a-*

*Structural Materials Properties Microstructure and Processing*, 489(1-2), pp. 403-412.

Cook, J., Azam, M., Leung, P. and Grupen, M. (1999) 'Performance of vertical power devices with contact-level copper metallization', *Thin Solid Films*, 348(1-2), pp. 14-21.

Danilatos, G.D. (1993) 'Introduction to the ESEM instrument', *Microscopy Research and Technique*, 25(5-6), pp. 354-361.

Dao, M., Chollacoop, N., Van Vliet, K.J., Venkatesh, T.A. and Suresh, S. (2001) 'Computational modeling of the forward and reverse problems in instrumented sharp indentation', *Acta Materialia*, 49(19), pp. 3899-3918.

Doerner, M.F. and Nix, W.D. (1986) 'A method for interpreting the data from depth-sensing indentation instruments ', *Journal of Materials Research*, 1, pp. 601-609.

Draissia, M., Boudemagh, H. and Debili, M.Y. (2004) 'Structure and hardness of the sputtered Al-Cu thin films system', *Physica Scripta*, 69(4), pp. 348-350.

Dub, S., Novikov, N. and Milman, Y. (2002) 'The transition from elastic to plastic behaviour in an Al-Cu-Fe quasicrystal studied by cyclic nanoindentation', *Philosophical Magazine a-Physics of Condensed Matter Structure Defects and Mechanical Properties*, 82(10), pp. 2161-2172.

Dub, S.N., Lim, Y.Y. and Chaudhri, M.M. (2010) 'Nanohardness of high purity Cu (111) single crystals: The effect of indenter load and prior plastic sample strain', *Journal of Applied Physics*, 107(4), p. 0435101.

Dunstan, D.J. and Bushby, A.J. (2004) 'Theory of deformation in small volumes of material', *Proceedings of the Royal Society of London Series a-Mathematical Physical and Engineering Sciences*, 460(2050), pp. 2781-2796.

Durst, K., Backes, B. and Goken, M. (2005) 'Indentation size effect in metallic materials: Correcting for the size of the plastic zone', *Scripta Materialia*, 52(11), pp. 1093-1097.

Edelstein, D., Heidenreich, J., Goldblatt, R., Cote, W., Uzoh, C., Lustig, N., Roper, P., McDevitt, T., Motsiff, W., Simon, A., Dukovic, J., Wachnik, R., Rathore, H., Schulz, R., Su, L., Luce, S. and Slattery, J. (1997) *Electron Devices Meeting, 1997. IEDM '97. Technical Digest., International. 7-10 Dec 1997.*

Egerton, R.F. (2005) *Physical Principles of Electron Microscopy: An Introduction to TEM, SEM, and AEM*. Springer.

Elmustafa, A.A. (2007) 'Pile-up/sink-in of rate-sensitive nanoindentation creeping solids', *Modelling and Simulation in Materials Science and Engineering*, 15(7), pp. 823-834.

Elmustafa, A.A. and Stone, D.S. (2003) 'Nanoindentation and the indentation size effect: Kinetics of deformation and strain gradient plasticity', *Journal of the Mechanics and Physics of Solids*, 51(2), pp. 357-381.

- Engler, O. and Randle, V. (2010) *Introduction to Texture Analysis: Macrotecture, Microtexture, and Orientation Mapping, Second Edition*. Taylor & Francis.
- Espinosa, H.D., Prorok, B.C. and Fischer, M. (2003) 'A methodology for determining mechanical properties of freestanding thin films and MEMS materials', *Journal of the Mechanics and Physics of Solids*, 51(1), pp. 47-67.
- Feng, G. and Ngan, A.H.W. (2002) 'Effects of creep and thermal drift on modulus measurement using depth-sensing indentation', *Journal of Materials Research*, 17(3), pp. 660-668.
- Feng, G. and Nix, W.D. (2004) 'Indentation size effect in MgO', *Scripta Materialia*, 51(6), pp. 599-603.
- Field, J.S. and Swain, M.V. (1993) 'A simple predictive model for spherical indentation', *Journal of Materials Research*, 8(2), pp. 297-306.
- Field, J.S. and Swain, M.V. (1995) 'Determining the mechanical-properties of small volumes of material from submicrometer spherical indentations', *Journal of Materials Research*, 10(1), pp. 101-112.
- Fischer-Cripps, A.C. (2000) *Introduction to Contact Mechanics*. Springer.
- Fischer-Cripps, A.C. (2001) 'Simulation of sub-micron indentation tests with spherical and Berkovich indenters', *Journal of Materials Research*, 16(7), pp. 2149-2157.
- Fischer-Cripps, A.C. (2004a) 'Multiple-frequency dynamic nanoindentation testing', *Journal of Materials Research*, 19(10), pp. 2981-2988.
- Fischer-Cripps, A.C. (2004b) 'A simple phenomenological approach to nanoindentation creep', *Materials Science and Engineering a-Structural Materials Properties Microstructure and Processing*, 385(1-2), pp. 74-82.
- Fischer-Cripps, A.C. (2011) *Nanoindentation*. Third Edition edn. New York: Springer.
- Fischer-Cripps, A.C., Karvankova, P. and Veprek, S. (2006) 'On the measurement of hardness of super-hard coatings', *Surface & Coatings Technology*, 200(18-19), pp. 5645-5654.
- Fleck, N.A. and Hutchinson, J.W. (1997) 'Strain gradient plasticity', in Hutchinson, J.W. and Wu, T.Y. (eds.) *Advances in Applied Mechanics, Vol 33*. pp. 295-361.
- Fleck, N.A. and Hutchinson, J.W. (2001) 'A reformulation of strain gradient plasticity', *Journal of the Mechanics and Physics of Solids*, 49(10), pp. 2245-2271.
- Ganneau, F.P., Constantinides, G. and Ulm, F.J. (2006) 'Dual-indentation technique for the assessment of strength properties of cohesive-frictional materials', *International Journal of Solids and Structures*, 43(6), pp. 1727-1745.
- Gao, H., Huang, Y., Nix, W.D. and Hutchinson, J.W. (1999) 'Mechanism-based strain gradient plasticity - I. Theory', *Journal of the Mechanics and Physics of Solids*, 47(6), pp. 1239-1263.

- Gao, H.J. and Huang, Y.G. (2003) 'Geometrically necessary dislocation and size-dependent plasticity', *Scripta Materialia*, 48(2), pp. 113-118.
- Garrido, M.A. and Rodriguez, J. (2007) 'Nanoindentation by multiple loads methodology: A pile up correction procedure', in Nam, S.W., Chang, Y.W., Lee, S.B. and Kim, N.J. (eds.) *Mechanical Behavior of Materials X, Pts 1 and 2*.
- Geetha, M., Singh, A.K., Asokamani, R. and Gogia, A.K. (2009) 'Ti based biomaterials, the ultimate choice for orthopaedic implants - A review', *Progress in Materials Science*, 54(3), pp. 397-425.
- Ghosh, S. and Roy, S. (2013) 'Electrochemical copper deposition from an ethaline-CuCl<sub>2</sub>.2H<sub>2</sub>O DES', *Surface and Coatings Technology*, (0).
- Giannakopoulos, A.E., Larsson, P.L. and Vestergaard, R. (1994) 'Analysis of Vicker's indentation', *International Journal of Solids and Structures*, 31(19), pp. 2679-2708.
- Giannakopoulos, A.E. and Suresh, S. (1999) 'Determination of elastoplastic properties by instrumented sharp indentation', *Scripta Materialia*, 40(10), pp. 1191-1198.
- Gilbert, J.L., Buckley, C.A. and Jacobs, J.J. (1993) 'In vivo corrosion of modular hip prosthesis components in mixed and similar metal combinations. The effect of crevice, stress, motion, and alloy coupling', *Journal of Biomedical Materials Research*, 27(12), pp. 1533-1544.
- Goldstein, J., Newbury, D.E., Joy, D.C., Lyman, C.E., Echlin, P., Lifshin, E., Sawyer, L. and Michael, J.R. (2003) *Scanning Electron Microscopy and X-ray Microanalysis*. 3 edn. Springer US.
- Gong, Y.S., Lee, C.P. and Yang, C.K. (1995) 'Atomic-force microscopy and Raman-spectroscopy studies on the oxidation of Cu thin-films', *Journal of Applied Physics*, 77(10), pp. 5422-5425.
- Goodall, R. and Clyne, T.W. (2006) 'A critical appraisal of the extraction of creep parameters from nanoindentation data obtained at room temperature', *Acta Materialia*, 54(20), pp. 5489-5499.
- Grupp, T.M., Weik, T., Bloemer, W. and Knaebel, H.-P. (2010) 'Modular titanium alloy neck adapter failures in hip replacement - failure mode analysis and influence of implant material', *Bmc Musculoskeletal Disorders*, 11.
- Hagan, J.T. and Swain, M.V. (1978) 'Origin of median and lateral cracks around plastic indents in brittle materials', *Journal of Physics D-Applied Physics*, 11(15), pp. 2091-&.
- Hainsworth, S.V., Chandler, H.W. and Page, T.F. (1996) 'Analysis of nanoindentation load-displacement loading curves', *Journal of Materials Research*, 11(8), pp. 1987-1995.
- Hainsworth, S.V., McGurk, M.R. and Page, T.F. (1998) 'The effect of coating cracking on the indentation response of thin hard-coated systems', *Surface & Coatings Technology*, 102(1-2), pp. 97-107.

- Hallam, P., Haddad, F. and Cobb, J. (2004) 'Pain in the well-fixed, aseptic titanium hip replacement - The role of corrosion', *Journal of Bone and Joint Surgery-British Volume*, 86B(1), pp. 27-30.
- Hamilton, J.C., Farmer, J.C. and Anderson, R.J. (1986) 'In situ Raman spectroscopy of anodic films formed on copper and silver in sodium hydroxide solution', *Journal of the Electrochemical Society*, 133(4), pp. 739-745.
- Hansen, D.C. (2008) 'Metal corrosion in the human body: The ultimate bio-corrosion scenario', *Electrochemical Society Interface*, 17(2), pp. 31-34.
- Harry, C. (1999) *Hardness Testing*. Ohio Asm International
- Hay, J.C., Bolshakov, A. and Pharr, G.M. (1999) 'A critical examination of the fundamental relations used in the analysis of nanoindentation data', *Journal of Materials Research*, 14(6), pp. 2296-2305.
- Hay, J.L. and Pharr, G.M. (2000) 'Instrumented Indentation Testing', *Materials Park, OH: ASM International, 2000.*, pp. 232-243.
- Herrmann, K. (2011) *Hardness Testing: Principles and Applications*. ASM International.
- Herrmann, K., Jennett, N.M., Wegener, W., Meneve, J., Hasche, K. and Seemann, R. (2000) 'Progress in determination of the area function of indenters used for nanoindentation', *Thin Solid Films*, 377, pp. 394-400.
- Hielscher, R. and Schaeben, H. (2008) 'A novel pole figure inversion method: specification of the MTEX algorithm', *Journal of Applied Crystallography*, 41, pp. 1024-1037.
- Holloway, K., Fryer, P.M., Cabral, C., Harper, J.M.E., Bailey, P.J. and Kelleher, K.H. (1992) 'Tantalum as a diffusion barrier between copper and silicon - failure mechanism and effect of nitrogen additions', *Journal of Applied Physics*, 71(11), pp. 5433-5444.
- Hong, S.H., Kim, K.S., Kim, Y.M., Hahn, J.H., Lee, C.S. and Park, J.H. (2005) 'Characterization of elastic moduli of Cu thin films using nanoindentation technique', *Composites Science and Technology*, 65(9), pp. 1401-1408.
- Hosseinzadeh, S., Eajazi, A. and Shahi, A.S. (2012) 'The Bearing Surfaces in Total Hip Arthroplasty –Options, Material Characteristics and Selection ', in Fokter, S.K. (ed.) *Recent Advances in Arthroplasty*. InTech.
- Howatson, A.M., Lund, P.G. and Todd, J.D. (1972) 'Properties of matter', in *Engineering Tables and Data*. Springer Netherlands.
- Hsu, C., Tsou, C. and Fang, W. (2007) 'Measuring thin film elastic modulus using a micromachined cantilever bending test by nanoindenter', *Journal of Micro-Nanolithography Memes and Moems*, 6(3), p. 0330111.
- Hu, C.K. and Harper, J.M.E. (1998) 'Copper interconnections and reliability', *Materials Chemistry and Physics*, 52(1), pp. 5-16.

Huang, Y., Zhang, F., Hwang, K.C., Nix, W.D., Pharr, G.M. and Feng, G. (2006) 'A model of size effects in nano-indentation', *Journal of the Mechanics and Physics of Solids*, 54(8), pp. 1668-1686.

Hysitron (2001) *Triboindenter User's Manual*. Available at: [http://grover.mirc.gatech.edu/equipment/instructions/triboindenter\\_user\\_manual.pdf](http://grover.mirc.gatech.edu/equipment/instructions/triboindenter_user_manual.pdf) (Accessed: 8th April).

Imam, M.A. and Fraker, A.C. (1996) *Proceedings of the 1994 Symposium on Medical Applications of Titanium and Its Alloys: The Material and Biological Issues, Nov 15 - 16 1994*. Phoenix, AZ, United states. ASTM.

ISO/FDIS 14577-1 (2002) 'Metallic materials — Instrumented indentation test for hardness and materials parameters'. ISO Central Secretariat, 1 rue de Varembe, 1211 Geneva 20 Switzerland.

Jahromi, G.B. (2008) *Investigation of the Near Surface Mechanical Properties of Gold-titanium Thin Films*. Oklahoma State University.

Jakkaraju, R. and Greer, A.L. (2002) 'Texture and hillocking in sputter-deposited copper thin films', *Journal of Materials Science: Materials in Electronics*, 13(5), pp. 285-294.

Jensen, R.J., Cummings, J.P. and Vora, H. (1984) 'Copper/polyimide materials system for high performance packaging', *IEEE transactions on components, hybrids, and manufacturing technology*, CHMT-7(4), pp. 384-393.

Ji, H., Li, M., Wang, C., Bang, H.S. and Bang, H.S. (2007) 'Comparison of interface evolution of ultrasonic aluminum and gold wire wedge bonds during thermal aging', *Materials Science and Engineering a-Structural Materials Properties Microstructure and Processing*, 447(1-2), pp. 111-118.

Jian, S.-R., Ku, S.-A., Luo, C.-W. and Juang, J.-Y. (2012) 'Nanoindentation of GaSe thin films', *Nanoscale Research Letters*, 7.

Jinno, T., Goldberg, V.M., Davy, D. and Stevenson, S. (1998) 'Osseointegration of surface-blasted implants made of titanium alloy and cobalt-chromium alloy in a rabbit intramedullary model', *Journal of Biomedical Materials Research*, 42(1), pp. 20-29.

Jones, I.P. (2001) *Materials Science for Electrical and Electronics Engineers*. Oxford University Press, Incorporated.

Joslin, D.L. and Oliver, W.C. (1990) 'A new method for analyzing data from continuous depth-sensing microindentation tests', *Journal of Materials Research*, 5(1), pp. 123-126.

Jungk, J.M., Boyce, B.L., Buchheit, T.E., Friedmann, T.A., Yang, D. and Gerberich, W.W. (2006) 'Indentation fracture toughness and acoustic energy release in tetrahedral amorphous carbon diamond-like thin films', *Acta Materialia*, 54(15), pp. 4043-4052.

Kalmykov, S.N. and Denecke, M.A. (2010) *Actinide nanoparticle research*. Springer Berlin Heidelberg.

- Kim, D.K., Nix, W.D., Vinci, R.P., Deal, M.D. and Plummer, J.D. (2001) 'Study of the effect of grain boundary migration on hillock formation in Al thin films', *Journal of Applied Physics*, 90(2), pp. 781-788.
- Kim, J.Y., Lee, B.W., Read, D.T. and Kwon, D. (2005) 'Influence of tip bluntness on the size-dependent nanoindentation hardness', *Scripta Materialia*, 52(5), pp. 353-358.
- King, R.B. (1987) 'Elastic analysis of some punch problems for a layered medium', *International Journal of Solids and Structures*, 23(12), pp. 1657-1664.
- Kobayashi, I., Miyazawa, T., Fujimoto, M., Kawaguchi, H. and Hara, T. (2004) 'Investigation of copper contamination into interlayer dielectrics by copper process', *Thin Solid Films*, 462, pp. 231-234.
- Korsunsky, A.M., McGurk, M.R., Bull, S.J. and Page, T.F. (1998) 'On the hardness of coated systems', *Surface & Coatings Technology*, 99(1-2), pp. 171-183.
- Kulkarni, A.V. and Bhushan, B. (1996) 'Nano/picoindentation measurements on single-crystal aluminum using modified atomic force microscopy', *Materials Letters*, 29(4-6), pp. 221-227.
- Kurosu, S., Nomura, N. and Chiba, A. (2006) 'Effect of sigma phase in Co-29Cr-6Mo alloy on corrosion behavior in saline solution', *Materials Transactions*, 47(8), pp. 1961-1964.
- Kurosu, S., Nomura, N., Yamaguchi, K., Fujinuma, S. and Chiba, A. (2005) 'Effects of 5th element addition to Co-29Cr-6Mo alloy containing impurity Ni on metal ion release', *Journal of the Japan Institute of Metals*, 69(10), pp. 886-891.
- Kurtz, S.M. (2009) *UHMWPE Biomaterials Handbook: Ultra High Molecular Weight Polyethylene in Total Joint Replacement and Medical Devices*. Academic Press.
- Lampe, F., Grischke, M., Wimmer, M.A., Nassutt, R., Klages, C.P., Hille, E. and Schneider, E. (1998) 'Influence of the femoral head surface hardness on abrasive wear mechanisms in the combination with polyethylene total hip replacement', *Biomedizinische Technik*, 43(3), pp. 58-62.
- Langton, D.J., Sidaginamale, R., Lord, J.K., Nargol, A.V.F. and Joyce, T.J. (2012) 'Taper junction failure in large-diameter metal-on-metal bearings', *Bone and Joint Research*, 1(4), pp. 56-63.
- Lawn, B.R. and Fuller, E.R. (1975) 'Equilibrium penny-like cracks in indentation fracture', *Journal of Materials Science*, 10(12), pp. 2016-2024.
- Lee, H.-J., Kim, D.I., Ahn, J.H. and Lee, D.N. (2005) 'Electron backscattered diffraction analysis of copper damascene interconnect for ultralarge-scale integration', *Thin Solid Films*, 474(12), pp. 250-254.
- Lee, S.Y., Choi, S.H. and Park, C.O. (2000) 'Oxidation, grain growth and reflow characteristics of copper thin films prepared by chemical vapor deposition', *Thin Solid Films*, 359(2), pp. 261-267.

- Li, B.Z., Sullivan, T.D., Lee, T.C. and Badami, D. (2004) 'Reliability challenges for copper interconnects', *Microelectronics Reliability*, 44(3), pp. 365-380.
- Li, H., Ghosh, A., Han, Y.H. and Bradt, R.C. (1993) 'The frictional component of the indentation size effect in low load microhardness testing', *Journal of Materials Research*, 8(5), pp. 1028-1032.
- Li, H. and Vlassak, J.J. (2009) 506 Keystone Drive, Warrendale, PA 15086, United States. Materials Research Society. Available at: <http://dx.doi.org/10.1557/jmr.2009.0144>.
- Li, J., Mayer, J.W. and Colgan, E.G. (1991) 'Oxidation and protection in copper and copper alloy thin-films', *Journal of Applied Physics*, 70(5), pp. 2820-2827.
- Li, X. and Bhushan, B. (2002) 'A review of nanoindentation continuous stiffness measurement technique and its applications', *Materials Characterization*, 48(1), pp. 11-36.
- Li, Y., He, K., Liao, C. and Pan, C. (2012) 'Measurements of mechanical properties of alpha-phase in Cu-Sn alloys by using instrumented nanoindentation', *Journal of Materials Research*, 27(1), pp. 192-196.
- Lian, J., Garay, J.E. and Wang, J. (2007) 'Grain size and grain boundary effects on the mechanical behavior of fully stabilized zirconia investigated by nanoindentation', *Scripta Materialia*, 56(12), pp. 1095-1098.
- Lilleodden, E.T., Bonin, W., Nelson, J., Wyrobek, J.T. and Gerberich, W.W. (1995) 'In-situ imaging of Mu-N load indents into gas', *Journal of Materials Research*, 10(9), pp. 2162-2165.
- Lim, Y.Y. and Chaudhri, M.M. (1999) 'The effect of the indenter load on the nanohardness of ductile metals: an experimental study on polycrystalline work-hardened and annealed oxygen-free copper', *Philosophical Magazine a-Physics of Condensed Matter Structure Defects and Mechanical Properties*, 79(12), pp. 2979-3000.
- Ling, C., Gross, M.E. and Brown, W.L. (1999) 'X-ray diffraction pole figure evidence for (111) sidewall texture of electroplated Cu in submicron damascene trenches', *Applied Physics Letters*, 74(5), pp. 682-684.
- Liu, R.F., Hu, C.K., Gignac, L., Harper, J.M.E., Lloyd, J., Liu, X.H. and Stamper, A.K. (2004) 'Effects of failure criteria on the lifetime distribution of dual-damascene Cu line/via on W', *Journal of Applied Physics*, 95(7), pp. 3737-3744.
- Lloyd, J.R., Clemens, J. and Snede, R. (1999) 'Copper metallization reliability', *Microelectronics Reliability*, 39(11), pp. 1595-1602.
- Long, M. and Rack, H.J. (1998) 'Titanium alloys in total joint replacement - a materials science perspective', *Biomaterials*, 19(18), pp. 1621-1639.
- López, H., Saldívar, A. and Huang, P. (2000) 'Development and Properties of  $\epsilon$ -Martensite in Co-Cr-Mo Alloys for Biomaterials Applications', in Meike, A., Gonis, A., Turchi, P.A. and Rajan, K. (eds.) *Properties of Complex Inorganic Solids 2*. Springer US.

Loubet, J.L., Georges, J.M. and Meille, G. (1986a) 'Microindentation Techniques in Materials Science and Engineering', in Blau, P.J. and Lawn, B.R. (eds.) Philadelphia: American Society for Testing and Materials.

Loubet, J.L., Georges, J.M. and Meille, J. (1986b) 'Vickers Indentation Curves of Elastoplastic Materials', in Blau, P.J. and Lawn, B.R. (eds.) *Microindentation Techniques in Materials Science and Engineering*. Philadelphia: American Society for Testing and Materials.

Lu, D. and Wong, C.P. (2008) *Materials for Advanced Packaging*. Springer.

Lucas, B.N. and Oliver, W.C. (1999) 'Indentation power-law creep of high-purity indium', *Metallurgical and Materials Transactions a-Physical Metallurgy and Materials Science*, 30(3), pp. 601-610.

Lucas, M., Gall, K. and Riedo, E. (2008) 'Tip size effects on atomic force microscopy nanoindentation of a gold single crystal', *Journal of Applied Physics*, 104(11).

Ma, Q. and Clarke, D.R. (1995) 'Size-dependent hardness of silver single-crystals', *Journal of Materials Research*, 10(4), pp. 853-863.

Majumdar, P., Singh, S.B. and Chakraborty, M. (2008) 'Elastic modulus of biomedical titanium alloys by nano-indentation and ultrasonic techniques - A comparative study', *Materials Science and Engineering a-Structural Materials Properties Microstructure and Processing*, 489(1-2), pp. 419-425.

Malzbender, J., de With, G. and den Toonder, J. (2000) 'The P-h(2) relationship in indentation', *Journal of Materials Research*, 15(5), pp. 1209-1212.

Mann, A. (2007) 'Nanomechanical Properties of Solid Surfaces and Thin Films', in Bhushan, B. (ed.) *Springer Handbook of Nanotechnology*. Springer Berlin Heidelberg.

Mann, A.B. and Pethica, J.B. (1996) 'Nanoindentation studies in a liquid environment', *Langmuir*, 12(19), pp. 4583-4586.

Matthews, A. (2012) *Advanced Surface Coatings: A Handbook of Surface Engineering*. Springer London, Limited.

Mencik, J., Quandt, E. and Munz, D. (1996) 'Elastic modulus of TbDyFe films - A comparison of nanoindentation and bending measurements', *Thin Solid Films*, 287(1-2), pp. 208-213.

Merchant, S.M., Kang, S.H., Sanganeria, M., Van Schravendijk, B. and Mountsier, T. (2001) 'Copper interconnects for semiconductor devices', *JOM*, 53(6), pp. 43-48.

Micromaterials Ltd 'Willow House, Yale Business Park, Ellice Way, Wrexham LL137YL UK'.

Min, K.H., Chun, K.C. and Kim, K.B. (1996) 'Comparative study of tantalum and tantalum nitrides (Ta<sub>2</sub>N and TaN) as a diffusion barrier for Cu metallization', *Journal of Vacuum Science & Technology B*, 14(5), pp. 3263-3269.

Miura, O., Miyazaki, K., Takahashi, A., Watanabe, R. and Miwa, T. (1993) 'Fabrication of thin-film multilayer substrate using copper clad polyimide sheets', *IEEE transactions on components, hybrids, and manufacturing technology*, 16(8), pp. 817-821.

Mohs, F. (1822) *Grundriss der Mineralogie*. Dresden.

Mondal, P., Northwestern University, C. and Environmental, E. (2008) *Nanomechanical Properties of Cementitious Materials*. Northwestern University.

Moriyama, M., Matsunaga, K. and Murakami, M. (2003) 'The effect of strain on abnormal grain growth in Cu thin films', *Journal of Electronic Materials*, 32(4), pp. 261-267.

Mueller, J., Balzar, D., Geiss, T.H., Read, D.T. and Keller, R.R. (2006) 'Comparison of texture in copper and aluminium thin films determined by XRD and EBSD', *Applications of X-Ray Analysis Conf.* Colorado Spring, Co National Institute of Standards and Technology pp. 201-206.

Murarka, S.P., Gutmann, R.J., Kaloyeros, A.E. and Lanford, W.A. (1993) 'Advanced multilayer metallization schemes with copper as interconnection metal', *Thin Solid Films*, 236(1-2), pp. 257-266.

Navamathavan, R., Park, S.-J., Hahn, J.-H. and Choi, C.K. (2008) 'Nanoindentation 'pop-in' phenomenon in epitaxial ZnO thin films on sapphire substrates', *Materials Characterization*, 59(4), pp. 359-364.

Navarro, M., Michiardi, A., Castano, O. and Planell, J.A. (2008) 'Biomaterials in orthopaedics', *Journal of the Royal Society Interface*, 5(27), pp. 1137-1158.

Necas, D. and Klapetek, P. (2012) 'Gwyddion: an open-source software for SPM data analysis', *Central European Journal of Physics*, 10(1), pp. 181-188.

Nix, W.D. and Gao, H.J. (1998) 'Indentation size effects in crystalline materials: A law for strain gradient plasticity', *Journal of the Mechanics and Physics of Solids*, 46(3), pp. 411-425.

Nohava, J., Randall, N.X. and Conte, N. (2009) 'Novel ultra nanoindentation method with extremely low thermal drift: Principle and experimental results', *Journal of Materials Research*, 24(3), pp. 873-882.

Nowicki, M., Richter, A., Wolf, B. and Kaczmarek, H. (2003) 'Nanoscale mechanical properties of polymers irradiated by UV', *Polymer*, 44(21), pp. 6599-6606.

Oliver, W.C., Hutchings, R. and Pethica, J.B. (1986) 'Microindentation Techniques in Materials Science and Engineering', in Blau, P.J. and Lawn, B.R. (eds.) *ASTM STP 889*. Philadelphia: American Society for Testing and Materials.

Oliver, W.C. and Pharr, G.M. (1992) 'An improved technique for determining hardness and elastic-modulus using load and displacement sensing indentation experiments', *Journal of Materials Research*, 7(6), pp. 1564-1583.

Oliver, W.C. and Pharr, G.M. (2004) 'Measurement of hardness and elastic modulus by instrumented indentation: Advances in understanding and refinements to methodology', *Journal of Materials Research*, 19(1), pp. 3-20.

Page, T.F. and Hainsworth, S.V. (1993) 'Using nanoindentation techniques for the characterization of coated systems - a critique', *Surface & Coatings Technology*, 61(1-3), pp. 201-208.

Palosz, B., Grzanka, E., Gierlotka, S., Stel'makh, S., Pielaszek, R., Lojkowski, W., Bismayer, U., Neufeind, J., Weber, H.P. and Palosz, W. (2003) 'Application of X-ray powder diffraction to nano-materials - Determination of the atomic structure of nanocrystals with relaxed and strained surfaces', *Phase Transitions*, 76(1-2), pp. 171-185.

Pecharsky, V. and Zavalij, P. (2008) *Fundamentals of Powder Diffraction and Structural Characterization of Materials, Second Edition*. Springer.

Pelletier, H., Krier, J., Cornet, A. and Mille, P. (2000) 'Limits of using bilinear stress-strain curve for finite element modeling of nanoindentation response on bulk materials', *Thin Solid Films*, 379(1-2), pp. 147-155.

Pellicer, E., Pane, S., Panagiotopoulou, V., Fusco, S., Sivaraman, K.M., Surinach, S., Baro, M.D., Nelson, B.J. and Sort, J. (2012) 'Localized Electrochemical Deposition of Porous Cu-Ni Microcolumns: Insights into the Growth Mechanisms and the Mechanical Performance', *International Journal of Electrochemical Science*, 7(5), pp. 4014-4029.

Perez-Prado, M.T. and Vlassak, J.J. (2002) 'Microstructural evolution in electroplated Cu thin films', *Scripta Materialia*, 47(12), pp. 817-823.

Perez-Robles, F., Garcia-Rodriguez, F.J., Jimenez-Sandoval, S. and Gonzalez-Hernandez, J. (1999) 'Raman study of copper and iron oxide particles embedded in an SiO<sub>2</sub> matrix', *Journal of Raman Spectroscopy*, 30(12), pp. 1099-1104.

Pethica, J.B. and Tabor, D. (1979) 'Contact of characterized metal-surfaces at very low loads - deformation and adhesion', *Surface Science*, 89(1-3), pp. 182-190.

Pham, V.-H., Yook, S.-W., Li, Y., Jeon, G., Lee, J.-J., Kim, H.-E. and Koh, Y.-H. (2011) 'Improving hardness of biomedical Co-Cr by deposition of dense and uniform TiN films using negative substrate bias during reactive sputtering', *Materials Letters*, 65(11), pp. 1707-1709.

Pharr, G.M. (1998) 'Measurement of mechanical properties by ultra-low load indentation', *Materials Science and Engineering a-Structural Materials Properties Microstructure and Processing*, 253(1-2), pp. 151-159.

Pharr, G.M., Oliver, W.C. and Brotzen, F.R. (1992) 'On the generality of the relationship among contact stiffness, contact area, and elastic modulus during indentation', *Journal of Materials Research*, 7(3), pp. 613-617.

Pinnel, M.R. (1979) 'Diffusion-related behaviour of gold in thin film systems', *Gold Bulletin*, 12(2), pp. 62-71.

- Pollock, H.M., Maugis, D. and Barquins, M. (1986) 'Microindentation Techniques in Materials Science and Engineering', in Blau, P.J. and Lawn, B.R. (eds.) Philadelphia, PA: American Society for Testing and Materials ASTM STP 889.
- Punt, I., Visser, V., Rhijn, L., Kurtz, S., Antonis, J., Schurink, G. and Ooij, A. (2008) 'Complications and reoperations of the SB Charité lumbar disc prosthesis: experience in 75 patients', *European Spine Journal*, 17(1), pp. 36-43.
- Qu, S., Huang, Y., Nix, W.D., Jiang, H., Zhang, F. and Hwang, K.C. (2004) 'Indenter tip radius effect on the Nix-Gao relation in micro- and nanoindentation hardness experiments', *Journal of Materials Research*, 19(11), pp. 3423-3434.
- Randle, V. (2008) *Microtexture Determination and Its Applications*. Maney, for the Institute of Materials, Minerals and Mining.
- Reid, A.C.E., Lua, R.C., Garcia, R.E., Coffman, V.R. and Langer, S.A. (2009) 'Modelling Microstructures with OOF2', *International Journal of Materials & Product Technology*, 35(3-4), pp. 361-373.
- Riviere, J.C. and Myhra, S. (2010) *Handbook of Surface and Interface Analysis: Methods for Problem-Solving, Second Edition*. Taylor & Francis.
- Roy, M.E., Whiteside, L.A., Xu, J. and Katerberg, B.J. (2010) 'Diamond-like carbon coatings enhance the hardness and resilience of bearing surfaces for use in joint arthroplasty', *Acta Biomaterialia*, 6(4), pp. 1619-1624.
- Ruoff, A.L., Kramer, E.J. and Li, C.Y. (1988) 'Developer-induced debonding of photoresist from copper', *Ibm Journal of Research and Development*, 32(5), pp. 631-635.
- Ryu, J.J., Dayal, V. and Shrotriya, P. (2007) 'Onset of surface damage in modular orthopedic implants: Influence of normal contact loading and stress-assisted dissolution', *Experimental Mechanics*, 47(3), pp. 395-403.
- Saha, R. and Nix, W.D. (2002) 'Effects of the substrate on the determination of thin film mechanical properties by nanoindentation', *Acta Materialia*, 50(1), pp. 23-38.
- Sahin, O., Uzun, O., Koelemen, U. and Ucar, N. (2008) 'Mechanical characterization for beta-Sn single crystals using nanoindentation tests', *Materials Characterization*, 59(4), pp. 427-434.
- Saldivar-Garcia, A.J. and Lopez, H.F. (2005) 'Microstructural effects on the wear resistance of wrought and as-cast Co-Cr-Mo-C implant alloys', *Journal of Biomedical Materials Research Part A*, 74A(2), pp. 269-274.
- Scales, J.T. (1991) 'Black staining around titanium-alloy prostheses - an orthopedic enigma', *Journal of Bone and Joint Surgery-British Volume*, 73(4), pp. 534-536.
- Schenk, R. (2001) 'The Corrosion Properties of Titanium and Titanium Alloys', in *Titanium in Medicine*. Springer Berlin Heidelberg.
- Schoberl, T., Gupta, H.S. and Fratzl, P. (2003) 'Measurements of mechanical properties in Ni-base superalloys using nanoindentation and atomic force

microscopy', *Materials Science and Engineering a-Structural Materials Properties Microstructure and Processing*, 363(1-2), pp. 211-220.

Schuh, C.A. (2006) 'Nanoindentation studies of materials', *Materials Today*, 9(5), pp. 32-40.

Schwartz, A.J. (2009) *Electron backscatter diffraction in materials science*. Springer Science+Business Media.

Schwartz, A.J. (2010) *Electron Backscatter Diffraction in Materials Science*. Springer Science+Business Media.

Schwartz, G.C. and Srikrishnan, K.V. (2006) *Handbook of Semiconductor Interconnection Technology, Second Edition*. Taylor & Francis.

Schwarzer, R.A. (1997) 'Automated crystal lattice orientation mapping using a computer-controlled SEM', *Micron*, 28(3), pp. 249-265.

Shan, Z.W., Mishra, R.K., Asif, S.A.S., Warren, O.L. and Minor, A.M. (2008) 'Mechanical annealing and source-limited deformation in submicrometre-diameter Ni crystals', *Nature Materials*, 7(2), pp. 115-119.

Shen, L., Cheong, W.C.D., Foo, Y.L. and Chen, Z. (2012) 'Nanoindentation creep of tin and aluminium: A comparative study between constant load and constant strain rate methods', *Materials Science and Engineering a-Structural Materials Properties Microstructure and Processing*, 532, pp. 505-510.

Siller, L., Peltekis, N., Krishnamurthy, S., Chao, Y., Bull, S.J. and Hunt, M.R.C. (2005) 'Gold film with gold nitride - A conductor but harder than gold', *Applied Physics Letters*, 86(22).

Skrzypczak, M., Guerret-Piecourt, C., Bec, S., Loubet, J.L. and Guerret, O. (2009) 'Use of a nanoindentation fatigue test to characterize the ductile-brittle transition', *Journal of the European Ceramic Society*, 29(6), pp. 1021-1028.

Smith, W.F. and Hashemi, J. (2009) *Foundations of materials science and engineering*. Michigan: McGraw-Hill Higher Education.

Sneddon, I.N. (1965) 'Relation between load and penetration in axisymmetric Boussinesq problem for punch of arbitrary profile', *International Journal of Engineering Science*, 3, pp. 47-57.

Soare, S., Bull, S.J., O'Neil, A.G., Wright, N., Horsfall, A. and dos Santos, J.M.M. (2004) 'Nanoindentation assessment of aluminium metallisation; the effect of creep and pile-up', *Surface & Coatings Technology*, 177, pp. 497-503.

Soifer, Y.M., Verdyan, A. and Rapoport, L. (2002) 'Nanoindentation size effect in alkali-halide single crystals', *Materials Letters*, 56(3), pp. 127-130.

Sonnweber-Ribic, P., Gruber, P., Dehm, G. and Arzt, E. (2006) 'Texture transition in Cu thin films: Electron backscatter diffraction vs. X-ray diffraction', *Acta Materialia*, 54(15), pp. 3863-3870.

Srivastava, A. (2006) *Dynamic Friction Measurement and Modeling at the Micro/nano Scale*. Santa Barbara: University of California

Stone, D.S., Yoder, K.B. and Sproul, W.D. (1991) 'Hardness and elastic-modulus of tin based on continuous indentation technique and new correlation', *Journal of Vacuum Science & Technology a-Vacuum Surfaces and Films*, 9(4), pp. 2543-2547.

Strehle, S., Menzel, S., Bartha, J.W. and Wetzig, K. (2010) 'Electroplating of Cu(Ag) thin films for interconnect applications', *Microelectronic Engineering*, 87(2), pp. 180-186.

Sun, S., Zheng, S., Bell, T. and Smith, J. (1999) 'Indenter tip radius and load frame compliance calibration using nanoindentation loading curves', *Philosophical Magazine Letters*, 79(9), pp. 649-658.

Sundgren, J.E., Bodo, P. and Lundstrom, I. (1986) 'Auger-electron spectroscopic studies of the interface between human-tissue and implants of titanium and stainless-steel', *Journal of Colloid and Interface Science*, 110(1), pp. 9-20.

Suresh, S., Nieh, T.G. and Choi, B.W. (1999) 'Nano-indentation of copper thin films on silicon substrates', *Scripta Materialia*, 41(9), pp. 951-957.

Swadener, J.G., George, E.P. and Pharr, G.M. (2002) 'The correlation of the indentation size effect measured with indenters of various shapes', *Journal of the Mechanics and Physics of Solids*, 50(4), pp. 681-694.

Tabor, D. (1954) 'Mohs's hardness scale - A physical interpretation', *Proceedings of the Physical Society. Section B*, 67(3), pp. 249-257.

Tabor, D. (2000) *The Hardness of Metals*. Oxford University Press, USA.

Takeuchi, M., Abe, Y., Yoshida, Y., Nakayama, Y., Okazaki, M. and Akagawa, Y. (2003) 'Acid pretreatment of titanium implants', *Biomaterials*, 24(10), pp. 1821-1827.

Taljat, B. and Pharr, G.M. (2004) 'Development of pile-up during spherical indentation of elastic-plastic solids', *International Journal of Solids and Structures*, 41(14), pp. 3891-3904.

Tan, E.P.S., Zhu, Y., Yu, T., Dai, L., Sow, C.H., Tan, V.B.C. and Lim, C.T. (2007) 'Crystallinity and surface effects on Young's modulus of CuO nanowires', *Applied Physics Letters*, 90(16), p. 1631121.

Taylor, G.I. (1938) 'Plastic strain in metals', *Institute of Metals -- Journal*, 62(1), pp. 307-324.

Tian, Z.Q., Ren, B. and Wu, D.Y. (2002) 'Surface-enhanced Raman scattering: From noble to transition metals and from rough surfaces to ordered nanostructures', *Journal of Physical Chemistry B*, 106(37), pp. 9463-9483.

Tohid, R.R. and Bull, S.J. (2007) 'Getting accurate nanoindentation data from zinc: Time-dependent and microstructural effects', *International Journal of Materials Research*, 98(5), pp. 353-359.

Tong, C.J., Hsing, K.S. and Lin, M.T. (2010) 'Anelastic Mechanical Behavior Measurement of thin Films Using Novel Beam deflection Method', in Bremand, F. (ed.) *Icem 14: 14th International Conference on Experimental Mechanics, Vol 6*.

Tsui, T.Y., Oliver, W.C. and Pharr, G.M. (1996) 'Influences of stress on the measurement of mechanical properties using nanoindentation: Part I. Experimental studies in an aluminum alloy', *Journal of Materials Research*, 11(3), pp. 752-759.

Tsui, T.Y., Oliver, W.C. and Pharr, G.M. (1997a) 'Indenter geometry effects on the measurement of mechanical properties by nanoindentation with sharp indenters', in Gerberich, W.W., Gao, H.J., Sundgren, J.E. and Baker, S.P. (eds.) *Thin Films: Stresses and Mechanical Properties Vi*.

Tsui, T.Y., Oliver, W.C. and Pharr, G.M. (1997b) 'Nanoindentation of soft films on hard substrates: The importance of pile-up', in Gerberich, W.W., Gao, H.J., Sundgren, J.E. and Baker, S.P. (eds.) *Thin Films: Stresses and Mechanical Properties Vi*.

Tsui, T.Y. and Pharr, G.M. (1999) 'Substrate effects on nanoindentation mechanical property measurement of soft films on hard substrates', *Journal of Materials Research*, 14(1), pp. 292-301.

Tymiak, N.I., Kramer, D.E., Bahr, D.F., Wyrobek, T.J. and Gerberich, W.W. (2001) 'Plastic strain and strain gradients at very small indentation depths', *Acta Materialia*, 49(6), pp. 1021-1034.

Tymiak, N.I., Volinsky, A.A., Kriese, M.D., Downs, S.A. and Gerberich, W.W. (2000) 'The role of plasticity in bimaterial fracture with ductile interlayers', *Metallurgical and Materials Transactions A: Physical Metallurgy and Materials Science*, 31(13), pp. 863-872.

Vanasupa, L., Joo, Y.C., Besser, P.R. and Pramanick, S. (1999) 'Texture analysis of damascene-fabricated Cu lines by x-ray diffraction and electron backscatter diffraction and its impact on electromigration performance', *Journal of Applied Physics*, 85(5), pp. 2583-2590.

VanLandingham, M.R. (2003) 'Review of instrumented indentation', *Journal of Research of the National Institute of Standards and Technology*, 108(4), pp. 249-265.

Vereecken, P.M., Binstead, R.A., Deligianni, H. and Andricacos, P.C. (2005) 'The chemistry of additives in damascene copper plating', *Ibm Journal of Research and Development*, 49(1), pp. 3-18.

Virtanen, S., Milosev, I., Gomez-Barrena, E., Trebse, R., Salo, J. and Konttinen, Y.T. (2008) 'Special modes of corrosion under physiological and simulated physiological conditions', *Acta Biomaterialia*, 4(3), pp. 468-476.

Vlassak, J.J. and Nix, W.D. (1992) 'A new bulge test technique for the determination of Young's modulus and Poisson ratio of thin-films', *Journal of Materials Research*, 7(12), pp. 3242-3249.

Vlassak, J.J. and Nix, W.D. (1993) 'Indentation modulus of elastically anisotropic half-spaces', *Philosophical Magazine a-Physics of Condensed Matter Structure Defects and Mechanical Properties*, 67(5), pp. 1045-1056.

- Vlassak, J.J. and Nix, W.D. (1994) 'Measuring the elastic properties of anisotropic materials by means of indentation experiments', *Journal of the Mechanics and Physics of Solids*, 42(8), pp. 1223-1245.
- Volinsky, A.A. and Gerberich, W.W. (2003) 'Nanoindentation techniques for assessing mechanical reliability at the nanoscale', *Microelectronic Engineering*, 69(2-4), pp. 519-527.
- Volinsky, A.A., Hauschildt, M., Vella, J.B., Edwards, N.V., Gregory, R. and Gerberich, W.W. (2002) 'Residual stress and microstructure of electroplated Cu film on different barrier layers', in Ozkan, C.S., Freund, L.B., Cammarata, B.C. and Gao, H. (eds.) *Thin Films: Stresses and Mechanical Properties IX*. Warrendale: Materials Research Society.
- Volinsky, A.A., Moody, N.R. and Gerberich, W.W. (2004) 'Nanoindentation of Au and Pt/Cu thin films at elevated temperatures', *Journal of Materials Research*, 19(9), pp. 2650-2657.
- Volinsky, A.A., Vella, J., Adhietty, I.S., Sarihan, V., Mercado, L., Yeung, B.H. and Gerberich, W.W. (2001) Boston, MA, United states. Materials Research Society.
- Voyiadjis, G.Z. and Peters, R. (2010) 'Size effects in nanoindentation: an experimental and analytical study', *Acta Mechanica*, 211(1-2), pp. 131-153.
- Wang, K. (1996) 'The use of titanium for medical applications in the USA', *Materials Science and Engineering a-Structural Materials Properties Microstructure and Processing*, 213(1-2), pp. 134-137.
- Wang, X., Shi, W., She, G. and Mu, L. (2012) 'Surface-Enhanced Raman Scattering (SERS) on transition metal and semiconductor nanostructures', *Physical Chemistry Chemical Physics*, 14(17), pp. 5891-5901.
- Wang, X.H., Jacobsen, S., He, J.Y., Zhang, Z.L., Lee, S.F. and Lein, H.L. (2009) 'Application of nanoindentation testing to study of the interfacial transition zone in steel fiber reinforced mortar', *Cement and Concrete Research*, 39(8), pp. 701-715.
- Wang, Y., Raabe, D., Kluber, C. and Roters, F. (2004) 'Orientation dependence of nanoindentation pile-up patterns and of nanoindentation microtextures in copper single crystals', *Acta Materialia*, 52(8), pp. 2229-2238.
- Waseda, Y., Matsubara, E. and Shinoda, K. (2011) *X-Ray Diffraction Crystallography: Introduction, Examples and Solved Problems*. Springer.
- Wiedenman, B., Sundaram, V., Liu, F., Krishnan, G., Roberts, H., Brooks, P., Johal, K., Iyer, M., Tummala, R.R. and Ieee (2007) 'Multi-layer copper-dielectric adhesion challenges of 5-12 micron lines/spaces for next generation SOP (System-on-Package)/microprocessor package substrates', in *57th Electronic Components & Technology Conference, 2007 Proceedings*.
- Wilkinson, A.J. and Hirsch, P.B. (1997) 'Electron diffraction based techniques in scanning electron microscopy of bulk materials', *Micron*, 28(4), pp. 279-308.
- Williams, D.F. (1981) *Fundamental aspects of biocompatibility*. CRC Press, pp. 87-94.

Wilson, C.J. (2009) *Stress Measurements in deep sub-micron damascene copper interconnects*. PhD thesis at Newcastle University.

Wolf, B. (2000) 'Inference of mechanical properties from instrumented depth sensing indentation at tiny loads and indentation depths', *Crystal Research and Technology*, 35(4), pp. 377-399.

Wolf, B. and Richter, A. (2003) 'The concept of differential hardness in depth sensing indentation', *New Journal of Physics*, 5, pp. 15.1-7.

Wong, S.S., Ryu, C., Lee, H., Loke, A.L.S., Kwon, K.W., Bhattacharya, S., Eaton, R., Faust, R., Mikkola, B., Mucha, J. and Ormando, J. (1998), Barrier seed layer requirements for copper interconnects, IEEE, San Francisco, pp. 107-109 .

Xiang, Y. (2005) *Plasticity in Cu thin films: an experimental investigation of the effect of microstructure*, PhD thesis at Harvard University

Xiang, Y., Chen, X. and Vlassak, J.J. (2002) 'The mechanical properties of electroplated Cu thin films measured by means of the bulge test technique', in Ozkan, C.S., Freund, L.B., Cammarata, B.C. and Gao, H. (eds.) *Thin Films: Stresses and Mechanical Properties Ix*, Materials Research society, 695 pp. L.4.9.

Xiang, Y., Tsui, T.Y. and Vlassak, J.J. (2006) 'The mechanical properties of freestanding electroplated Cu thin films', *Journal of Materials Research*, 21(6), pp. 1607-1618.

Xue, Z., Huang, Y., Hwang, K.C. and Li, M. (2002) 'The influence of indenter tip radius on the micro-indentation hardness', *Journal of Engineering Materials and Technology-Transactions of the Asme*, 124(3), pp. 371-379.

Yamanaka, K., Mori, M. and Chiba, A. (2013) 'Nanoarchitected Co–Cr–Mo orthopedic implant alloys: Nitrogen-enhanced nanostructural evolution and its effect on phase stability', *Acta Biomaterialia*, 9(4), pp. 6259-6267.

Yeap, K.B., Iacopi, F., Geisler, H., Hangen, U. and Zschech, E. (2013) 'Nanoindentation for reliability assessment of ULK films and interconnects structures', *Microelectronic Engineering*, 106, pp. 182-187.

Yost, F.G. (1983) 'On the definition of microhardness', *Metallurgical transactions. A, Physical metallurgy and materials science*, 14 A(5), pp. 947-952.

Yu, N., Bonin, W.A. and Polycarpou, A.A. (2005) 'High-resolution capacitive load-displacement transducer and its application in nanoindentation and adhesion force measurements', *Review of Scientific Instruments*, 76(4).

Zhang, J.M., Ma, F. and Xu, K.W. (2004) 'Calculation of the surface energy of FCC metals with modified embedded-atom method', *Applied Surface Science*, 229(1-4), pp. 34-42.

Zhang, T.-Y. and Xu, W.-H. (2002a) 'Surface effects on nanoindentation', *Journal of Materials Research*, 17(7), pp. 1715-1720.

Zhang, T.Y. and Xu, W.H. (2002b) 'Surface effects on nanoindentation', *Journal of Materials Research*, 17(7), pp. 1715-1720.

Zheng, L., Schmid, A.W. and Lambropoulos, J.C. (2007) 'Surface effects on Young's modulus and hardness of fused silica by nanoindentation study', *Journal of Materials Science*, 42(1), pp. 191-198.

Zhou, W. and Wang, Z.L. (2007) *Scanning microscopy for nanotechnology*. Springer-Verlag New York.

Zhou, Y.-L., Niinomi, M., Akahori, T., Nakai, M. and Fukui, H. (2007) 'Comparison of various properties between titanium-tantalum alloy and pure titanium for biomedical applications', *Materials Transactions*, 48(3), pp. 380-384.

## *Nomenclature*

---

### *Latin Characters:*

A	Plate area
$A_c$	Contact area
a	Contact radius
$a_c$	Characteristic contact radius
$a_0$	Contact circle radius
$C_r$	Creep factor
C	Tip geometry factor
$C_f$	Frame compliance
$C_n$	Area function coefficient
$C_s$	Sample compliance
$C_{total}$	Total compliance
d	Spacing between crystallographic planes
E	Young's modulus
$E_c$	Young's modulus of coating
$E_i$	Young's modulus of indenter
$E_i$	Young's modulus of interlayer
$E_r$	Reduced modulus (contact modulus)
$E_s$	Young's modulus of substrate
$E^*$	Normalised Young's modulus
$F_e$	Electrostatic force
$F_m$	Mechanical force
$F_{max}$	Maximum load
H	Hardness
$H_v$	Vickers hardness
h	Displacement
$h_c$	Contact depth
$h_e$	Elastic distance into the surface
$h_f$	Final displacement after complete unloading
$h_i$	Initial penetration depth
$h_{max}$	Displacement at peak load
$h_s$	Sample displacement
$h_{total}$	Total displacement
$\dot{h}_h$	Total displacement rate
$\dot{h}^t$	Thermal drift rate
$K_e$	Loading curve fitting parameter
$K_{ep}$	Loading curve fitting parameter
$K_{exp}$	Loading curve fitting parameter
$K_m$	Loading curve fitting parameter

$K_p$	Loading curve fitting parameter
$K_s$	Stiffness of support spring
$k$	Initial penetration depth calculation constant
$m_i$	Initial penetration depth calculation exponent
$m$	Power-law exponent
$n$	Order of reflection
$P$	Load
$P_i$	Lowest attainable contact force
$P_{\max}$	Maximum load
$\dot{P}$	Unload rate at the onset of unloading
$R$	Relative radius of curvature
$R_i$	Radius of the curvature of the indenter
$R_p$	Plastic zone radius
$R_r$	Radius of the curvature of the residual impression
$R_a$	Average roughness
$r$	Indenter radius
$S$	Contact stiffness
$T$	Temperature
$T_H$	Homologous temperature
$T_{mp}$	Melting point temperature
$t_c$	Thickness of coating
$t_i$	Thickness of interlayer
$t_s$	Thickness of substrate
$U$	EBSD accelerating voltage
$V$	Applied voltage
$Y$	Yield stress

***Greek Characters:***

$\alpha$	Power-law constant
$\alpha$	Semi-angle of load supporting cone of material
$\beta$	Correction factor
$\gamma$	Correction factor
$\delta$	Displacement
$\delta_e$	Elastic depth of indentation
$\delta_l$	Size of each movement of the electron beam
$\delta_p$	Plastic depth of indentation
$\partial_c$	Coating displacement
$\partial_i$	Interlayer displacement
$\partial_s$	Substrate displacement
$\varepsilon$	Tip dependent contact depth factor
$\varepsilon_{ind}$	Indenter strain
$\varepsilon_0$	Dielectric constant of air

$\theta$	Half apical angle of cone
$\lambda$	Electromagnetic radiation wavelength
$\nu_s$	Poisson ratio of sample
$\nu_i$	Poisson ratio of indenter
$\xi$	Correction factor
$\sigma_{\text{ind}}$	Indenter stress
$\phi$	Empirical constant
$\psi$	Empirical constant

***Acronyms:***

AE	Auger electrons
AFM	Atomic force microscopy
BE	Binding energy
BSE	Back-scattered electrons
CMP	Chemical-mechanical polishing
CSM	Continuous stiffness measurement
DSI	Depth-sensing indentation
EBSD	Electron back-scattered diffraction
ECP	Electro-chemical plating
EDX	Energy dispersive X-ray spectroscopy
ESCA	Electron spectroscopy for chemical analysis
ESEM	Environmental scanning electron microscopy
GND	Geometrically necessary dislocations
IC	Interconnect
IL	Ionic liquid
ISE	Indentation size effect
KE	Kinetic energy
OOF2	Object Oriented Finite 2
PVD	Physical vapour deposition
RGB	Red, green, blue
RIE	Reactive ion etching
RMS	Root mean-square
RTIL	Room temperature ionic liquid
SE	Secondary electrons
SEM	Scanning electron microscopy
SPM	Scanning probe microscopy
UHMWPE	Ultra high molecular weight polyethylene
UHV	Ultra high vacuum
ULSI	Ultra large-scale integration
XPS	X-ray photoelectron spectroscopy
XRD	X-ray diffraction